REPORT NO.
UCB/EERC-78/05
APRIL 1978

EARTHQUAKE ENGINEERING RESEARCH CENTER

HYSTERETIC BEHAVIOR OF REINFORCED CONCRETE COLUMNS SUBJECTED TO HIGH AXIAL AND CYCLIC SHEAR FORCES

by

STAN W. ZAGAJESKI
VITELMO V. BERTERO
JACK G. BOUWKAMP

Report to Sponsor:
National Science Foundation

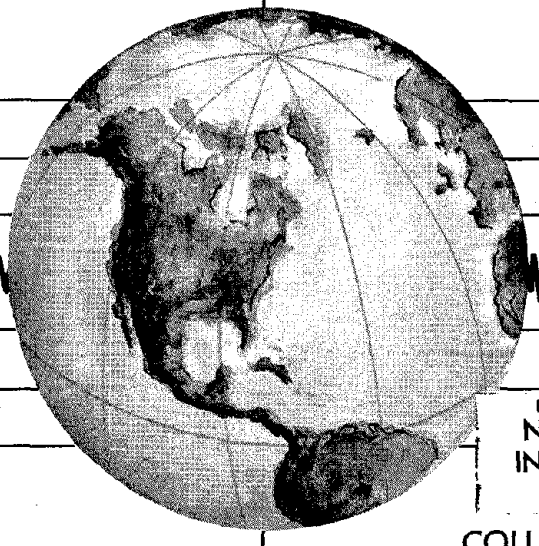

COLLEGE OF ENGINEERING

UNIVERSITY OF CALIFORNIA · Berkeley, California

HYSTERETIC BEHAVIOR OF REINFORCED CONCRETE COLUMNS SUBJECTED TO HIGH AXIAL AND CYCLIC SHEAR FORCES

by

Stan W. Zagajeski
Senior Engineering Aide
University of California, Berkeley

Vitelmo V. Bertero
Professor of Civil Engineering
University of California, Berkeley

Jack G. Bouwkamp
Professor of Civil Engineering
University of California, Berkeley

A report on research sponsored by
the National Science Foundation

Report No. UCB/EERC-78/05
Earthquake Engineering Research Center
College of Engineering
University of California
Berkeley, California

April 1978

ABSTRACT

An investigation of the inelastic behavior of short reinforced concrete columns is presented. The results of both experimental and analytical studies are reported.

The experimental program was planned to evaluate the hysteretic behavior of short reinforced concrete columns subjected to high axial loads and cyclic shear forces. Column transverse reinforcement was designed with the objective of providing a shear strength, as defined by the UBC 1973 requirements for ductile moment-resisting frames, which would be sufficient to develop the column moment capacity under selected design axial loads. The columns were tested as components of a one bay, two story subassemblage of a typical spandrel wall frame. The magnitude of the axial load, the type of transverse reinforcement, and the deformation history were varied to evaluate their influence on column behavior.

All model columns tested experience significant inelastic deformation, and all but one develop the shear force corresponding to their respective analytical moment capacity, before either a sudden diagonal tension failure or a significant degradation in column shear strength. Shear degradation is caused by either bond deterioration or a degradation in the longitudinal shear transfer mechanism. Cyclic stiffness degradation is associated with cyclic inelastic behavior. The results demonstrate that spiral transverse reinforcement is more effective in maintaining a member's shear strength than rectangular ties. Bond deterioration, however, can still lead to significant shear degradation

and create anchorage problems for the longitudinal reinforcement in spiral columns.

The intent of the analytical phase of the investigation was to formulate a model which would facilitate the analytical study of crack behavior, i.e., crack formation and propagation and the force transfer across cracks, in reinforced concrete members. The analytical model is based on the finite element method of structural analysis. Concrete is modeled as plane stress finite elements and steel reinforcement is modeled as bar elements. Nonlinear material behavior of both steel and concrete is approximated. Concrete cracking is included in the model by a crack line approach. Bond between steel and concrete is included by using different nodes to define the steel and concrete elements and coupling these nodes with dimensionless bond-link elements. The shear forces developed across cracks by aggregate interlock and dowel action of the reinforcement are also modeled by using dimensionless links.

The solution strategy developed enables the changes in structure topology, which are required to effect cracking in the model, to be made within the context of an incremental solution process. In its current stage of development, the cracking model has limited application. Suggestions to remedy shortcomings which limit application are made.

ACKNOWLEDGMENTS

This report is based on the dissertation written for the degree of Doctor of Philosophy in Engineering by Stanley W. Zagajeski under the supervision of Professors Vitelmo V. Bertero and J. G. Bouwkamp.

The financial support provided by the National Science Foundation under Grant No. GI-36387 during the experimental phase of the investigation and Grant No. ENV76-01419 during the analytical phase is greatly appreciated.

The facilities of the Computer Center of the University of California are acknowledged.

In the experimental phase of the investigation the help of J. Foster, G. Hayler, R. Lawrence, T. Costa, J. Hanson, H. Williams, R. Tully, and S. Killian was appreciated.

Finally, the authors would like to thank those who helped create the final manuscript. The graphics were done by A. Klash, L. Rambeau, G. Feazell, and L. Hashizume, and the typing by N. Deerinck. L. Tsai provided technical guidance.

TABLE OF CONTENTS

Table of Contents (continued) Page

Table of Contents (continued) Page

Table of Contents (continued) Page

LIST OF TABLES

LIST OF FIGURES

List of Figures (continued)

List of Figures (continued)

List of Figures (continued)

List of Figures (continued)

List of Figures (continued)

List of Figures (continued)

NOTATIONS

a = shear span

A = hysteresis area

A_c = area of confined concrete core

A_s = area of longitudinal reinforcement

A_{SA} = crack surface area

A_w = area of transverse reinforcement

b = section width

b_n = net width of concrete associated with one reinforcing bar

$\underline{B}$ = strain displacement transformation matrix

$\underline{B}^T$ = transpose of $\underline{B}$

$\underline{B}_i^c$ = that part of $\underline{B}$ associated with the cracked node in element i

BETA = direction of principal tensile stress at node to be cracked

$\overline{\text{BETA}}$ = orientation of crackline

c = crack width

d = (effective) depth of member

$d\varepsilon_i'$ = strain increment in ith global coordinate direction

$d\gamma_{12}'$ = incremental global shear strain

$d\sigma_i'$ = stress increment in ith global coordinate direction

$d\tau_{12}'$ = incremental global shear stress

D = diameter of reinforcing bar

D_F = dowel splitting load

DOF = degrees of freedom

E = modulus of elasticity of steel

E_i = tangent modulus in ith material coordinate

E_{SH} = strain hardening modulus of bilinear steel stress-strain relationship

f'_c = nominal compressive strength of plain concrete

f'_t = tensile strength of plain concrete

f_Y = steel yield stress

F_T = biaxial tensile strength criterion

h = column height

h_c = clear column height

H = imposed shear force

H_d = percentage decrease in shear strength

$H_{P-\Delta}$ = equivalent shear force including approximation to P-Δ effect

H_1 = absolute value of recorded shear force at +Δ in cyclic deformation history

H_2 = absolute value of recorded shear force at -Δ in cyclic deformation history

$\underline{K}$ = structure stiffness matrix

K_A = aggregate interlock link stiffness

K_H = bond link stiffness parallel to reinforcement axis

K_V = bond link stiffness perpendicular to reinforcement axis

$\underline{K}_j^k$ = structure tangent stiffness in k<u>th</u> iteration of j<u>th</u> load step

$\underline{K}_0$ = initial structure stiffness matrix

KEL = element-element connectivity array

ℓ = bond link spacing

L = length

L_G = gage length in curvature measurements

L_s = distance from mid-column height to steel strain gage location

m = number of reinforcing bars corresponding to a given bond link

M = moment

M_B = moment capacity at balance point axial load

M_E = moment at column end

M_0 = moment capacity at zero axial load

M_S = column moment at steel strain gage location

M_y = member yield moment

NCRK = node to be cracked

NPP = node-element connectivity array

NT = crack tip

P = axial load

P_B = balance point axial load

$\underline{P}_R$ = residual nodal forces

$\underline{P}_R^D$ = difference between nodal forces corresponding to the stress field in a quadrilateral element and those corresponding to that in an equivalent pair of triangular elements

$\underline{P}_{R_i}^C$ = nodal forces corresponding to the stress field in the ith element at the newly cracked node

$\underline{P}^Q$ = nodal forces corresponding to the stress field in a quadrilateral element to be replaced by two triangular elements

$\underline{P}^{TRI}$ = vector sum of nodal forces corresponding to the stress field in the triangular elements necessary to incorporate an inclined crack

P_{ult} = ultimate axial load capacity

R = relative story rotation

$\underline{R}$ = structure load vector

R_y = yield relative story rotation

RA = relative hysteresis area

ROT = array defining the inclinations of lines from NCRK to nodes in neighborhood of NCRK

s = spacing of transverse reinforcement

S_d = cyclic shear degradation

STOL = stress convergence tolerance

TOLD = displacement convergence tolerance

u = bond stress

$\underline{u}$ = nodal displacement vector

$\underline{u}_T$ = total nodal displacement vector

v = nominal shear stress

v_c = concrete shear strength

v_f = flexural shear stress

V = shear force

V_{cgd} = component of shear resistance associated with concrete compression block, aggregate interlock, and dowel action

V_d = dowel shear force

V_F = flexural shear capacity

V_s = component of shear resistance associated with transverse reinforcement

V_y = shear force corresponding to member yield moment

α = principal stress ratio

β = factor establishing upper bound on the principal tensile stress in determining tension failure

$|\underline{\gamma}|_{ss}$ = square root of the sum of the squares of the components of $\underline{\gamma}$

δ_A = measured deformation at depth A used to compute average rotation

δ_B = measured deformation at depth B used to compute average rotation

Δ = model tip displacement

Δ_F = model failure tip displacement

Δ_{max} = maximum tip displacement

Δ_s = shear displacement across crack

Δ_y = yield tip displacement

Δ_3 = measured displacement at upper end of model column

Δ_5 = measured displacement at lower end of model column

$\Delta \underline{R}_j^k$ = incremental load vector in kth iteration of jth load step

$\Delta \underline{u}_j^k$ = incremental displacement vector in kth iteration of jth load step

$\Delta \underline{\sigma}_j^k$ = incremental element stresses in kth iteration of jth load step based on previous constitutive relationship

$\Delta \underline{\bar{\sigma}}_j^k$ = incremental element stresses in kth iteration of jth load step based on updated constitutive relationship

$\Delta\phi_{AVG}$ = change in ϕ_{AVG} in going from zero to peak displacement level in cyclic deformation history

ε_{AVG} = measured average compressive concrete strains

ε_{AVG}^c = extrapolated average compressive concrete strains at core boundary

$\varepsilon_{AVG}^{2.5}$ = average compressive concrete strains measured at a distance of 63.5 mm (2.5 in.) from column edge

ε_{core} = ε_{AVG}^c

ε_{max} = maximum concrete strain (failure strain)

ε_s = measured steel strains

Θ = angle defining rotation of material coordinates with respect to global coordinates

μ_R = relative story rotation ductility

μ_Δ = tip displacement ductility

μ_ϕ = curvature ductility

ν = effective Poisson's ratio

ρ = percentage of longitudinal reinforcement

ρ_w = percentage of transverse reinforcement

$\underline{\sigma}$ = element stresses

σ_y = analytical steel yield stress

σ_1 = maximum principal stress

σ_2 = minimum principal stress

τ_A = aggregate interlock shear stress

τ_{max} = maximum allowable shear stress in reinforced concrete members

ϕ = curvature

ϕ_{AVG} = average curvature

ϕ_{ST} = curvature based on steel strain data

ϕ_u = curvature at 'failure'

ϕ_y = yield curvature

$\phi_{1.0}$ = curvature at displacement level of 25.4 mm (1 in.) in cyclic deformation history

1. INTRODUCTION

1.1 General

The performance of short reinforced concrete columns in structures experiencing moderate to severe earthquakes in recent years has caused concern for the adequacy of accepted design practices. After reviewing recent experimental studies of concrete columns subjected to cyclic shear forces and recent advances in the analytical modeling of reinforced concrete, the author conducted an investigation of short reinforced concrete columns. The investigation consisted of an experimental phase and an analytical phase.

In the experimental phase the behavior of short concrete columns subjected to high axial loads and simulated pseudo-dynamic earthquake loading is studied. The column transverse reinforcement is designed in accordance with UBC 1973 requirements for ductile moment resistant frames. Both rectangular tied and circular spiral types of transverse reinforcement are studied.

In the analytical phase a finite element model is formulated to study the cracking behavior of reinforced concrete members.

1.2 Experimental Phase

1.2.1 Practical Aspects

Short reinforced concrete columns are commonly found in spandrel-

wall frame systems. This structural system, which is used as the exterior frames in low- to medium-rise concrete buildings, is characterized by deep spandrel-beams and short columns.* A number of concrete frame structures in which the exterior framing consisted of spandrel-wall frames experienced severe damage in recent earthquakes (4,5). In most cases the columns in the lower stories failed in shear. The shortness of the columns, as well as the effect of axial loads were identified as factors influencing the failure.

In a major earthquake, the lateral deformations induced in a structural system by inertial forces will exceed the elastic capacities of members and cause inelastic deformation. In moment resisting frames, these deformations usually occur at regions of high bending moment which are considered as plastic hinges. This hinging action is desirable if the structural element is able to experience large inelastic cyclic deformation without losing its ability to resist at least the effects of existing gravity loads. Reinforced concrete members may be designed to perform in this way if sufficient transverse reinforcement is provided to confine the core concrete and prevent brittle shear failures.

In short concrete columns a problem arises in preventing a shear failure because the shortness of the column and the effect of axial load, especially high axial loads**, cause the shear at the moment capacity to be high.

A typical moment diagram caused by lateral loading on a moment resisting frame is shown in Fig. 1.1. If the column inflection points are

---

* In this study short columns are columns with a span to depth ratio (a/d) of less than 2.0.

** In this study high axial loads are axial loads near or above the balance point of the axial force-moment interaction relationship.

assumed at mid height, the shear force V_y, which will cause the yield moment, M_y, to be reached is given by the expression

$$V_y = M_y/h/2 \qquad 1.1$$

where h is the clear column height. It is evident from this expression that the shear force for the same yield moment is greater in a short column than it would be in a long column.

By definition, columns are subjected to axial loads. In reinforced concrete the axial load affects the yield moment. A typical axial force bending moment interaction relationship for a reinforced concrete member is shown in Fig. 1.2. From this relationship it is seen that as the axial load increases from zero to P_B, the balance point axial load, the yield moment increases from M_o to M_B. Consequently, in a column with an axial load near P_B, the shear force at the yield moment will be greater than the shear force in the same column with a smaller axial load.

The axial load also affects the inelastic deformation capacity. The curvature ductility μ_ϕ defined by the expression

$$\mu_\phi = \frac{\phi_u}{\phi_Y} \qquad 1.2$$

where

ϕ_u = the curvature at the concrete failure strain

ϕ_Y = the curvature at the initial yield of the longitudinal steel

is commonly used as a measure of inelastic flexural deformation. The variation of μ_ϕ with axial load for unconfined concrete is shown in Fig.

1.2. It can be seen that the deformation capacity decreases as the axial load increases.

The above discussion demonstrates that the shorter the column and the higher the axial load below the balance point axial load the larger the shear force will be at the yield moment. Although the contribution of the concrete to the shear resistance increases with axial load, it may be said that in general, for columns with the same cross sectional properties, the shorter the column and the higher the axial force, the larger the possibility of a shear failure. In addition, increasing the axial load will decrease the deformation capacity.

The above effects of axial load and shear span to depth ratio have been investigated in the past. Some of these studies are reviewed in the next section.

1.2.2 Review of Past Research

Investigations into the behavior of reinforced concrete members have been conducted for a number of years. Short columns have received increased attention since the Tokachi-Oki earthquake in Japan in 1968 (4). As indicated previously, a number of short reinforced concrete columns experienced severe damage in this earthquake. Recent studies of the behavior of reinforced concrete columns subjected to lateral shear forces are reviewed below.

Yamada (6) studied the monotonic behavior of concrete columns subjected to lateral shear forces and axial load. The test model and loading scheme is shown in Fig. 1.3a. Yamada investigated the effects of the shear span to depth ratio (a/d), the magnitude of axial load and the amount of transverse reinforcement. The variation of these parameters

is summarized in Table 1.

The failures in columns with a/d ratios less than 2 were by shear explosion. They were sudden and violent. Yamada concluded that inelastic behavior improved with larger amounts of transverse reinforcement, smaller axial loads and larger a/d ratios.

Yamada (7) later extended this study to include cyclic deformation histories. He considered two histories. In one the model was subjected to cyclic reversals at a constant deflection amplitude. In the other the model was subjected to a series of incrementally increasing cyclic deflection amplitudes. The axial load and the amount of transverse reinforcement were also varied (Table 1). Shear explosion occurred in both deformation histories. In the incremental history the shear explosion was not as violent as in the previous monotonic tests. The inelastic deformation before failure decreased for columns with higher axial loads and with smaller amounts of transverse reinforcement. In the constant deflection history the number of cycles to failure and the deflection amplitude increased in long columns and in columns with smaller axial loads. In his paper Yamada proposed that a transition from flexural yielding to shear yielding is the criterion for shear explosion. The transition is defined by a critical a/d ratio which depends on the axial load, the strength of the steel and concrete, and the amount of longitudinal reinforcement. He also recommended that the transverse reinforcement ratio

$$\rho_w = A_w/bs \qquad 1.3$$

where

A_w = area of transverse reinforcement

b = section width

s = spacing of transverse reinforcement

be greater than 1% to provide sufficient ductility when the a/d ratio indicates that shear yielding will occur.

Wight and Sozen (8) considered members subjected to cyclic shear forces and constant axial forces. The test model and loading scheme are shown in Fig. 1.3b. They investigated the effects of the amount of transverse reinforcement and the magnitude of axial load (Table 1). Two load histories were considered. In one the column was cycled at a displacement ductility of 4. In the other the displacement level was increased in steps to a ductility of 4. The columns were long, the a/d ratio being 2.8, and the maximum axial load was small. They observed a cyclic stiffness degradation and a pinching effect near zero load in the shear displacement hysteresis behavior. The stiffness degradation and pinching effect were less prominent in models with higher axial loads. Cyclic shear degradation occurred and was attributed to a deterioration of the core concrete. The degradation was directly related to the amount of transverse reinforcement, being smaller in models with more reinforcement. They recommended that the concrete contribution to the shear capacity must be reduced for all members subjected to shear reversals and should be ignored for members with no axial load.

Hirosawa, Ozaki, and Wakabayashi (9) investigated the effects of the a/d ratio, the amounts of longitudinal and transverse reinforcement and the magnitude of the axial load on the cyclic behavior of reinforced

concrete columns (Table 1). The test model and loading scheme is shown in Fig. 1.3c. They consider an incrementally increasing cyclic displacement history. They found that if enough transverse reinforcement was provided to develop the shear force corresponding to the flexural capacity of the column, the behavior was ductile. They concluded, however, that if τ_{max}, the nominal shear stress, was greater than 3.0 MPa a brittle shear failure would coccur even if substantial transverse reinforcement is provided. It should be noted that the latter conclusion was based on tests of columns with a nominal compressive strength of 20.7 MPa.

Küstü (10) considered columns at different story levels in a ten story spandrel-wall frame. The magnitude of the axial load and the amounts of transverse and longitudinal reinforcement were varied (Table 1). A two story-one bay subassemblage was used as the test specimen (Fig. 1.3d). The test column was subjected to an incrementally increasing series of cyclic displacements. All columns experience shear failures. The columns in the subassemblages representing the upper stories of the ten story prototype structure experienced more brittle shear failures, i.e., the column behavior was less ductile. The columns in these subassemblages had smaller axial loads than the columns in the lower story subassemblages.

The above studies have identified the shear span to depth ratio (0.6 to 2.8)*, the magnitude of axial load (0 to 1.1 P_B), and the amount of transverse reinforcement (ρ_w = 0%, to 2.6%) as parameters influencing

* This ratio is a measure of the nominal shear stress a given section must resist. In the range indicated above, the nominal shear stress varied from 1.38 MPa - 13.8 MPa (0.2 ksi to 2 ksi).

inelastic behavior in reinforced concrete columns. In general inelastic behavior improved with longer shear spans, smaller axial load and larger amounts of transverse reinforcement. There is a strong interaction between the latter two parameters. The results of Küstü (10) and Wight (8) indicate that a decrease in axial force does not guarantee an improvement in behavior. The effect of axial force on cyclic concrete shear strength must be recognized, and the transverse reinforcement designed accordingly. The intent of this investigation was to obtain additional information concerning the influence of axial force and type of transverse reinforcement on inelastic column behavior. The investigation represents an extension of the work of Küstü (10).

1.2.3 Objectives and Scope

The major objective of the experimental phase of this investigation was to study the inelastic behavior of short reinforced concrete columns when subjected to high axial loads and the shear forces induced by earthquake ground motion. In the course of the investigation it was desired to evaluate the adequacy of the UBC 1973 requirements for ductile moment resisting frames when applied to the design of short reinforced concrete columns. Of particular interest was whether the amount of transverse reinforcement provided in accordance with the UBC requirements would prevent the brittle shear failures observed in recent earthquakes (4, 5) and previous experimental investigations (6-10) and would permit significant inelastic deformation to occur before failure.

The effect of different types of transverse reinforcement was also

studied.

A one bay two story subassemblage of a spandrel wall frame was tested (Fig. 1.3d). The subassemblage contains one full column length, which was the element studied. It is felt that this particular subassemblage provides a good idealization of a short concrete column as a component of a moment resisting frame. A typical double curvature pattern of deformation can be reproduced and beam-column joint behavior is included. The test model was a half-scale model of a lower story subassemblage of a 10 story prototype structure. The test model and testing system are described in detail in Chapter 2.

Two column series, differentiated by the type of transverse reinforcement, were tested. Rectangular ties were used as the transverse reinforcement in the R-series. A continuous circular spiral was used as the transverse reinforcement in the S-series. The column cross section in both series was 305 mm by 305 mm (12 in. by 12 in.) (Fig. 1.4).

Seven models were tested in all, five in the R-series and two in the S-series. Models 2R, 4R, and 1S were subjected to a monotonic deformation history. Models 3R, 5R, 6R and 2S were subjected to a cyclic deformation history with incrementally increasing displacement amplitudes.

The moment-axial force interaction relationship for both the R and S-series columns is given in Fig. 1.5. The balance point axial load*, points B and B' in Fig. 1.5, was applied to models 2R, 3R, 4R, 1S and 2S. Models 5R and 6R were subjected to axial loads less than the balance

*The balance point is defined as that combination of axial force and bending moment at which the concrete compressive strain reaches its assumed ultimate value and the tensile reinforcement reaches its yield stress simultaneously. How the balance point and the moment axial force interaction relationship were determined are described in Appendix B.

point load. The magnitudes are indicated in Fig. 1.5. Properties of the columns tested in this investigation are compared with those in previous investigations in Table 1.

The results of the experimental program are presented and discussed in Chapter 3.

1.3 Analytical Phase

Structural systems designed to resist moderate to severe earthquakes are usually expected to exhibit significant inelastic behavior. A reliable analytical model should be available to determine the inelastic structural response to the largest expected earthquake and to determine the amount of inelastic deformation members of the structural system experience in this response. The analytical model should be based on the mechanical characteristics of the component materials in order for the model to be applicable to general problems.

1.3.1 Characteristics of the Hysteretic Behavior of Reinforced Concrete

A number of difficulties arise in formulating an accurate analytical model for reinforced concrete. Cracking of concrete, bond failure between reinforcing steel and concrete, anchorage failures at joints, crushing of concrete, yielding of reinforcing steel, the confining effect of the transverse reinforcement and the stiffness and strength degradation should be included to obtain an accurate mathematical idealization.

To date most models for the cyclic behavior or reinforced concrete frame members have assumed that the predominant deformation component is caused by flexure. A common approach is to use stiffness degradation

laws, dependent on the amount of inelastic deformation, in conjunction with a 'virgin' force-deformation relationship, to represent the hysteretic behavior of flexural members. The virgin force-deformation relationship is in most cases determined by

i. assuming a linear strain distribution.

ii. either neglecting concrete's tensile strength altogether, or allowing a small tensile strength with cracking after it is exceeded.

iii. using realistic stress-strain relationships for concrete and steel.

A pinching effect in the force displacement hysteresis loops near zero load is a common feature of the cyclic behavior of reinforced concrete. The pinching effect is due to the fact that cracks formed in one load direction remain open in the initial stages of a load reversal. Most flexural formulations do not consider the opening and closing of cracks and consequently will not reproduce the pinching in the hysteretic behavior. In flexural models which do consider the opening and closing of cracks (13), only flexural cracking is considered and the pinching due to inclined shear cracking is neglected. In addition all flexural hysteresis formulations neglect shear deformations.

The results of the experimental phase of this investigation indicated that shear cracking and its effect on the hysteretic behavior was an important phenomenon in the response of short columns. In addition, the column shear span to depth ratio of 1.5 implies that the column shear deformations will be significant. The fact that the effect of shear cracking and shear deformations are usually neglected in a flexural

hysteresis formulation was considered a serious shortcoming to such an approach. A more accurate approach for such problems appears to be a finite element idealization in which nonlinear aspects such as cracking, crushing, yielding, and bond degradation and bond failure are considered.

Recent studies based on both flexural hysteretic models and finite element models are reviewed in the next section.

1.3.2 Review of Hysteretic Models

Recent analytical studies (10-13) of the hysteretic behavior of reinforced concrete frame members have concentrated on modeling stiffness degradation, a common characteristic of concrete members experiencing inelastic cyclic deformation, and on flexural deformations.

Stiffness degradation was considered by Clough (11) in 1966. Motivated by a desire to represent the stiffness degradation observed in reinforced concrete members, he proposed degrading hysteretic behavior based on a virgin bilinear force displacement relationship (Fig. 1.6a). The degradation in the loading stiffness was dependent on the previous inelastic deformation. The unloading stiffness remained constant at the value of the initial loading stiffness. Typical force-displacement loops are shown in Fig. 1.6a.

Takeda et al (12), in order to generate hysteretic behavior more representative of reinforced concrete members, proposed a model which is based on a trilinear virgin force displacement relationship and includes a degrading unloading stiffness (Fig. 1.6b). Typical force displacement loops are shown in Fig. 1.6b.

Park and Kent (13) used a quite different approach. They divided

a typical cross section into layers, monitored the strain history of each layer and idealized the hysteretic stress-strain behavior of concrete and steel. They assumed a linear strain distribution and were able to generate moment curvature hysteretic behavior, from which force displacement hysteretic behavior was calculated.

Küstü (10), in order to include the pinching effect associated with shear cracking, proposed, in addition to a flexural hysteresis law, a hysteresis relationship for deformations due to inclined shear cracking. The virgin curve was a shear force-shear rotation relationship derived from the stirrup strains across an assumed shear crack. A degradation in the unloading stiffness of the shear force rotation relationship was included. The shear and flexural deformation components were considered independent. A pinching effect in the force deflection hysteresis loops was produced. The degradation of the unloading stiffness introduced through the shear model proved to be insufficient, especially at large ductilities.

1.3.3 Review of Finite Element Models

The application of the finite element method to the analysis of reinforced concrete behavior has received increased attention in recent years (14-22). A finite element model is attractive because it depends on basic material properties and because it is possible to consider behavior such as progressive cracking, aggregate interlock, bond slip between steel and concrete, dowel action and nonlinear material behavior. Two general approaches, differentiated by how concrete cracking is modeled, exist. Work in both areas has been generally limited to two-dimensional problems.

i. Crack Line Approach

Cracks are actually formed in the crack line approach. Cracks are included by node separation, i.e., two 'unconnected' nodes exist at the same point in the finite element mesh. Recent work employing the crack line approach is reviewed below.

Ngo and Scordelis (14) demonstrated the feasibility of using the finite element method to study the behavior of reinforced concrete beams. They performed linearly elastic analysis of simply supported beams. In these analyses both the steel and concrete were represented by constant strain triangles, cracking was predefined and a physically dimensionless constant stiffness linkage element was used between the steel and concrete to incorporate bond slip. They found that variations in the stiffness of the bond linkage elements had only minor effects on the beam deflection and crack widths.

Ngo, Franklin and Scordelis (15) performed finite element analyses of reinforced concrete beams with diagonal tension cracks. Both steel and concrete were idealized as linear elastic materials. Bond slip was included by using dimensionless constant stiffness linkage elements between the steel and concrete. They studied the effect of web reinforcement which was represented by linear elastic bar elements, and aggregate interlock, which was included by using dimensionless constant stiffness linkage elements parallel to the diagonal crack. Their analyses was confined to beams with only one predefined diagonal crack. They found that web reinforcement was effective only when there is a crack crossing it and that web reinforcement decreases the maximum principal tensile stresses in the region near the head of the diagonal crack.

Nilson (16) extended the method of Ngo and Scordelis (15) to include nonlinear material properties and a nonlinear bond slip relationship. Concrete was modeled as a nonlinear orthotropic material. A maximum stress criterion of failure for tension and a maximum strain criterion of failure for compression were used. The tracing of crack propagation was accomplished by redefining the finite element mesh manually when the failure criterion was met at one or more points in the loaded member. When the failure criterion was met the structure was completely unloaded, redefined and reloaded from zero. The proposed model's prediction of stress distributions, displacements, crack history, crack extent and crack width in a concentrically and an eccentrically reinforced member showed good agreement with experimental data.

Ngo (17), in order to eliminate the tedious job of manually redefining a mesh to include cracking (16) proposed a finite element model capable of automatically producing crack lines to simulate progressive crack growth. He suggested a network topological approach as a unified treatment for the various problems encountered in analyzing crack growth. Although the cracking criteria, and crack geometry, were restricted due to the simplified assumptions in modeling, satisfactory progressive crack growth was still achieved.

The above work, employing the crack line approach, considered only monotonic load histories.

ii. Crack Zone Approach

In the crack zone approach, the element stiffness properties are modified to reflect a tensile failure in the direction perpendicular to

a predicted crack. Recent work in this area is reviewed below.

Isenberg and Adham (18) proposed a composite reinforced concrete element based on the properties of the reinforcing steel and plain concrete, and bond slip between the steel and concrete. Concrete was considered an orthotropic material. The material axes were defined by the principal stress directions and the effect of orthogonal stresses on the material behavior was approximated. The steel was assumed smeared through the concrete. Cracking was included by setting the constitutive modulus in the direction perpendicular to a crack to zero. Bond slip in elements with steel was modeled by retaining a portion of the concrete stiffness in tension after cracking. The smearing of the reinforcement makes this model attractive for large structures which have nearly uniform steel distribution.

Valliappan and Doolan (19) applied the 'stress transfer' method to the finite element analysis of tensile crack propogation in reinforced concrete beams. The concrete was represented by triangular elements and the reinforcing steel was represented by bar elements. Perfect bond was assumed between the steel and concrete. Both materials were assumed to be elastic perfectly plastic. A von Mises yield criterion was used in biaxial compression. Concrete cracking was included by assuming zero strength and stiffness after the tensile failure criterion was met.

A constant stiffness iteration solution technique was employed. Changes in the material properties due to cracking and yielding were included by a stress transfer technique which eliminated the need to reform and retriangularize the structure stiffness in the iteration process.

Salem and Mohraz (20) proposed a finite element model in which the 'elastic' modulus perpendicular to a predicted crack was zero. Concrete was modeled by isoparametric quadrilaterals and idealized as an elastic perfectly plastic material in biaxial compression. An octohedral shearing stress yield criterion based on observed biaxial behavior of concrete was used. Cracking was assumed to occur when the principal tensile stress exceeded the failure criterion. The crack was assumed perpendicular to the direction of the principal tensile stress. An unloading region for the concrete tensile stress-strain relationship was included to incorporate the fact that the average tensile stress in a newly cracked element is not zero. A reduction in the shear capacity of a cracked element is achieved by using a reduced shear modulus. Steel was modeled as elastic perfectly plastic bar elements. Bond was considered by including dimensionless links. In comparisons with experimental behavior they found that this idealization predicted failure loads well. However, it was generally too stiff in deep members in which shear deformation is important.

The preceding studies were limited to monotonic load histories. Recent studies by Litton (21) and Darwin and Pecknold (22) have considered cyclic load histories.

Litton (21) proposed a cracking element to predict the response of reinforced concrete under cyclic loading conditions. The element monitored the opening and closing of cracks by decomposing the strain associated with a cracked element into an elastic part and a cracked part. The constitutive equation for a cracked element was established by relating the stress increment to the elastic strain increment. Reinforcing steel was idealized as one dimensional bar elements with a bilinear stress-

strain relationship. Results obtained using this model compared well with monotonic experimental results. In a comparison with cyclic loading experiments, the model reproduced the essential character of the hysteretic loops but overestimated maximum loads.

Darwin and Pecknold (22) proposed an inelastic composite material finite element model for the cyclic biaxial loading of reinforced concrete. The concrete was modeled as an orthotropic material. The material axes were determined by the directions of the most current principal stresses. The stiffness moduli of the orthotropic constitutive equation were dependent on the existing biaxial stress condition. Stiffness and strength degradation, characteristics of the cyclic compressive behavior of concrete, were included. Cracking was modeled by setting the stiffness modulus perpendicular to a predicted crack to zero. Shear transfer across the crack was included by retaining a portion of the shear stiffness after cracking. The crack width was monitored by accumulating strains perpendicular to the crack.

The reinforcing steel was treated as an uniaxial material that was smeared through the concrete. The steel stress-strain relationship was represented by a bilinear curve to include the effect of strain hardening. Perfect bond between the steel and concrete was assumed. Analytical results compared well with experimental results for shear wall structures subjected to both monotonic and cyclic loading histories.

1.3.4 Objectives and Scope

The objective of the analytical phase of the investigation was to formulate a mathematical model to study cracking behavior in reinforced

concrete members. The results of the experimental phase indicated that crack propagation and the force transfer mechanisms across principal cracks had a significant influence on the inelastic member behavior. As a result the formulation of a model which could be used to investigate crack behavior was considered an important step in understanding the overall member behavior.

The proposed model is based on a finite element formulation which employs a crack line approach to model concrete cracking. Concrete is modeled as plane stress finite elements and steel reinforcement is modeled as bar elements. Nonlinear material behavior of both steel and concrete is considered. Bond between the steel and concrete and the shear forces developed across cracks by aggregate interlock and dowel action of the reinforcement are included in the model. The model is limited to monotonic load histories.

The current development is intended to provide direction for future work in this area. The proposed cracking model is simple and limited in application. In the analyses carried out the solution strategy employed to introduce cracking into the finite element mesh was evaluated and the effect on crack behavior of various characteristics of the proposed model, particularly the modeling of bond, aggregate interlock and dowel action was investigated. Details of the analytical formulation and results are presented and discussed in Chapter 4.

2. DESCRIPTION OF EXPERIMENTAL WORK

2.1 General

The objective of the experimental program was to study the inelastic behavior of short reinforced concrete columns subjected to high axial loads and cyclic shear forces. The test model was a two story one bay subassemblage of a typical spandrel wall frame. The subassemblage consisted of 4 half span beams, 2 half column lengths and one full column length (Fig. 2.1). This subassemblage was used previously by Küstü (10) in an investigation of spandrel wall frames. The components of the subassemblage were designed to limit inelastic behavior and failure to the full column length. It was felt that this subassemblage provides a good representation of the deformation pattern and boundary conditions of a column as a component of a lateral load resistant frame.

The model dimensions were determined from a ten story, five bay prototype structure designed according to UBC 1970 requirements. The design of the column cross-section and the column longitudinal reinforcement was based on the gravity and lateral loads in a lower story column of the prototype structure (Fig. 2.2). The test model was a half-scale model of the prototype subassemblage.

The model was tested in a horizontal position and was subjected to quasi-static lateral loads which simulate the inertial forces induced by earthquake ground motion. The model column was subjected to an axial load to simulate gravity loads. The axial load was kept constant during the test. The effect of uniform gravity loads on the beam and column moments

was neglected. Imposed forces, reactions, and model displacements and deformations were recorded electronically in both digital and plotted form.

2.2 Considerations in Design of Test Model

2.2.1 Idealizations

The fundamental objective in the design of the test model was to adequately represent the loading and boundary conditions of a reinforced concrete column as a component of a spandrel-wall frame subjected to the lateral forces induced by earthquake excitations. A typical moment diagram for a structural frame resulting from imposed lateral loads (gravity effects are neglected) is shown in Fig. 1.1a. A general double curvature pattern is observed in the deflected shape of a typical subassemblage (Fig. 1.1b). The location of the inflection points depend on the relative stiffness of adjacent frame elements. If the stiffness distribution is symmetrical and the loading pattern is anti-symmetric, the beam inflection points will be located at mid-span and they will remain at the same elevation as the intersection of the beam and column centerlines. Also the column inflection points will be at mid-height.

A major assumption in this idealization is that uniform gravity loads on the beams do not appreciably affect the behavior of a frame subjected to lateral loads. The results of a linear-elastic frame analysis of the prototype structure used in the design of the test model indicated that the effect of uniform beam loads on the beam moments was

significant but their effect on the moments in the lower story columns was small, being less than 1% (Fig. 2.3). Since only the behavior of the columns was of interest, neglecting the influence of these gravity loads on the frame moments is considered a reasonable assumption. If, however, the behavior of a frame subassemblage including the beams was to be studied, neglecting the influence of uniform beam loads would be questionable since a significant part of the real beam loading would be ignored.

2.2.2 Model Selection

Based on the above idealizations, i.e. neglecting the effects of uniform gravity loads on frame moments, and assuming that beam inflection points are at mid span and column inflection points are at mid height, the two story one bay subassemblage circled in Fig. 2.2 was chosen as the test model. Advantages in choosing this particular subassemblage are,

a) It can produce a double curvature pattern of deformation in the model column.

b) It includes one full column length with realistic frame-type boundary conditions. The full column length permits the investigation of the column P-Δ effect. The frame-type boundary conditions allow the study of bond slip, cracking and other local beam-column joint behavior.

c) It facilitates easy modeling of boundaries. The subassemblage boundary conditions are inflection points in the idealized prototype structure, which, being points of zero moment, can be modeled relatively easily in the laboratory as hinges.

d) It results in a model which is statically determinant, allowing direct determination of force components at any section.

2.3 Design of Members

2.3.1 Prototype Structure

The model member designs were based on a prototype structure in which the exterior framing consists of spandrel-wall frames. The height of the prototype structure is 36.6m (120 feet), ten stories at 3.66m (12 feet). Two factors influenced the choice of height. First, typical spandrel wall frame structures are medium rise and generally less than 36.6m (120 feet). Second, in the initial phase of this investigation (10) UBC 1970 was the design code. One provision of this code allowed the design of reinforced concrete frames without extensive ductile concrete requirements provided the total height of the structure was less than 48.8 m, (160 feet).

A symmetric 36.6m by 36.6m (120 foot by 120 foot) floor plan was chosen for simplicity. The structural system consists of two exterior spandrel-wall frames and four typical interior beam-column frames in each principal direction (Fig. 2.4). It was assumed that the lateral load resistance was provided by the spandrel-wall frames only.

2.3.2 Prototype Member Size

The cross-sectional dimensions of the beams were determined by archi-

techtural considerations. The dimensions of the column cross section and the column longitudinal reinforcement were determined by using ACI 318-71 ultimate strength design requirements. The column design loads due to gravity forces and the lateral forces caused by earthquake ground motion were determined by UBC 1970 ultimate load requirements. The design axial load, shear force and bending moment are based on first story load conditions. An f'_c of 34.5 MPa (5,000 psi) and an f_y of 413.7 MPa (60,000 psi) were used. Details of the calculations are given in Appendix B.

2.3.3 Scaling of Prototype

A scaling factor of 1/2 was used in the linear dimensions. This scale factor proves convenient in that it allowed an easy conversion from the prototype reinforcing steel to the test model reinforcing steel and permitted the use of common construction materials in the test model. For example a #8 deformed bar in the prototype becomes a #4 deformed bar in the model.

Since the material characteristics of the prototype structure and the test models were to be identical, a unit-stress factor was employed. The scale factors between the test model and prototype structure are summarized below.

Length	1:2	(L)
Stress	1:1	(σ)
Force	1:4	($\sigma \cdot L^2$)
Moment	1:8	($\sigma \cdot L^3$)

A benefit of this model scaling was that the maximum forces which had to be provided by the testing system were reduced to 1/4 of the forces in the prototype structure.

2.3.4 Reinforcement Details

The prototype design established the model cross-sectional dimensions and the column longitudinal reinforcement. The column transverse reinforcement was designed to insure that the moment capacity at the maximum axial load considered in this investigation could be attained before a shear failure occured. The maximum axial load considered in this study was the balance point axial load of the column cross-section established by the prototype design. The beam reinforcement, both the longitudinal and transverse reinforcement, was designed with the objective of forcing inelastic behavior and model failure to occur in the column. The design calculations are based on the UBC 1973 requirements for ductile moment resistant frames. Limiting code values are introduced wherever required. Steel properties determined by stress strain tests of specimens cut from the steel bars used in the investigation (Appendix A) were used in determining the balance point for both the rectangular tied and spirally reinforced columns. Details of the design calculations are given in Appendix B. The final test member reinforcement details are shown in Fig. 2.5.

It should be noted that the weak column-strong beam design philosophy is not conventional. The conventional approach is to force inelastic behavior into the beams by a strong column-weak beam design. The use of the weak column design here is not intended as a recommendation for its use

in design practice. It is used here because the inelastic behavior of the column is being studied to determine if short reinforced concrete columns can be designed to behave in a ductile manner.

2.3.5 Choice of the Balance Point

The choice of the balance point axial load was based on the desire to create the most unfavorable load conditions in the model column. The balance point corresponds to a bending moment which is very close to the maximum bending moment that a given reinforced concrete section may resist. In the subassemblage to be tested, the column shear, V, is related to the column end moment, M, by the expression

$$V = M/a \qquad 2.1$$

where a is the shear span and is equal to 1/2 the clear column height.

Since the flexural moment capacity corresponding to the balance point axial load is typically a maximum, the balance point axial load will typically maximize the shear force which may be applied to the model column. However, since concrete shear capacity increases as the axial compressive force increases, an axial load other than that defining the balance point may be critical with respect to shear related failure, the type of failure expected. This is not the case for the column cross sections considered in this investigation. The increase in the concrete shear strength, v_c, with axial compressive stress allowed by UBC 1973 is compared in Fig. 2.6 with the variation of the flexural shear stress,

v_f*, with compressive stress for both column cross sections considered here. From Fig. 2.6 it can be seen that v_f increases more rapidly than v_c as the axial compressive stress increases from zero to the balance point stress, and that the maximum difference between v_c and v_f occurs very near the balance point axial stress. The balance point should therefore be the most critical point with respect to a shear failure.

Another factor considered in the choice of the balance point axial load is the ability of a member to undergo inelastic deformation. As discussed in Section 1.2.1, the axial load effects the inelastic deformation capacity. For a column subjected to the balance point axial load, the assumption that the maximum possible concrete strain is the crushing strain of unconfined concrete would result in a curvature ductility, μ_ϕ, of 1. A μ_ϕ of 1 indicates that the member will be unable to experience inelastic deformation, a characteristic not desired in members designed to resist lateral loads induced by earthquake ground motion.

But μ_ϕ does not have to be 1 at the balance point. Concrete, properly confined, can experience strains substantially larger than the crushing strain of unconfined concrete and still maintain a load. It is hoped to determine what magnitude of $\mu_\phi(\varepsilon_{max})$ can be developed in columns subjected to high axial loads if the concrete core is adequately confined.

---

*$v_f = M/abd$

where M = moment capacity

a = shear span

b = column width

d = column effective depth

2.4 Test Model

2.4.1 General

A plain view of the test model is given in Fig. 2.7. The model represents a two story-one bay subassemblage of a typical spandrel wall frame. Points A and F represent the column inflection points at mid height of the upper and lower stories. Points G, H, I, and J represent beam inflection points at mid span of adjacent bays. The column length between C and D is the element being investigated.

It was desired to simulate the lateral loads induced by earthquake ground motion on the total subassemblage and to simulate the effect of gravity loads on the model column only. To accomplish this the force components indicated in Fig. 2.7 at points A, F, G, H, I, and J must be provided. Imposed lateral loads required the horizontal force components at A and F and the vertical force components at G, H, I, and J. Vertical loads at A and F must be provided for gravity loads on the column. In addition, the distance between GI, BE and HJ must remain the same if the typical shear motion caused by lateral loading was to be reproduced.

How these conditions are met in the test model is discussed in the next section.

2.4.2 Experimental Setup

A plan of the test system, including the test model, is given in

Fig. 2.8. The end of the model where the axial load and horizontal load jacks are located is referred to as the upper end. The opposite end, with the adjustable reaction links and associated reaction blocks is referred to as the lower end.

The model was tested horizontally. It was supported on five low-friction teflon pads located at A, B, C, D and E as indicated in Fig. 2.8. A sixth support point was provided by the lower column hinge. Five reinforced concrete reaction blocks, prestressed to the floor, were used to provide the necessary retraint for the hydraulic jacks and support reactions.

The model was loaded at the upper end. The axial load was applied to the column by means of a 1334 kN (300 kip) capacity hydraulic cylinder. The cylinder was connected by hinges to the test model and its support block. The hinge connection allowed an unrestrained horizontal motion at the connection point, but the rotation of the load cylinder results in a horizontal force component proportional to the imposed displacement. This lateral force is easily evaluated and was considered in the data reduction. The axial load was controlled by a manually operated pump and was kept constant during the test.

The lateral load was controlled by the horizontal displacement at the center of the hinge at the upper end of the model. This displacement is referred to as the model tip displacement. The lateral load was applied by a 890 kN (200 kip) capacity load cylinder. The cylinder was double acting and had a 305 mm (12 inch) stroke in either direction.

The desired model motion was a shear motion between floors (Fig. 1.1b). The straight lines AC and DE in Fig. 2.8 would remain parallel

in the shear motion. Two 534 kN (120 kip) capacity double acting hydraulic cylinders between the beam ends (AD and CE) and two adjustable length reaction links at the beam ends D and E were introduced to keep the lines AC and DE parallel. The lengths of the reaction links were long enough so that the small horizontal displacements at D and E did not alter the reaction in the links appreciably.

To insure that the desired shear motion between floors occurred, a special closed loop displacement servo-controlled system was set up. The column length between the points of intersection of the beam and column centerlines was monitored continuously by a linear potentiometer. The output from this potentiometer served as a master signal to the servo-valves of the hydraulic cylinders between the beams. A change in the column length activated the cylinders. When activated the cylinders changed the distance between the beams in the same sense as the column length had changed. For example, if the column shortens the distance between the beams would decrease.

Measurements of the distances between the beams (AD and CE in Fig. 2.8) by potentiometers similar to the one monitoring the column length were used as feedback signals to the cylinder valves. The distances AD and CE were initially equal to the column length between the points of intersection of the beam and column centerlines. The feedback signals provided by the potentiometers monitoring the distances AD and CE caused the cylinder valves to close when the new distance between the beam equaled the changed column length.

The above control system prevented the introduction of forces into the beams by changes in the column length and insured that a lateral

displacement at the upper end of the subassemblage resulted in a parallel shear motion between floors.

Due to the rigidity of the reaction links at D and E, shortening of the column stub at the lower end,caused by the initial application of the axial load, introduced compressive forces in the links. Attempts to eliminate these forces were not entirely successful and shear forces were introduced into the beams. The forces were small [17.8 kN to 35.6 kN (4 to 8 kips)] and did not effect the column behavior.

2.5 Model Design Details

The final model reinforcement details are shown in Fig. 2.9a and b. The model was symmetric about the vertical and horizontal centerlines. The upper and lower column half lengths were shortened to 305 mm (12 inches). Hinges brackets at the ends increased the length to 457 mm (18 inches), half the typical column length of 914 mm (36 inches). Additional longitudinal and diagonal reinforcement was provided in the column half lengths (stubs) to insure that failure occurred in the full column length rather than in the column stubs.

The diagonal reinforcement in the beams was provided to insure a column failure by protecting against a shear failure in the beams.

The taper at the beam ends was necessary to allow the installation of the 534 kN (120 kip) hydraulic cylinders. The distance of 0.91 m (3 feet) from the column face for the start of the taper was believed sufficient to avoid any effects due to the change in beam stiffness on the behavior of the subassemblage. The tie spacing at the start of the

taper was reduced to alleviate the effects of stress concentrations which might be caused by the change in cross section.

The 356 mm by 356 mm (14 inch by 14 inch) blocks at the beam ends were provided so that the reaction links at D and E and hydraulic cylinders between BD and CE (Fig. 2.8) could be adequately secured to the beams and so that the forces produced by the hydraulic cylinders and reaction links did not cause local failures at the beam ends.

2.6 Instrumentation and Test Procedure

2.6.1 Instrumentation

The testing system and test models were instrumented to yield the following data:

i Applied loads and reaction forces

ii Displaced shape of the test model

iii Member deformations

iv Steel strains

i Load and Reaction Data

The column axial load, the applied lateral load and the beam shears were measured. The column axial load was monitored by a 1334 kN (300 kip) capacity load cell attached to the cylinder piston. The applied lateral load was measured by a 890 kN (200 kip) capacity load cell attached to the double acting hydraulic

cylinder. The beam shears were measured by pairs of pressure transducers mounted on the two 534 kN (120 kip) capacity hydraulic cylinders and by two 890 kN (200 kip) load cells built into the adjustable reaction links. The load and reaction instrumentation are illustrated in Fig. 2.10.

ii Displaced Shape

Model displacements were monitored by linear potentiometers at the points indicated in Fig. 2.10. The potentiometers were positioned so that the contributions of the beams, column stubs and full column length to the tip displacement can be identified.

iii Member Deformations

Average rotations of 152 mm (6 inch) segments of the column length were measured by 'clip gages' mounted on rods which were placed in the concrete during casting. The mechanism on which the rotation measurements are based is given in Fig. 2.12. Column 'clip gage' locations are shown in Fig. 2.11.

Beam rotations were measured by 'clip gages' mounted on aluminum frames pin-connected to metal tabs epoxied to the concrete surface. Beam 'clip gage' locations are shown in Fig. 2.11.

Cast in rods rather than epoxied tabs were used for the column rotation measurements in order to obtain reliable data in the post-yield, crushing stages of the test. The epoxied tabs could not be counted on to measure the core concrete deformations after substantial cracking and crushing had occurred because either the epoxy would fail and the tabs would separate from the concrete, or the concrete to which the tabs were epoxied would separate from the core concrete.

iv Steel Strains

The model was instrumented internally by means of water resistant microdot strain gages welded to the steel reinforcement. Both the longitudinal and transverse steel were instrumented. Gage locations in the S and R-series columns are shown in Fig. 2.13. Curvature data obtained from the longitudinal strain data was to be compared with average curvatures measured externally by clip gages. The gages on the rectangular ties in the R-series columns aided in detection of inclined shear cracking.

2.6.2 Data Acquisition System

The data from all instrumentation was recorded at selected load steps by a low speed scanner data acquisition system. The data was printed digitally and punched on papertape. The papertape was used to convert experimental readings to a more readable form.

The variation of lateral force with tip displacement was recorded continuously during each test on an X-Y recorder. Similar recorders, with the lateral force as a common axis, were used to continuously monitor

i. the average curvature measured by clip gages at the upper portion of the full column length (Fig. 2.11)

ii. the displacements of points 3 and 5 in Fig. 2.11

iii. a longitudinal steel strain (1 in Fig. 2.12a)

iv. a transverse steel strain (7 in Fig. 2.13a and 6 in Fig. 2.13b)

Cracking patterns were observed visually and recorded by marking crack propagation.

2.6.3 Deformation History

One of the parameters studied in this investigation was the deformation history. Two deformation histories were considered. Models 2R, 4R and 1S were subjected to a monotonic history, referred to as history I (Fig. 2.14a). The model was loaded in one direction until a tip displacement 4 times the observed yield displacement* was imposed. The load was then reversed and an equal displacement was imposed in the opposite load direction. After the full reversal the model was reloaded in the initial direction. The extent of additional loading was determined by the condition of the model at this stage of the test.

The yield displacement was taken as 22.9 mm (0.9 inches) in the first test of a model subjected to history I (2R), and 91.6 mm (3.6 inches) was the maximum displacement imposed. A maximum displacement of 91.6 mm was imposed in the subsequent models subjected to history I in order to make comparisons among the different models.

Models 3R, 5R, 6R and 2S were subjected to a series of incrementally increasing cyclic displacements. This deformation history is referred to as history II. A graphical representation of typical cyclic displacements are shown in Fig. 2.14b. The displacement levels range from 5.1 mm to 76.2 mm (0.2 to 3.0 inches).

The effects of different deformation histories on the behavior of reinforced concrete structures is not well known. Therefore, it is not possible to define a typical or critical load history for testing pur-

* The yield displacement is defined in Section 3.1.

poses. However, it is believed that valuable information can be gained by comparing the behavior of models subjected to cyclic and monotonic load histories.

2.6.4 Testing Sequence

The axial load was applied first and was held constant for the duration of the test in both deformation histories. The lateral load (displacement) sequence is presented below for each of the deformation histories.

i. History I

The load was increased in 66.7 kN (15 kip) intervals until yielding was observed. After yield the displacement was increased in 12.7 mm (1/2 inch) increments until the maximum displacement was reached. The same load and displacement increments were used on reversal. The loading process was incremental so that the instrumentation could be read.

Readings were taken at zero displacement and at the maximum displacement in a particular direction during loading after the full reversal.

ii. History II

A typical loading sequence, in which Δ is the model tip displacement, is given below.

a. take zero readings prior to any imposed displacement, (Δ=0)

b. load in the positive direction until reaching $\Delta = +\Delta_i$. Take

a full set of readings. Unload until $\Delta = 0$ after taking readings. Again take a full set of readings.

c. Load in the negative direction until $\Delta = -\Delta_1$. Take readings. Unload until $\Delta = 0$. Take readings.

d. Repeat cycle outlined in b and c three times without taking any readings.

e. Repeat a fourth time, taking all the readings indicated in a, b, and c.

f. Repeat sequence a-e for each displacement increment. Displacement levels of 5.1 (0.2), 10.2 (0.4), 15.2 (0.6), 20.3 (0.8), 25.4 (1.0), 31.7 (1.25), 38.1 (1.5), 44.4 (1.75), 50.8 (2.0), 63.5 (2.5) and 76.2 (3.0) mm (inches) were imposed.

2.7 Model Column Data

A summary of the mechanical characteristics of the concrete and steel, the applied axial load, the moment and shear capacity, and the deformation history for each model is given in Table 2.

The concrete compressive strength, found from tests of 152 mm × 305 mm (6 inch × 12 inch) cylinders, ranged in value from 32.4 MPa to 36.5 MPa (4700 psi to 5300 psi). The average yield strength of the longitudinal steel was 496 MPa (72,000 psi) for the rectangular tied columns and 538 MPa (78,000 psi) for the spirally reinforced columns.

The model axial load ranged from 1067 kN (240 kip) to 640 kN (144 kip), corresponding to nominal compressive stresses of 11.5 MPa and 6.9 MPa (1670 psi and 1000 psi) respectively. Balance point axial

loads are indicated by *.

The column moment capacity was determined by using the measured material properties and by assuming:

a) A linear strain distribution

b) Zero concrete tensile strength

c) A parabolic stress-strain relationship for concrete, with a linear descending branch (Fig. 2.15a). The descending branch of the stress-strain relationship is based on an idealization of the improvement in inelastic concrete behavior due to the confining effect of the transverse reinforcement (12)

d) A linear elastic perfectly plastic steel stress-strain law (Fig. 2.15b).

The shear capacity in column 7 of Table 2, referred to as the flexural shear capacity, V_F is the shear force corresponding to the moment capacity given in column 6, and is defined by the expression

$$V_F = M/a \qquad 2.2$$

where

$$a = h_c/2$$

h_c = the clear column height [914 mm (36 inches)]

V_F for models 2R, 3R, 4R, 1S and 2S is slightly larger than that used in the design of the column transverse reinforcement (Appendix B). The difference is due to the different concrete stress-strain idealizations used in determining the respective moment capacities. The moment capacity employed in the column design was determined on the basis of an un-

confined concrete idealization while, as indicated above, the moment capacity in column 6 was determined on the basis of a confined concrete idealization. Typically, because the slope of the descending branch of the confined concrete idealization is not as steep as that for unconfined concrete, the confined concrete idealization results in larger moment capacities.

3. EXPERIMENTAL RESULTS

3.1 Preliminary Remarks

The results of the experimental program are presented and discussed in this chapter. As discussed in Chapter 2, the test model consisted of a two story-one bay subassemblage of a typical spandrel wall frame and the model beams and half length column segments were designed to limit inelastic behavior and failure to the full column length (Fig. 2.1). Test results indicated that this design objective was achieved and the following discussions will therefore concentrate on the behavior of the full column length. In these discussions two definitions of model failure are employed. First, failure defines that point in a test at which the model column is unable to resist the original (design) axial load. Failure is also used to define the point in a test at which the original column shear resistance has decreased significantly.

The latter definition of failure was determined during each test and was based on the shape and stability of the shear force-tip displacement relationship and the general condition (visual) of the model column. This definition was established primarily to prevent damage to the electronic instrumentation. For purposes of comparison in the following discussions failure is assumed to be that point at which the original column shear resistance had decreased by 50%. Models for which this definition of failure applied were generally tested beyond this point. The shear resistance continued to decrease in all cases in which testing was continued.

Before beginning the discussion of column behavior, the term yielding deserves some comment. As used here, yielding refers to the initiation of significant inelastic behavior and is indicated by a flattening of the force-deformation relationship under discussion (Fig. 3.1) . The model yield displacement is defined as the displacement level at which yielding of the tensile reinforcement is first indicated by steel strain data.

3.2 General Description of Column Behavior

The general characteristics of column behavior prior to failure may be illustrated by referring to the variation of applied shear force, H, with tip displacement, Δ. It should be noted that Δ is a measure of the response of the total subassemblage and does not depend solely on the column behavior. However, since inelastic behavior was limited to the model column, Δ should reflect the inelastic column behavior.

As illustrated in Fig. 3.2, the relative story rotation, R, is defined by the expression

$$R = \Delta_3 - \Delta_5/h_c \qquad 3.1$$

where

Δ_3 = the measured displacement at upper end of the column

Δ_5 = the measured displacement at lower end of the column

h_c = clear column height

The parameter R provides a better measure of inelastic column behavior

and is discussed in Section 3.6.1. A brief discription of the H-Δ behavior in both the monotonic and cyclic deformation histories is presented below.

3.2.1 Behavior under Monotonic Deformation History

Models 4R and 1S were subjected to their respective balance point axial loads [1068kN and 890kN (240 kip and 200 kip) respectively] and the monotonic deformation history. After application of the axial load, P, H was applied in 66.7kN (15 kip) increments. As H was increased, flexural cracks and eventually diagonal tension cracks formed and propagated at both ends of the column in the vicinity of the beam-column joint (Fig. 3.3 and 3.4). A summary of the load intervals in which flexure and inclined cracking were first observed is given in Table 3. Crack formation and propagation causes the gradual stiffness degradation in the H-Δ relationship shown in Fig. 3.5. At a Δ of approximately 25.4 mm (1 inch), yielding of the longitudinal reinforcement and inelastic concrete deformation (spalling of the concrete cover was observed) causes the column regions adjacent to the beam-column joints to behave as plastic hinges (Fig. 3.6). This results in a significant reduction in the subassemblage stiffness as is evident by the flattening of the H-Δ relationship. The behavior of Models 4R and 1S was somewhat different after the formation of the plastic zones at the column ends and is discussed in Sections 3.3 and 3.4.

3.2.2 Behavior under Cyclic Deformation History

The behavior of columns subjected to the cyclic deformation history was similar to the behavior observed during the monotonic history. One difference is that in the cyclic deformation history similar crack patterns occurred on both sides of the column depth and inclined cracks formed in a typical X-pattern (Fig. 3.7 and 3.8).

The first cycle hysteresis loops for model 3R (Fig. 3.9) indicate a gradual stiffness degradation with increasing deformation level. This degradation is due not only to the effects of increased load levels as in the monotonic history but is also a consequence of cycling at constant deformation levels.

Hysteretic behavior at a given displacement level prior to failure was stable, i.e., the potential column shear resistance did not decrease. This is illustrated by Fig. 3.10 which summarizes the shear degradation, S_d, defined by the expression

$$S_d = \frac{H_{\substack{\text{first}\\\text{cycle}}} - H_{\substack{\text{fifth}\\\text{cycle}}}}{H_{\substack{\text{first}\\\text{cycle}}}} \cdot 100 \qquad 3.2$$

at each displacement level for models 2S, 3R, 5R and 6R. In all models but 2S the shear degradation is less than 10% prior to the failure displacement, Δ_f, the displacement level at which significant shear degradation occurred. In model 2S the shear degradation jumps above 10% at 31.7 mm (1.25 inches). This jump is attributed to sudden spalling of the concrete cover which was observed during cycling at this displacement

level.

The small values of S_d prior to Δ_F reflects the stiffness degradation associated with cycling at constant deformation. This degradation is illustrated by a direct comparison of the monotonic and cyclic deformation histories (Fig. 3.11-3.12). Fig. 3.11 compares the monotonic H-Δ relationship for model 4R with the first cycle H-Δ cyclic envelope for model 3R. The cyclic envelope depicts the applied shear force at the peak displacement amplitude. Models 4R and 3R were subjected to the same axial load of 1068 kN (240kip).

Although the cyclic H-Δ envelope and the monotonic H-Δ relationship exhibit significant inelastic behavior at the same value of Δ [25.4 cm (1 inch)], the maximum shear resistance in the cyclic deformation history was smaller than that in the monotonic one. This apparent decrease in potential column shear resistance associated with the cyclic deformation history is a consequence of cyclic stiffness degradation. A comparison of the monotonic H-Δ relationship for model 4R with the initial loading segment of the first cycle hysteretic loops for model 3R at displacement levels of 25.4 and 31.7 mm (1.0 and 1.25 inches) provides a clear illustration of this stiffness degradation (Fig. 3.12). If the displacement would have been increased as indicated by the dashed projections of the cyclic H-Δ relationships, the shear resistance obtained in the monotonic history would have been obtained, but at an increase in displacement of approximately 40%.

As in the monotonic deformation history column behavior following formation of plastic zones at the column ends differed among the various models and is discussed later.

3.3 Model Failures

All failures occurred in the columns. The column flexural shear capacity was equaled or exceeded in all models but 2S and all columns experienced significant inelastic deformation prior to a brittle shear failure or significant shear degradation (Table 4). Three basic failure modes were observed, a shear-compression failure (models 2R, 3R, 5R), a bond failure (models 1S and 2S) and a diagonal tension failure (4R and 6R). The magnitude of the axial force, the type of transverse reinforcement, and the deformation history influenced the failure mode. The shear-compression failure and the bond failure were gradual, resulting in shear and stiffness degradation. However, model columns failing by either shear-compression or bond were able to maintain the design gravity load at test conclusion. A load reversal was necessary before either of these failures could occur. The shear and stiffness degradation in the shear-compression failure was due to a decrease in the ability to transfer longitudinal shear forces across what is referred to as the mid-depth longitudinal crack. The failure was preceded by yielding of the transverse reinforcement crossing this crack. The shear and stiffness degradation in the bond failure was due to a gradual deterioration of bond between the longitudinal steel and concrete in the column length.

The diagonal tension failure was sudden, being caused by a sudden propagation of a diagonal tension crack and the rupture of the transverse reinforcement crossing the critical diagonal crack. Model columns which failed in diagonal tension could not resist shear forces or maintain the design gravity load at test conclusion.

The shear-compression failure and the diagonal tension failure are associated with the behavior of a critical crack. High shear stresses were a major factor influencing the formation and propagation of the critical crack. The nominal shear stress, v, defined by the expression

$$v = \frac{H}{bd} \qquad 3.3$$

where

H = the imposed shear force

b = the section width

d = the effective depth

was high in all models (Table 4). The shear stresses range from 4.0 MPa (580 psi) to 5.2 MPa (760 psi) when the nominal cross section is considered, and from 4.3 MPa (630 psi) to 5.9 MPa (852 psi) when only the confined core area is considered.

The three failure modes are described in detail in the following sections.

3.3.1 Shear-Compression Failure

The failure mechanism in models 2R, 3R and 5R was the same and is referred to as shear-compression. High nominal shear and compressive stresses (Tables 2 and 4), a mid-depth longitudinal crack and stiffness and shear degradation were common to the failure in all three models. Characteristics of the shear-compression failure mode will be elaborated on by a discussion of the steps leading to failure in model 5R.

The critical crack involved in the shear-compression failure is referred to as the mid-depth longitudinal crack. This crack began as a series of inclined cracks (15-30°) at mid-depth near mid-column height (Fig. 3.13). The inclined cracks were first observed during cycling at a displacement level of 15.2 mm (0.6 inches). The formation of these cracks is attributed to the combined effect of local stress concentrations caused by the longitudinal reinforcement and cross ties at mid-depth, the tensile stresses at mid-depth caused by high shear stresses, and the tensile Poisson strains associated with high compressive stresses. The existance of the tensile stresses is illustrated by Fig. 3.14. If it is assumed that

1) the axial load causes a uniform stress distribution
2) mid-column height is an inflection point and the moment is zero
3) the shear force causes a parabolic shear stress distribution through the depth
4) the above shear and compressive stresses are the only stresses

the Mohr's circle in Fig. 3.14b defines the state of stress in a typical element at mid-depth. The direction of the principal tensile stress indicated by Mohr's circle would cause the formation of cracks with inclinations (21°) similar to those observed in Model 5R. However, the magnitude of the corresponding tensile stress does not indicate that cracking would occur. It should be noted that the stress state assumed above probably does not reflect the actual stress state which caused the observed cracking as a number of effects have been neglected. These include

a) Stress concentrations caused by steel reinforcement. The discontinuities in the concrete caused by the longitudinal bars and cross ties at mid-depth (Fig. 1.4), in addition to the local stresses associated with bearing of the bar deformations against the surrounding concrete generate stress concentrations in the concrete.

b) The cracks initially did not form at mid-height. As a result flexural stresses exist.

c) In the core concrete, the transverse poisson strains are restrained by the transverse reinforcement. The absence of this restraint in the core concrete may cause stress concentrations in the boundary zone between the core and cover concrete.

It is felt that the inclined cracks at mid-depth were initially a local phenomenon, i.e., the cracks did not extend through the width of the column but extended only through the immediate vicinity of the reinforcement, in particular through the unconfined cover. It should be noted that this series of cracks was observed in all models (Fig. 3.3, 3.4, 3.8).

The series of inclined cracks at mid-depth became continuous during cycling at a displacement level of 31.7 mm (1.25 inches) forming the mid-depth longitudinal crack. The crack extended through the width of the column and relative motion between opposite faces of the longitudinal crack was observed (Fig. 3.15).

The formation of a continuous longitudinal crack is a result of crack propagation. The inclined cracks which had formed in one load direction continued to propagate as the displacement level in that direc-

tion was increased. When the crack propagation in a given load direction (A in Fig. 3.13a) reached a crack formed in the opposite load direction (B in Fig. 3.13a), further propagation occurred along the existing crack since it offered the least resistance to the propagation. A continuous crack formed when all the inclined cracks in one direction began to propagate along cracks in the other direction.

A similar continuous crack at column mid-depth was observed in the spiral column (models 1S and 2S), however, is extended only through the cover concrete. It is felt that the weak plane created by the longitudinal steel and cross ties at mid-depth in the tied columns contributed to the formation of the mid-depth longitudinal crack through the width of the column.

The formation of the mid-depth longitudinal crack occurred at approximately the same time as the formation of plastic zones at the beam column joints. Concrete spalling, and yielding of the longitudinal reinforcement, observed initially during cycling at 25.4 mm, caused the regions adjacent to the beams to experience concentrated inelastic rotations. At this stage of the deformation history, the model column may be idealized as two plastic zones, one at each end of the column, spanned by two parallel flexural elements which are coupled by a series of longitudinal and transverse links (Fig. 3.16). The longitudinal links develop longitudinal shear forces across the two flexural elements and would have stiffness properties characteristic of aggregate interlock and dowel action of the transverse reinforcement. The transverse links are required to include the restraint of the transverse reinforcement to widening of the gap (crack) between these two elements.

The deformation associated with motion along the mid-depth longitudinal crack will tend to reduce the inelatic rotations in the plastic zones. The column with a mid-depth longitudinal crack is not as stiff as an identical column without such a crack. Consequently, the inelastic rotations required to produce the same tip displacement is less for a 'cracked' column than for an 'uncracked' one.

After the formation of the mid-depth longitudinal crack, the column's shear capacity was governed by the longitudinal shear transfer mechanism across this crack, i.e., by the force deformation characteristics of the longitudinal links in Fig. 3.16. An important factor affecting the link characteristics is the longitudinal crack width. Prior to cycling at a displacement level of 63.5 mm (2.5 inches), the width of the mid-depth longitudinal crack and the relative motion along the crack remained small [between 1.6 and 3.2 mm (1/16 and 1/8 of an inch) as compared to approximately 9.5 mm (3/8 of an inch) at a displacement of 63.5 mm] and the strength of the longitudinal shear transfer mechanism was stable, i.e., the potential column shear resistance did not degrade.

The stability of the shear transfer mechanism is illustrated by the shear degradation caused by cycling at a given displacement level (Fig. 3.17). The degradation was less than 10% prior to a displacement of 63.5 mm, and as discussed previously, reflects a cyclic stiffness degradation. If loading was continued and the displacement level increased in the last cycle, the first cycle shear resistance would have been attained in the last cycle (Fig. 3.18). An examination of the change in shear required to increase the displacement level supports this observation (Fig. 3.17a). The shear force required to impose the first cycle of a new larger cyclic displacement level was greater than the shear force re-

quired to impose the last cycle of the previous smaller displacement level.

Cycling at a displacement level of 63.5 mm led to a 44% degradation in column shear resistance. A comparison of the initial portion of the H-Δ hysteretic loops in the first and last cycle at 63.5 mm and the first cycle at a new displacement level of 76.2 mm (3.0 inches) indicates that this shear degradation is not entirely due to stiffness degradation. The shear required to increase the displacement to 76.2 mm is less than the shear resistance in the last cycle at 63.5 mm. In addition the flatness of the loops indicate that an unrealistically large displacement would be required to reach the shear resistance attained in the first cycle at 63.5 mm. Therefore an actual degradation in the column shear resistance must have occurred as a result of cycling at 63.5 mm.

The change in behavior during cycling at 63.5 mm is attributed to yielding of the transverse reinforcement crossing the mid-depth longitudinal crack. Yielding was indicated by the strain gage data during the initial cycle at 63.5 mm and is caused primarily by the axial strains developed in restraining the width of the mid-depth longitudinal crack. Yielding of the reinforcement which reduced the restraint to crack widening initiated a cyclic degradation of the transfer shear mechanism, the aggregate interlock component in particular. Widening of the mid-depth longitudinal crack, increased relative crack motion, and a decrease in the effectiveness of aggregate interlock were amplified with each cycle because of their interdependance. The end result was a significant degradation in shear resistance.

Since the original column shear resistance had decreased by nearly 50% (actually 48%), the displacement level of 63.5 mm is considered the

failure displacement in model 5R. The testing of the model was continued, however, and the shear degradation initiated at 63.5 mm continued during cycling at a displacement level of 76.2 mm (3.0 inches). After five cycles the column shear resistance had decreased to 44.5 kN (10 kip).

The only notable difference in the shear-compression failure sequence from that presented for model 5R was found in model 2R which was subjected to the monotonic deformation history. The initial shock to $4\Delta_y$ did not result in the formation of the mid-depth longitudinal crack. The principal crack in the initial load direction was an inclined shear crack (Fig. 3.20) . After the load was reversed, however, a mid-depth longitudinal crack did form and relative crack motion was observed as in model 5R.

A comparison of the shear degradation in models 2R and 3R, both of which were subjected to an axial load of 1068 kN (240 kip), indicates that the complete deformation cycle of the monotonic history had essentially the same effect on the column shear resistance as cycling at the failure displacement. In model 2R, the original column shear resistance had decreased by 50% on reloading after the complete deformation cycle, while in model 3R a decrease of 54% resulted after five cycles at the failure displacement.

In models 3R and 5R, cycling at the failure displacement had a detrimental effect on the concrete in the area at the end of the mid-depth longitudinal crack (Fig. 3.15). The discontinuities in the highly stressed compression zones created by the shear flexure cracking associated with the opposite load direction crossing the extended mid-depth longitudinal crack (Fig. 3.13a) caused localized compressive

failures. These failures spread and became quite severe as a result of cycling at the failure displacement (Fig. 3.21 and 3.22).

This deterioration is illustrated by the effect of cycling on the column axial stiffness. The 1.83 m (6 foot) gage length indicated in Fig. 3.23a was monitored in each test and may be used as a measure of the axial stiffness. A comparison of the increases in column shortening due to cycling at the failure displacement and at the displacement level prior to failure indicates that a significant degradation in axial stiffness occurred as a result of cycling at the failure displacement (Fig. 3.23b). Although the concrete deterioration at the ends of the mid-depth longitudinal crack was not the only cause of this degradation, it is believed a major factor influencing the degradation.

3.3.2 Bond Failure

The spirally reinforced columns experienced a bond failure. The essential characteristics of the bond failure were similar to the characteristics of the shear compression failure. The failure was gradual, resulting in shear and stiffness degradation, and the model column was able to maintain the design gravity load at test conclusion. The major difference between the bond failure mode and the shear-compression failure mode was the mechanism of shear degradation. In the bond failure mode the degradation was a consequence of bond deterioration, i.e. a degradation in the stress transfer mechanism between the longitudinal reinforcement and concrete. Although a continuous mid-depth longitudinal crack was observed in the spiral columns, it existed only in the cover

concrete. At the level of the core concrete, two cracks were observed running along the longitudinal reinforcement on either side of mid-depth (Fig. 3.24). These cracks did not extend through the width of the cross section but were localized in the vicinity of the rebar. Similar longitudinal cracks were observed along the reinforcement located at the extremes of the column depth (Figs. 3.25 and 3.26).

The longitudinal cracks along the reinforcement indicate a bond failure, i.e., a significant deterioration in the stress transfer mechanism between the reinforcement and concrete. These cracks and consequently the bond deterioration extended through the full column height. The bond deterioration also extended a distance into the beam column joint. Spalling of the concrete cover within the beam column joint was not as extensive as that along the column length and the extent of bond deterioration into the joint was not observed.

The effect of bond deterioration is evident in Fig. 3.27 which shows the hysteretic loops for model 2S at a displacement level of 63.5 mm (2.5 inches). The loops in Fig. 3.27 exhibit a cyclic stiffness and shear degradation and a pinching effect near zero load which reflects slip between the steel and concrete. The pinching becomes more pronounced with each cycle, indicating that the slip, and thus the bond deterioration, increases with each cycle. The increased slip results in the observed stiffness and shear degradation.

The longitudinal steel strain data for model 2S during cycling at the same displacement level provides a more quantitative measure of bond deterioration. In the initial cycle the compressive steel strain (gage 2 Fig. 2.13 b) changed by -.022 mm/mm and the tensile steel strain (gage

1 in Fig. 2.13b) changed by 0.023 mm/mm. In the fifth cycle the strain increments were -0.002 mm/mm for the compressive steel and 0.005 mm/mm for the tensile steel. Bond failure was also indicated by significant slip observed at mid-column height in the final cycles at this displacement level.

It should be noted that for a bond failure to occur a complete load reversal is necessary. For example, bond failure was not evident in model 1S (which was subjected to the monotonic deformation history) until reloading after the full deformation reversal (Fig. 3.28).

At test conclusion the core concrete in the spirally reinforced columns failing by bond was in better condition than the core concrete in the tied columns failing by shear-compression. This difference is attributed to

a) the concrete deterioration at the ends of the mid-depth longitudinal crack which was observed in the tied columns did not occur in the spiral columns.

b) the spiral reinforcement provided more effective confinement and improved the inelastic concrete behavior

A quantitative measure of the column condition at test conclusion is provided by the effect of cycling on the column axial shortening (Fig. 3.23b). A comparison of the change in shortening due to cycling at the respective failure displacements in models 5R and 2S, both of which were subjected to axial forces of 890 kN (200 kip) illustrates that the increase in column shortening is significantly greater in the tied column than in the spiral column.

Bond failure may be attributed to two characteristics of the spiral

columns. First, spiral transverse reinforcement, because of its continuity and because of the fact that its shape is ideal for resisting radial pressure, possesses generally superior confinement characteristics and offers a stiffer restraint to crack widening than rectangular ties. As a result, significant shear degradation due to losses in the column transverse shear capacity is prevented, creating conditions for a 'non-shear' failure. Second, the longitudinal reinforcement in the spiral columns consisted of No. 5 bars which, being larger than the No. 4 bars used in the tied columns, increased the possibility of a bond failure.

3.3.3 Diagonal Tension Failure

Models 4R and 6R experienced a sudden and brittle failure mode. The model column was unable to resist any shear forces or maintain the design axial load after failure. The failure in both models is attributed to a force redistribution among the various components of the shear resistance mechanism which ultimately caused rupture of the transverse reinforcement crossing a critical inclined crack. The formation of the critical crack was associated with diagonal tension and this failure mode is referred to as diagonal tension failure.

The shear resistance of a reinforced concrete member with a principal inclined crack is determined by the shear strength of the concrete compression block, the interlocking stresses developed across the inclined crack, the transverse reinforcement, and the dowel action of the longitudinal steel (Fig. 3.29). As the imposed shear force is increased the contribution of the concrete compression block, aggregate interlock

and possibly dowel action decrease, and the contribution of the transverse reinforcement increases. In model 6R this phenomenon is amplified by the cyclic deformation history. The decrease in the shear force resisted by the concrete compression block is initially more significant than the decrease in the other components, particularly in model 4R which was subjected to the monotonic load history. The decrease is caused by two factors. First, the size of the compression block is reduced by propogation of the inclined shear crack. Second, the compression block is part of the plastic zone which formed at the end of the column adjacent to the beam-column joint. The inelastic concrete deformations associated with the plastic zone cause spalling of the concrete cover, further reducing the size of the compression block, and since the core concrete strains will typically be on the descending branch of the concrete stress-strain (σ-ε) relationship (Fig 3.30a) a decrease in the shear strength of the compression block concrete is expected (8).

In both models, cover spalling was observed after formation of the plastic zones. In addition average compressive strain data, ε_{AVG}, measured in the plastic zones indicate that concrete strains would be on the descending branch of the σ-ε relationship. For example, the variation of ε_{AVG} with tip displacement in model 4R is shown in Fig. 3.30b. Two relationships are given. The solid line shows the variation of concrete strains measured at a distance of 63.5 mm (2.5 inches) from the column edge, $\varepsilon^{2.5}_{AVG}$. The dashed line shows the variation of the strains at the edge of the column core, ε^{c}_{AVG}, which were determined from the measured strains by a linear extrapolation. The magni-

tude of ε^c_{AVG}, after a displacement of 25.4 mm is greater than 0.0025 mm/mm, a strain typically on the descending branch of a concrete σ-ε relationship.

As noted previously, the decrease in the shear resistance of the concrete compression block, as well as the decreases in the aggregate interlock and dowel action mechanisms, are compensated for by an increase in the shear force resisted by the transverse reinforcement. This force redistribution is illustrated by the transverse steel strain data.

In model 4R, the geometry of the critical inclined crack indicates that it was crossed by five ties. The strains, and thus the forces, are known in one of the four tie legs (Fig. 3.31a). If it is assumed that the strains in all four legs is the same as that measured, and that the force in the fifth tie is equal to the average of the forces in the other four ties, the contribution of the transverse reinforcement to the shear resistance, V_s, may be calculated. The results are summarized in Fig. 3.31b. Also shown is the combined contribution of the compression block, aggregate interlock and dowel action to the shear resistance, V_{cgd}

$$V_{cgd} = H - V_s \qquad 3.4$$

The jump in V_s in going from a displacement level of 15.2 mm (0.6 inches) to 25.4 mm (1.0 inch) indicates that the diagonal tension crack initially formed in this displacement increment at a load level between 280 kN (63 kip) and 356 kN (80 kip). As the displacement level was increased beyond 25.4 mm, V_s increased and V_{cgd} decreased as H increased, demonstrating that shear forces are transferred to the transverse reinforcement from the other components of the shear resistance mechanism.

The decrease in shear resistance of the concrete compression block in model 6R is illustrated by the cyclic variation of strain for a tie crossing the critical inclined crack (Fig. 3.32 and 3.33). The initiation of inclined cracking is indicated by the sudden jump in the steel strain in the first cycle at 15.2 mm (0.6 inches) (Fig. 3.32). In all subsequent displacement cycles there is a region in which the steel strain increases very little (Fig. 3.32-3.33). This region reflects the column shear resistance prior to crack opening and relative crack motion, and it is assumed to be a measure of the contribution of the compression block to the column shear resistance. After the initial crack formation, the compression block resisted approximately 142 kN (32 kip) or 59% of the applied shear force (Fig. 3.32). As the displacement level was increased the shear resistance of the compression block decreased gradually, going from the original 142 kN at 15.2 mm (0.6 inches) to approximately 80 kN [(18 kip) 29% of the applied shear force] at 44.4 mm [(1.75 inches) Fig. 3.33].

The gradual increase in the steel strains as the cyclic displacement level increases beyond 25.4 mm (1 inch) combined with the fact that the applied shear force changes only slightly beyond this displacement level illustrates the transfer of shear force from other components of the shear resistance mechanism to the transverse reinforcement.

The shear transfer to the transverse reinforcement was stable, i.e., the column shear resistance did not decrease, until the transverse reinforcement yielded. In model 4R, a reduction in the column shear resistance does not occur until the displacement increment from 63.5 mm to 76.2 mm (2.5 inches to 3.0 inches) (Fig. 3.34). Strain data indicated

initiation of yielding of the transverse reinforcement at the start of this increment. In model 6R, the cyclic shear degradation was less than 10% prior to a displacement level of 63.5 mm (2.5 inches) and, as discussed previously, reflects a cyclic stiffness degradation (Fig. 3.35). In addition an increase in shear resistance was required to increase the displacement level (Fig. 3.35). During cycling at 63.5 mm, however, yielding of the transverse reinforcement crossing the critical inclined cracks caused a significant degradation in the column shear resistance (Fig. 3.35).

Yielding of the transverse reinforcement effects the shear capacity in two ways.

a) the ability of the transverse reinforcement to compensate for shear loss in the other components of the shear resistance mechanism is reduced

b) a decrease in the restraint to crack widening which is provided by the transverse reinforcement occurs. This permits the crack to widen which leads to a reduction in the effectiveness of aggregate interlock and dowel action

The shear degradation initiated by yielding of the transverse reinforcement was amplified by the cyclic deformation history. The inclined cracks widened and relative motion along the cracks increased with each cycle, resulting in degradation of the shear resistance mechanism, in particular the aggregate interlock component.

A brittle failure occurred shortly after the decrease in column shear strength was initiated by yielding of the transverse reinforcement. Failure occurred at a tip displacement of 88.9 mm (3.5 inches) in model 4R and with the start of a new displacement cycle after five complete

cycles at a displacement level of 63.5 mm (2.5 inches) in model 6R. A sudden propagation of the diagonal crack caused a separation of the model into two parts which were connected by the longitudinal and transverse reinforcement (Fig. 3.36 and 3.37). The sudden loss of shear resistance which was previously provided by the compression block, resulted in large increases in the transverse reinforcement strains, which caused this reinforcement to neck and rupture. Rupture led to a complete loss in shear resistance and to a reduction in the capacity of the column to support gravity loads. After failure, the maximum axial load which could be applied without causing relative motion between the two parts of the column was 467 kN (105 kip) in model 4R and 445 kN (100 kip) in model 6R. These final axial load capacities represent reductions of 60% and 30% from the respective design capacities of 1068 kN (240 kip) and 641 kN (144 kip).

3.4 Shear Force-Tip Displacement Response

3.4.1 Shear Force-Tip Displacement Response Under Monotonic Deformation History

The shear force-tip displacement (H-Δ) relationships for models 2R, 4R and 1S are shown in Figs 3.38-3.40 . Two relationship are shown for each model. The upper curve represents an equivalent shear, $H_{P-\Delta}$, which includes the P-Δ effect. $H_{P-\Delta}$ was determined by the expression

$$H_{P-\Delta} = H + R \cdot P \qquad 3.5$$

where

H = the imposed shear force

P = the axial load, and R is defined in equation 3.1

All models exhibited yield behavior, which is indicated by a flattening of the H-Δ relationship, at a displacement of approximately 25.4 mm (1 inch). Since the steel strain data indicated initial tensile yielding in the load increment leading to this value of Δ, the yield displacement was taken as 25.4 mm. After yielding, the shear resistance in models 2R and 4R first increased before a loss in shear resistance occurred. In model 1S, however, there was a sudden drop in shear resistance followed by a gradual loss of shear strength. The loss in shear resistance just before the maximum displacement was 44 (10), 62 (14) and 80 (18) kN (kip) in models 2R, 4R and 1S respectively.

This decrease in shear resistance is attributed to a decrease in the shear strength of the concrete compression block. The difference in post yield behavior between the rectangular tied columns and the spiral column, and the greater loss in shear resistance in the spiral column are attributed to the effect of cover spalling. Spalling was observed in all models, however, it was sudden and resulted in a greater area loss in the spiral column [the core area of the spiral column was 55,490 mm^2 (86 in^2) compared to 70,970 mm^2 (110 in^2) for the tied columns].

On reaching the maximum displacement, model 4R failed suddenly in the diagonal tension mode and the test was terminated. Models 2R and 1S, however, were unloaded and subjected to a load reversal. A pinching effect in the H-Δ relationship was observed in both models on reversal (Figs. 3.38 and 3.40). The pinching effect is due to the fact that

cracks which had formed in the previous load direction did not close completely at zero load. As a result the stiffness due to contact between opposite crack surfaces is not completely effective as loading begins. The contact stiffness becomes effective gradually as the load increases and the cracks close because the crack faces are rough and there are small loose granulates (asperities) and some stress transfer due to contact of these asperities, aggregate interlock, and/or friction is possible before the crack is closed completely.

After existing cracks have closed and the pinching effect is no longer present, a degradation in the elastic, or initial loading stiffness is observed (Figs. 3.38 and 3.40). This stiffness degradation was more pronounced in model 1S. Model 1S also experienced a significant decrease in shear resistance with the load reversal. The maximum shear resistance in the initial load direction was 347 kN (78 kip), while on reversal it was only 214 kN (48 kip). Model 2R faired better. In the initial load cycle the maximum shear resistance was 409 kN (92 kip), decreasing to 356 kN (80 kip) on reversal. The behavior of models 1S and 2R was quite different as the displacement level was increased beyond the displacement corresponding to the maximum shear resistance. In model 1S the shear resistance decreased very little. In fact, when the P-Δ effect is included the shear resistance increases. In model 2R however the shear resistance decreased from a maximum of 356 kN at a displacement of -38.1 mm (-1.5 inches) to 249 kN (56 kip) at a displacement of -76.2 mm (-3.0 inches).

The difference in the post-yield behavior during the load reversal is due to the different failure modes which these two models experienced.

The failure in model 1S was due to a bond failure and did not occur until the complete load reversal had been applied and the model was reloaded in the initial load direction. Model 2R failed by the shear compression mode and the decrease in shear resistance during the load reversal is due to the degradation in the horizontal shear transfer capacity across the mid-depth longitudinal crack.

On reloading in the original load direction the pinching effect is more pronounced than in the initial load reversal and a significant decrease in strength was recorded in both models. In model 1S the shear resistance decreased to 138 kN (31 kip) at a displacement of 88.9 mm (3.5 inches). In model 2R the shear resistance decreased to 200 kN (45 kip) at a displacement of 63.4 mm (2.5 inches)*. At test termination both models were capable of resisting the original axial load.

3.4.2 Shear Force-Tip Displacement Response under Cyclic Deformation History

H-Δ cyclic envelopes for models subjected to the cyclic deformation history are shown in Fig. 3.41-44. The envelopes for the first and fifth cycle and the first cycle $H_{P-\Delta}$-Δ envelope are shown.

A decrease in model ductility μ_ϕ , defined by the expression

$$\mu_\Delta = \frac{\Delta_{max}}{\Delta_y} \qquad 3.6$$

* The deformation history of model 2R continued beyond that indicated in Fig. 3.31. It was subjected to three displacement reversals at 63.5 mm. The results are presented in section 3.6.

where

Δ_y = the displacement level at which the tensile steel strain data indicated yielding (It was taken as 25.4 mm (1 inch) in all models)

Δ_{max} = maximum displacement in History I or the failure displacement in History II

is caused by the cyclic history. μ_Δ is 3.5 for models subjected to the monotonic deformation history and is less than or equal to 2.5 for models subjected to the cyclic deformation history.

The first cycle envelopes for all models subjected to the cyclic deformation history are compared in Fig. 3.45. In models 3R, 5R and 6R the only parameter varied was the axial load. As expected from the axial force-moment interaction relationship (Fig. 1.5), higher axial loads increase the shear force the column is required to resist.* From a comparison of the behavior of models 3R and 5R it may be concluded that smaller axial loads improve the inelastic cyclic behavior provided the failure mode is the same. μ_Δ increased from 2.0 to 2.5, and the shear degradation decreased from 54% to 48% as the axial load was reduced from 1068 kN (240 kip) in model 3R to 890 kN (200 kip) in model 5R. Since the shear stresses in these two models are approximately the same (Table 4), the only difference in the stress condition existing in the two models is the difference in axial compressive stresses. The decrease in axial compressive stress appears to improve behavior. But why?

* Model 5R does have a higher shear resistance in one direction than model 3R. This is believed to be a consequence of the cyclic stiffness degradation which apparently is greater in model 3R (Figs. 3.46 and 3.47).

The failure, or more appropriately the shear degradation in models 3R and 5R, was caused by the increased relative motion along the mid-depth longitudinal crack. Longitudinal splitting along the core boundaries through the length of the column, which indicated spalling of the concrete cover, was observed at the same time as the increased crack motion. Since the axial load remains the same, and the concrete area resisting it was reduced by spalling, the compressive stresses in the concrete core increased as a result of the longitudinal splitting. This increase in concrete compression increased the transverse strains due to the Poisson effect. The larger transverse strains increased the strains in the transverse reinforcement which contributed to yielding of this reinforcement. As discussed in Section 3.3.1, yielding of the transverse reinforcement initiated the shear degradation observed in models 3R and 5R.

Longitudinal splitting was first observed during cycling at 44.5 mm (1.75 inches) in model 3R, while in model 5R it was observed during cycling at 63.5 mm (2.5 inches). It is apparent that the smaller axial load in model 5R delayed the longitudinal splitting and resulted in an improvement in the inelastic behavior.

3.5 Hysteretic Behavior and Energy Dissipation

Shear force-tip displacement hysteretic behavior for models 3R, 5R, 6R and 2S during the first full deformation cycle of the cyclic deformation history are shown in Figs. 3.46-3.49. A summary of the energy dissipation represented by the hysteretic loops is presented in Table 5.

Both an absolute magnitude and a relative magnitude (RA) of hysteresis area are given. RA is defined by the expression

$$RA = \frac{A}{H_1 \cdot 2\Delta + H_2 \cdot 2\Delta} \qquad 3.7$$

where

A = the hysteresis area

Δ = the tip displacement (positive)

H_1 = the absolute value of the recorded shear at $+\Delta$

H_2 = the absolute value of the recorded shear at $-\Delta$

RA will be used as an indication of the shape of the loops, larger values of RA indicating wider loops.

The first cycle hysteretic loops are similar for all models prior to yielding. RA remains essentially constant to a displacement of 25.4 mm (1 inch). This indicates that the shape of the loops did not change and that the increase in energy dissipation was due to increases in the imposed shear. Prior to yielding, models subjected to the balance point axial load (3R and 2S) dissipate more energy and have wider loops. In all models, the hysteretic loops at a given displacement level are similar, and a gradual stiffness degradation with increasing displacement level is evident.

Energy dissipation increased and the hysteretic loops got wider after yielding. For the rectangular tied columns, the energy dissipation was in general greater for models with higher axial loads. Model 2S had the smallest dissipation after the start of inelastic behavior.

This is attributed to the small shear capacity of model 2S. At the same displacement level, the value of RA for model 2S is approximately the same as the value for models 3R, 5R and 6R. This indicates that the shape of the hysteretic loops is similar for all models. Consequently it can be assumed that the shape of the loops did not have a significant effect on energy dissipation. However, the magnitude of the shear forces did. The shear forces developed in model 2S were significantly smaller than those developed in the rectangular tied columns (Fig. 3.45).

The H-Δ hysteretic loops at the failure displacement for models 3R, 5R, 6R and 2S are shown in Figs. 3.50-3.53. A summary of the energy dissipation represented by each loop is given in Table 6.

The hysteretic loops for the rectangular tied columns are similar. A pinching effect and stiffness and shear degradation are observed. These effects are more pronounced in models with higher axial loads. For example the shear degradation was 44, 43 and 22 percent for models 3R, 5R, and 6R respectively. The hysteretic loops for model 2S exhibit a more pronounced pinching effect and a larger shear degradation (57%) than models in the R-series. Both of these characteristics are attributed to the bond failure mode which this model experienced.

In general energy dissipation decreased and the hysteretic loops widened with cycling at the failure displacement (Table 6). Model 6R is an exception. Initially a decrease was observed, but when the loops started to widen the energy dissipation increased. After five cycles the decrease in the energy dissipation was less than 1%.

The observed loss of energy dissipation is primarily a consequence of shear degradation rather than a change in loop shape resulting from

stiffness degradation and pinching effects. In all models, cycling causes an increase, or no change in the values of RA, indicating that the loops have widened or remained with the same shape. The loop widening can in some circumstances compensate for the loss of energy dissipation caused by shear degradation. This is the case in model 6R. Model 6R experienced the smallest shear degradation and the loop widening results in a minimal decrease in energy dissipation. This effect of loop widening also occurred during the last cycle in model 3R. The shear degradation in this cycle was small, the loop widened and the energy dissipation increased from 1660 kN-m to 1806 kN-m (102 kip-in to 111 kip-in) (Table 6).

The influence of load history on hysteretic behavior can be seen in Fig. 3.54 in which the H-Δ hysteretic loops at a displacement of 63.5 mm (2.5 inches) for models 2R and 3R are compared. The corresponding energy dissipation is given in Table 6. After the initial deformation cycle in model 2R, the hysteretic loops are similar when loading from zero to a positive displacement, and when unloading from the negative tip displacement to zero. A difference is observed in the unloading and subsequent loading represented by the segment ABCD. This difference is a consequence of the load history. The inclined shear crack which formed in model 2R during the initial load cycle was quite different from that in Model 3R (Figs. 3.7 and 3.20). In model 2R the crack spanned the full depth of the section, causing a more pronounced pinching effect in the portion ABCD of the hysteretic loop of model 2R. Cracking associated with the opposite load direction was similar in both models, resulting in the observed similarities in hysteretic behavior.

3.6 Column Deformations

A major objective of the experimental investigation was to characterize the inelastic behavior of short reinforced conrete columns subjected to simulated earthquake loading. As discussed previously in Chapter 1, reinforced concrete members designed to resist moderate to severe earthquakes are expected to experience large inelastic cyclic deformations. As a result an important factor in the characterization of member behavior is the member's ability to deform inelastically. Both overall and local deformation qualities are presented to illustrate the amount of inelastic deformation the model column experienced. The relative story rotation is used as a measure of overall deformation and the average curvature at the beam-column joint is presented as a measure of local deformation. In addition the longitudinal steel strain behavior is presented and discussed.

3.6.1 Relative Story Rotation

The relative story rotation, R, was defined in equation 3.1 (Fig. 3.2). This definition of R includes the rotation of the beam-column joint associated with the beam deformations. Consequently, the story rotation defined by equation 3.1 will be larger than that attributed solely to column deformations. However, since the subassemblage beams remain 'elastic' for the duration of the deformation history, the contribution of beam deformations to inelastic values of R are small and will remain essentially the same as the value at the initiation of in-

elastic behavior. As a result, it is felt that the values of R obtained from equation 3.1 provide an adequate measure of the inelastic deformation characteristics of the model column.

The variation of R with the tip-displacement Δ is shown in Figs. 3.55 and 3.56 for models 4R and 1S and in Figs. 3.57-3.59 for models 3R, 5R and 6R. The relationships for models 3R, 5R and 6R are envelopes, giving the value of R recorded at the peak displacement of each displacement level in the cyclic deformation history. The envelopes for the first and fifth cycle are given.

The nature of the R-Δ relationship is similar for all models. To a tip displacement of 25.4 mm (1 inch) the relationship is essentially linear. After a displacement of 25.4 mm the slope increases and linearity no longer exists.

The knee in the R-Δ relationship at a displacement of 25.4 mm is caused by inelastic behavior in the model column and indicates that the initiation of significant inelastic behavior occurs at the assumed yield displacement of 25.4 mm. The formation of plastic hinges in the column at the beam-column joints changes the rotational stiffness at the ends of the column. This causes an increase in the column's contribution to the tip displacement. The increase occurred in both deformation histories and is illustrated by the comparison of the measured deflected shapes at displacement levels before and after the onset of yield behavior for models 4R and 3R given in Fig. 3.60.

In the cyclic deformation history, deformation cycles at a constant tip displacement, Δ, did not guarantee cycles at a constant value of R. Cyclic stiffness degradation causes a decrease in the shear force neces-

sary to impose Δ. As a result, since Δ remains constant, the component of Δ attributed to the essentially 'elastic' deformations of the model beams and upper and lower column stubs will decrease and the component attributed to the column deformations (of which R is a measure) will increase. As discussed in Section 3.2.2, the shear degradation associated with cyclic stiffness degradation is small prior to the failure displacement, Δ_F, and, as indicated in Figs. 3.57-3.59, R changed very little as a result of cycling at displacement levels less than Δ_F. However, the shear and stiffness degradation which occurred during cycling at Δ_F caused a significant reduction in the shear force necessary to impose Δ_F and the column deformations (Fig. 3.61), and consequently, R (Figs. 3.57-3.59), do increase noticeably.

The increase in the relative story rotation which occurred during cycling at Δ_F was proportional to the observed shear degradation. The increase was 21% in models 3R and 5R and 9% in model 6R, while the shear degradation was 44% in model 3R, 43% in model 5R and 22% in model 6R.

The variation of R with the imposed shear force H in models 4R and 1S is shown in Fig. 3.62. The H-R relationships are similar to the H-Δ relationships presented earlier (Fig. 3.38 and 3.40), and indicate that the model columns experienced significant inelastic deformation. For example, if the yield rotation, R_y, is taken as the value indicated in Fig. 3.55, the story rotation ductility, μ_R, defined by the expression

$$\mu_R = \frac{R}{R_y} \qquad 3.8$$

is approximately 6 in both models.

H-R envelopes for models 3R, 5R and 6R are shown in Fig. 3.63. The envelopes give the peak values of R and H in the first cycle of each displacement level of the cyclic deformation history. If R_y is taken as the value indicated in Fig. 3.63, the values of μ_R for the first cycle at the failure displacement are 4.0, 4.5 and 4.7 in models 3R, 5R and 6R respectively. So even when subjected to a cyclic deformation history with complete reversals the model columns could undergo significant inelastic deformation before 'failure' occurred.

As previously discussed, R, and consequently μ_R, increased as a result of cycling at the failure displacement (Fig. 3.57-3.59). However, a shear degradation also occurred. The increase in μ_R and the corresponding shear degradation for models 3R, 5R and 6R are summarized in Fig. 3.63.

3.6.2 Local Deformations

The average curvature of the 152 mm (6 inch) length closest to the beam-column joint was monitored during the experiments. The arrangement of the instrumentation (Fig. 2.12), and the equation used to relate displacement readings to average curvatures were based on the classical assumption of flexural behavior; plane sections remain plane during bending. The local deformations at two locations across the depth were recorded (Fig. 3.64) and converted to the average curvature, ϕ_{AVG}, by the expression

$$\phi_{AVG} = \frac{\delta_A - \delta_B}{a\ L_G} \qquad 3.9$$

where

δ_A = measured deformation at depth A

δ_B = measured deformation at depth B

a = distance between depth A and depth B

L_G = gage length

The accuracy of curvature data based on a plane section assumption is questionable in this particular case. The possibility of significant shear deformation (the column shear span to depth ratio is 1.5) and the effect of cracking and crack motion make the validity of this assumption questionable. Typical plastic hinge behavior at the beam-column joint was observed, however, and the curvature data obtained should provide some measure of the inelastic flexural deformation experienced by the model column.

i Flexural Deformations under Monotonic Deformation History

Monotonic moment curvature relationships for models 4R and 1S are given in Figs. 3.65 and 3.66. Three relationships are given for each model. The solid line is the variation of the average curvature, ϕ_{AVG}, with the column end moment, M_E. M_E is defined by the expression

$$M_E = H \cdot h_c/2 \qquad 3.10$$

where

H = the imposed shear force

h_c = clear column height

The dashed line is the variation of the curvature determined from the steel strain data, ϕ_{ST}, with the moment at the location of the gages, M_S . M_S is defined by the expression

$$M_S = H \cdot L_s \qquad 3.11$$

where

L_s = the distance from mid column height to the gage location

= 406 mm (16 inches)

The third relationship is an analytical moment curvature relationship based on the material properties of the model column. The analytical steel stress-strain relationship was based on the behavior of test specimens cut from reinforcement used in the model columns (Figs. A.2 and A.3). The concrete stress-strain relationship used is defined in Fig. 2.15a. The descending branch slope corresponding to confined concrete was considered in the evaluation of the moment curvature relationship.

A similarity exists between the ϕ_{AVG} and ϕ_{ST} relationships, demonstrating a consistancy in the independent measurements. A comparison of the analytical and experimental M-ϕ relationships indicates that

a) initial yielding, which is indicated by a flattening of the M-ϕ relationship, occurs at approximately the same curvature in both the analytical and experimental relationship.

b) the analytical yield moment is smaller than the experimental value for the tied column (approximately 12%) but it is essentially the same as the experimental value for the spiral column.

c) the analytical model for spalling is not representative of the experimental behavior. The sudden drop in the analytical moment capacity after the maximum moment is attained is the result of spalling. In the experimental M-ϕ relationship spalling does not cause such a drop in the tied column while in the spiral column a drop in the moment capacity due to spalling does occur, but it is much smaller.

d) after the decrease in moment capacity due to spalling in the analytical relationship occurs, the experimental and analytical relationships exhibit similar behavior. But this is only coincidental. Most of the decrease in the moment capacity in the experimental M-ϕ relationship is due to a loss of shear strength* and not a loss in flexural strength. Since the analytical model does not include shear strength, any decrease in the moment capacity is due to a loss of flexural strength. Thus the analytical relationship does not reflect the actual

* see Section 3.4.1

post yield behavior.

The curvature ductility, μ_ϕ , defined by the expression

$$\mu_\phi = \phi/\phi_y \qquad 3.12$$

where

ϕ_y = the curvature when the M-ϕ relationship begans to flatten.

is commonly used as a measure of inelastic deformation. μ_ϕ , at a displacement of 88.9 mm (3.5 inches) is equal to 20 in models 1S, 10 in model 4R and 11 in model 2R, a model identical to model 4R. The average concrete compressive strains at a distance of 63.5 mm (2.5 inches) from the column's edge (Fig. 3.64), associated with these values of μ_ϕ are 0.06, 0.014 and 0.01 mm/mm in models 1S, 2R and 4R respectively. Assuming a linear strain distribution across the depth of the section, the corresponding strains at the outer edge of the concrete core are 0.086 mm/mm in model 1S, 0.022 mm/mm in model 2R, and 0.019 mm/mm in model 4R. These are significantly higher than the failure strain of unconfined concrete* and demonstrate the improvement in the inelastic deformational characteristics of concrete attributed to the confinement provided by transverse reinforcement.

Analytical curvature ductilities corresponding to the above compressive strains are 26 for model 1S and 8 for models 4R and 2R. The

* typically between 0.003 mm/mm and 0.005 mm/mm.

analytical ductilities are of the same order as the experimental ductilities, being conservative for the tied columns and unconservative for the spiral column. The analytical results indicate that while the confining effect of rectangular ties was underestimated, that of the spiral reinforcement was overestimated.

Based on the respective values of μ_ϕ , it may be concluded that the flexural deformation requirements at the maximum displacement were greater in the spirally reinforced column than in the rectangular tied column. The large difference in μ_ϕ is attributed to two factors. First the beams and half column lengths make a larger contribution to the tip displacement in the rectangular tied columns. For example a comparison of deflected shapes at a tip displacement of 76.2 mm (3.0 inches) demonstrates that the beam rotations in model 4R are larger than those in model 1S (Fig. 3.67). However this is expected since the beam shears are also larger in Model 4R [178 kN vs. 125 kN (40 kip vs. 28 kip)].

The second factor is that shear deformation, particularly that due to inclined shear cracking, is greater in model 4R. As discussed previously (Section 3.3.2) the spiral transverse reinforcement provides a greater restraint to crack widening than rectangular ties. As a result the inclined shear crack widths and related deformations are smaller in model 1S than in model 4R.

ii Flexural Deformations under Cyclic Deformation History

Moment curvature (M-ϕ) cyclic envelopes for models 3R, 5R, and 6R are given in Fig. 3.68-3.70. The envelopes indicate the M and ϕ values recorded at the peak displacement in the first cycle of each displacement

level. Envelopes for ϕ_{AVG} and ϕ_{ST} are given.

The ϕ_{AVG} envelopes for models 5R and 6R have a common unsymmetric feature after inelastic behavior is initiated. A bias in the curvature data to one side of zero is observed. An examination of the change in curvature, $\Delta \phi_{AVG}$, in going from zero displacement to a given tip displacement in these two models (Fig. 3.71 and 3.72) indicates that the change in curvature for a given displacement level is approximately the same in either load direction. The symmetry of the $\Delta \phi_{AVG} - \Delta$ envelope and also of the $M - \phi_{ST}$ envelope indicates that the bias in the $M - \phi_{AVG}$ envelopes is probably the result of a slightly unsymmetric $M - \phi_{AVG}$ response caused by the minor differences in the cracking patterns associated with opposite load directions. This results in a residual curvature which increases gradually as the cyclic displacement level is increased.

The curvature ductility for the cyclic history is defined by the expression

$$\mu_\phi = \frac{\phi}{\phi_{1.0}} \qquad 3.13$$

where

$\phi_{1.0}$ = the curvature at a tip displacement of 1.0 inch, which is the yield displacement in the cyclic deformation history.

A summary of μ_ϕ for models 3R, 5R, 6R and 2S is given in Table 8. Ductility values in the first and last cycle at the failure displacement, and the respective average compressive strains at the edge of the core concrete (Fig. 3.64) are presented. Curvature ductilities greater than

5 were obtained in all models at the initiation of failure. The small ductility in model 3R is due to the fact that failure was initiated at a tip displacement of 50.8 mm (2.0 inches) while in models 5R, 6R and 2S failure was initiated at a displacement of 63.5 mm (2.5 inches).

As in the monotonic deformation history, μ_ϕ in models subjected to the balance point axial load (3R and 2S), is significantly greater than 1, the expected ductility if the maximum concrete strain was limited to the failure strain of unconfined concrete. The concrete strain data in Table 7 indicates this strain was exceeded and demonstrates the effectiveness of the transverse reinforcement in improving the inelastic cyclic behavior of concrete.

A comparison of μ_ϕ for the first and fifth cycle shows that the increase in μ_ϕ due to cycling is small (μ_ϕ actually decreasing in model 3R) for models failing in shear compression (3R, 5R) but it is large in the model failing by diagonal tension (6R). A similar phenomenon is evident in the changes in compressive strains. In all three models, the relative story rotation increased with cycling at the failure displacement, indicating that the column's deformation increased (Section 3.6.1). If model 6R, in which a three fold increase in μ_ϕ resulted in a 9% increase in the relative story rotation, is used as a basis, the changes in μ_ϕ in models 3R and 5R cannot account for the 21% increase in the relative story rotation which occurred in both these models. Consequently another deformation component must have increased in models 3R and 5R as a result of cycling at the failure displacement.

Models 3R and 5R both failed by the shear-compression mode. In this failure mode significant increases in relative motion along a mid-depth longitudinal crack were an essential feature of the failure

mechanism. This increased crack motion was the deformation component primarily responsible for the cyclic increase in the relative story rotation in models 3R and 5R at the failure displacement.

iii Steel Strains

Longitudinal steel strains were measured in all columns at a distance of two inches from the face of the beam-column joint. A summary of when yielding was first indicated by the strain gage data is given in Table 8. Whether the initial yielding was tensile or compressive is indicated. Initial yielding was observed by, or during cycling at, a displacement level of 25.4(1 inch) in all models but 2S.

The shear force (H) - longitudinal strain (ε_s) hysteretic behavior at various displacement levels in models 2S and 6R are given in Figs. 3.73-3.79. Behavior in both the first and fifth cycles is given in most cases. The H-ε_s hysteretic behavior presented is typical.

Stiffness degradation and a loss of linearity is apparent after first yield and may be attributed in part to the Bauschinger effect, a common characteristic of the cyclic stress strain behavior of steel (Figs. 3.73 and 3.77).

A pinching effect is evident in the initial phase of the compression cycle (Figs. 3.74, 3.76, 3.78). The pinching is a result of flexural cracking in the previous load direction. Before the cracks close and the concrete becomes effective in compression, the steel provides the only resistance to compressive forces. The interval in which the steel acts alone increases as the displacement increases because the cracks widen and larger steel strains are required to close them (Figs. 3.74

and 3.75).

The H-ε_s hysteretic loops experience a gradual shift to the compressive side of the strain axis (Figs. 3.74 and 3.78). This shift is caused by the degradation of the column axial stiffness. This stiffness degradation resulted in an increase in the compressive steel strains and stresses resisting the axial load.

The compressive strain behavior is quite different from the tensile behavior (3.74 and 3.75). After the pinching effect has ceased, the H-ε_s loop is stiffer in compression and has a definite linearity. This difference is attributed to the presence of concrete.

3.7 Summary

Three distinct failure modes were observed in the model columns, a shear-compression failure, a bond failure, and a diagonal tension failure. In the shear-compression and bond failure modes, the failure was gradual, resulting in significant shear and stiffness degradation, however, the model column was still able to maintain the design gravity load. If columns in a frame structure should experience either of these failures during the response to an earthquake ground motion, the resulting stiffness degradation could amplify the P-Δ effect and as a result, increase the possibility of collapse. In contrast to the above gradual failure, the diagonal tension failure was sudden. After failure, the model column was unable to resist shear forces or maintain the design gravity load.

The shear-compression failure was primarily the result of the reinforcing details. The longitudinal bar and cross ties at mid-depth of

the column created a weak plane which resulted in the formation of a continuous longitudinal crack at mid-depth through the width of the column. It was the degradation of the shear transfer capacity across this crack which caused the shear-compression failure. What would have happened in the models which failed by shear-compression if the reinforcing details were different is a question which might warrant further investigation.

The bond failure in the spirally reinforced columns demonstrates the effectiveness of spiral transverse reinforcement in maintaining the member's shear strength. Its principal advantage over rectangular ties is that the continuous spiral is more effective in maintaining the integrity of the column concrete than ties. The spiral's superior confinement characteristics and its stiffer restraint to crack widening prevented significant shear degradation due to losses in the column transverse shear capacity. Although the spiral reinforcement prevented a shear failure, a significant shear and stiffness degradation did occur in the spiral columns as a result of bond deterioration. Bond deterioration may also lead to problems with respect to anchorage of the longitudinal reinforcement.

From the response of the rectangular tied columns subjected to the cyclic deformation history it appears that a more ductile failure occurs with higher axial load. Models 3R [1068 kN (240 kip) and 5R [890 kN 200 kip)] both failed gradually in a shear-compression mode while model 6R [640 kN (144 kip)] failed suddenly in a diagonal tension mode. However, the influence of reinforcing details on the shear-compression failure mode must be evaluated before a definite conclusion can be made.

In models subjected to the cyclic deformation history the hysteretic behavior prior to the failure displacement was stable regardless of the failure mode. A gradual stiffness degradation was observed with cycling and with increasing displacement levels, but the potential column shear resistance did not decay.

The results of the experimental program illustrate that reinforced concrete columns, if detailed properly, can respond in a ductile manner when subjected to high axial loads and significant inelastic excursions. Relative story rotation ductilities greater than 4 were developed in all models tested prior to a brittle diagonal tension failure or a substantial shear degradation. Locally, average plastic rotations greater than 0.02 rad were developed over a 152 mm (6 inch) length. The average concrete strains corresponding to these rotations ranged from 0.02 mm/mm to 0.10 mm/mm. The magnitude of these strains are significantly greater than the crushing strain of unconfined concrete (0.003 mm/mm to 0.005 mm/mm) demonstrating that concrete can behave as a ductile material. However, the concrete must be adequately confined by providing sufficient and properly detailed transverse reinforcement.

High nominal shear stresses ($8.5\sqrt{f'_c}$ to $10.5\sqrt{f'_c}$)*, which exceeded those corresponding to the computed flexural capacities in all but one model (2S), were developed and maintained while the model columns experienced significant inelastic cyclic deformation. This indicates that moderate ductile behavior and the development of high shear stresses are compatible. It should be emphasized, however, that the observed ductile behavior was limited, i.e. if the inelastic deformation requirements are

* The range of shear stresses given is for f'_c in psi. If f'_c is in MPa this range becomes $0.70\sqrt{f'_c}$ to $0.87\sqrt{f'_c}$.

too large, a brittle shear failure, or significant shear and stiffness degradation will occur.

Two aspects of the model columns contributed to the observed ductile behavior, the presence of significant transverse reinforcement and the beneficial effect of relatively high axial force on a member's cyclic shear capacity. In addition to contributing to shear resistance, the transverse reinforcement is beneficial because it confines the core concrete and restrains crack widening. Consequently, cyclic degradation of the concrete shear strength is controlled. As noted above, the confinement provided by spiral reinforcement controlled shear degradation to the extent that a non-shear failure occurred. In the rectangular tied columns, shear degradation began only after the transverse reinforcement crossing the critical crack had yielded. Yielding reduced the restraint to crack widening and consequently led to a degradation of the concrete shear resistance, particularly the aggregate interlock mechanism.

As found in previous investigations (8, 10) and also as recognized in the current UBC seismic design provisions for ductile moment-resisting frames, the presence of significant axial force (UBC recommends that $P > 0.12\ f'_c\ A_g$) can enhance a member's cyclic shear resistance. The axial load tends to restrain crack widening, particularly widening of inclined cracks, and thus limits deterioration of the concrete shear resistance. However, the magnitude of the axial load should be less than, or at most equal to, the balance point axial load, and sufficient and properly detailed transverse reinforcement must be provided.

4. ANALYTICAL INVESTIGATION

4.1 Introduction

The analytical phase of the investigation is based on a finite element formulation. Concrete is assumed in a state of plane stress and is represented by four-node isoparametric quadrilaterals. A nonlinear constitutive equation which approximates the effects of a biaxial stress condition on concrete compressive strength and stiffness is employed. A crack line approach is used to include concrete cracking in the analysis.

Both the longitudinal and transverse reinforcements are represented by elasto-plastic bar elements with linear strain hardening. Bond between steel reinforcement and concrete is modeled by dimensionless bond link elements. The dowel action of steel reinforcement crossing cracks and the forces due to aggregate interlock stresses are included by connecting dimensionless link elements across crack lines.

Material nonlinearities and the changing structure topology due to cracking require that a nonlinear solution strategy be employed. An incremental iterative solution scheme is used in the proposed model.

Details of the material models used for concrete, the reinforcing steel, and the link elements, details of the solution technique employed, and a discussion of analytical results are presented below. First a discussion of why the proposed model was selected is presented.

4.2 Discussion of the Proposed Model

4.2.1 Structural Idealization

The results of the experimental phase of the investigation indicated that crack behavior was a very important system parameter. For example, all model failures are related to crack behavior; the diagonal tension failure was the result of a sudden propagation of a diagonal tension crack; the shear-compression failure was the result of a degradation in the shear transfer mechanism across a longitudinal crack; finally, the bond failure is due in part to local cracking around the longitudinal reinforcement caused by the stress transfer between steel and concrete. Because of the significant influence of crack behavior on the observed experimental response, the development of a mathematical model which would incorporate crack formation and propagation, and which would include the force transfer mechanisms across cracks was considered an important step in understanding more fully the complete behavior of reinforced concrete members with characteristics similar to those studied experimentally.

The desired characteristics of the model made a finite element formulation very attractive. In such a formulation, cracks may be easily defined in the spatial model of the member by specifying two independent mesh points with the same coordinates (14-17), and force transfer across cracks may be included by coupling nodes defining a crack line with dimensionless links which would have stiffness properties characteristic

of aggregate interlock and dowel action of reinforcement.

4.2.2 State of Stress

The proposed model is limited to conditions of plane stress. This limitation was imposed so that a two-dimensional finite element model may be used, thus reducing the size of the problem to be analyzed, and also simplifying the crack formation procedure. It is felt that the stress state existing in reinforced concrete members which are components of plane frames should be adequately represented by the plane stress assumption. For example, in the experimental column the significant stress components are the normal stresses due to the axial load and bending moment and the shear stresses due to the applied shear forces (Fig. 4.1). Additional normal stresses in the two directions orthogonal to these stresses are caused by the restraint of the beams at the beam-column joint and the transverse reinforcement (the confinement steel) to the Poisson straining. However, these stresses should be small* and it is felt that ignoring the stress normal to the plane of loading should have little effect on member behavior.

4.3 Concrete Idealization

4.3.1 Finite Element Used

The assumption that the concrete is in a state of plane stress simplifies the analysis in that a two-dimensional finite element model can

* Compared to the normal stresses caused by axial compression and bending moment

reproduce the idealized stress field. A number of two-dimensional elements which may be applied to plane stress problems have been developed over the years (23,24,25). The simplest two-dimensional element is the constant strain triangle (Fig. 4.2a). More accurate and also more complex two-dimensional elements are the four-node isoparametric quadrilateral, Q4, element (Fig. 4.2b), and the eight-node isoparametric quadrilateral, Q8, element (Fig. 4.2c). The basic element used in this investigation is the Q4 element.* This element was chosen primarily to simplify the procedure to form crack lines. Basic element properties are presented in Appendix C.

4.3.2 Material Law

Concrete is assumed to be an incrementally linear orthotropic material. The constitutive relationship used is that proposed by Darwin and Pecknold (22) and is discussed in detail in Appendix D. The incremental stress-strain relationship in global coordinates is:

$$\begin{Bmatrix} d\sigma_1' \\ d\sigma_2' \\ d\tau_{12}' \end{Bmatrix} = \frac{1}{1-\nu^2} \begin{bmatrix} E_1\cos^2\theta+E_2\sin^2\theta & \nu\sqrt{E_1 E_2} & \tfrac{1}{2}(E_1-E_2)\sin\theta\cos\theta \\ & E_1\sin^2\theta+E_2\cos^2\theta & \tfrac{1}{2}(E_1-E_2)\sin\theta\cos\theta \\ \text{SYMMETRIC} & & \tfrac{1}{4}(E_1+E_2-2\nu\sqrt{E_1E_2}) \end{bmatrix} \begin{Bmatrix} d\varepsilon_1' \\ d\varepsilon_2' \\ d\gamma_{12}' \end{Bmatrix} \qquad 4.1$$

* The constant strain triangle is used to incorporate an inclined crack line as described in Section 4.3.3.

where E_1 and E_2 are the tangent moduli in the respective material coordinates, ν is an equivalent Poisson ratio, and θ defines the angle between the material and global coordinates.

The material coordinates always correspond to the direction of the principal stresses, that is, they rotate as the principal stresses rotate. The tangent moduli, E_i, are defined with the aid of the concept of 'equivalent' uniaxial strain proposed by Darwin and Pecknold (22). This concept is employed in conjunction with a family of uniaxial compressive stress-strain relationships in order to approximate the biaxial compressive behavior of plain concrete (for details, see Appendix D). In tension concrete is assumed to be a linear-elastic brittle material.

Poisson ratio, ν, is assumed constant and equal to 0.2 for either biaxial compression or tension. For uniaxial compression or a tension-compression stress state, ν varies according to the expression suggested by Darwin and Pecknold.

$$\nu = 0.2 + 0.6 \left(\frac{\sigma_2}{f'_c}\right)^4 + 0.4 \left(\frac{\sigma_1}{f'_t}\right)^4 \leq 0.99 \qquad 4.2$$

ν, as defined by equation 4.2, differs little from 0.2 until relatively high values of stress. For example if σ_1 is equal to zero and σ_2 is equal to $0.6f'_c$ ν is 0.277. The variation of ν defined by equation 4.2 reflects experimental observations. For example, Kupfer, Hilsdorf, and Rusch (27) found that concrete's Poisson ratio starts to increase at a stress level of approximately $0.8f'_c$.

As noted by Darwin and Pecknold, values of ν greater than 1/2 (the value for an incompressible material) are acceptable in plain concrete

because material volume does increase. A limiting value of 0.99 is imposed to ensure stabilty of the numerical solution.

In the finite element model the material stress-strain behavior is monitored at the numerical integration points used to evaluate the element stiffness integral (see Appendix C) and the constitutive relationship at these points is updated to reflect the current stress state.

4.3.3 Tension Failure and Cracking

A principal objective of this study was to formulate a model of reinforced concrete members which includes crack formation and propagation and the force transfer across the cracks. To achieve this objective, concrete cracking is included in the current development by a crack line approach (14-17). The basic feature of the crack line approach is that discrete cracks are formed in the structure by having a series of node pairs with the same coordinates in the finite element mesh (Fig. 4.3). The two nodes of any given pair are independent except for possible coupling to include dowel action of the reinforcement and aggregate interlock (Fig. 4.3).

In the model developed, the crack lines are defined by nodes at which the biaxial tensile strength has been exceeded. The direction of the crack line is determined by the direction of the principal tensile stress at the cracked node. The procedure used to form crack lines in a finite element mesh is detailed below. The work of Ngo (17) provided the guidance and inspiration for the procedure presented.

i Formation of crack lines

A crack line is formed when and where the principal tensile stress, σ_1, exceeds the biaxial tensile strength criterion, F_T.

$$\sigma_1 \geq F_T \tag{4.3}$$

F_T is equal to the uniaxial strength, f_t'*, for biaxial tension and for a tension-compression stress state when

$$|\sigma_2| \leq 0.65 f_c' \tag{4.4}$$

On the other hand, when $|\sigma_2|$ exceeds this limit:

$$F_T = \frac{\alpha(1 + 3.28\ \alpha)}{(1 + \alpha)^2}\ f_c' \tag{4.5}$$

where α is equal to the stress ratio σ_1/σ_2. This tensile failure criterion was proposed by Darwin and Pecknold (22) and is based on experimental behavior observed by Kupfer (27).

In the current model, an upper bound was placed on σ_1 with respect to F_T. If :

$$\sigma_1 > \beta F_T \tag{4.6}$$

the applied load increment was reduced so the σ_1 was equal to F_T and a new solution corresponding to the reduced load was obtained. The unapplied portion of the load was reapplied as a new load step.

The upper bound on σ_1 was imposed in order to limit the magnitude of the force redistribution associated with cracking (Section 4.6.1).

* In this study, $f_t' = 0.1 f_c'$

In the model development it was found that redistribution of large forces could lead to unrealistic crack formation. For the analysis carried out in this study, β was taken as 1.2.

In the proposed cracking scheme only one node is allowed to crack in a given solution step. In any given solution step, the stresses at the numerical integration points of each element are evaluated and checked to determine whether:

$$\sigma_1 \geq F_T$$

The integration point at which σ_1 exceeds F_T by the largest amount is identified and the node associated with it is the node that will be cracked (Fig. 4.3). Once the cracked node has been identified, the program alters the structure topology to form a crack line as described below.

ii Crack formation procedure

The substructure in Fig. 4.4a will be used to illustrate the formation of a crack line. The steps in the procedure are:

a. Extract the element data of elements connected to the cracked node, NCRK, from the element data storage file. NCRK is assumed to be node 5 in Fig. 4.4a.

b. Establish connectivity arrays: 1) the node-element connectivity array, NPP, which identifies the elements connected to a given node (Fig. 4.4b); 2) the element-element connectivity array, KEL, which identifies elements adjacent to each other.

c. Determine the direction of the principal tensile stress at NCRK, BETA. The crack orientation, $\overline{\text{BETA}}$, is set perpendicular to BETA.

d. Determine the inclinations of the lines from NCRK to all other nodes and store them in ROT array (Fig. 4.5).

e. Establish the crack tip, NT, by comparing $\overline{\text{BETA}}$ with the ROT array and checking for existing crack lines. NT is the node whose ROT value is closest to $\overline{\text{BETA}}$. For example, if $\overline{\text{BETA}}$ was 45° and if neither node 9 or node 1 (Fig. 4.5) were previously cracked, there would be two values of NT, node 1 and node 9.

f. Once NT is established, a check is made to determine whether: 1) the new crack line is along a current element boundary (in Fig. 4.4a if NT is equal to 6 or 8); or 2) the new crack line will cause the splitting of an existing element (in Fig. 4.4a if NT is equal to 9 or 7). For both cases a new node is created at NCRK. Using the element-element connectivity array KEL, the existing element node numbers are redefined to form the new crack line. For example, if NT is equal to 8 and 2, the new substructure in Fig. 4.6a would result. To incorporate a crack line across an element, the existing quadrilateral element is replaced by two triangular elements. For example, if NT is equal to 9 and 1, the quadrilateral elements a and d in Fig. 4.4 are replaced by the triangular elements e, f, g, and h shown in Fig. 4.6b.

g. After adding a new node and redefining the node numbers of

elements connected to the crack node pair, the element LM array, which relates the element degrees of freedom (DOF) to the global DOF, is modified to incorporate the crack line in the structure. The DOF associated with the new nodes must first be given global equation numbers. For example, one could simply place the equations for the new DOF at the end of the current set of equilibrium equations. However, this was considered undesirable since in general the band width of the global stiffness matrix would increase. This is turn would increase the computational effort required to solve the equilibrium equations. Instead the new DOF are assigned the equation numbers next in sequence following the equation numbers associated with the newly cracked node. This requires a complete reordering of the equilibrium equations. However, since the structure stiffness matrix is reformed in each solution step to account for the nonlinear material behavior, the equilibrium equations can be reordered rather easily.

iii Limitations

The current crack formation procedure has two limitations. First crack closing is not handled automatically. In the current procedure the crack width is checked at each node pair and if it becomes negative (a condition which cannot exist), the program stops. The previous solution is saved, however, and crack closing can be effected as part of a restart option in the program. Crack closing was handled in this

way because possible crack patterns were limited by the mesh definition. This limitation might cause a crack to propagate incorrectly and the force redistribution associated with this propagation might result in a negative crack width. For example consider the situation in Fig. 4.7. As the crack at the fixed end propagates through the depth, the shear stresses increase and the principal tensile stresses will become more inclined with respect to the Y-axis. As a result, the crack propagation should become inclined; however, because of the mesh definition (the fixed support), the crack formed by the current model will remain vertical and the crack width of a newly formed crack segment could be negative.

Since the current development is limited to monotonic deformation histories, the above treatment of crack closing should be adequate for the purposes of this study.

The second limitation is somewhat more severe. Besides being limited by the mesh, possible crack propagation is limited to propagation into uncracked elements, that is, a new crack segment cannot propagate as a branch from an existing crack (Fig. 4.7). This limitation was unintentional and was discovered late in the model development. It could be eliminated by identifying existing crack lines as structure boundaries and establishing appropriate crack formation criteria. However, because of time considerations, this limitation was not corrected.

4.4 Steel Idealization

For simplicity both the longitudinal and transverse steel reinforce-

ment are idealized as bar elements. The predominant stress in steel bars used in reinforced concrete members is along the axis of the bar, and the use of bar elements should provide an adequate idealization of the steel behavior. The basic behavior which is omitted by using bar elements is the dowel action of reinforcement crossing a crack. Dowel action is a local phenomenon, however, and is effective only when the reinforcing steel crosses a crack line and only in the region of the crack line. Due to its local nature, dowel action has been idealized by placing a dimensionless link across the crack line with stiffness perpendicular to the axis of the bar. The properties of the dowel link are discussed in Section 4.5.

4.4.1 Material Law

The reinforcing steel is assumed to behave according to a symmetric bilinear stress-strain relationship until the yield stress, σ_y, is attained. After yielding, a constant hardening modulus, E_{SH} is used to relate stress to strain. The values of E and E_{SH} used in this investigation are indicated in Fig. 4.8. It is felt that this bilinear material model includes the essential features of the monotonic stress-strain behavior of reinforcing steel.

4.4.2 Bond

The stress transfer between tension reinforcing steel and concrete is of major concern when one attempts to predict concrete cracking. This

phenomenon, commonly referred to as bond, is included in this formulation by specifying different nodal points with the same global coordinates for the steel and concrete elements, and by defining dimensionless links with stiffness properties representative of bond stress-slip behavior to couple the steel and concrete elements (Fig. 4.9). This approach, first employed by Ngo and Scordelis (14), allows relative motion between the steel and concrete.

A typical bond link consists of two orthogonal springs: one parallel to the axis of the steel bar element, the other perpendicular to it (Fig. 4.9). The link element properties are discussed in Appendix C. The following bond stress-slip relationship, suggested by Houde and Mirza (31), was used to derive the parallel link stiffness:

$$u = 1.95 \times 10^{6}d - 2.35 \times 10^{9}d^{2} + 1.39 \times 10^{12}d^{3} - 0.33 \times 10^{15}d^{4} \quad 4.7*$$

where

u = bond stress (psi)

d = relative motion (slip) between the steel and concrete (in.)

This relationship is plotted in Fig. 4.10. At the peak bond stress, the stiffness is assumed to remain constant and be effectively zero (a small positive value is used).

The parallel link stiffness, K_H, is found as a function of the slip, d, by differentiating equation 4.7 with respect to d and then multiplying

---

* Equation 4.7 becomes
$u = .529 \times 10^{3}d - .251 \times 10^{5}d^{2} + .585 \times 10^{6}d^{3} - .546 \times 10^{7}d^{4}$
if u is in MPa and d is in mm.

the result by the effective link area, A.

$$K_H(d) = \frac{du}{dd} \cdot A \qquad 4.8$$

where

$A = m\pi D\ell$

m = number of bars

ℓ = link spacing (at a given node, i, $\ell = \ell_1/2 + \ell_2/2$ where ℓ_1 and ℓ_2 are the respective lengths of the two bar elements connected to node i)

D = bar diameter

The stiffness of the link perpendicular to the bar axis, K_V, was assigned a large constant value (10^{10}) which in effect constrains this bar degree of freedom (DOF) to be equal to the corresponding concrete DOF. If the bar axis lies parallel to a global coordinate axis, this stiffness can be set to zero and the bar DOF fixed.

During the solution process, the bond links are modified to simulate bond failures at and near cracks. When a node cracks, any parallel bond link connected to the cracked node is destroyed by setting K_H to zero. The force previously carried by this link is eliminated by appropriate nodal forces in the next solution step. In addition bond elements adjacent to crack lines are identified and they are assumed to unload after reaching the maximum bond force (Fig. 4.10).

The influence of the bond idealization on crack behavior, i.e., the use of dimensionless links, is evaluated in the analyses conducted.

4.5 Aggregate Interlock and Dowel Action

The force transfer across cracks attributed to aggregate interlock and dowel action was incorporated into the model by connecting dimensionless links across crack lines generated in the finite element mesh. Characteristics of the linkage element used in this investigation are presented in Appendix C. The general element consists of three uncoupled dimensionless links (Fig. 4.3). Two of the links account for dowel action and the third link accounts for aggregate interlock. The dowel action links are assumed to act perpendicular to the reinforcing bars crossing the crack. If the bar is parallel to a crack, or if no bar crosses a crack, the stiffness of the dowel link is set to zero. The aggregate interlock link is assumed to act parallel to the crack line. To completely define the linkage element, 'stiffness' functions are required to relate the shear force to the crack shear displacement for both the dowel action link and the aggregate interlock link. A discussion of dowel action and aggregate interlock, and details of the respective link stiffness functions used in this investigation are presented below.

4.5.1 Dowel Action Stiffness Function

Dowel action is a result of the resistance of the reinforcing steel crossing a crack against motion perpendicular to the axis of the bar. Dowel resistance across a crack can be developed by three mechanisms (30):

a. the flexure of reinforcing bars (Fig. 4.11a)

b. pure shear resistance across the bar (Fig. 4.11b) and

c. the kinking of the reinforcement (Fig. 4.11c)

In Fig. 4.11 the shear force, V_d, associated with each of these mechanisms is expressed in terms of the bar yield strength. It should be noted, however, that the yield strength of a bar in shear or flexure cannot be fully developed if the same bar is resisting an axial tensile force.

Experimental investigations into the contribution of dowel action to shear strength (30,31,32,33) have shown that the following parameters influence the dowel resistance: the tensile strength of the concrete; the net width of concrete associated with one reinforcing bar; transverse reinforcement, whether it is present or not and its spacing; and the percentage of steel reinforcement. The importance of the first two parameters is due to the fact that the experimental dowel resistance was generally limited by the formation of a horizontal splitting crack along the reinforcing bar. The formation of this crack is influenced by the concrete tensile strength and the width of concrete resisting the tensile stresses which cause the splitting crack.

Typical dowel shear force, V_d, shear displacement, Δ_s, relationships are shown in Fig. 4.12. A bilinear idealization of the experimental V_d-Δ_s behavior is used in this investigation to account for the change in dowel effectiveness associated with the formation of the splitting crack along the reinforcing bar. The knee in the bilinear relationship corresponds to the magnitude of V_d at which a hypothetical splitting crack occurs. This force is referred to as the dowel splitting load, D_F, and it is defined by the following relationship suggested by Houde

and Mirza (31).

$$D_F(\text{lbs}) = 40\, b_n\, (f'_c)^{1/3} \qquad \text{[for } f'_c \text{ in psi and } b_n \text{ in inches]}$$

$$D_F(\text{kn}) = .037\, b_n\, (f'_c)^{1/3} \qquad \text{[for } f'_c \text{ in MPa and } b_n \text{ in mm]} \qquad 4.9$$

where

b_n = net width of concrete associated with one reinforcing bar

$(f'_c)^{1/3}$ = a measure of the concrete tensile strength

The following V_d-Δ_s relationship is used in conjunction with the definition of D_F in equation 4.9 (31).

$$V_d(\text{lbs}) = 2000 \cdot D_F \cdot \Delta_s \quad V_d < D_F \qquad \text{[for } D_F \text{ in lbs and } \Delta_s \text{ in in.]}$$

$$V_d(\text{kN}) = 79 \cdot D_F \cdot \Delta_s \qquad \text{[for } D_F \text{ in kN and } \Delta_s \text{ in mm]}$$

$$V_d(\text{lbs}) = 20 \cdot D_F \cdot \Delta_s \quad V_d \geq D_F$$

$$V_d(\text{kN}) = .79 \cdot D_F \cdot \Delta_s \qquad 4.10$$

It should be noted that this dowel stiffness function does not depend explicitly on the transverse reinforcement, in particular its spacing. However, as indicated in Fig. 4.12, the influence of transverse reinforcement on dowel action is not effective until after splitting occurs. Consequently only the post splitting stiffness should reflect this influence. The fact that the effect of transverse reinforcement on dowel behavior has not been quantified and the desire to keep

the function simple led to the post splitting stiffness defined by equation 4.10.

Another point which should be made is that the same dowel link stiffness function is employed for both the longitudinal and transverse reinforcement links. Its use for the latter link may be questionable since the stiffness function is based on experimental behavior of specimens in which the dowel steel placement was characteristic of longitudinal reinforcement. However, for the sake of simplicity, possible differences in dowel behavior which may be attributed to the location of the reinforcement are ignored.

4.5.2 Aggregate Interlock Stiffness Function

When a shear displacement between two faces of a crack occurs, a number of coarse aggregate particles projecting across a crack will enable shear forces to be transmitted. This phenomenon is referred to as aggregate interlock. Experimental investigations of the contribution of aggregate interlock to shear strength (31, 32, 33) have indicated that the width of the crack, the shear displacement, and the strength characteristics of the aggregate particles are the principle variables influencing the magnitude of the shear resistance developed by aggregate interlock. Typical experimental results are shown in Fig. 4.13.

As one would expect, the stiffness of the shear stress, τ_A, shear displacement, Δ_s, relationship decreases as the crack width increases. Houde and Mirza (31) idealized the dependence of the τ_A-Δ_s relationship on the crack width by the expression:

$$\tau_A(\text{psi}) = 57\left(\frac{1}{c}\right)^{3/2} \Delta_s \qquad \text{[for c and } \Delta_s \text{ in inches]}$$

$$\tau_A(\text{MPa}) = 1.98\left(\frac{1}{c}\right)^{3/2} \Delta_s \qquad \text{[for c and } \Delta_s \text{ in mm]} \qquad 4.11$$

where c is the crack width.

Equation 4.11 is used in this investigation with the following modification:

$$\tau_A(\text{psi}) = 57\left(\frac{1}{c}\right)^{3/2} (.0225 \cdot \sqrt{f'_c} - .409)\Delta_s \qquad \text{[for } f'_c \text{ in psi]}$$

$$\tau_A(\text{MPa}) = 1.98\left(\frac{1}{c}\right)^{3/2} (.272 \cdot \sqrt{f'_c} - .409)\Delta_s \qquad \text{[for } f'_c \text{ in MPa]} \qquad 4.12$$

The additional term is due to Fenwick and Paulay (33) and is included to account for different concrete strengths.

In order to determine the aggregate interlock link stiffness, K_A, equation 4.12 is differentiated with respect to Δ_s:

$$\frac{d\tau_A}{d\Delta_s} (\text{lb/in}^3) = 57\left(\frac{1}{c}\right)^{3/2} (.0225 \sqrt{f'_c} - .409) \qquad 4.13$$

and the result is multiplied by the crack surface area, A_{SA}, associated with the node pair across which the link is connected:

$$K_A(\text{lb/in}) = \frac{d\tau_A}{d\Delta_s} \cdot A_{SA} = 57\left(\frac{1}{c}\right)^{3/2} (.0225 \sqrt{f'_c} - .409)(A_{SA}) \qquad 4.14$$

Though independent of the shear displacement, K_A is a nonlinear function because of its dependence on the crack width.

From equation 4.14 it is seen that as the crack width goes to zero,

K_A continues to increase and could reach values greater than the shear modulus of uncracked concrete. In order to prevent this, a minimum fictitious crack width is assumed in the computation of K_A. A value of 0.025 mm (0.001 in.) was used in the current development and was selected to ensure that the effective shear modulus associated with K_A was less than the shear modulus of uncracked concrete.

4.6 Solution Technique

A finite element idealization of a structural system results in the following equilibrium equation.

$$\underline{K}\ \underline{u} = \underline{R} \qquad 4.15$$

where $\underline{K}$ is the structure stiffness matrix, $\underline{u}$ is the unknown nodal displacement vector and $\underline{R}$ is the nodal load vector. Equation 4.15 is solved for $\underline{u}$ which is then used to determine element stresses. Because of nonlinear material behavior, and the changing structure topology due to cracking, the relationship between $\underline{u}$ and $\underline{R}$ in the proposed model is nonlinear, that is, $\underline{K}$ is not constant but depends on $\underline{u}$ (Fig. 4.14a). As a result an incremental iterative solution technique is employed to solve equation 4.15. In this scheme the external load component of $\underline{R}$ is applied in a number of increments. For each load increment, a number of iterations are performed in which $\underline{K}$ is updated to reflect the most recent stress-strain field and structure topology. Iteration is continued until the established convergence criteria are met or until an iteration limit is exceeded. Details of the solution procedure are given below.

4.6.1 Solution of Equilibrium Equations

The first step in the analysis is to define the structure to be analyzed. The nodes, elements, and associated material properties which compromise the finite element model of the structure are specified. The initial structure stiffness, $\underline{K}_o$, is then established from this mesh definition. After all element stresses and the total displacement vector, $\underline{u}_T$, are initialized to zero, the solution procedure begins. A step-by-step description of the solution procedure, starting at an arbitrary load step, j, is given below. Two subscripts are used to label terms used in the discussion; the lower subscript indicates the load step, and the upper subscript indicates the iteration number. The initial solution in a given load step is labeled iteration 0.

4.6.2 Steps in Solution Procedure

a. Solve

$$\underline{K}_j^o \, \underline{\Delta u}_j^o = \underline{\Delta R}_j^o \quad \text{for } \underline{\Delta u}_j^o \tag{4.16}$$

where $\underline{\Delta R}_j^o$ contains the new increment of external load plus any residual element nodal loads (Step c.5) remaining from the previous load step.*

b. Update $\underline{u}_T$

$$\underline{u}_T = \underline{u}_T + \underline{\Delta u}_j^o \tag{4.17}$$

c. For each element, using $\underline{\Delta u}_j^o$:

1. find the increment in element stresses, $\underline{\Delta \sigma}_j^o$, based

* In equation 4.16 it is assumed that the inverse of $\underline{K}_j^o$ exists and is unique

on the constitutive equation used to form $\underline{K}_j^o$.

2. reformulate the constitutive equation based on the current stress-strain state and evaluate the actual stress increment, $\underline{\overline{\Delta\sigma}}_j^o$.
3. reform the element stiffness matrix using the new constitutive equation.
4. update the element stresses

$$\underline{\sigma} = \underline{\sigma} + \underline{\overline{\Delta\sigma}}_j^o \qquad 4.18$$

5. find the residual element nodal forces

$$\underline{P}_R = \int_{Vol} \underline{B}^T \left(\underline{\Delta\sigma}_j^o - \underline{\overline{\Delta\sigma}}_j^o \right) \, dVol \qquad 4.19$$

6. check for stress convergence. The square root of the sum of the squares of the element stresses is used as a norm in the convergence criterion

$$\frac{\left| \underline{\Delta\sigma}_j^o - \underline{\overline{\Delta\sigma}}_j^o \right|_{ss}}{\left| \underline{\sigma} \right|_{ss}} \leq STOL \qquad 4.20$$

where

$$\left| \underline{\sigma} \right|_{ss} = \sqrt{\sigma_{11}^2 + \sigma_{22}^2 + \tau_{12}^2}$$

STOL = the stress convergence tolerance

The convergence criterion expressed by equation 4.20 is evaluated at each stress point in an element.

7. check for a concrete tensile failure (only in concrete elements).

d. If the stress convergence criterion is satisfied for all elements, that is, if equation 4.20 is satisfied for all elements, and no new crack line is to be formed, increase the load step count by one:

$$j = j + 1$$

and read the next load increment. Then the procedure is started from step 'a' again. If the stress convergence criterion is not satisfied for all elements, or a new crack line is to be formed, the procedure is continued. The solution steps 'a' through 'c' are illustrated in Fig. 4.14b.

e. check displacement convergence. As in the stress convergence criterion, the square root of the sum of the squares of the displacements is used as a norm:

$$\frac{|\Delta \underline{u}_j^o|_{ss}}{|\underline{u}_T|_{ss}} \leq \text{TOLD} \qquad 4.21$$

where

$$|\underline{u}_T|_{ss} = \sqrt{u_{1T}^2 + u_{2T}^2 + \ldots + u_{nT}^2}$$

$u_1, u_2, \ldots, u_n$ = the components of the displacement vector.

TOLD = displacement convergence tolerance.

f. Check for crack formation. If both the stress and displacement convergence criteria are not satisfied proceed with-

out forming crack line. This condition on crack formation was established to allow stress redistribution associated with nonlinear material behavior to occur. In the development of the solution scheme, it was found that this stress redistribution could change the crack formation. If both convergence criteria are satisfied or if the displacement criterion is satisfied and one iteration has already been completed to obtain stress convergence, a new crack line is formed. The second criterion for crack formation was established to reduce the number of stress iterations before crack formation was allowed. It was found that, typically, the concrete element stresses changed very little after one iteration. It is felt that requiring displacement convergence, which is a measure of global convergence, will account for cases in which concrete stress convergence takes more than one iteration.

g. Form the new structure stiffness matrix, $\underline{K}_j^1$. The matrix $\underline{K}_j^1$ includes any additional degrees of freeedom and any element modifications necessary to include a new crack line in the structure.

h. Solve:

$$\underline{K}_j^1 \, \underline{\Delta u}_j^1 = \underline{\Delta R}_j^1 \qquad \text{for } \underline{\Delta u}_j^1 \tag{4.22}$$

where

$$\underline{\Delta R}_j^1 = \sum_{\text{elements}} \underline{P}_R \qquad 4.23$$

In addition to the nodal loads defined by equation 4.19, $\Sigma \underline{P}_R$ includes the following nodal forces.

1. The forces previously transferred across a newly cracked node are redistributed to the cracked structure. In the crack formation procedure the nodal forces corresponding to the existing element stress field, $\underline{P}_{Ri}^c$ are evaluated at the node to be cracked (NCRK in Fig. 4.15) by the expression:

$$\underline{P}_{R_i}^c = \int_{Vol} \underline{B}_i^{cT} \underline{\sigma}_i \, dVol \qquad 4.24$$

where $\underline{\sigma}_i$ is the current stress field in element and $\underline{B}_i^{cT}$ is the transpose of that part of the strain displacement transformation matrix associated with the cracked node in element i.

2. When an inclined crack is formed a nonequilibrium condition will in general exist at the nodal points defining the new triangular elements because the stress approximation in the triangular and quadrilateral elements are different. In order to eliminate any unbalanced forces which result from the element replacement, the following equilibrium correction is made.
   The nodal forces corresponding to the stress fields in the new triangular elements

$$\underline{P}^{TRI} = \int_{Vol_1} \underline{B}_1^T \underline{\sigma}_1 \, dVol_1 + \int_{Vol_2} \underline{B}_2^T \underline{\sigma}_2 \, dVol_2 \quad 4.25$$

are subtracted from the nodal forces corresponding to the stress field in the old quadrilateral element, $\underline{P}^Q$:

$$\underline{P}_R^D = \underline{P}^Q - \underline{P}^{TRI} \quad 4.26$$

The difference, $\underline{P}_R^D$ is applied in the next solution step. It should be noted that in the summation defined by equation 4.25, only terms corresponding to the same global degrees of freedom are combined.

3. In order to effect a bond failure at a cracked node the force in any bond link connected to the node is set to zero by adding the global components of the link force to the nodal forces corresponding to the reinforcement degrees of freedom.

The above force redistribution associated with cracking permits the structure topology to be changed as part of an incremental solution scheme. This is considered an attractive feature of the proposed solution strategy. Without force redistribution, the solution process would have to be restarted from a zero stress state each time a new crack segment is formed. This was undesirable for two reasons. First, the computational effort required to obtain a given solution would increase if it was necessary to restart the solution because iteration attributed to material nonlinearity would

have to be repeated each time the solution was restarted. Second, path dependent characteristics of material nonlinearities might be lost if the solution had to be restarted.

i. Update the displacement vector:

$$\underline{u}_T = \underline{u}_T + \underline{\Delta u}_j^1 \qquad 4.27$$

j. Repeat procedure in step c, 1-7 with the stresses found from the displacement increment, $\underline{\Delta u}_j^i$.

The solution steps of the first iteration are illustrated in Fig. 4.14c.

k. If both convergence criteria are satisfied and no new crack lines are to be formed, the next load increment is applied and the procedure is started from step a with j = j+1. If not, the iteration count is increased by 1 and steps e through j are repeated. Iteration in a given load step is continued until all convergence criteria are met and all crack lines are formed or until a preset iteration limit is exceeded. If the iteration limit is exceeded, the solution is stopped. Restart capabilities are built into the program, permitting the solution up to the stop point to be saved and used again if the causes of nonconvergence can be corrected. The solution procedure is illustrated schematically in Fig. 4.16.

4.7 Evaluation of the Proposed Model

4.7.1 Problems Analyzed

In order to evaluate the effectiveness of the proposed equilibrium corrections in implementing structure topology changes within the context of an incremental solution strategy, and in order to determine the sensitivity of crack formation and propagation to the proposed idealization of local phenomenon such as bond, aggregate interlock, and dowel action, two relatively simple problems have been analyzed, a cantilever member subjected to axial tension and a cantilever member subjected to axial compression and a tip shear force (Fig. 4.17). The same material properties were used in both problems (Fig. 4.17b). Except for the longitudinal reinforcement at mid-depth, the cross section of the cantilever analyzed is a third-scale model of the rectangular tied columns studied in the experimental phase. The results of the analyses are discussed in the following sections.

4.7.2 Evaluation of Solution Strategy

A basic feature of the proposed cracking model is that the structure topology changes as new cracks form and existing cracks propagate, i.e., element connectivity is altered, existing elements eliminated (bond failure) and new elements are created (triangular elements to incorporate inclined cracking and dowel and aggregate interlock links). The topology changes can be incorporated into the finite element idealization quite

easily by proper modification of the mesh (Section 4.3.3), however, the existing stress field must also be modified to reflect the new topology. One approach to modify the stress field is to restart the solution from a state of zero stress each time a new crack segment is formed. Because material nonlinearities are included in the proposed model, this was considered inappropriate (Section 4.6.1 (h)). Instead, the topology changes associated with cracking were effected as part of an incremental solution strategy by applying additional nodal forces to correct nonequilibrium conditions attributed to crack formation (Section 4.6.1 (h)).

The effectiveness of the proposed solution strategy may be checked by comparing results which are obtained incrementally with those obtained by restarting the solution from a zero stress state. Provided the path dependent characteristics of the material nonlinearities are not significant, the results of the two solutions should be essentially the same if the proposed equilibrium corrections adequately redistribute the unbalanced nodal forces associated with cracking. As an illustration, the results of an incremental and a restart analysis of a cantilever subjected to axial compression and shear forces are compared below.

The finite element mesh employed is shown in Fig. 4.18a. The crack pattern indicated in Fig. 4.18b was obtained after six load steps. During the incremental solution, bond failure was effected at node A and an inclined crack was formed (Fig. 4.18b). Consequently, all possible equilibrium corrections have been applied to obtain the crack pattern indicated.

The cracked mesh indicated in Fig. 4.18b was defined externally and analyzed starting at a zero stress condition. From a comparison of the results of the restart solution with the results obtained incrementally,

the following observations may be made.

1. The global behavior and behavior away from the crack lines was virtually the same. For example, the tip displacement was .00934 in the incremental solution and 0.00932 in the restart solution.
2. The difference in tension steel stresses was small and the stresses in the bars connected to the node at which a bond failure was effected are essentially the same (Fig. 4.19b).
3. The difference in crack displacements was small (Fig. 4.19c).
4. A significant variation in the two solutions occurred in concrete element stresses adjacent to crack lines (Fig. 4.20b). These differences may be attributed to path-dependent characteristics of the material behavior. In the incremental solution, the axial load was applied first, imposing compression on the entire cross section. With the application of shear force, there is a stress reversal in the elements on the tension side of the specimen (Fig. 4.20). This stress reversal did not occur in the restart solution because the total shear and axial force were applied simultaneously. Consequently, a difference in material behavior is expected in the two solutions. It should be noted that the actual difference in the two solutions was small (items 1-3) and only appear large in this comparison because the stresses being compared are small. If the stresses are large*, for example element D in Fig. 4.20a, the differences in stress were only minor (Fig. 4.20b).

* In this discussion, a large stress is of the order of magnitude of the tensile failure strength 3.44 MPa (500 psi).

5. A comparison of principal concrete stresses at the crack tip defined by node e is given in Fig. 4.20c. The relatively large difference in the principal tensile stresses (as high as 20%) is attributed not only to the path-dependent material behavior (item 4), but also to the correction forces associated with the triangular element replacement in the incremental solution. Although relatively large, these differences are considered acceptable because:
   a) they are not solely the result of the triangular element replacement
   b) the direction of the stresses is essentially the same in both solutions (Fig. 4.20c).
   c) the difference in tensile stress is smallest (13%) at the point with the largest stress, i.e., the point at which the next tensile failure is expected (Fig. 4.20c).
   d) items 1-4 indicate very little difference between the two solutions.
   e) finally, concrete tensile strength cannot be defined with any more accuracy than the potential variation in tensile stresses indicated by this comparison.

It is felt that the similarities betweeen the incremental and restart solutions presented above demonstrate that the proposed equilibrium corrections permit the structure topology to be changed during an incremental solution process.

4.7.3 Use of Link Elements

A number of dimensionless link elements have been incorporated into the proposed idealization to model bond between steel and concrete and to include the force transfer across cracks attributed to aggregate interlock and dowel action. As discussed in the following sections, the analyses carried out indicate that crack formation and propagation are sensitive to the presence of these links.

i. Bond Link

Consideration of the stress transfer between steel and concrete (the bond phenomenon) is essential for prediction of realistic crack patterns in reinforced concrete members, particularly crack spacing. The modeling of this phenomenon by dimensionless links, however, can distort the stress field in the vicinity of the bond link. This is illustrated by the analysis of a cantilever subjected to axial tension (Fig. 4.17). The mesh employed is shown in Fig. 4.21a. A symmetric boundary condition is imposed at mid-depth to reduce the size of the problem. In the analysis, concrete is assumed to be an elastic isotropic material.

Application of axial tension resulted in the formation of a crack at the support. The crack propagated through the depth as the axial tension load remained constant. After this crack had formed, the load was increased and a second crack formed at 40.6 mm (1.6 in.) from the support at node i (Fig. 4.21b), the node at which the bond link was connected. This crack propagated down to node j and then at node k the

propagation became inclined (the principal tensile stress indicated an inclination of approximately 30°). Inclined crack propagation is attributed to the shear stress associated with the force transferred to the concrete elements from the steel elements by the bond link. An examination of the stresses in element 1 before cracking demonstrates the existance of this shear stress (Fig. 4.21c). Although similar shear stresses would exist in real reinforced concrete members, the magnitude of shear stress found in this analysis is believed high because of stress concentrations associated with the bond link. In addition, it is felt that the finite element mesh used in the analysis does not adequately reflect the actual shear stress gradient through the member depth (the shear stress should decrease more rapidly than indicated in the analysis). Consequently, the observed inclined crack propagation is considered unrealistic. In addition to mesh refinement, the use of a continuous bond element similar to the joint element (Fig. 4.21d) developed by Goodman, Taylor and Brekke (35) is recommended in order to eliminate the inclined propagation. It is felt that a continuous bond element should provide a more uniform stress transfer between steel and concrete elements and consequently should reduce stress concentrations attributed to dimensionless links.

ii. Aggregate Interlock and Dowel Links

In order to include the stress transfer across cracks, dimensionless links with stiffness properties characteristic of aggregate interlock and dowel action were connected across crack lines (Fig. 4.3). As with the bond link, the concentrated nodal forces transferred to the

concrete elements by these links appear to effect crack propagation. This is illustrated in the following example.

As discussed previously (Section 4.7.1), the crack pattern for the cantilever subjected to axial compression and shear depicted in Fig. 4.22a was obtained after 6 load steps. In the next load increment, the tensile failure criterion was exceeded at nodes j and ℓ (Fig. 4.22a). The program attempted to form a crack at node j since the tensile failure criterion was exceeded by a larger amount at this node. As previously noted (Section 4.3.3iii), crack propagation as a branch from an existing crack line was not incorporated into the crack formation procedure and as a result subsequent analysis was incorrect.

An examination of the stresses in the elements connected to node j (Fig. 4.22b), however, indicates that the tensile failure may be a consequence of the concentrated force applied to this node by the dowel and aggregate interlock links [a total force of 1.47 kN (330 lbs) was transferred by the links]. The large difference in element stresses at the integration points corresponding to node j (Fig. 4.22b) indicates a stress concentration which may be attributed to this nodal force.

Two changes would be required to reduce this stress concentration. First, as with the bond phenomenon, aggregate interlock should be modeled by a continuous joint element (Fig. 4.21d). Secondly, the dowel behavior of the reinforcement should be considered directly by modeling the reinforcement as plane stress elements.

4.7.4 Mesh Size

The sensitivity of crack formation to the finite element mesh size,

which has been alluded to previously (Section 4.7.3), was also investigated. It was found that a relatively refined mesh is required to obtain reasonable crack behavior. Basically, it is necessary to define a mesh which will accurately reproduce the expected stress gradients through the depth and along the length of the member being analyzed. To illustrate this point the crack patterns obtained for two different meshes (Fig. 4.23) used in the analyses of the cantilever subjected to axial compression and shear are compared in Fig. 4.24.

A difference between the two crack patterns is evident in crack formation away from the fixed end of the cantilever. In mesh A, the tensile failure criterion was exceeded first in element 1 at the stress integration point corresponding to node i (Fig. 3.24a), and a new crack segment is formed at this node. In the next solution step, a new crack line forms at node j and propagates upward. The resulting crack pattern is considered unrealistic and is attributed to the coarse element grid in this region.

It should be noted that when the crack formed at node i, the principal tensile stresses in element 1 at the stress integration points corrresponding to nodes i and j were, as one would expect from the element stress approximation, essentially constant [3.37 MPa (488 psi) at node j and 3.41 MPa (495 psi) at node i]. However, since cracking is effected at the node where the tension failure criterion is exceeded by the largest amount, the crack was formed at node i. In addition, the tensile failure criterion was exceeded at the stress point in element 2 corresponding to node j. In the next solution step, because of the coarseness of the element grid in this region, the equilirium corrections

associated with crack formation at node i had essentially no effect on the stresses in element 2. As a result, the tensile failure criterion was still exceeded at the stress point in element 2 corresponding to node j.

The crack pattern obtained using mesh A indicates that the stress field approximation corresponding to this mesh is inadequate and, since crack behavior depends on the stress field, the resulting crack behavior is unrealistic. The crack pattern obtained with the refined mesh confirms this conclusion as only one crack formed away from the fixed end.

4.8 Summary

The results presented in Section 4.7 demonstrate that the proposed incremental solution strategy can be used to incorporate topology changes into a finite element mesh, i.e., the proposed equilibrium corrections adequately redistribute nodal forces previously transferred across newly cracked nodes.

In order to obtain realistic crack behavior the fineness of the finite element mesh must adequately reproduce the stress field in the member being analyzed.

A number of problems exist in the current formulation with respect to prediction of crack formation and propagation. Besides limitations in the crack formation procedure with respect to crack closing and possible crack propagation, the use of dimensionless links to model bond between steel and concrete, and the force transfer attributed to

aggregate interlock and dowel action appears to cause stress concentrations which effect crack formation and propagation. It is clear that before the proposed model can be used in the study of the problem investigated experimentally it is necessary to

1. generalize the crack formation procedure so that crack closing and reopening is considered and so that crack segments can form as branches of existing crack lines.
2. develop continuous joint elements which can be used to include the bond-slip and aggregate interlock phenomena in the model so that stress concentrations associated with the dimensionless links currently used to model these phenomena can be eliminated
3. explore the use of plane elements to model the reinforcing steel so that dowel action can be considered directly and the need for dowel links eliminated.

5. CONCLUSIONS AND RECOMMENDATIONS

This chapter reemphasizes the more important observations made during the evaluation and discussion of results and suggests some areas, both experimental and analytical, which should be explored in the future.

5.1 Experimental Phase

From the experimental results it is apparent that short ($a/d \leq 2$) reinforced concrete columns subjected to high axial loads [axial loads near or above the balance point axial load ($P_B \tilde{=} .3P_{ULT}$)] can, if reinforced to satisfy code recommendations for ductile moment resisting frames (3), behave in a ductile fashion when subjected to cyclic inelastic deformations induced by earthquake ground motion. Relative story rotation (story drift) ductilities greater than 6 were observed in models subjected to the monotonic deformation history and greater than 4 in models subjected to the cyclic history before brittle shear failure or substantial shear degradation. The corresponding member plastic rotations were greater than 0.06 radians and 0.03 radians respectively.

The above results demonstrate that cyclic inelastic excursions reduce the maximum inelastic deformation a member can experience in a given direction. On the basis of this observation it is recommended that when deformation capacity controls design it is necessary to specify not only the magnitude of the peak deformation but also the number and type (full or partial deformation reversals) which can be expected at this peak deformation.

Although the observed inelastic behavior prior to failure has been termed significant, the context in which it is considered significant must be emphasized. In the event of a severe earthquake ground motion, the experimental deformation capacities are considered adequate for columns which are components of ductile moment-resisting frames designed on the basis of a weak girder-strong column philosophy. In such structural systems, the number of inelastic excursions that a column will experience is small and the magnitude of deformation limited (36). However, it is felt that the observed inelastic behavior could prove inadequate for columns of lateral force resisting systems which do not conform to a weak girder-strong column design philosophy.

The observed inelastic behavior indicates that columns which are designed and constructed on the basis of the 1973 UBC code requirements for ductile moment-resisting frames should possess sufficient ductility to experience a limited degree of inelastic behavior without detrimental effects. It should be emphasized that the model columns were constructed under what may be considered ideal conditions. Anchorage and splicing of the column longitudinal reinforcement were not considered, the workmanship involved in the fabrication of the model was exceptional, e.g., ties were carefully placed and hooked around the longitudinal reinforcement, and the concrete used in the models was of high quality. The influence of these factors on member behavior should be evaluated.

Spiral transverse reinforcement appears more effective in preventing diagonal tension and shear-compression type failures than rectangular ties. A spiral's principal advantage over rectangular ties is that it provides more effective confinement of the core concrete. However, the

spiral transverse reinforcement creates conditions conducive to bond failure. The relatively close spacing of the spiral (when compared to typical tie spacing), and the fact that cover spalling is more extensive in spirally reinforced columns reduce the concrete in contact with the reinforcement. In addition, for a given column size spirally reinforced columns will typically contain larger longitudinal bars than rectangular tied columns with the same design moment capacity. It should be noted that the observed bond deterioration along the longitudinal reinforcement in the spirally reinforced columns could lead to problems with respect to the anchorage of this reinforcement.

The results for the rectangular tied columns subjected to the cyclic deformation history indicate that higher axial loads (provided the axial load remains less than or equal to the balance point axial load) lead to a more ductile failure mode. Although all columns developed story drift ductilities greater than 4 prior to failure, the characteristics of the two failure modes observed were quite different. The failure mode (shear-compression) in columns subjected to axial loads of 1068kN (240 kip) and 890 kN (200 kip) was characterized by a gradual shear degradation and the fact that the model column could sustain the design gravity load and is considered more ductile than the failure mode (diagonal tension) in the column subjected to an axial force of 640 kN (144 kip), which was sudden and caused a reduction in the column's capacity to resist gravity loads. It should be emphasized, however, that this conclusion is not meant to be general but applies only to the columns tested.

A comparison of the experimental shear strengths at yielding with strengths computed on the basis of analytical flexural capacities indi-

cates that the experimental strengths were equal to or greater than the analytical strengths in all cases but one. If actual material properties are considered and if code capacity reduction factors are ignored, the shear capacity computed on the basis of the UBC design requirements (3) is equivalent to the shear strength required to develop a member's analytical flexural capacity (Section 2.7). Consequently, the experimental results indicate that the code provisions adequately define a member's shear strength. However, the shear degradation (shear failure) which was observed in the experimental program, in particular the failures in models 4R and 6R, indicate that if the severity of the expected inelastic deformation is greater than that observed here, the code provisions for computing shear strength are inadequate.

Concrete degradation (indicated by cover spalling and severe cracking of the core concrete) attributed to severe inelastic excursions will cause a significant, if not complete, degradation in the concrete shear strength and code provisions for shear strength, which are based on a completely different deformation state (service load diagonal cracking), are not reliable. Consequently, a relationship to define the concrete shear strength as a function of a design inelastic deformation level, which should reflect the influence of the type and number of reversals, is required. Since the extent of concrete degradation will also depend on the degree of confinement, this parameter should also be considered in such a function.

The behavior of models 6R and 4R indicates that the shear strength of the concrete core is lost suddenly and, as now designed (according to UBC provisions), a sudden diagonal tension failure occurs. To prevent

or delay such a failure, properly detailed shear reinforcement can be provided to resist the entire design shear. Instead of increasing the shear reinforcement, a sudden diagonal tension failure could be prevented by providing adequate confinement to control the degradation of the core concrete. The behavior of the spirally reinforced columns suggests a design in which the reinforcement cage of a rectangular tied column would include a circular spiral in the zones of expected inelastic deformation. These design alternatives to prevent brittle shear failures should be investigated in order to evaluate their effectiveness and also their practicality.

In order to establish design criteria for inelastic deformation, one question remains. What magnitude of inelastic deformation is a given member expected to experience in response to a severe earthquake ground motion? The answer is not easily attained. It depends on the structural system of which the member is a component, the design philosophy employed in proportioning members of the structural system, and the characteristics and severity of the ground motion. An investigation should be undertaken which attempts to answer this question by assessing the nonlinear response of realistic structural systems to typical earthquake ground motions of different severity.

In addition to the questions raised above, future studies of inelastic column behavior should attempt to answer the following.

1. How much transverse reinforcement is required to ensure ductile column behavior? In this study the percentage of transverse reinforcement is high. The effect of decreasing the amount of transverse reinforcement should be evaluated, particularly in the case of spiral

reinforcement. Based on the inelastic behavior of spirally reinforced columns observed in this investigation, the current code requirement to consider only two-thirds of the spiral area in the shear design computations is considered conservative and should be reevaluated.

2. What is the effect on the inelastic column behavior of compressive axial forces above the balance point load, tensile axial forces, and axial forces which vary with lateral loading?

3. Would a more heavily reinforced section behave differently? The longitudinal steel percentage in both columns tested was low (1.4% and 1.7%). The effect of higher steel percentages (3%-4%) on column behavior should be evaluated.

4. Did the reinforcing details in the rectangular tied columns influence the failure mode? It is felt that the longitudinal bar at mid-depth and the cross ties spaced at 2 in. played a significant role in the formation of the mid-depth longitudinal crack. Studies should be conducted to evaluate the validity of this conclusion.

5. What effect does biaxial loading have on inelastic column behavior? In real structures, columns are components of three-dimensional frameworks. When these systems are excited by a real earthquake, the columns will be subjected to biaxial loading. The effect of biaxial bending moments and shear forces on column behavior should be studied.

5.2 Analytical Phase

From the problems encountered in the development of an analytical model which could predict the behavior of reinforced concrete columns

such as those tested in this investigation, as well as the results obtained by applying the model developed to simple cases, the following observations can be made.

1. There is a need for an analytical model which will predict formation, propagation and closing of cracks in reinforced concrete members. The finite element method of analysis seems to be the most rational approach for the development of such a model.

2. It is felt that a finite element model of reinforced concrete which includes the main features of the one formulated here, in particular the use of a crack line approach to model concrete cracking and the consideration of force transfer across cracks, would be a useful tool in the study of inelastic behavior of reinforced concrete members.

3. An incremental solution strategy is essential if realistic nonlinear material behavior is to be incorporated into the mathematical idealization and it is felt that the strategy developed here can be used as a basis for future work in this area. The proposed equilibrium corrections permit changes in structure topology to be implemented within the context of an incremental solution strategy, thus avoiding restarting the solution from a zero stress state each time a new crack segment is formed.

4. The main parameters (bond slip, aggregate interlock, and dowel action) controlling the behavior of cracked reinforced concrete have been incorporated in the model. Additional experimental data is required in order to establish

a) A refined tensile failure criterion for concrete subjected to multiaxial states of stress.

b) more accurate and general idealizations of the bond-slip, aggregate interlock and dowel action phenomena.

5. The use of dimensionless links to model bond between steel and concrete, and the force transfer attributed to aggregate interlock and dowel action appears to cause stress concentrations which effect crack formation and propagation.

6. In order to obtain realistic crack behavior the fineness of the finite element mesh must adequately reproduce the expected stress gradients in the member being analyzed.

It is hoped that the problems associated with link elements which were revealed in this study can be eliminated and the crack formation procedure generalized by future work in this area to enable the full potential of such a model to be evaluated.

When such a model is able to predict the general inelastic behavior of reinforced concrete members, the use of substructure techniques to study the nonlinear behavior of simple structures should be explored. In such analytical techniques, refined finite element idealizations of regions of expected inelastic behavior such as the ends of beams and columns and/or beam-column joints, may be defined as macro-elements. By defining proper boundary constraints, the macro-elements can be connected by conventional beam elements to define a simple frame or experimental subassemblage. It is felt that such an idealization would supplement experimental studies in deriving a more global mathematical idealization to predict the nonlinear behavior of reinforced concrete members.

REFERENCES

1. Building Code Requirements for Reinforced Concrete (ACI 318-71), American Concrete Institute, Detroit, 1971.

2. Uniform Building Code, International Conference of Building Officials, Whittier, California, 1970.

3. Uniform Building Code, International Conference of Building Officials, Whittier, California, 1973.

4. Suzuki, Ziro, Chief Editor, General Report on the Tokachi-Oki Earthquake of 1968, Tokyo, 1971.

5. Bertero, V. V., "Studies of Olive View Building Damage," Proceedings of the U. S. Japan Seminar on Earthquake Engineering, Berkeley, California, September 4-9, 1973.

6. Yamada, M. and Fumi, S., "Shear Resistance and Explosive Cleavage Failure of Reinforced Concrete Members Subjected to Axial Load," Eighth International Congress, IABSE, New York, September 1968, pp. 1091-1102.

7. Yamada, M., and Yagi, S., "Shear Explosion of Reinforced Concrete Short Columns," Proceedings of the Fifth World Conference on Earthquake Engineering, Rome, June 1973.

8. Wight, J. and Sozen, M., "Shear Strength Decay in Reinforced Concrete Columns Subjected to Large Deflection Reversals," Civil Engineering Studies, Structural Research Series No. 403, University of Illinois, Urbana-Champaign, 1973.

9. Hirosawa, M., et al., "Experimental Study on Large Models of Reinforced Concrete Columns," Proceedings of the Fifth World Conference on Earthquake Engineering, Rome, June 1973.

10. Küstü, Ö, "Behavior of Reinforced Concrete Deep Beam-Column Subassemblages under Cyclic Loads," Earthquake Engineering Research Center, Report No. EERC 73-8, University of California, Berkeley, May 1975.

11. Clough, R. W., "Effect of Stiffness Degradation on Earthquake Ductility Requirements," Report No. SESM 66-16 Structures and Materials Research, University of California, Berkeley, October 1966.

12. Takeda, T., Sozen, M., and Nielson, N. N., "Reinforced Concrete Response to Simulated Earthquakes," Journal of Structural Division, ASCE, Vol. 96, No. ST12, December 1970, pp. 2557-2573.

13. Park, R. and Kent, D. C., "Flexural Members with Confined Concrete," Journal of Structural Division, ASCE, Vol. 97, No. ST7, July 1971, pp. 1968-1990.

14. Ngo, D., and Scordelis, A. C., "Finite Element Analysis of Reinforced Concrete Beams," Journal of the American Concrete Institute, Vol. 64, No. 3, March 1967, pp. 152-163.

15. Ngo, D., Franklin, H.A., and Scordelis, A. C., "Finite Element Study of Reinforced Concrete Beams with Diagonal Tension Cracks," Report No. SESM 70-19 Structures and Materials Research, University of California, Berkeley, December 1970.

16. Nilson, A. H., "Finite Element Analysis of Reinforced Concrete," Ph.D. Dissertation, Division of Structural Engineering and Structural Mechanics, University of California, Berkeley, March 1967.

17. Ngo, D., "A Network Topological Approach to the Finite Element Analysis of Progressive Crack Growth in Concrete Members," Ph.D. Dissertation, Division of Structural Engineering and Structural Mechanics, University of California, Berkeley, December 1975.

18. Isenberg, J., and Adham, S., "Analysis of Orthotropic Reinforced Concrete Structures," Journal of Structural Division, ACSE, Vol. 96 No. ST12, December 1970, pp. 2607-2624.

19. Valliappan, S., and Doolan, T. F., "Nonlinear Stress Analysis of Reinforced Concrete," Journal of Structural Division, ASCE, Vol. 98, No. ST4, April 1972, pp. 885-898.

20. Salem, M. H., and Mohraz, B., "Nonlinear Analysis of Planar Reinforced Concrete Structures," Civil Engineering Studies, Structural Research Series, No. 410, Univeristy of Illinois, Urbana-Champaign, July 1974.

21. Litton, R. W., "A Contribution to the Analysis of Concrete Structures Under Cyclic Loading," Ph.D. Dissertation, Division of Structural Engineering and Structural Mechanics, University of California, Berkeley, June 1975.

22. Darwin, D., and Pecknold, D. A., "Inelastic Model for Cyclic Biaxial Loading of Reinforced Concrete," Civil Engineering Studies, Structural Research Series No. 409, University of Illinois at Urbana-Champaign, Urbana, Illinois, July 1974.

23. Clough, R. W., Stress Analysis, Chapter 7, O. C. Zienkiewicz and G. S. Holister, eds., Wiley 1965.

24. Zienkiewicz, O. C., The Finite Element Method in Engineering Studies, McGraw-Hill, 1971.

25. Bathe, K. J., Ozdemir, H., and Wilson, E. L., "Static and Dynamic Geometric and Material Nonlinear Analysis," Report No. SESM 74-4, Structures and Materials Research, University of California, Berkeley, 1974.

26. Saenz, L. P., discussion of "Equation of the Stress-Strain Curve of Concrete," by Dasayi and Kirshan, Journal of the American Concrete Institute, Vol. 61, No. 9, September 1964, 1229-1235.

27. Kupfer, H., Hilsdorf, H., and Rüsch, H., "Behavior of Concrete under Biaxial Stresses," Journal of the American Concrete Institute, Vol. 66, No. 8, August 1969.

28. Nelissen, L. J. M., "Biaxial Testing of Normal Concrete," HERON, Volume 18, No. 1, 1972.

29. Liu, T. C. Y., Nilson, A. H., and Slate, F. O., "Stress-Strain Response and Fracture of Concrete in Uniaxial and Biaxial Compression," Journal of the American Concrete Institute, Vol. 69, No. 5, May 1972.

30. Phillips, M. H., Pauley, T., and Park, R., "Horizontal Construction Joints in Cast in Place Reinforced Concrete," ACI SP-42, Vol. 2, pp. 599-616.

31. Houde, J., Mirza, M. S., "A Finite Element Analysis of Shear Strength of Reinforced Concrete Beams," ACI SP-42, Vol. 1, pp. 103-128.

32. Taylor, H. P. J., "The Fundamental Behavior of Reinforced Concrete Beams in Bending and Shear," ACI SP-42, Vol. 1, pp. 43-78.

33. Fenwick, R. C., and Pauley, T., "Mechanism of Shear Resistance of Concrete Beams, Journal of Structural Division, ASCE, Vol. 94, ST10, October 1968, pp. 2325-2350.

34. Kupfer, H. B., and Gerstle, K. H., "Behavior of Concrete under Biaxial Stresses," Journal of Engineering Mechanics Division, ASCE, Vol. 99, No. EM4, August 1973.

35. Goodman, R. E., Taylor, R. L., and Brekke, T. L., "A Model for the Mechanics of Jointed Rocks," Journal of Soil Mechanics and Foundations Division, ASCE, Vol. 94, No. SM3, May 1968, pp. 637-659.

36. Zagajeski, S. W., Bertero, V. V., "Computer Aided Optimum Design of Ductile Reinforced Concrete Moment-Resisting Frames," Earthquake Engineering Research Center Report No. UCB/EERC-77/16, University of California, Berkeley, 1977.

T A B L E S

TABLE 1 SUMMARY OF PREVIOUS EXPERIMENTAL STUDIES

INVESTIGATION	CROSS SECTION b × h (in.×in.)	AVG f'_c (psi)	AVG f_y (psi)	ρ $\frac{A_s}{bh} \times 100$	BALANCE LOAD RATIO P_B/bh (ksi)	AXIAL LOAD RATIO P/bh (ksi)	$\frac{P}{P_B}$	CALCULATED MOMENT CAPACITY M (k-in)	$\frac{a}{d}$	NOMINAL SHEAR STRESS M/abd (psi)	ρ_w $\frac{A_w}{bs} \times 100$
YAMADA ONE WAY SHEAR (6)	6.4×6.4	4700	47,000	2.1	1.8	1.90	1.10	200	0.6	2100	0
									1.2	1060	0, .22, .44, .88, 1.0
									1.8	700	0
									2.4	520	0
						.98	.54	170	0.6	1645	0
									1.2	820	0
									1.8	550	0
									2.4	410	0
						0	0	90	0.6	820	0
									1.2	410	0
									1.8	270	0
									2.4	200	0
YAMADA CYCLIC SHEAR (7)	6.4×6.4	4700	47,000	2.1	1.8	1.90	1.10	200	1.2	1060	1.18, .71, .29, .59
						.98	.54	170	1.2	820	1.18, .71, .29, .44
WIGHT (8)	6 × 12	4500	72,000	2.4	1.4	.55	.40	705	2.8	385	.33, .48, .67, .92, 1.47
						.35	.25	650	2.8	350	.33
						0	0	440	2.8	235	.33, .48, .67, 1.05 1.47
HIROSAWA (9)	10 × 10	3000	50,000	.68	1.20	.750	.62	400	1.0	500	1.83
									2.0	250	.87, .45
						.375	.31	290	1.0	370	1.12, .54
									2.0	190	.24, .12
				1.22	1.20	.375	.31	380	1.0	490	2.55, 1.32
									2.0	245	.52, .26
				1.90	1.20	.750	.62	600	2.0	405	2.65, 1.32
						.375	.31	500	2.0	325	1.43, .72
KÜSTÜ (10)	12 × 12	5000	72,000	1.40	1.70	1.00	.60	1240	1.5	610	.56
						.60	.37	900	1.5	430	.47
				1.10	1.60	.21	.13	640	1.5	300	.30
ZAGAJESKI	12 × 12	5000	72,000	1.39	1.67	1.67	1.00	1400	1.5	760	.83
						1.40	.84	1340	1.5	710	.83
						1.00	.60	1240	1.5	610	.83
	12 × 12	5000	78,000	1.67	1.40	1.40	1.00	1270	1.5	690	1.11

Note: numbers in ( ) are references from which data was taken

1 in = 25.4 mm; 1000 psi = 1 ksi = 6.895 MPa; 1 k-in = 0.113 kN-m

TABLE 2

SUMMARY OF MODEL COLUMN DATA

1	2	3	4	5	6	7	8
MODEL	f'_c (psi)	f_y (ksi)	ρ A_s/bh	AXIAL LOAD P (kip)	MOMENT CAPACITY (k-in)	FLEXURAL SHEAR (kip)	DEFORMATION HISTORY
2R	5270	72	1.4	240*	1420	79	MONOTONIC
3R	5260	72	1.4	240*	1420	79	CYCLIC
4R	5000	72	1.4	240*	1418	79	MONOTONIC
5R	5100	72	1.4	200	1340	75	CYCLIC
6R	4700	72	1.4	144	1190	66	CYCLIC
1S	4900	78	1.67	200*	1260	70	MONOTONIC
2S	5000	78	1.67	200*	1260	70	CYCLIC

Note: *indicates balance point axial load

1000 psi = 1 ksi = 6.895 MPa; 1 kip = 4.45 kN; 1 k-in = 0.113 kN-m

TABLE 3 SUMMARY OF OBSERVED BEHAVIOR

MODEL	AXIAL LOAD (kip)	FLEXURAL CRACKING (kip)	INCLINED CRACKING (kip)	FLAKING CRUSHING (kip)	MID-DEPTH LONGITUDINAL CRACKING (kip)	Δ [a] CRACK CONTINUITY (in)	Δ AT START [b] OF SHEAR DEGRADATION S_d (in)	S_d (%)	H_d [c] (%)
2R	240	30-45	61-75	75-90	75-90	on reversal	-	-	64
3R	240	32-50	64[d]	66-72	60-66	1.25	2.0	44	54
4R	240	30-45	63-70	70-80	80-88	-	-	-	-
5R	200	35-54	66[d]	72-78	54-72	1.25	2.5	40	48
6R	144	20-33	53	64-68	56-61	-	2.5	25	-
1S	200	15-30	48-64	66-72	66-72	-	-	-	59
2S	200	25-40	40-56	62-65	44-57	-	2.5	57	63

(a) model tip displacement, only for models failing by shear compression mode

(b) only for models subjected to cyclic deformation history, $S_d = \frac{H_{first\ cycle} - H_{fifth\ cycle}}{H_{first\ cycle}} \cdot 100$

(c) $H_d = \frac{H_{maximum} - H_{final}}{H_{maximum}} \cdot 100$

(d) from stirrup strain data

Note: 1 kip = 4.45 kN; 1 in = 25.4 mm

TABLE 4 SUMMARY OF TEST RESULTS

MODEL	DEFORMATION HISTORY	AXIAL LOAD P (kip)	FAILURE TYPE	MAXIMUM SHEAR H [a] (kip)	$\frac{H}{V_F}$ [b]	NOMINAL SHEAR STRESS v [c]		μ_R [e]
						V/bd (psi)	V/A_c [d] (psi)	
2R	MONOTONIC	240	Shear-Compression	92	1.17	766 (10.6)	852 (11.7)	-
3R	CYCLIC	240	Shear-Compression	79 (83) [f]	1.0 (1.05)	658 (8.8)	731 (10.0)	4.0
4R	MONOTONIC	240	Diagonal Tension	90	1.15	750 (10.5)	833 (11.8)	6
5R	CYCLIC	200	Shear-Compression	82	1.09	683 (9.6)	745 (10.4)	4.5
6R	CYCLIC	144	Diagonal Tension	70	1.06	583 (8.5)	636 (9.3)	4.7
1S	MONOTONIC	200	Bond Failure	72	1.03	660 (9.5)	832 (11.9)	6
2S	CYCLIC	200	Bond Failure	64	0.91	601 (8.5)	751 (10.6)	-

(a) Does not include P-Δ effect

(b) V_F is from column 7 in Table 2

(c) Numbers in parenthesis are $v/\sqrt{f'_c}$

(d) For rectangular tied columns A_c = (b-2 · cover)(h-2 · cover)
For spiral columns $A_c = \frac{\pi}{4}(h-2 \cdot cover)^2$

(e) $\mu_R = \frac{R_{max}}{R_y}$ where R is the story rotation (see Section 3.6.1)

(f) A larger shear was reached in the opposite direction

Note: 1 kip = 4.448 kN, 1,000 psi = 6.895 MPa

TABLE 5 SUMMARY OF FIRST CYCLE ENERGY DISSIPATION

MODEL	AXIAL LOAD (kip)	TIP DISPLACEMENT (in)	HYSTERETIC AREA A (k-in)	RELATIVE AREA RA (%)
3R	240	.6	14.1	10
		.8	26.1	12
		1.0	37.4	12
		1.25	53.4	14
		1.5	70.3	15
		1.75	96.3	17
		2.0	123.1	24
		2.5	163.5	44
5R	200	.6	14.1	10
		.8	21.0	9
		1.0	28.7	9
		1.25	43.3	11
		1.5	65.3	14
		1.75	83.9	15
		2.0	112.7	18
		2.5	179.3	25
6R	144	.6	11.6	9
		.8	18.2	9
		1.0	22.5	9
		1.25	39.6	12
		1.5	62.2	15
		1.75	82.9	18
		2.0	105.5	20
		2.5	175.0	27
2S	200	.6	16.3	12
		.8	22.9	11
		1.0	29.4	11
		1.25	39.8	14
		1.5	53.3	14
		1.75	67.0	15
		2.0	85.4	19
		2.5	140.5	28

TABLE 6 SUMMARY OF CYCLIC BEHAVIOR OF ENERGY DISSIPATION

MODEL	AXIAL LOAD (kip)	TIP DISPLACEMENT (in)	CYCLE	HYSTERETIC AREA A (k-in)	RELATIVE AREA RA (%)	ENERGY LOSS (k-in/%)
3R	240	2.0	1	123.1	24	
			2	111.8	26	
			3	103.4	28	
			4	102.0	30	
			5	111.3	38	11.8/10
3R	240	2.5	1	163.5	44	
			2	142.5	44	21.0/13
2R	240	2.5	1	140.9	33	
			2	112.0	33	28.9/20
5R	200	2.5	1	179.3	25	
			2	162.7	24	
			3	159.8	25	
			4	154.7	31	
			5	150.8	37	28.5/16
6R	144	2.5	1	175.0	27	
			2	166.5	27	
			3	161.9	27	
			4	162.3	29	
			5	174.2	36	.8/<1
2S	200	2.5	1	140.5	28	
			2	114.6	29	
			3	100.7	32	
			4	90.2	35	
			5	90.0	44	50.5/36

Note: 1 kip = 4.45 kN; 1 in = 25.4 mm; 1 k-in = 0.113 kN-m

TABLE 7

CURVATURE DUCTILITIES

MODEL	Δ (in)	CYCLE	μ_ϕ	ε_{core}
3R	2.0	1^{st}	6	.017
		5^{th}	4	.012
5R	2.5	1^{st}	11	.043
		5^{th}	12	.061
6R	2.5	1^{st}	9	.018
		5^{th}	27	.105
2S	2.5	1^{st}	11	.021
		5^{th}	12	.031

Note: 1 in = 25.4 mm

TABLE 8

STEEL YIELD DATA

MODEL	FIRST YIELD	TYPE
3R	Δ = 1.0 first cycle	compressive
4R	Δ = 1.0	compressive
5R	Δ = 1.0 first cycle	tensile
6R	Δ = 1.0 fifth cycle	compressive
1S	Δ = 1.0	tensile
2S	Δ = 1.25 first cycle	compressive

F I G U R E S

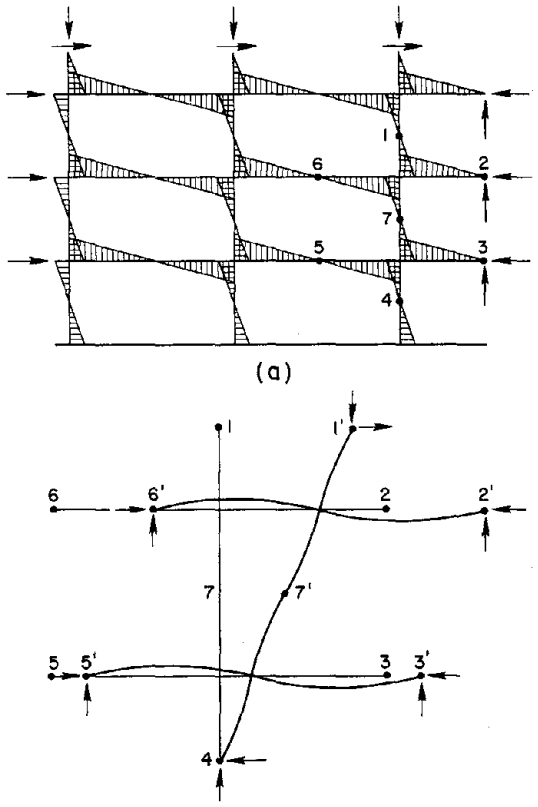

FIG. 1.1 TYPICAL MOMENT DIAGRAM AND DEFORMATION PATTERN FOR A MOMENT RESISTING FRAME SUBJECTED TO LATERAL LOAD

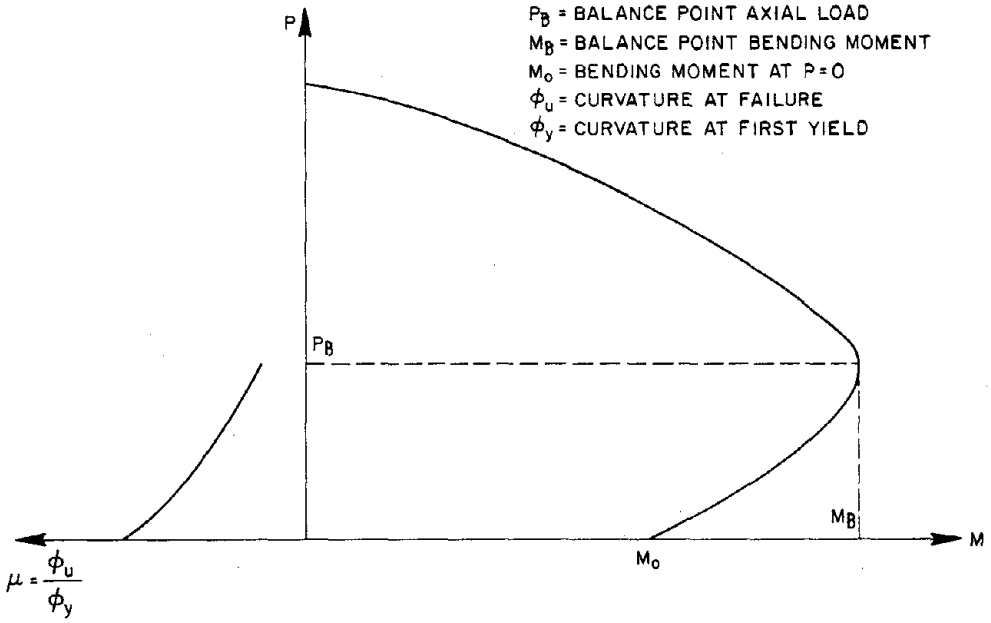

FIG. 1.2 INTERACTION OF AXIAL FORCE WITH BENDING MOMENT AND CURVATURE DUCTILITY

Preceding page blank

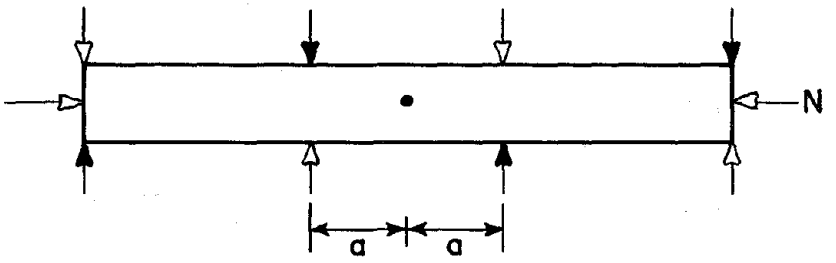

(a) YAMADA CYCLIC TESTING METHOD

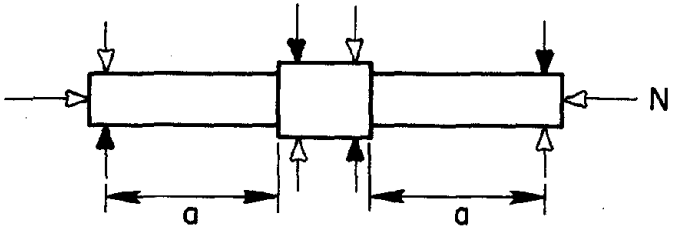

(b) WIGHT TESTING METHOD

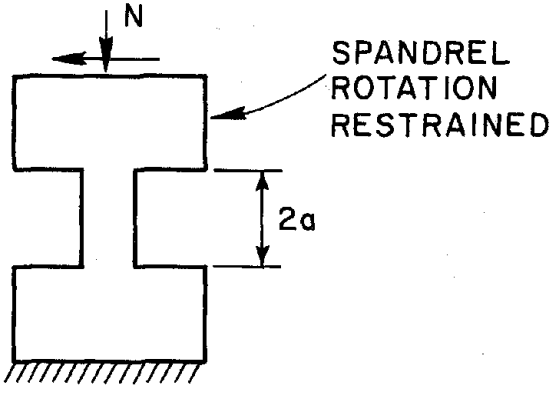

(c) HIROSAWA TESTING METHOD

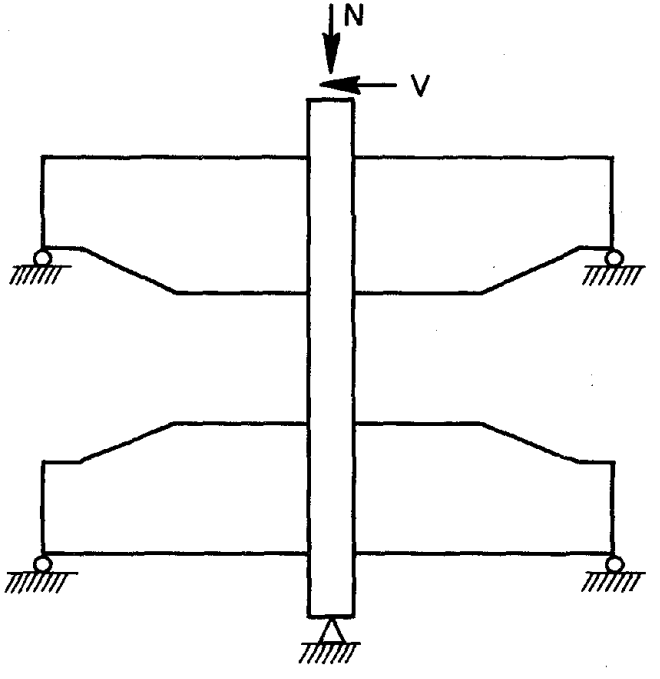

(d) KÜSTÜ TESTING METHOD

FIG. 1.3 PREVIOUS TEST MODELS AND LOADING SCHEMES

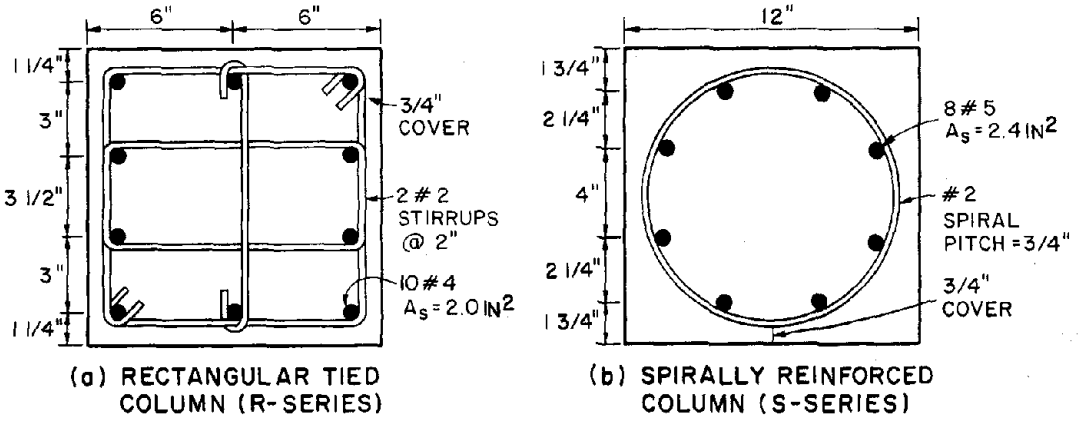

FIG. 1.4 MODEL COLUMN CROSS SECTIONS (1 IN. = 25.4 MM)

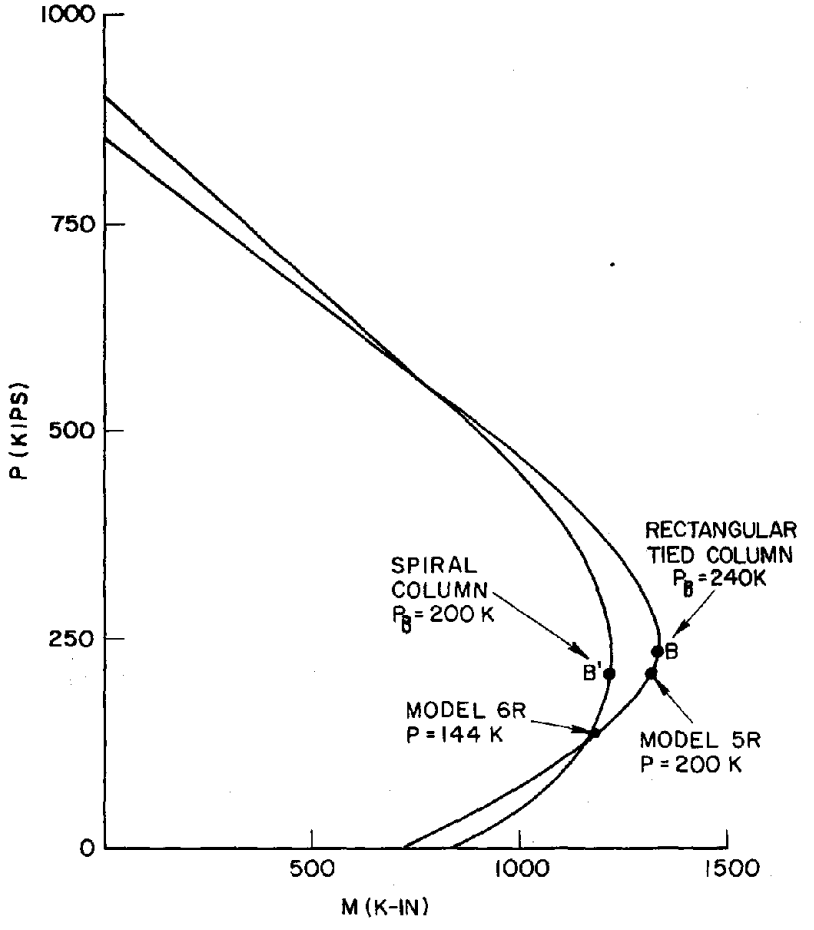

FIG. 1.5 MODEL COLUMN AXIAL FORCE-MOMENT INTERACTION RELATIONSHIPS (1 K = 4.448 kN, 1 K-IN. = 0.113 kN·M)

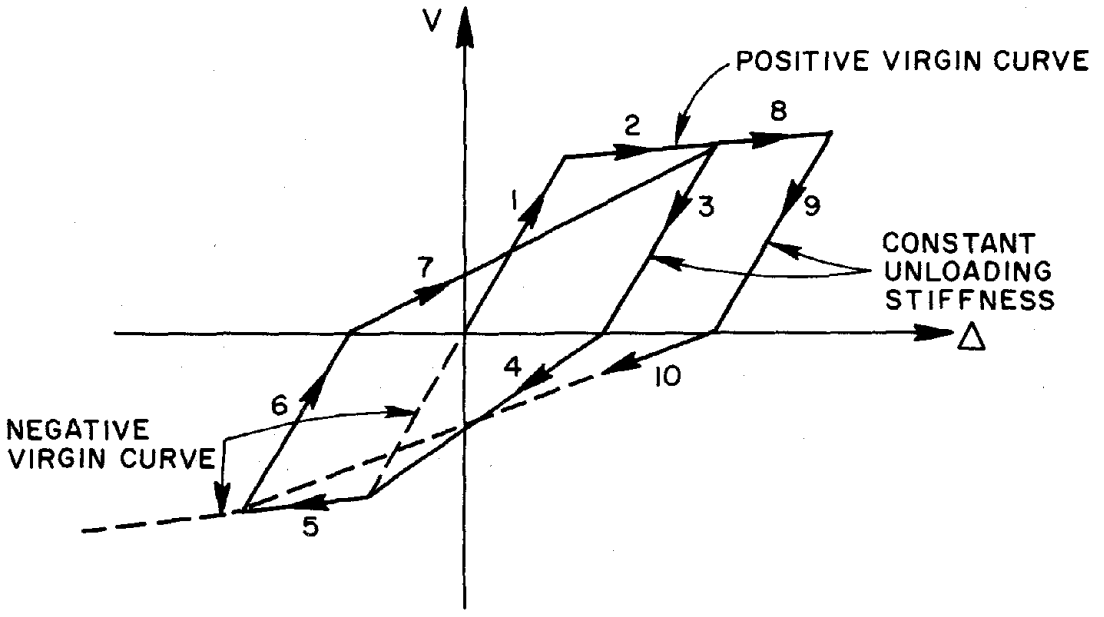

(a) CLOUGH'S BILINEAR HYSTERESIS MODEL

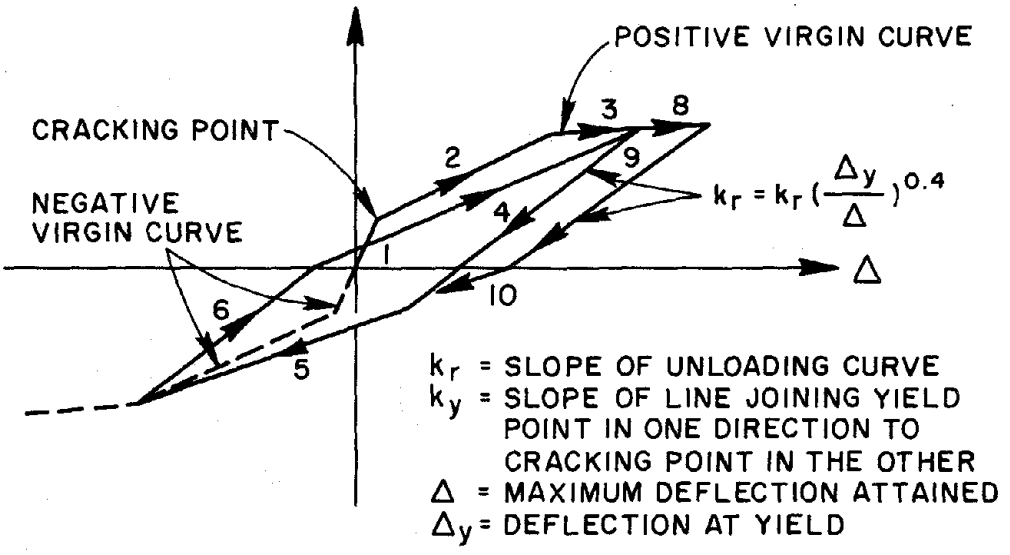

(b) TAKEDA'S TRILINEAR HYSTERESIS MODEL

FIG. 1.6 STIFFNESS DEGRADING HYSTERESIS MODELS

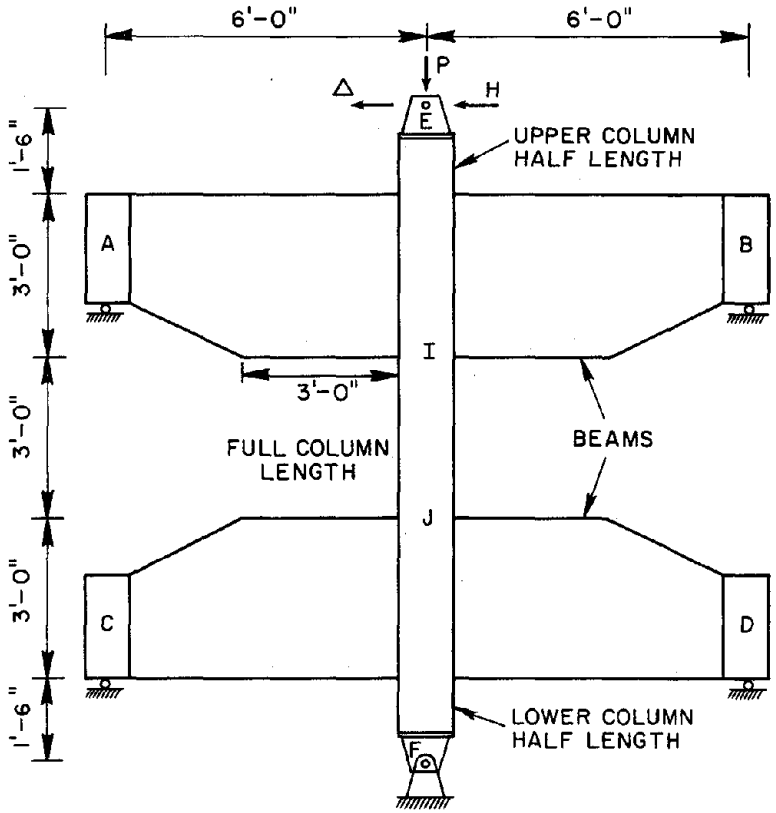

FIG. 2.1 TEST MODEL (1 FT = 0.305 M)

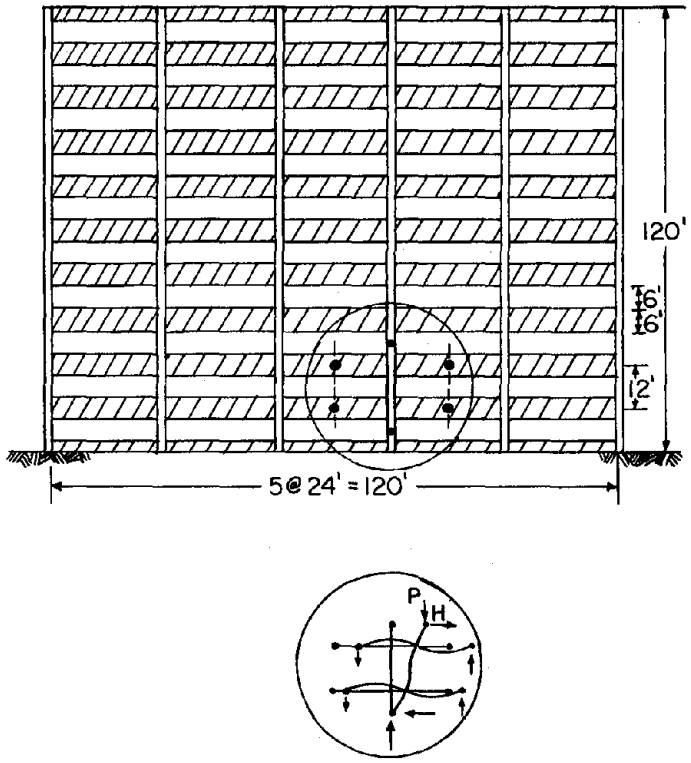

FIG. 2.2 SUBASSEMBLAGE OF PROTOTYPE FRAME CHOSEN AS A TEST MODEL (1 FT = 0.305 M)

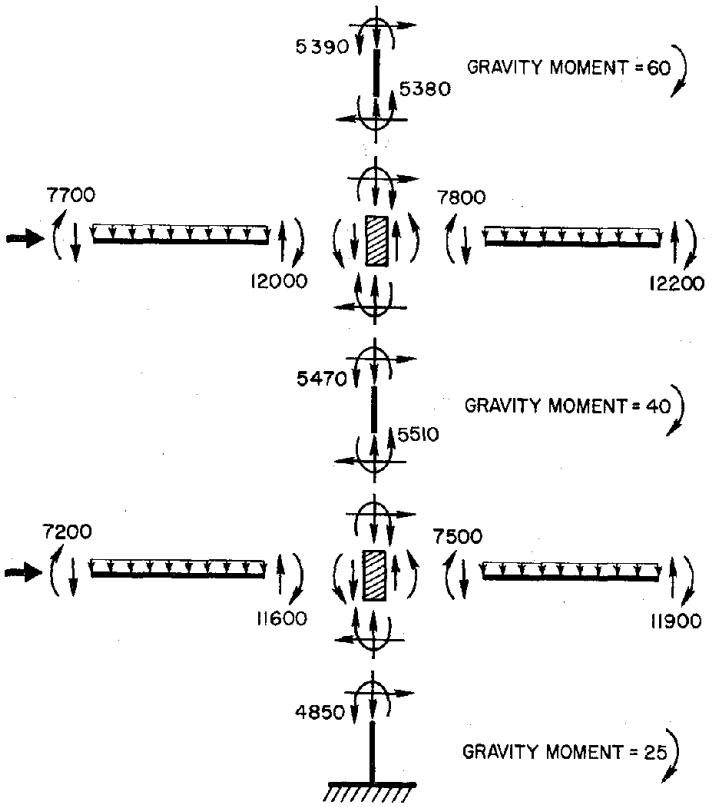

FIG. 2.3 MOMENTS IN LOWER PORTION OF FRAME AT AN INTERIOR COLUMN LINE (1 K-IN. = 0.113 kN•M)

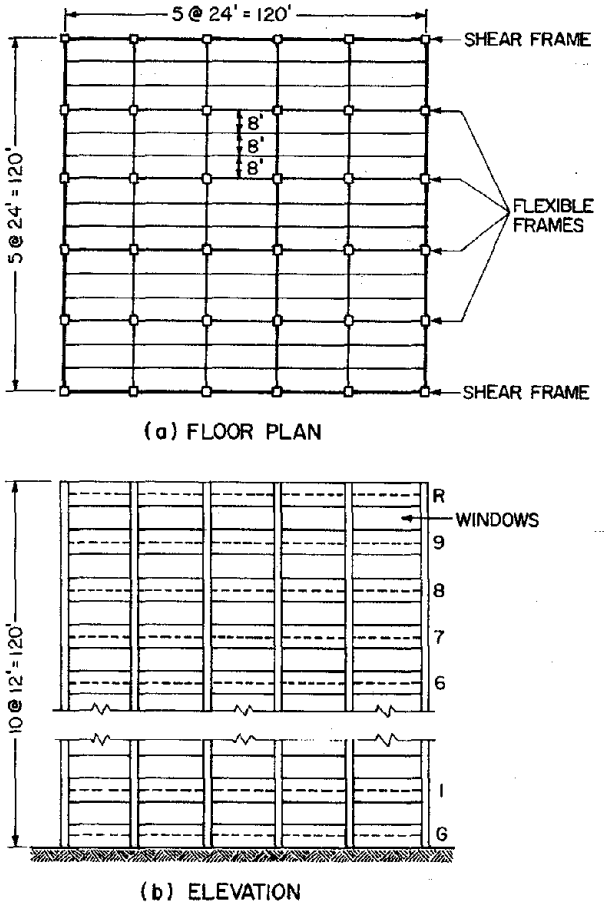

FIG. 2.4 PROTOTYPE STRUCTURE (1 FT = 0.305 M)

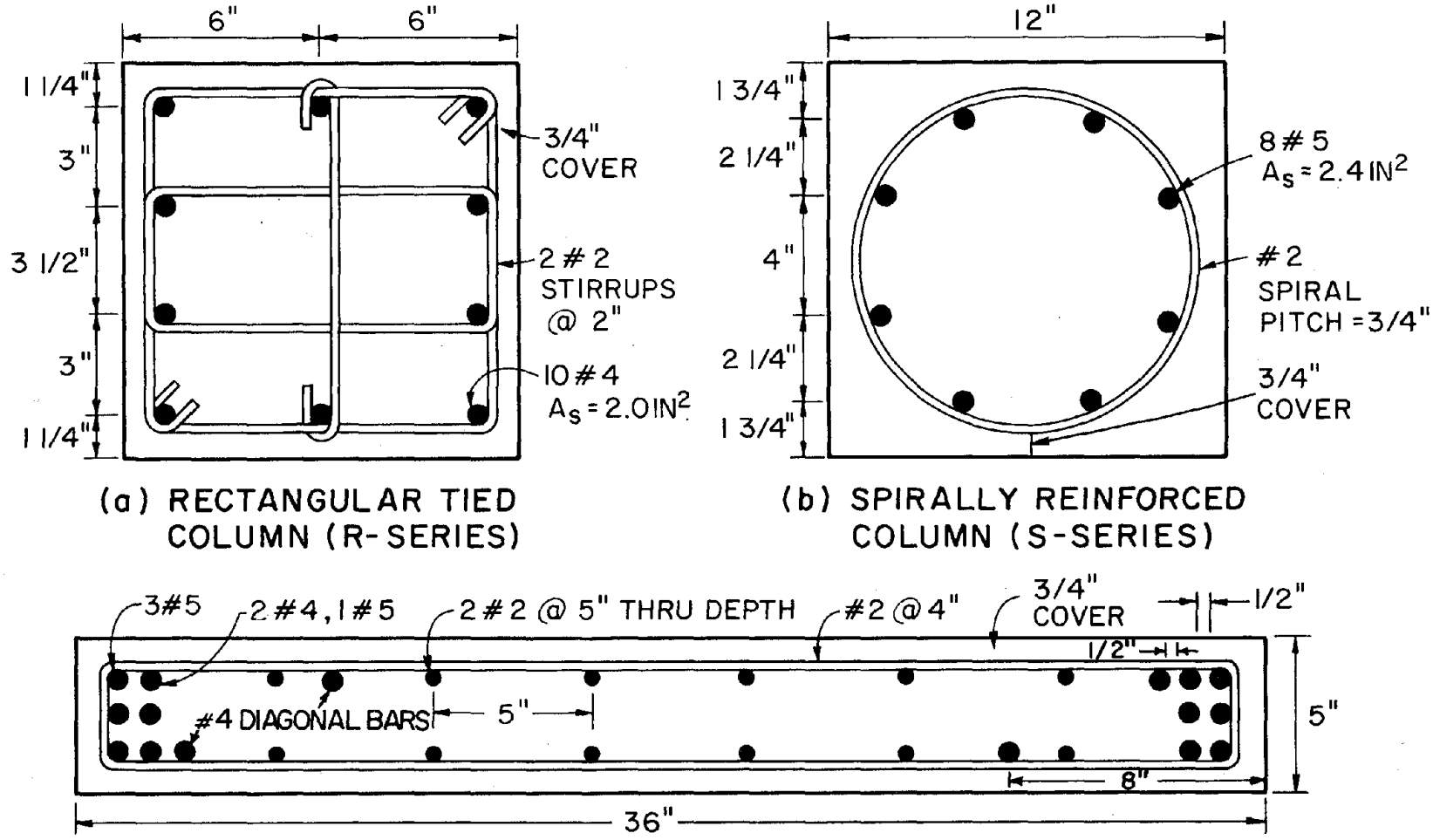

FIG. 2.5 TEST MEMBER CROSS SECTIONS (1 IN. = 25.4 MM)

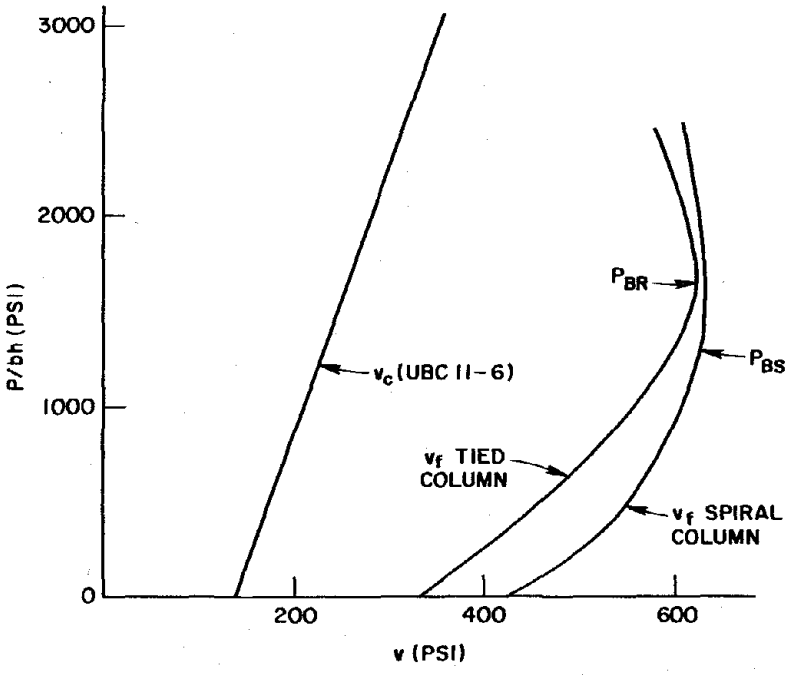

FIG. 2.6 VARIATION OF SHEAR STRESS WITH AXIAL COMPRESSIVE STRESS (1 PSI = 6895 Pa)

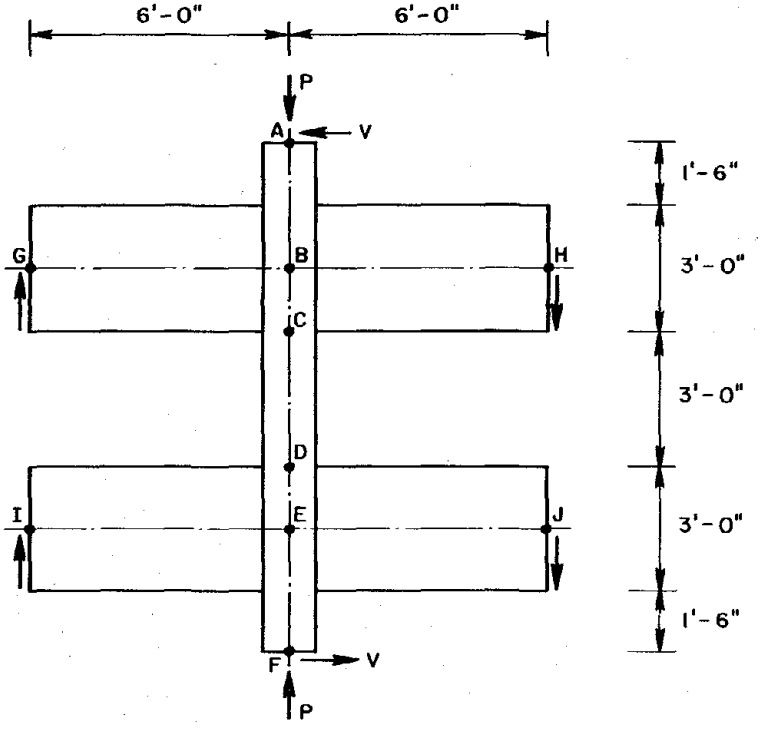

FIG. 2.7 GENERAL SHAPE AND DIMENSIONS OF TEST MODEL (1 FT = 0.305 M, 1 IN. = 25.4 MM)

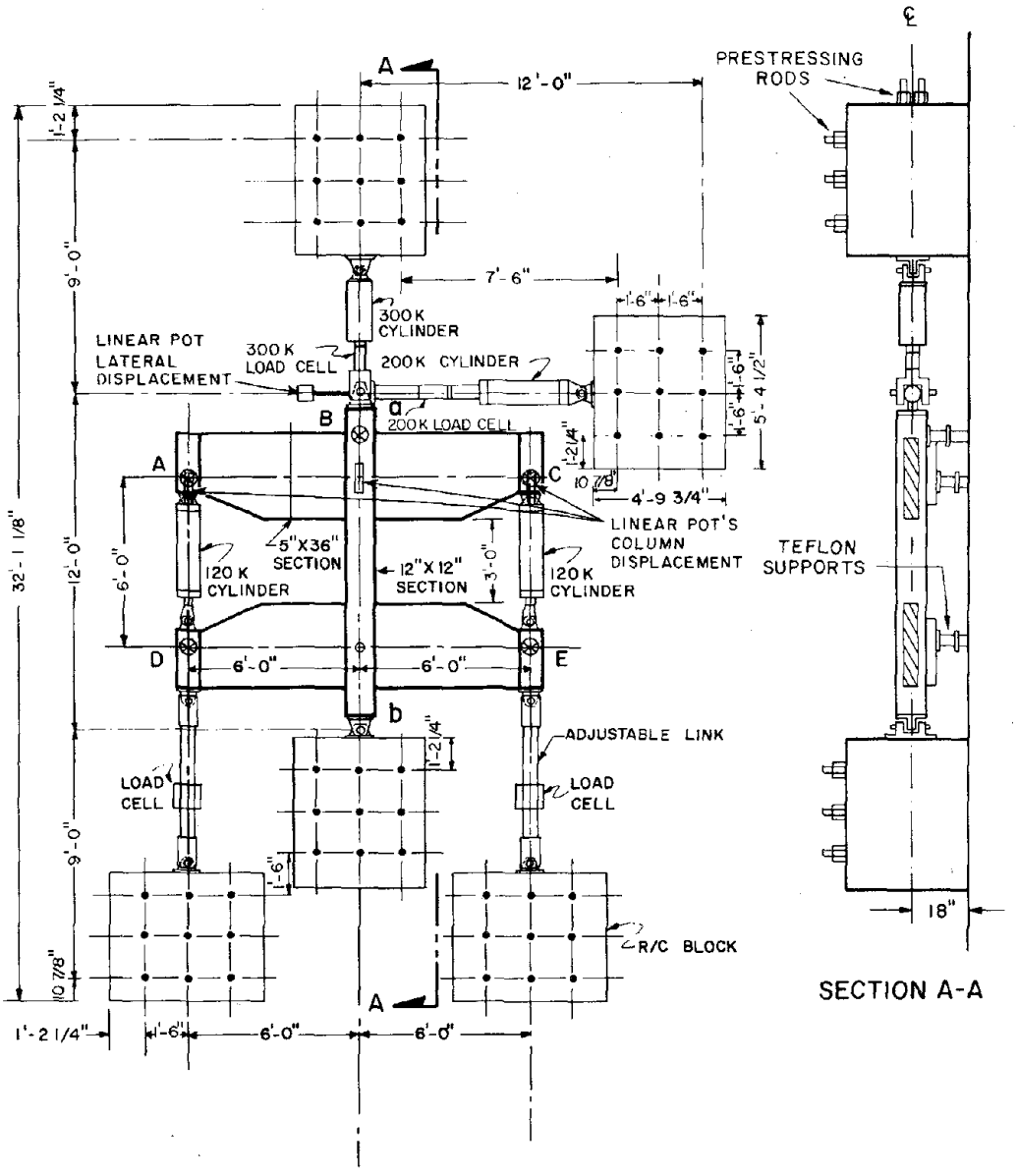

FIG. 2.8 GENERAL PLAN OF TEST SYSTEM (10)
(1 FT = 0.305 M, 1 IN. = 25.4 MM,
1 KIP = 4.448 kN)

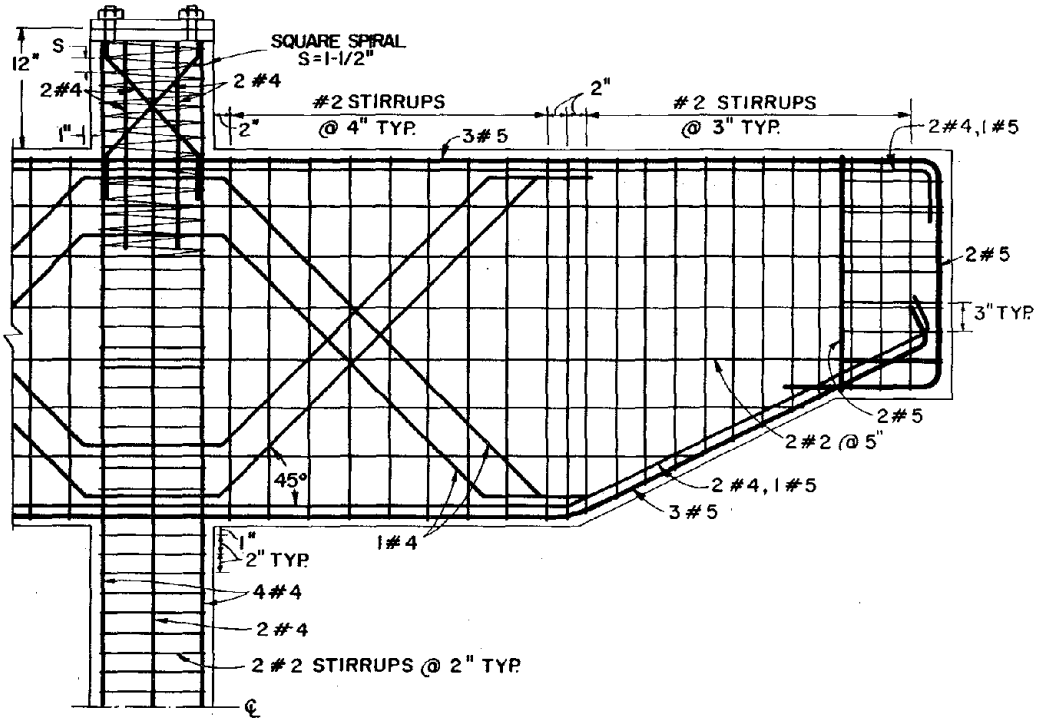

(a) R-SERIES COLUMNS

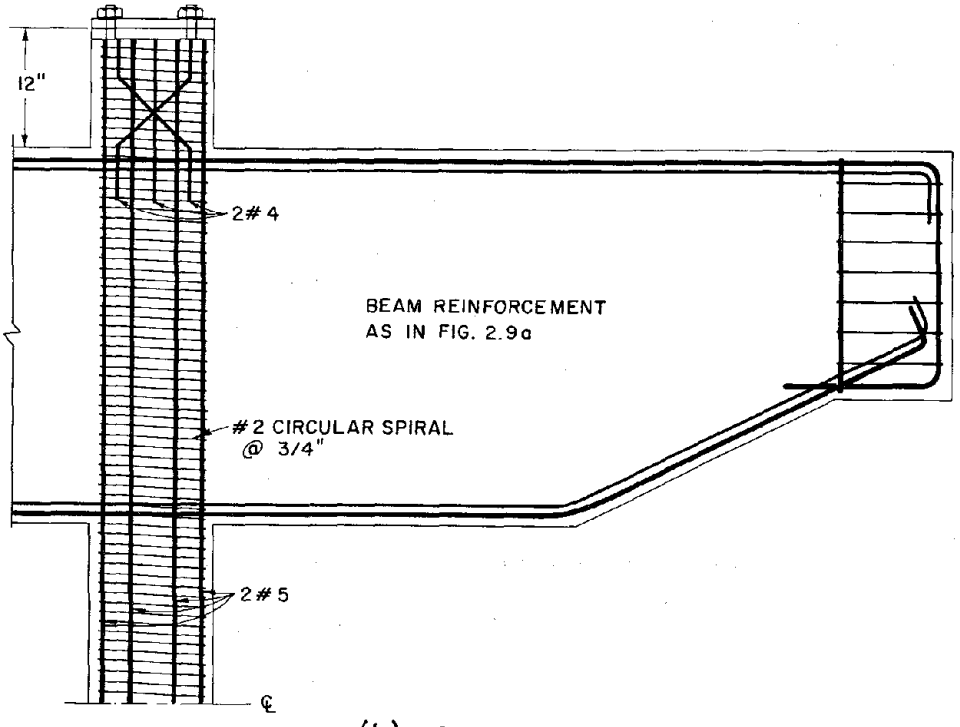

(b) S-SERIES COLUMNS

FIG. 2.9 COLUMN REINFORCEMENT DETAILS (1 IN. = 25.4 MM)

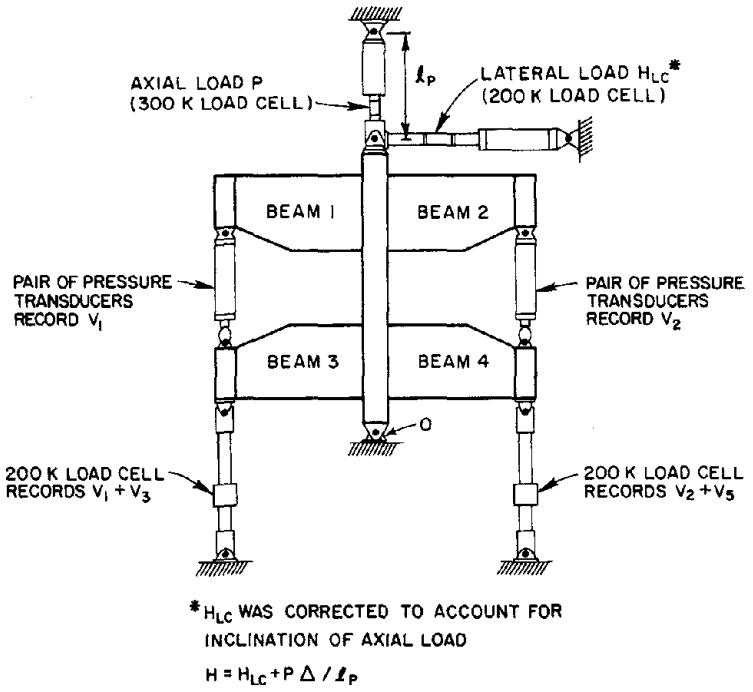

FIG. 2.10 LOAD AND REACTION DATA
(1 K = 4.448 kN)

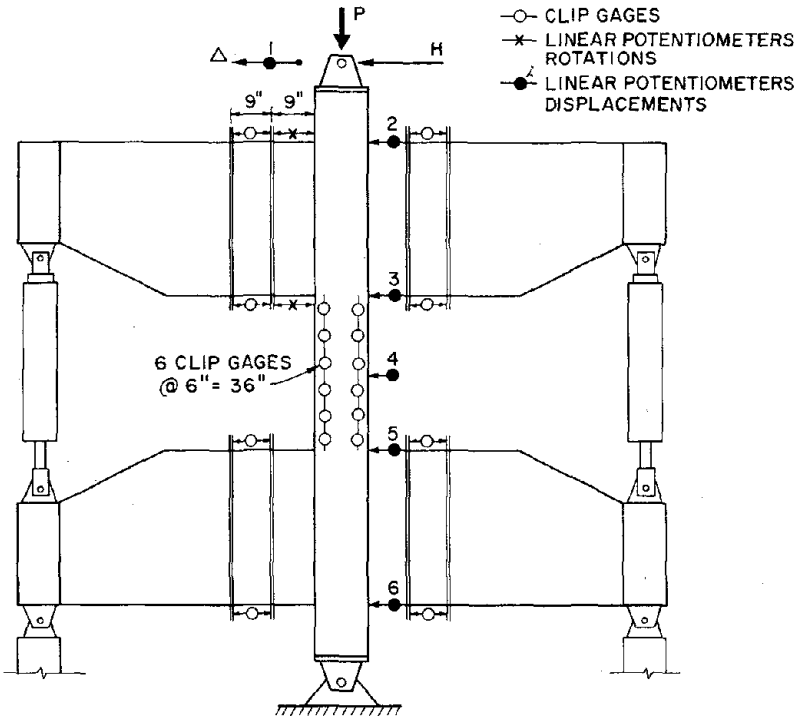

FIG. 2.11 LOCATIONS OF EXTERNAL INSTRUMENTATION (1 IN. = 25.4 MM)

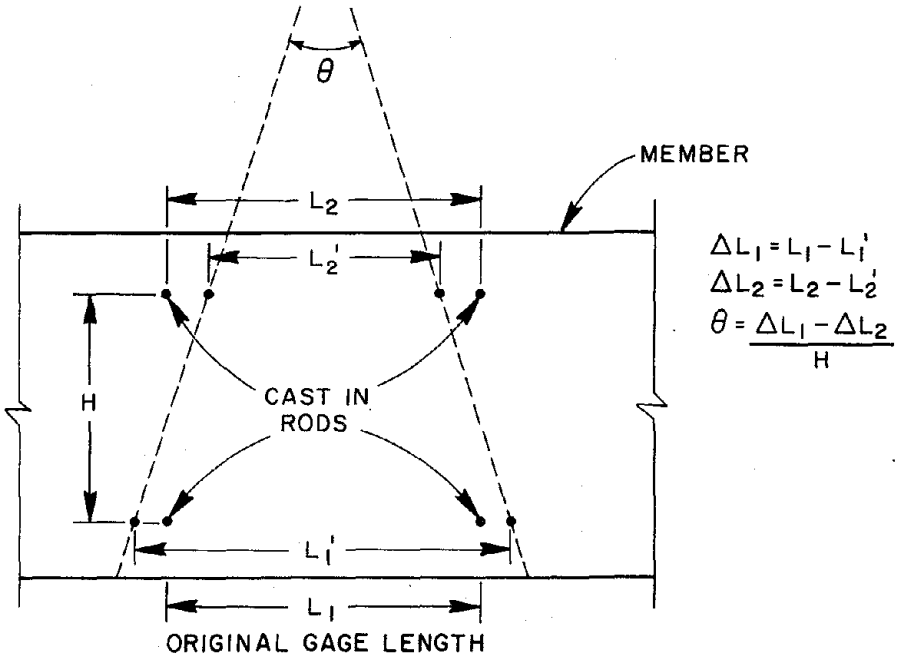

FIG. 2.12 MECHANISM OF ROTATION MEASUREMENTS

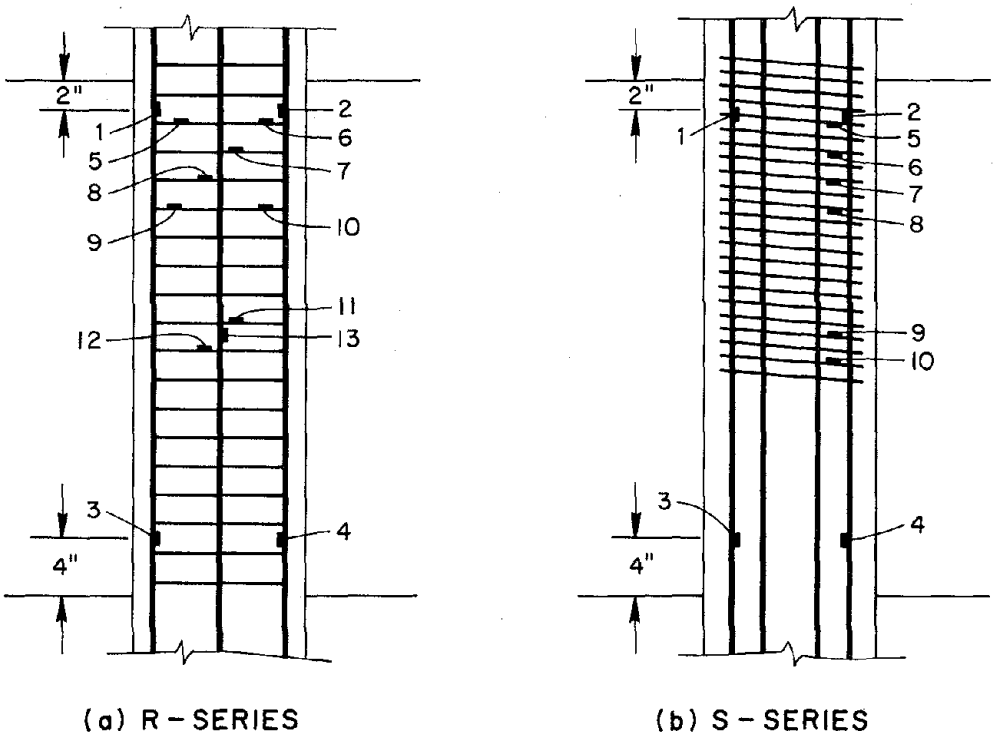

FIG. 2.13 STRAIN GAGE LOCATIONS (1 IN. = 25.4 MM)

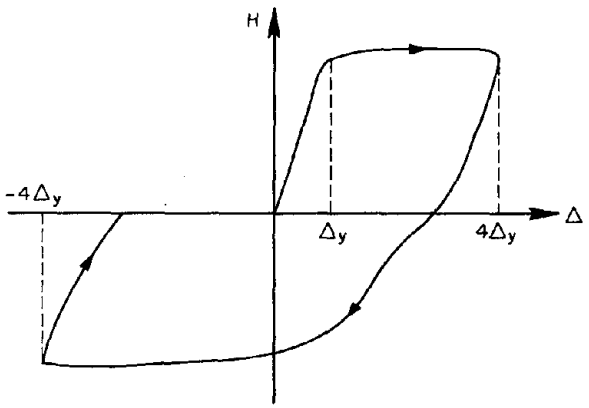

(a) HISTORY I

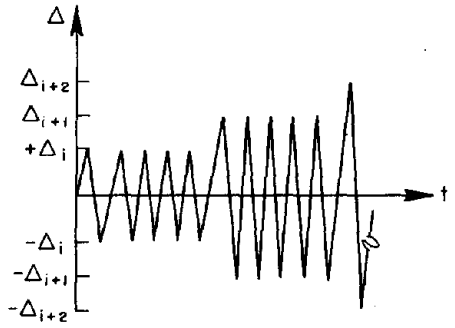

(b) TYPICAL SEQUENCE IN HISTORY II

FIG. 2.14 DEFORMATION HISTORIES

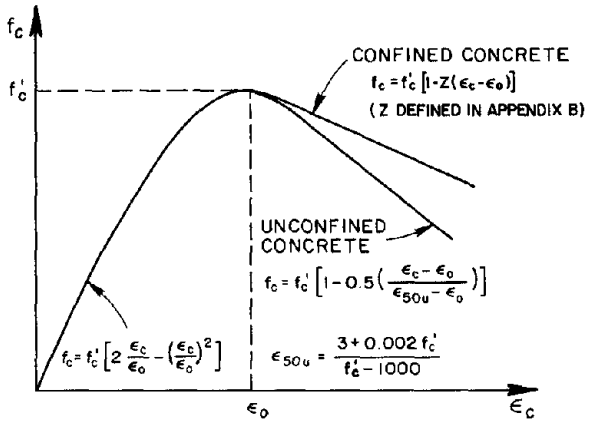

(a) CONCRETE

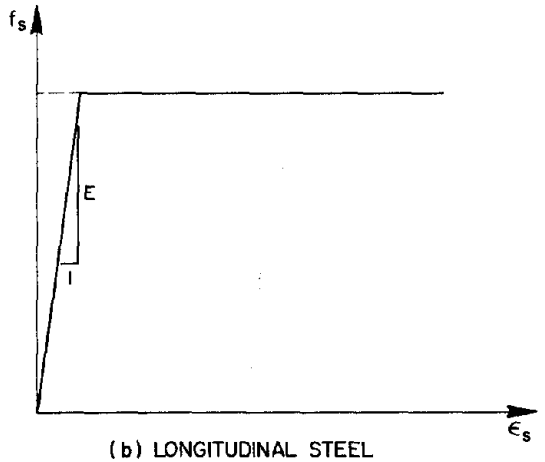

(b) LONGITUDINAL STEEL

FIG. 2.15 CONCRETE AND STEEL STRESS-STRAIN RELATIONSHIPS

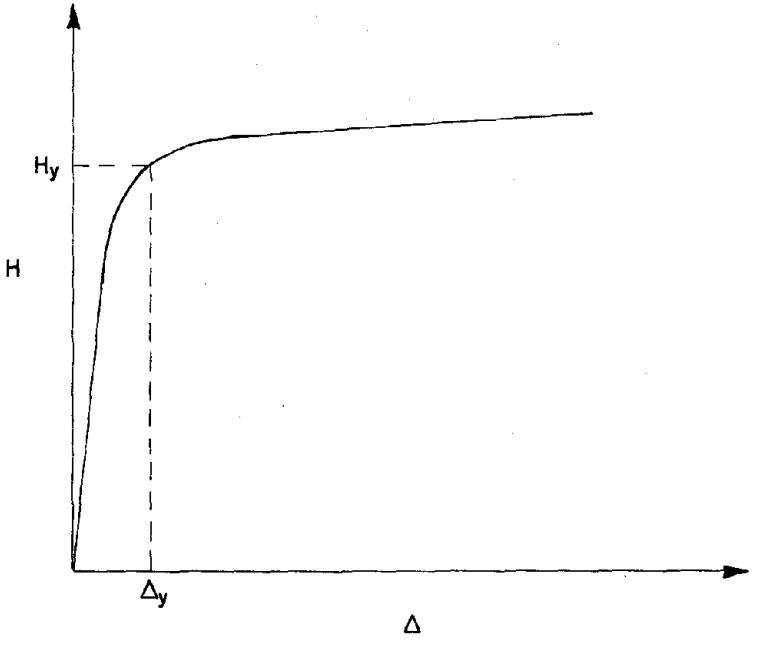

FIG. 3.1 TYPICAL SHEAR DISPLACEMENT RELATIONSHIP

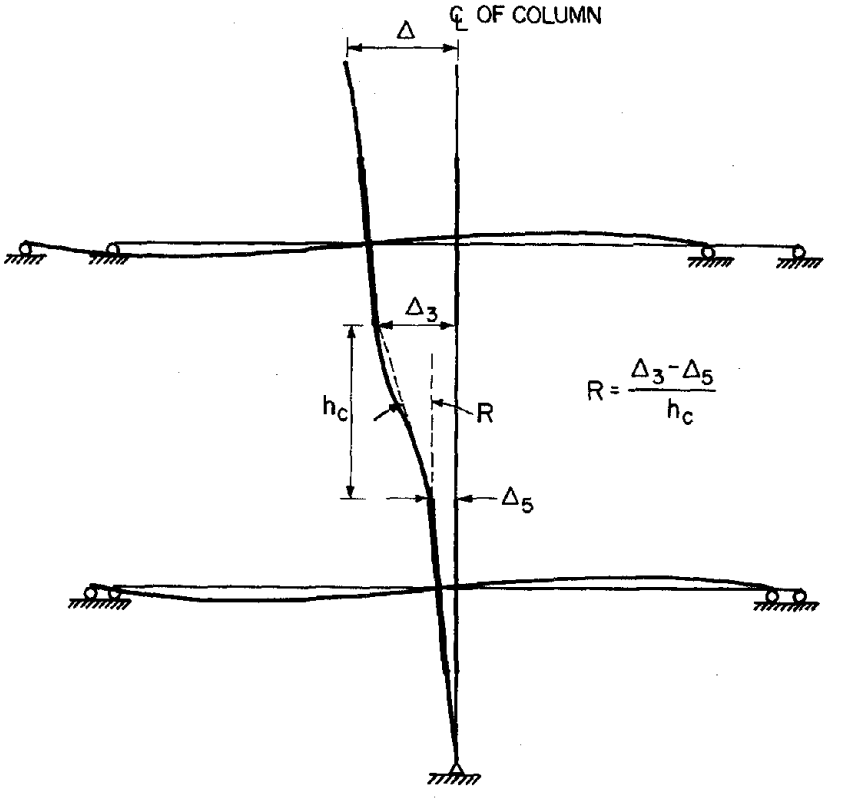

FIG. 3.2 DEFINITION OF RELATIVE STORY ROTATION

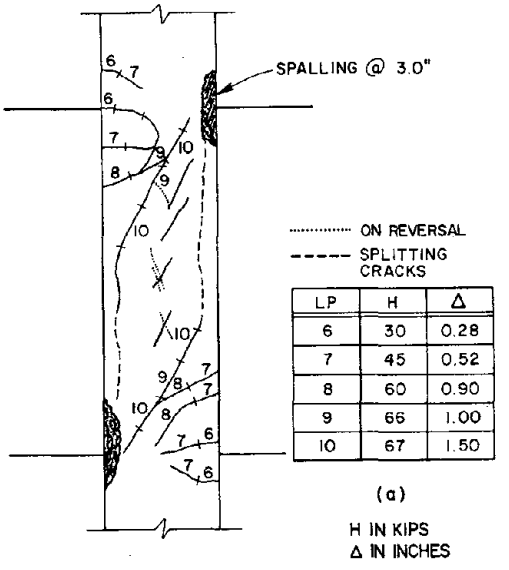

LP	H	Δ
6	30	0.28
7	45	0.52
8	60	0.90
9	66	1.00
10	67	1.50

FIG. 3.3 CRACKING IN MODEL 1S (1 KIP = 4.448 kN, 1 IN. = 25.4 MM)

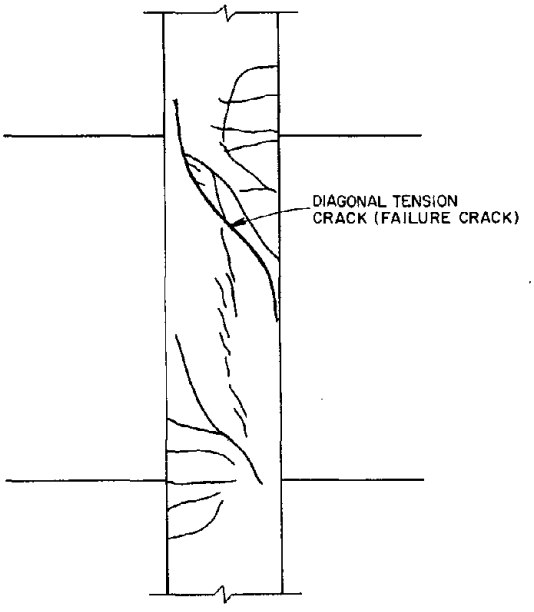

FIG. 3.4 CRACKING IN MODEL 4R

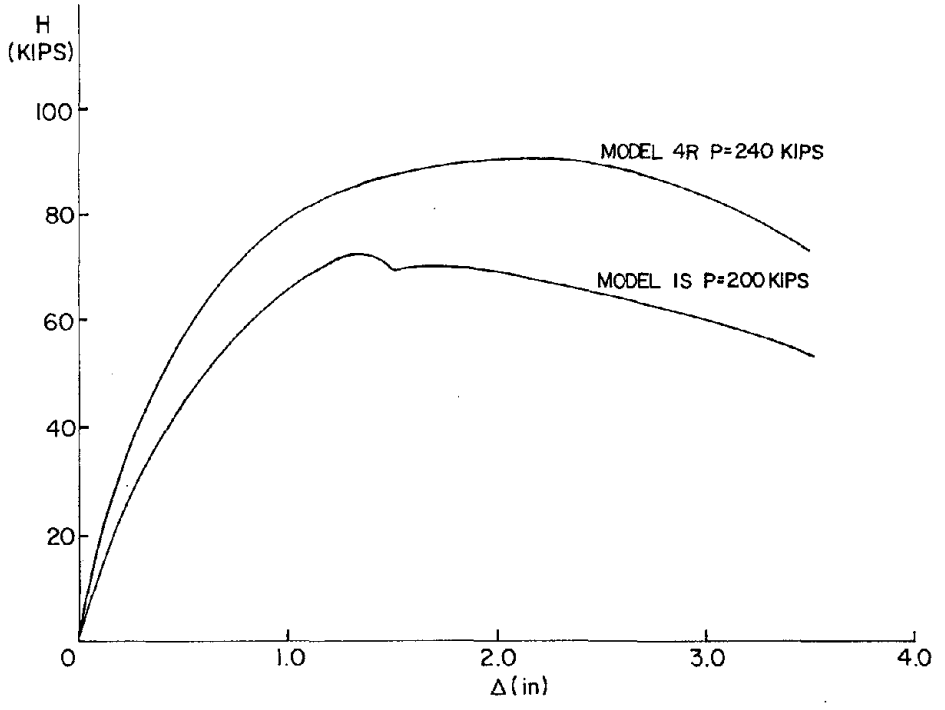

FIG. 3.5 COMPARISON OF MONOTONIC SHEAR FORCE-TIP DISPLACEMENT RELATIONSHIPS FOR MODELS 4R AND 1S (1 KIP = 4.448 kN, 1 IN. = 25.4 MM)

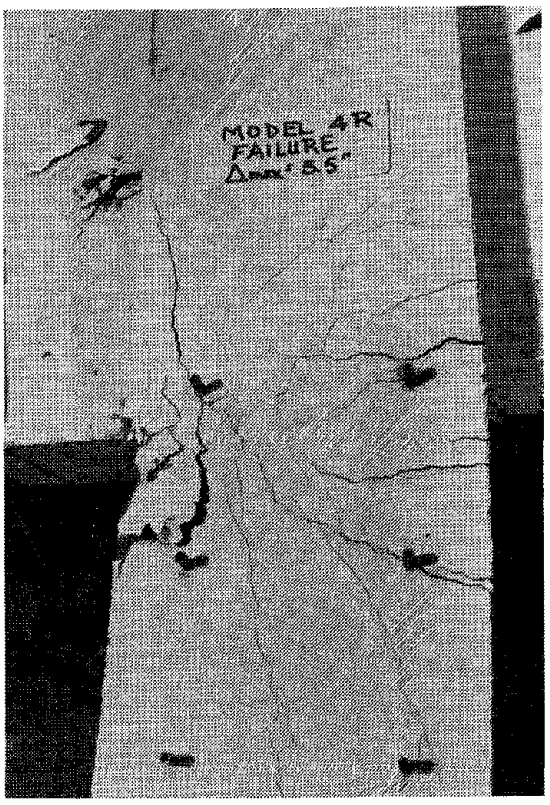

FIG. 3.6 PLASTIC HINGE IN MODEL 4R
(1 IN. = 25.4 MM)

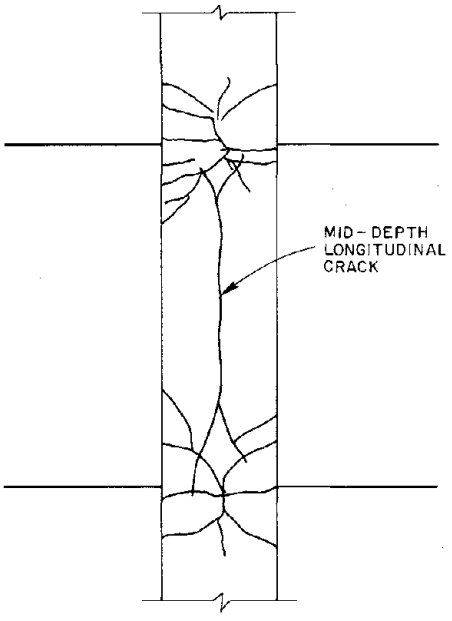

FIG. 3.7 CRACKING IN MODEL 3R

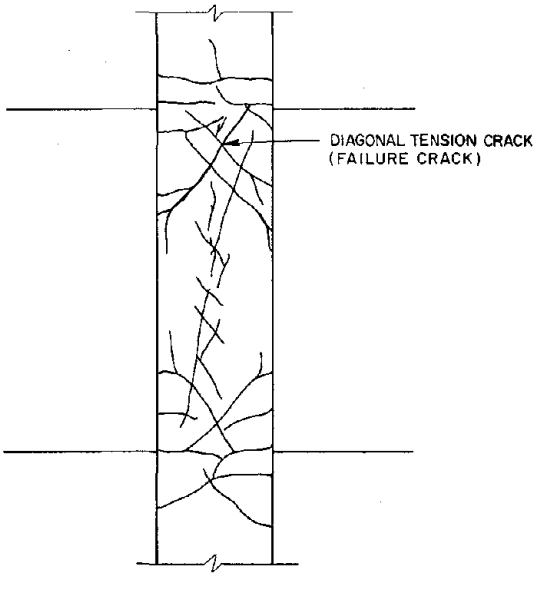

FIG. 3.8 CRACKING IN MODEL 6R

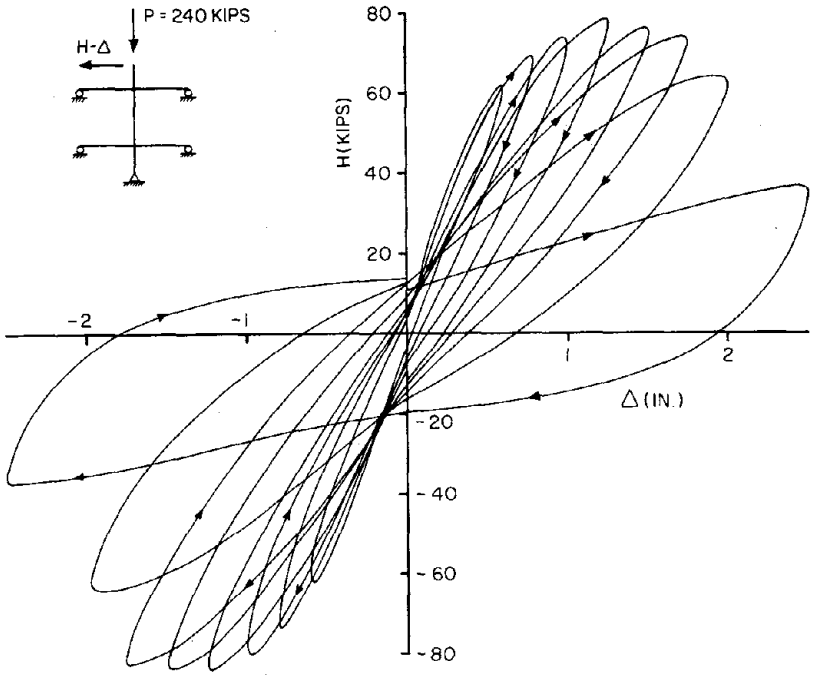

FIG. 3.9 FIRST CYCLE SHEAR FORCE-TIP DISPLACEMENT HYSTERETIC LOOPS FOR MODEL 3R (1 KIP = 4.448 kN, 1 IN. = 25.4 MM)

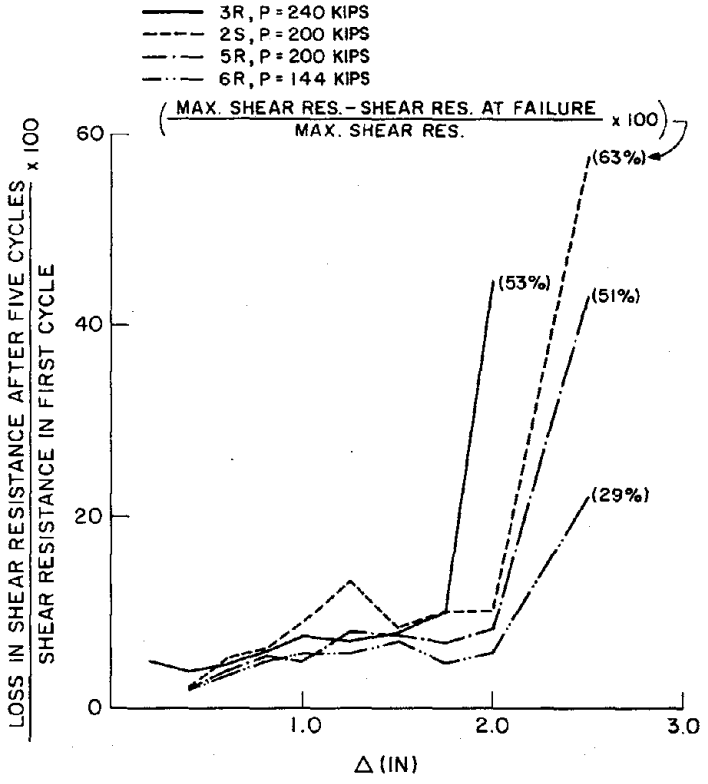

FIG. 3.10 VARIATION OF CYCLIC SHEAR DEGRADATION WITH PEAK DISPLACEMENT LEVEL (1 KIP = 4.448 kN, 1 IN. = 25.4 MM)

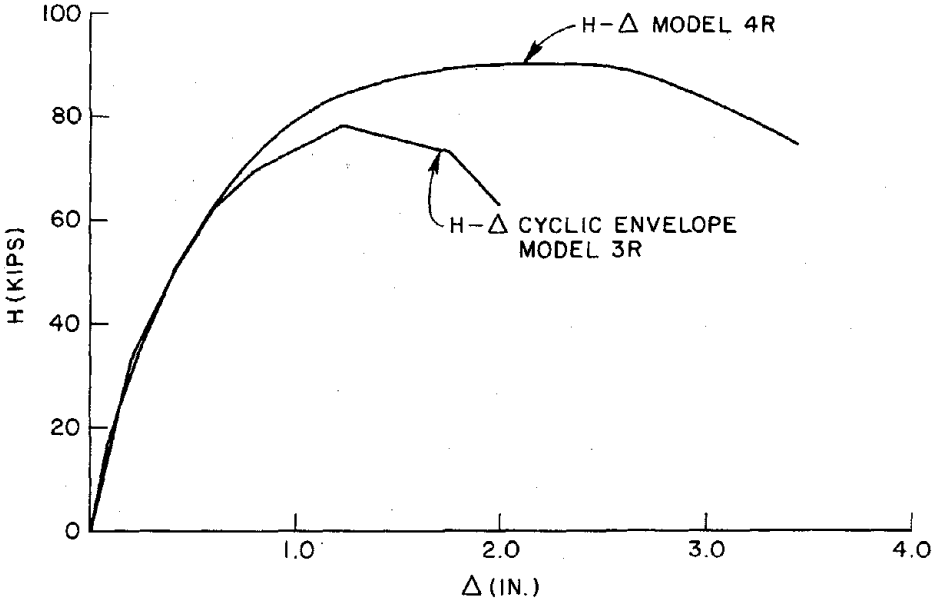

FIG. 3.11 COMPARISON OF SHEAR DISPLACEMENT RELATIONSHIP AND SHEAR DISPLACEMENT CYCLIC ENVELOPE (1 KIP = 4.448 kN, 1 IN. = 25.4 MM)

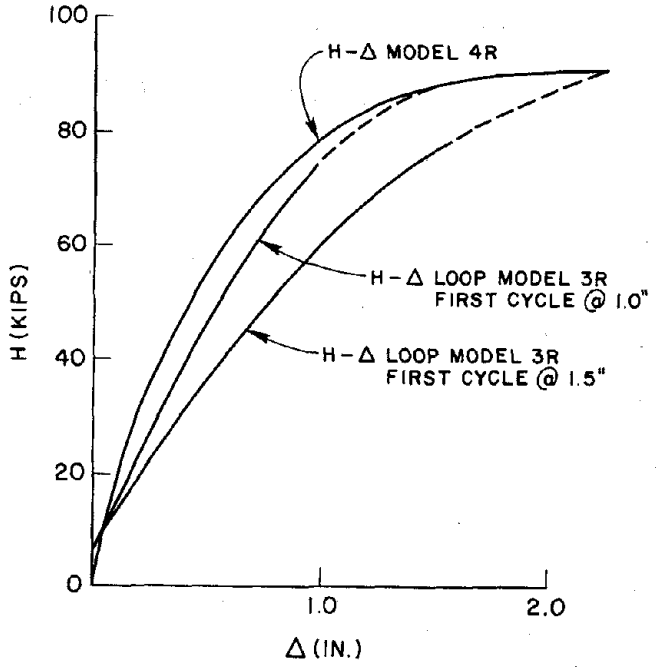

FIG. 3.12 COMPARISON OF MONOTONIC AND CYCLIC SHEAR DISPLACEMENT RELATIONSHIP (1 KIP = 4.448 kN, 1 IN. = 25.4 MM)

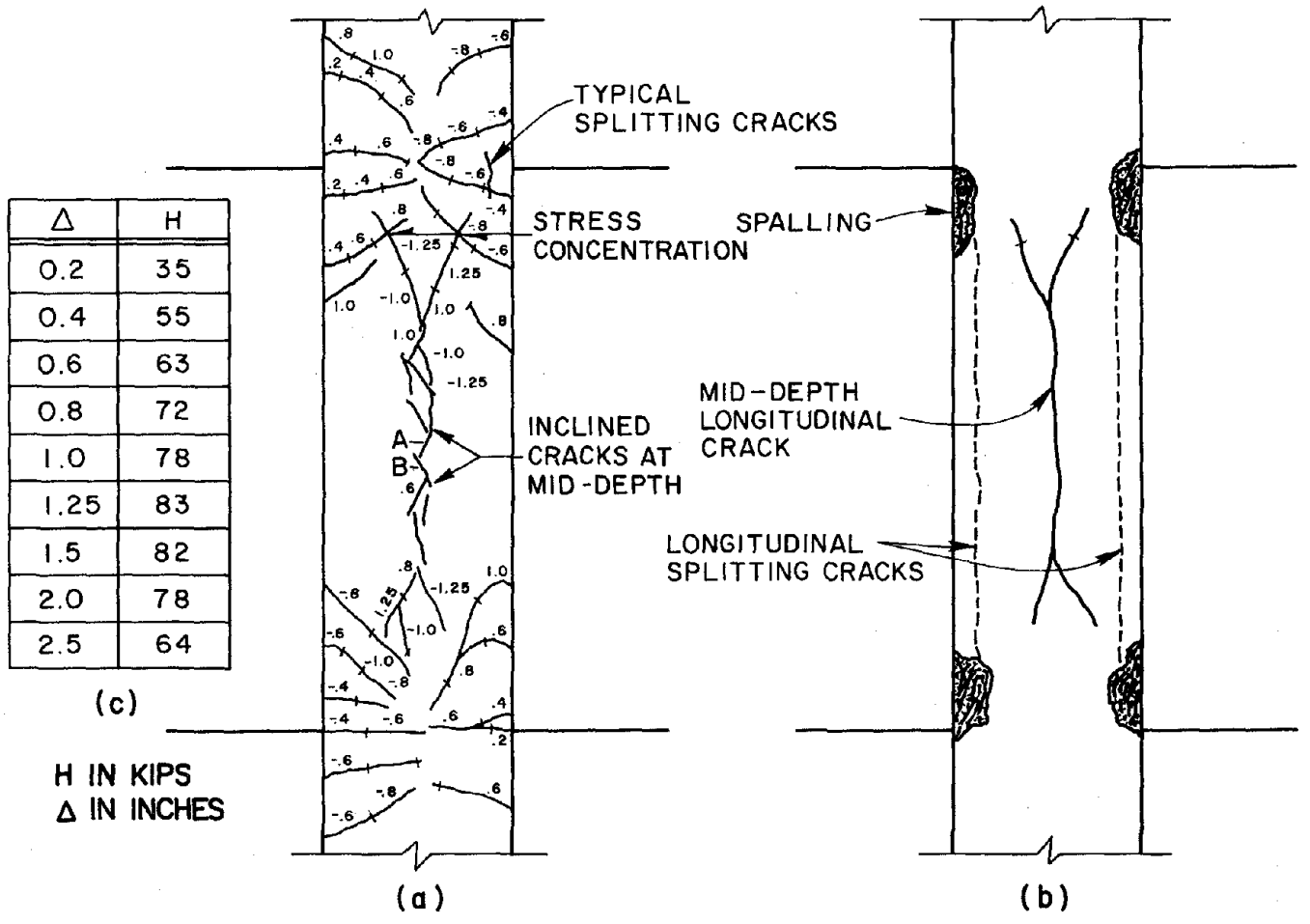

Δ	H
0.2	35
0.4	55
0.6	63
0.8	72
1.0	78
1.25	83
1.5	82
2.0	78
2.5	64

(c)

H IN KIPS
Δ IN INCHES

FIG. 3.13 CRACKING IN MODEL 5R (1 KIP = 4.448 kN, 1 IN. = 25.4 MM)

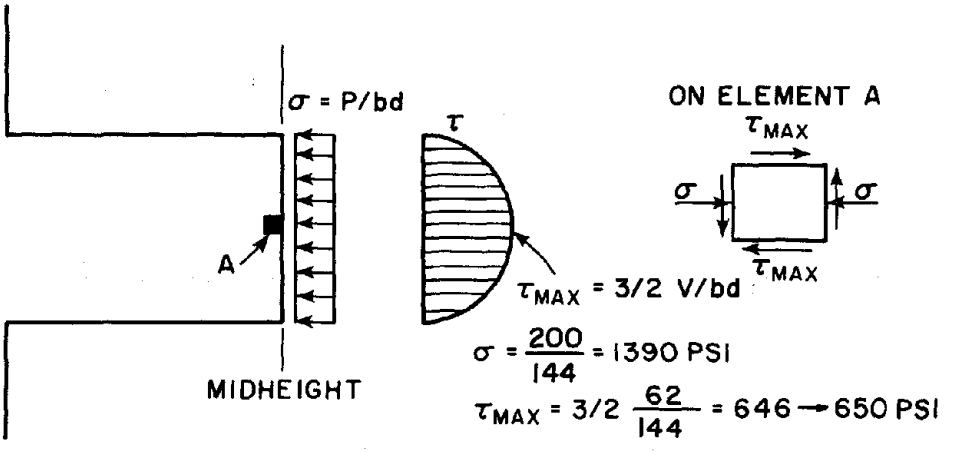

(a) ASSUMED STRESS CONDITION AT MID COLUMN HEIGHT

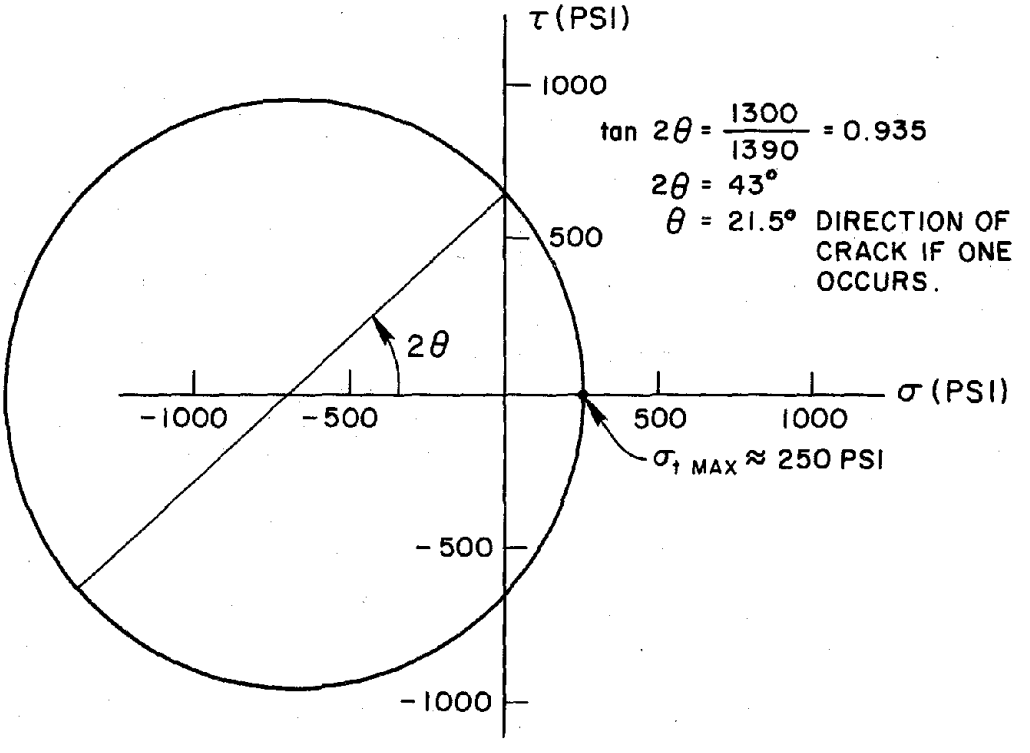

(b) MOHR'S CIRCLE FOR ELEMENTS A

FIG. 3.14 TENSILE STRESSES AT MID-COLUMN HEIGHT
(1 PSI = 6895 Pa)

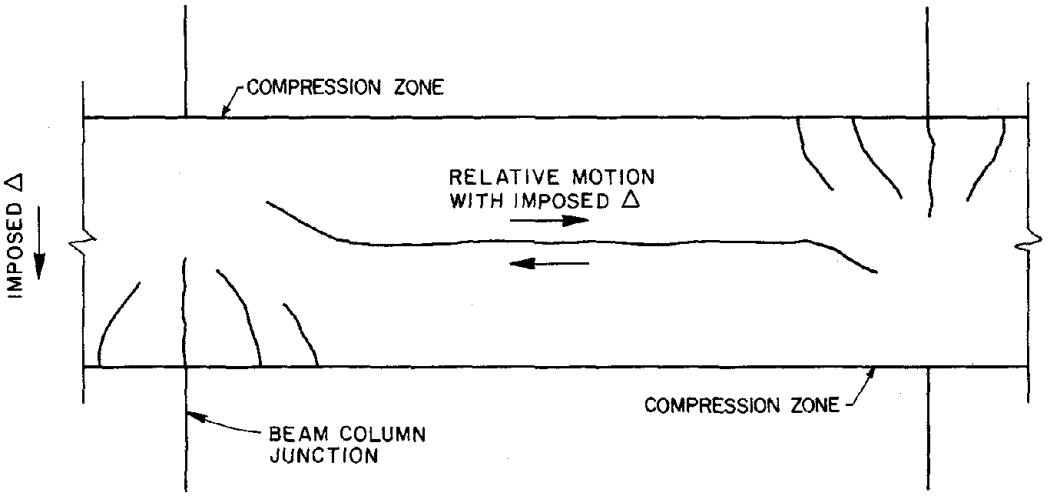

FIG. 3.15 RELATIVE MOTION ALONG MID-DEPTH LONGITUDINAL CRACK

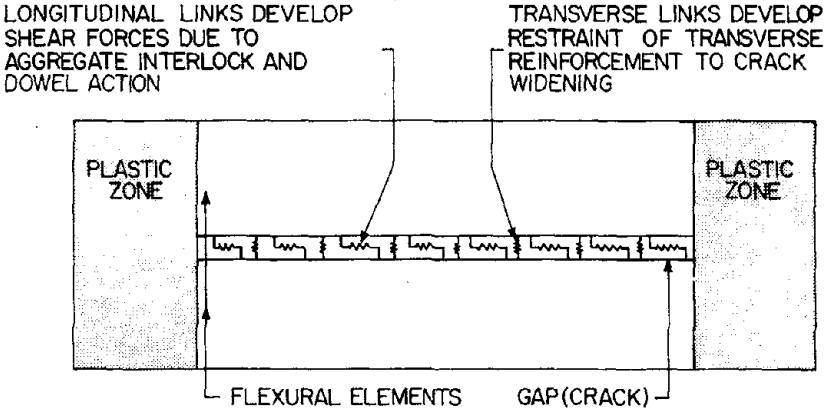

FIG. 3.16 IDEALIZATION OF COLUMN BEHAVIOR
WITH MID-DEPTH LONGITUDINAL CRACK

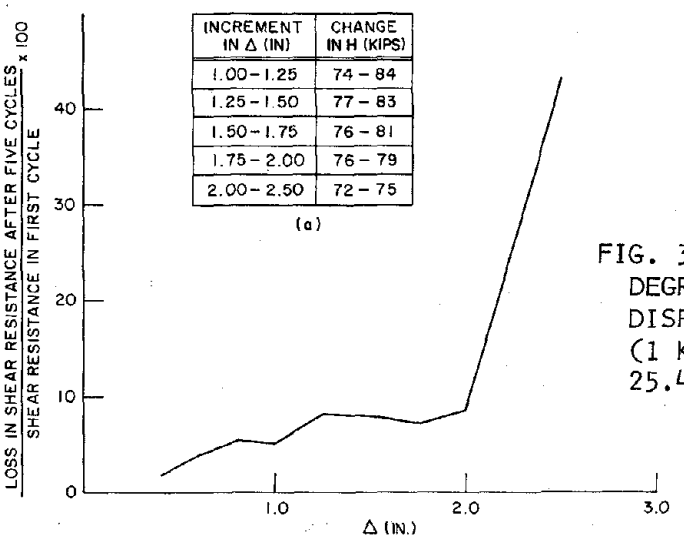

INCREMENT IN Δ (IN)	CHANGE IN H (KIPS)
1.00-1.25	74 - 84
1.25-1.50	77 - 83
1.50-1.75	76 - 81
1.75-2.00	76 - 79
2.00-2.50	72 - 75

(a)

FIG. 3.17 VARIATION OF SHEAR DEGRADATION WITH PEAK DISPLACEMENT LEVEL IN MODEL 5R (1 KIP = 4.448 kN, 1 IN. = 25.4 MM)

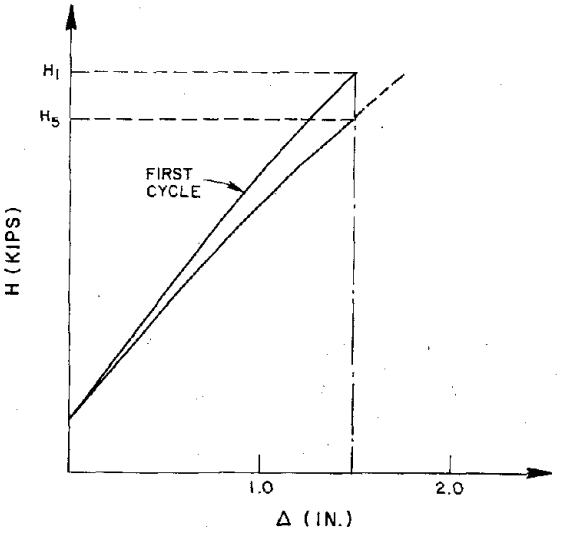

FIG. 3.18 STIFFNESS DEGRADATION BETWEEN FIRST AND FIFTH CYCLE AT 1.5 INCHES IN MODEL 5R (1 KIP = 4.448 kN, 1 IN. = 25.4 MM)

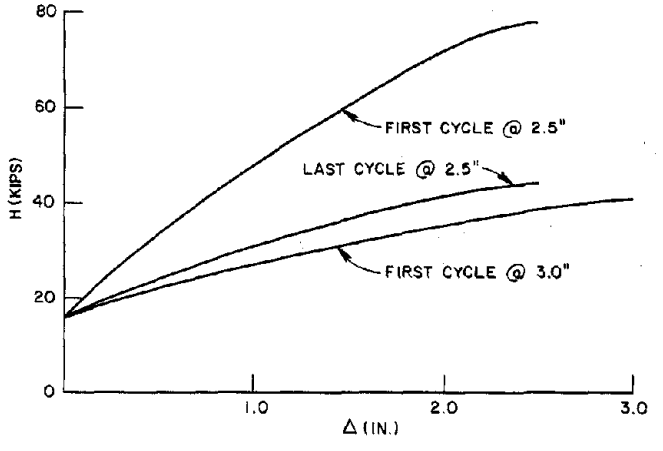

FIG. 3.19 COMPARISON OF SHEAR DISPLACEMENT RELATIONSHIPS AT 2.5 AND 3.0 INCHES FOR MODEL 5R (1 KIP = 4.448 kN, 1 IN. = 25.4 MM)

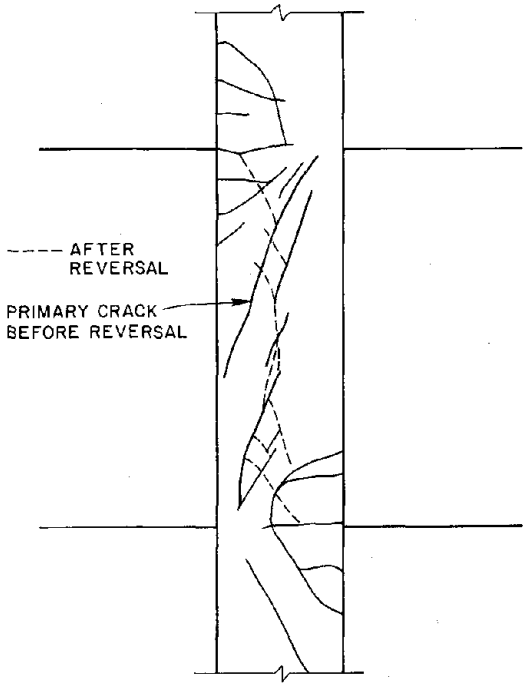

FIG. 3.20 CRACKING IN MODEL 2R

FIG. 3.21 COMPRESSIVE FAILURE AT END OF MID-DEPTH LONGITUDINAL CRACK IN MODEL 3R (1 IN. = 25.4 MM)

FIG. 3.22 COMPRESSIVE FAILURE AT END OF MID-DEPTH LONGITUDINAL CRACK IN MODEL 5R

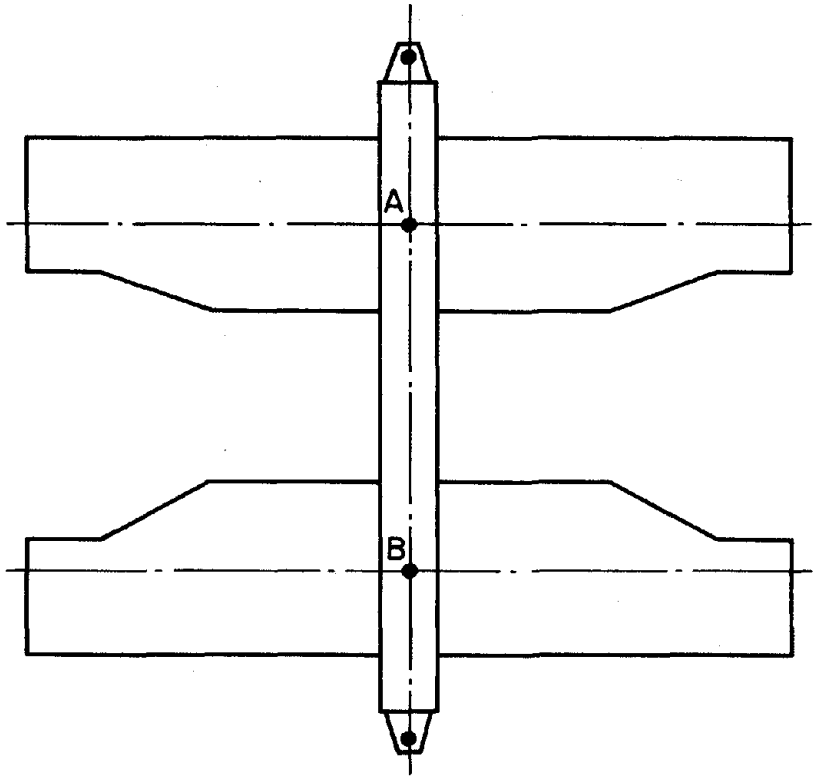

(a) COLUMN SHORTENING MEASURED BETWEEN A & B

MODEL	Δ (IN)	COLUMN SHORTENING	
		BEFORE CYCLING	AFTER CYCLING
3R	1.75	0.13	0.19
	2.0	0.19	0.35
5R	2.0	0.12	0.17
	2.5	0.17	0.37
2S	2.0	0.10	0.13
	2.5	0.13	0.19

(b) COLUMN SHORTENING DATA IN INCHES

FIG. 3.23 CYCLIC CHANGES IN COLUMN SHORTENING (1 IN. = 25.4 MM)

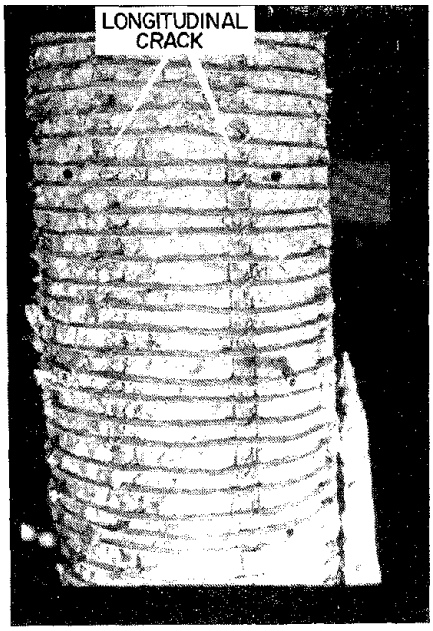

FIG. 3.24 LONGITUDINAL CRACKS ALONG REINFORCEMENT ON EITHER SIDE OF MID-DEPTH IN MODEL 2S

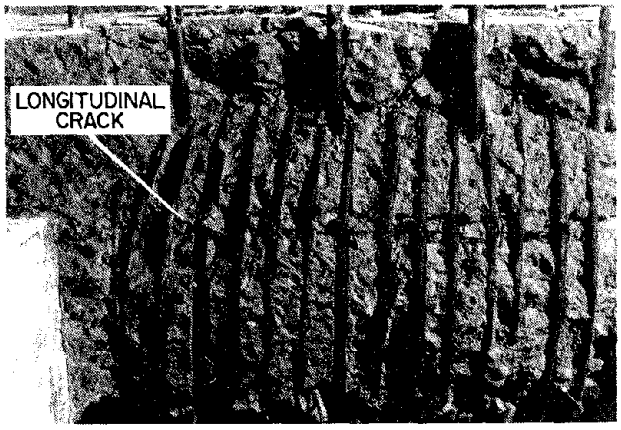

FIG. 3.25 BOND FAILURE IN MODEL 1S

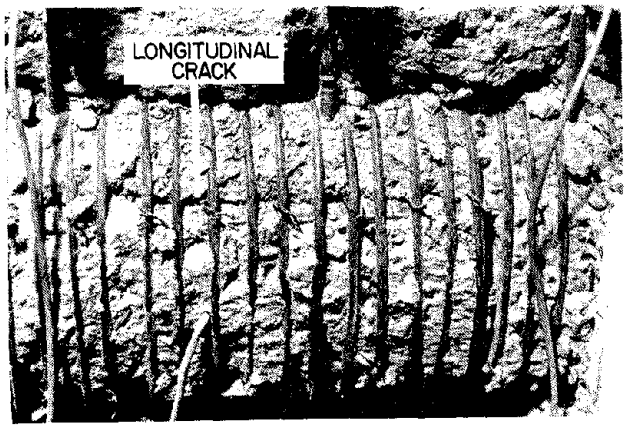

FIG. 3.26 BOND FAILURE IN MODEL 2S

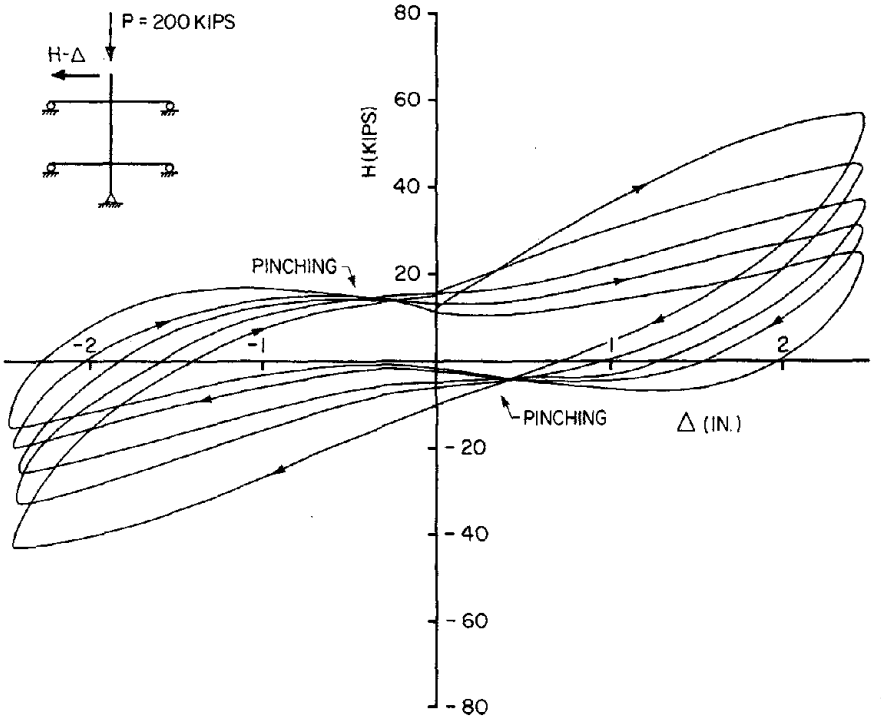

FIG. 3.27 EFFECT OF BOND DETERIORATION ON HYSTERETIC BEHAVIOR IN MODEL 2S (1 KIP = 4.448 kN, 1 IN. = 25.4 MM)

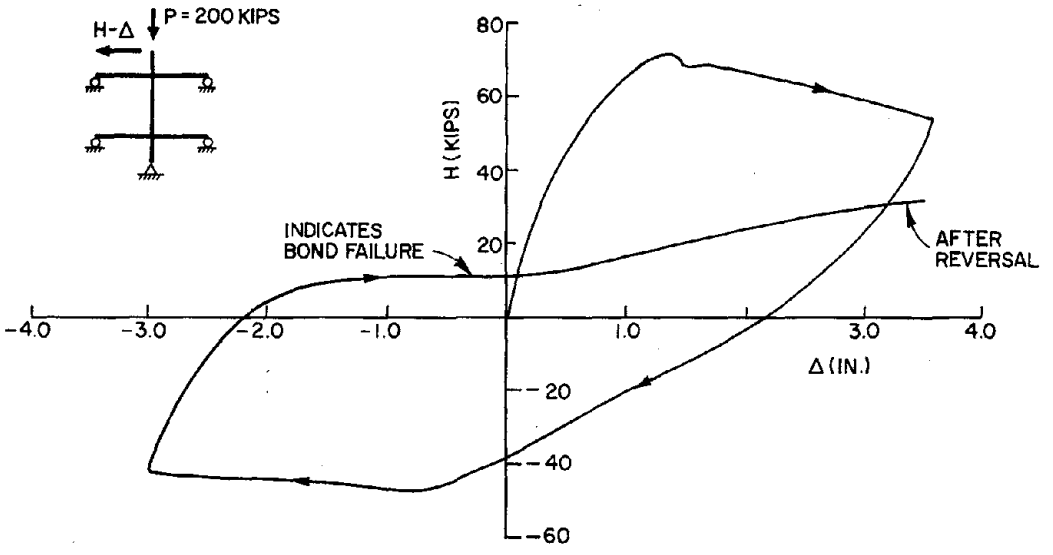

FIG. 3.28 MONOTONIC SHEAR FORCE-TIP DISPLACEMENT RELATIONSHIP MODEL 1S (1 KIP = 4.448 kN, 1 IN. = 25.4 MM)

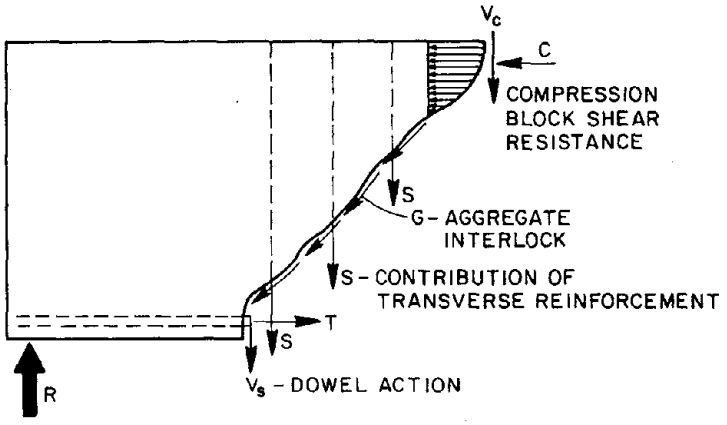

FIG. 3.29 COMPONENTS OF SHEAR RESISTANCE

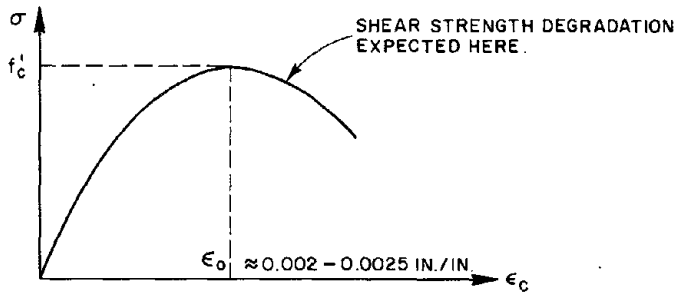

(a) TYPICAL CONCRETE $\sigma - \epsilon$ RELATIONSHIP

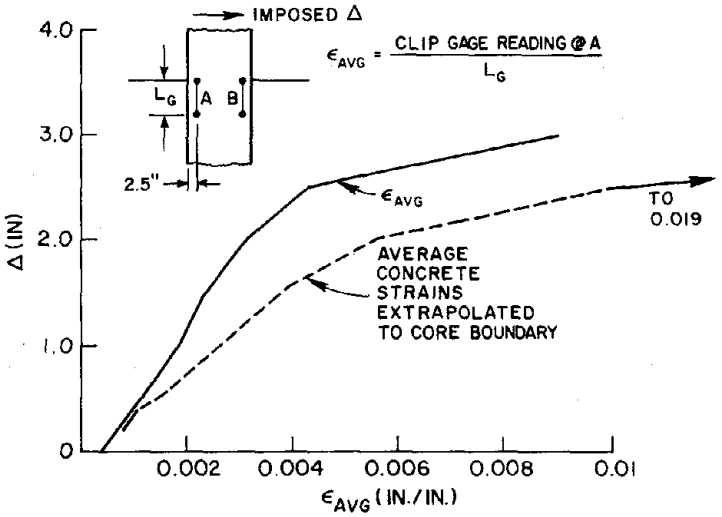

(b) Δ vs. ϵ_{AVG} MODEL 4R

FIG. 3.30 COMPRESSIVE CONCRETE STRAINS IN MODEL 4R (1 IN. = 25.4 MM)

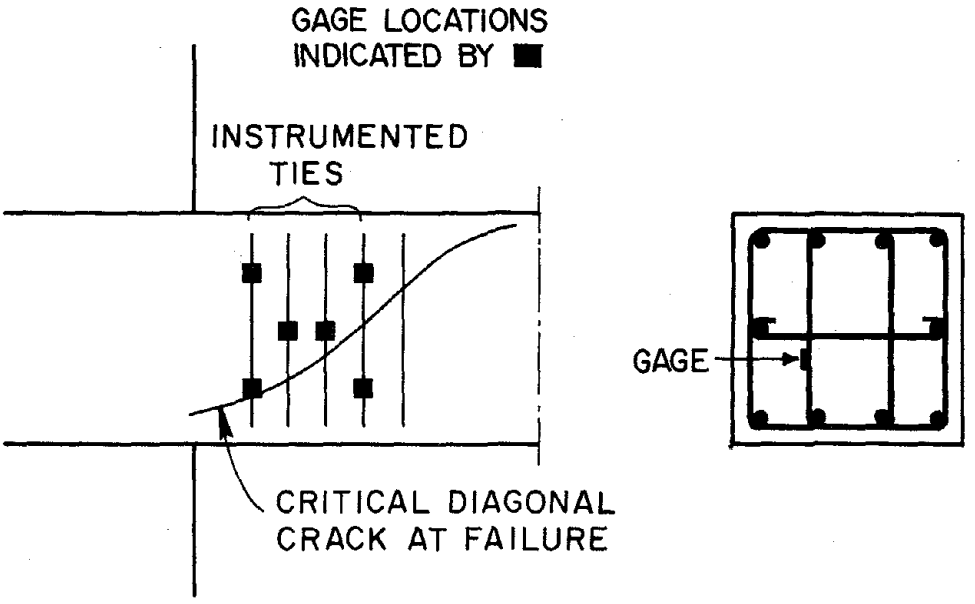

(a) REINFORCEMENT CROSSING CRITICAL CRACK

Δ IN.	H KIPS	V_s KIPS	V_{cgd} $(H-V_s)$
0.6	63	3.0	60.0
1.0	80	12.5	67.5
1.5	88	25.0	63.0
2.0	89	31.0	58.0
2.5	89	37.0	52.0
3.0	82	35.0	47.0

(b) SUMMARY OF TRANSVERSE REINFORCEMENT SHEAR CONTRIBUTION

FIG. 3.31 COMPONENTS OF COLUMN SHEAR RESISTANCE IN MODEL 4R
(1 KIP = 4.448 kN, 1 IN. = 25.4 MM)

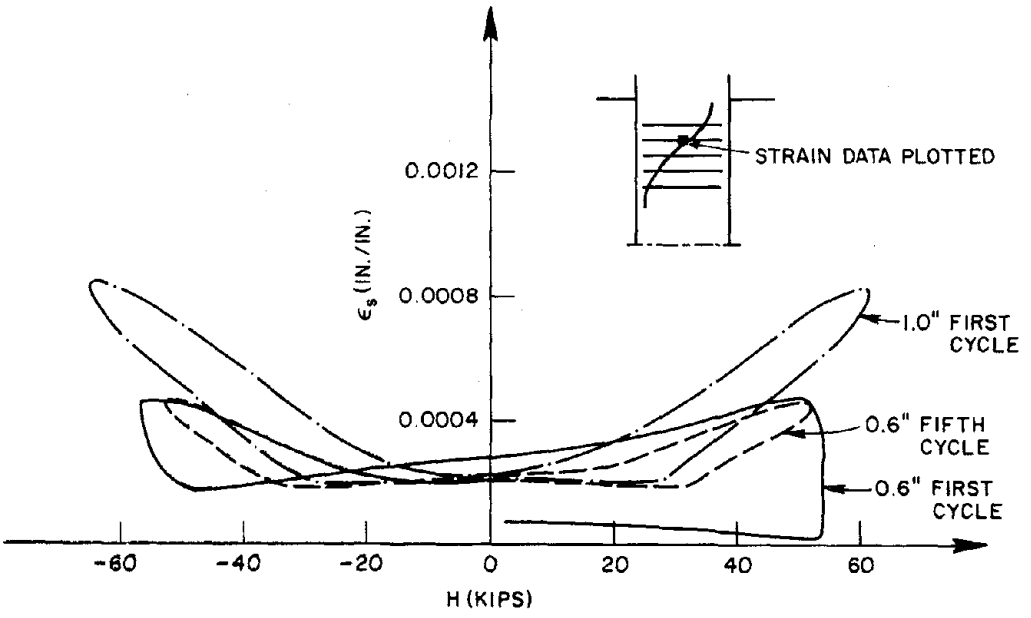

FIG. 3.32 CYCLIC VARIATION OF TRANSVERSE STEEL STRAINS AT 0.6 AND 1.0 INCHES IN MODEL 6R (1 KIP = 4.448 kN, 1 IN. = 25.4 MM)

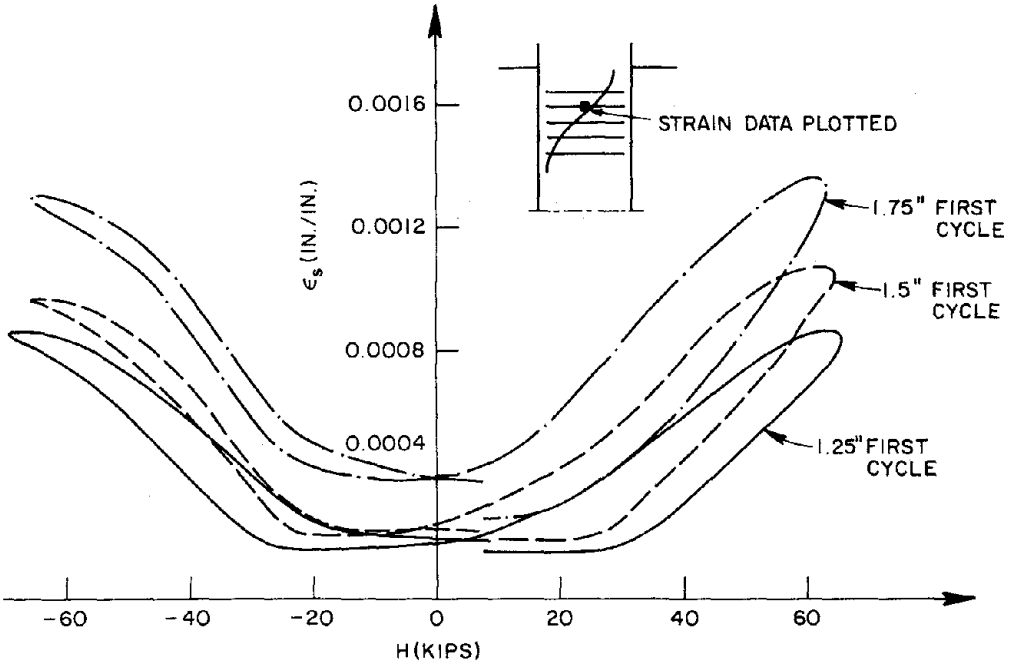

FIG. 3.33 CYCLIC VARIATION OF TRANSVERSE STEEL STRAINS AT 1.25, 1.5 AND 1.75 INCHES IN MODEL 6R (1 KIP = 4.448 kN, 1 IN. = 25.4 MM)

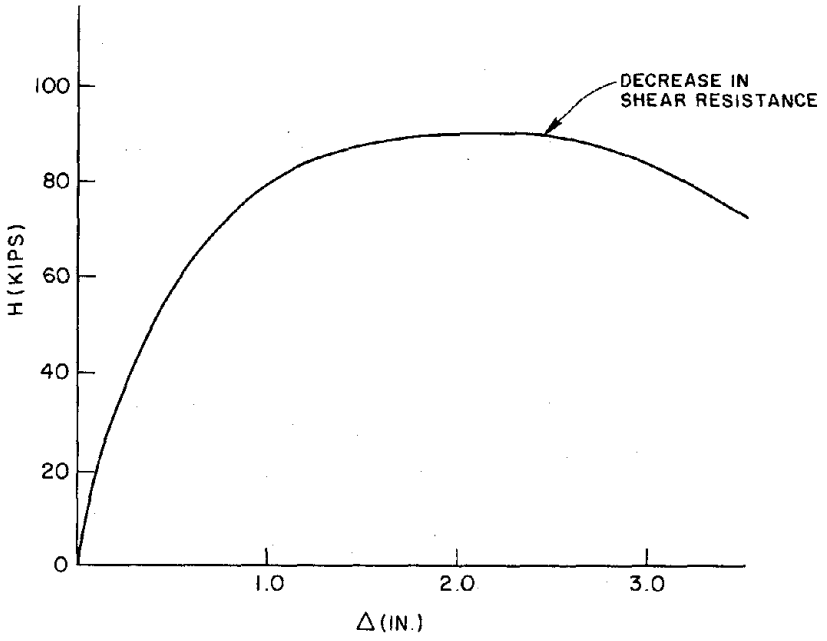

FIG. 3.34 SHEAR FORCE-TIP DISPLACEMENT RELATIONSHIP IN MODEL 4R (1 KIP = 4.448 kN, 1 IN. = 25.4 MM)

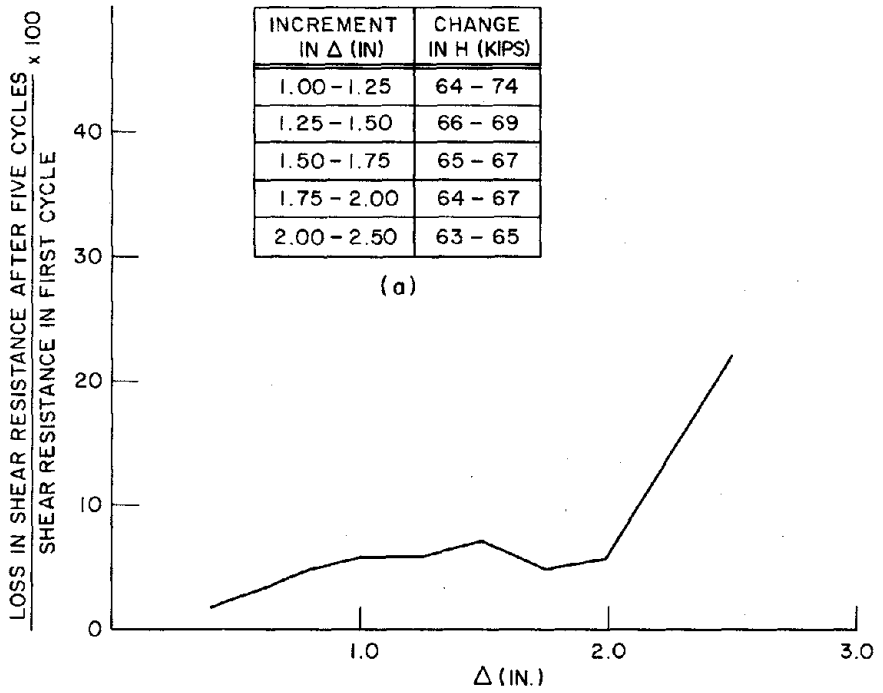

INCREMENT IN Δ (IN)	CHANGE IN H (KIPS)
1.00 - 1.25	64 - 74
1.25 - 1.50	66 - 69
1.50 - 1.75	65 - 67
1.75 - 2.00	64 - 67
2.00 - 2.50	63 - 65

(a)

FIG. 3.35 VARIATION OF SHEAR DEGRADATION WITH PEAK DISPLACEMENT LEVEL IN MODEL 6R (1 KIP = 4.448 kN, 1 IN. = 25.4 MM)

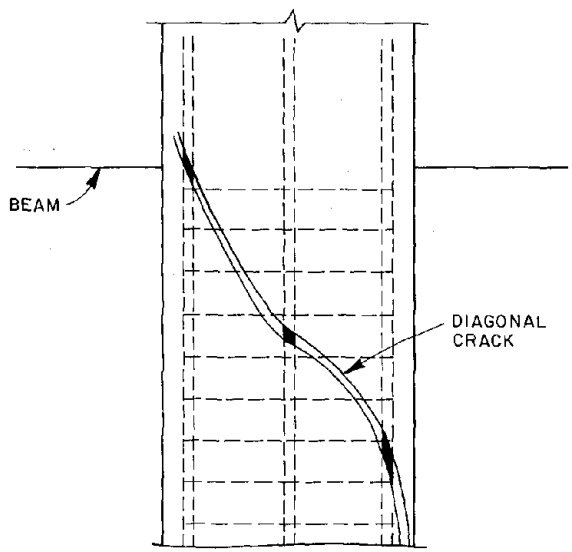

FIG. 3.36 FINAL PROPAGATION OF DIAGONAL TENSION CRACK IN MODEL 4R

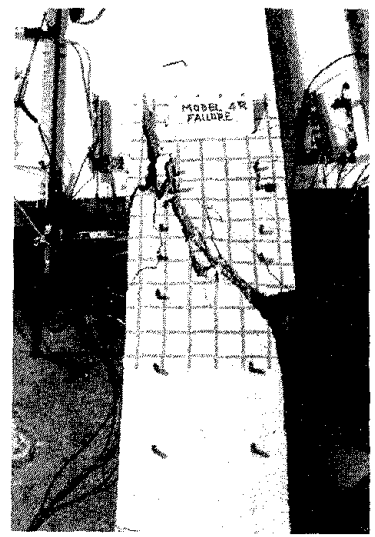

a) AT FAILURE

b) AFTER REAPPLICATION OF AXIAL LOAD

FIG. 3.37 CRITICAL INCLINED CRACK IN FALIURE OF MODEL 4R

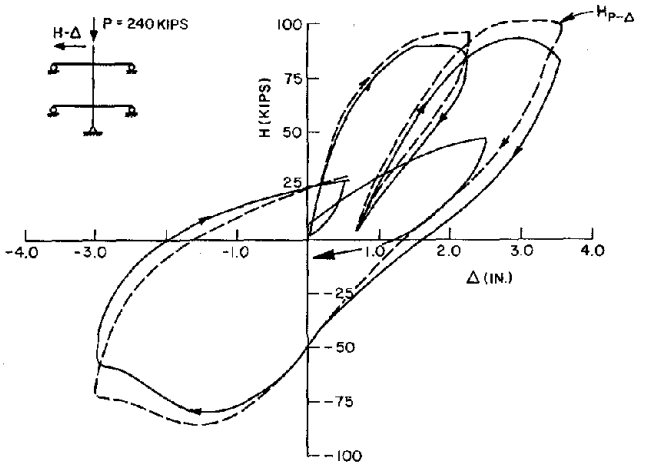

FIG. 3.38 SHEAR FORCE-TIP DISPLACEMENT RELATIONSHIP FOR MODEL 2R (1 KIP = 4.448 kN, 1 IN. = 25.4 MM)

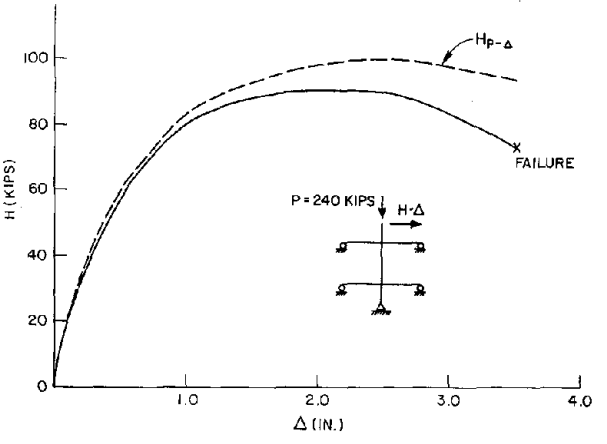

FIG. 3.39 SHEAR FORCE-TIP DISPLACEMENT RELATIONSHIP FOR MODEL 4R (1 KIP = 4.448 kN, 1 IN. = 25.4 MM)

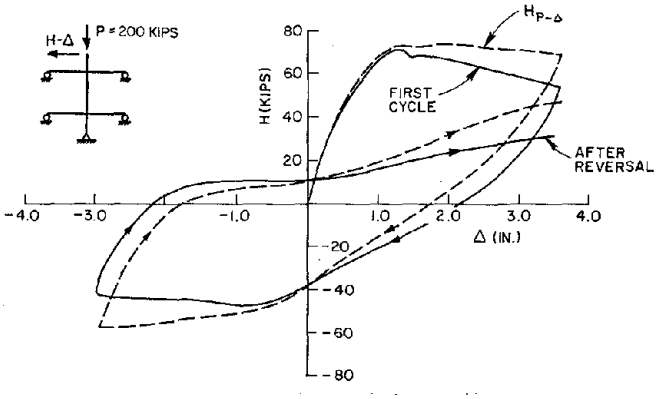

FIG. 3.40 SHEAR FORCE-TIP DISPLACEMENT RELATIONSHIP FOR MODEL 1S (1 KIP = 4.448 kN, 1 IN. = 25.4 MM)

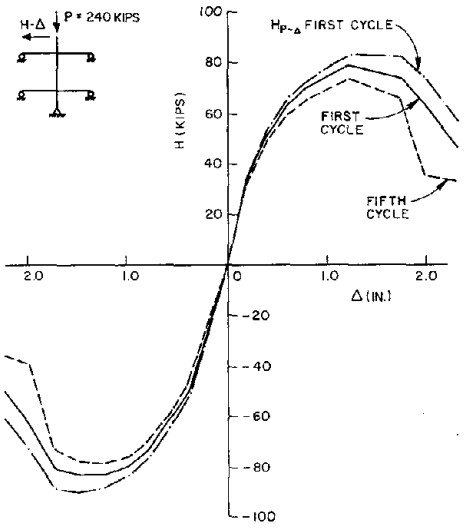

FIG. 3.41 SHEAR FORCE-TIP DISPLACEMENT CYCLIC ENVELOPES FOR MODEL 3R (1 KIP = 4.448 kN, 1 IN. = 25.4 MM)

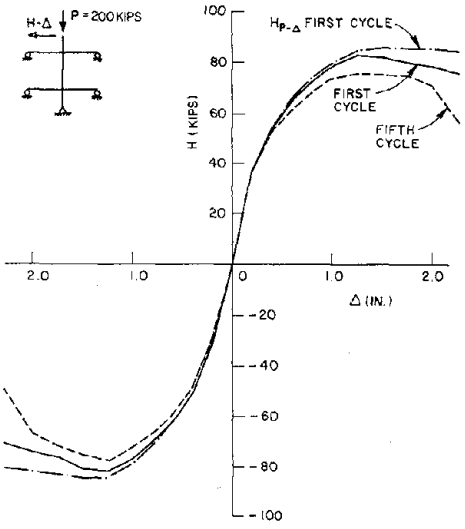

FIG. 3.42 SHEAR FORCE-TIP DISPLACEMENT CYCLIC ENVELOPES FOR MODEL 5R (1 KIP = 4.448 kN, 1 IN. = 25.4 MM)

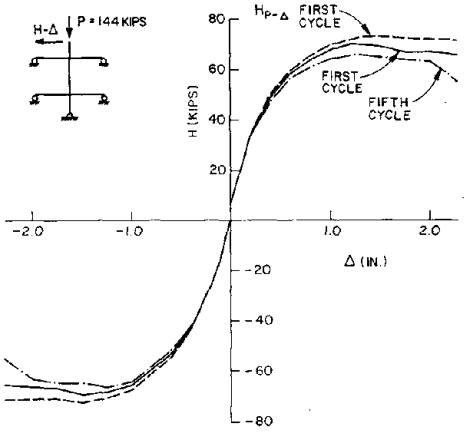

FIG. 3.43 SHEAR FORCE-TIP DISPLACEMENT CYCLIC ENVELOPES FOR MODEL 6R (1 KIP = 4.448 kN, 1 IN. = 25.4 MM)

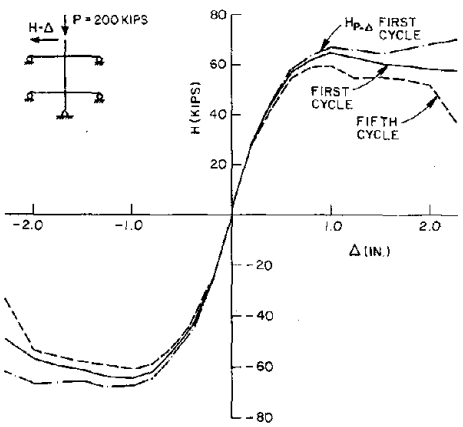

FIG. 3.44 SHEAR FORCE-TIP DISPLACEMENT CYCLIC ENVELOPES FOR MODEL 2S (1 KIP = 4.448 kN, 1 IN. = 25.4 MM)

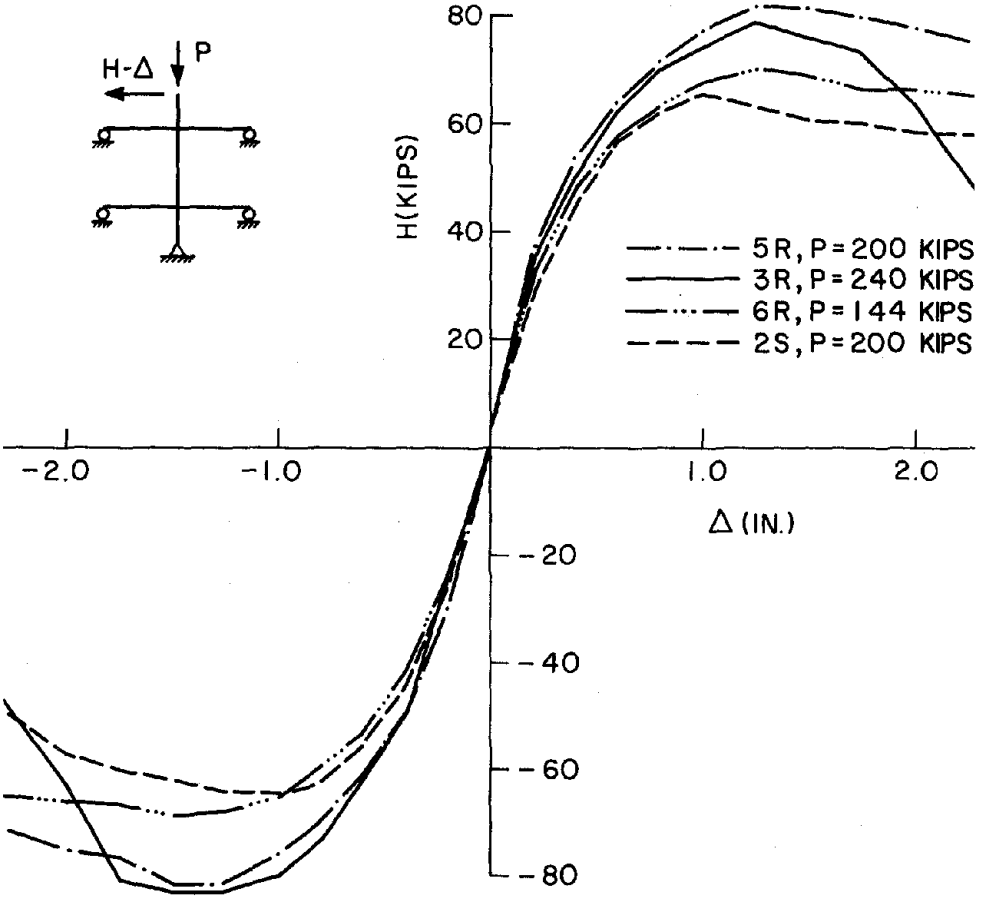

FIG. 3.45 COMPARISON OF FIRST CYCLE SHEAR FORCE-TIP DISPLACEMENT CYCLIC ENVELOPES (1 KIP = 4.448 kN, 1 IN. = 25.4 MM)

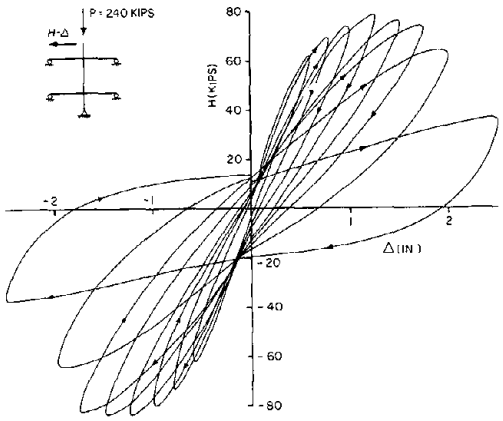

FIG. 3.46 FIRST CYCLE SHEAR FORCE-TIP DISPLACEMENT HYSTERETIC LOOPS FOR MODEL 3R (1 KIP = 4.448 kN, 1 IN. = 25.4 MM)

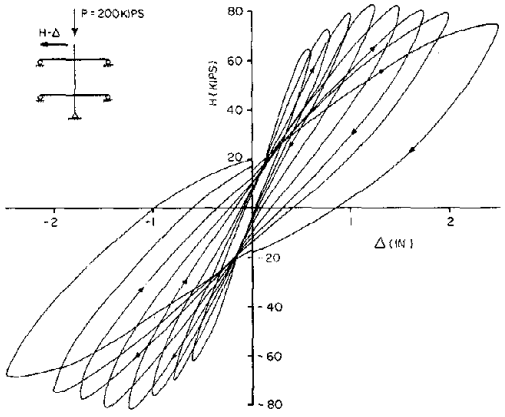

FIG. 3.47 FIRST CYCLE SHEAR FORCE-TIP DISPLACEMENT HYSTERETIC LOOPS FOR MODEL 5R (1 KIP = 4.448 kN, 1 IN. = 25.4 MM)

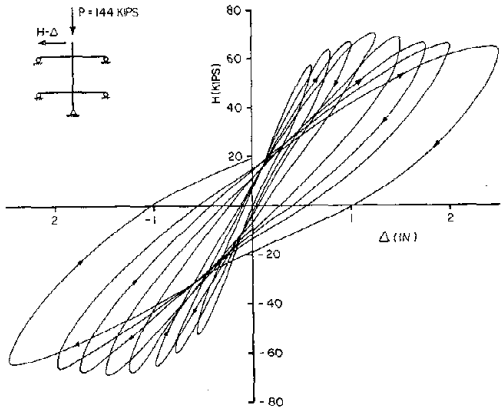

FIG. 3.48 FIRST CYCLE SHEAR FORCE-TIP DISPLACEMENT HYSTERETIC LOOPS FOR MODEL 6R (1 KIP = 4.448 kN, 1 IN. = 25.4 MM)

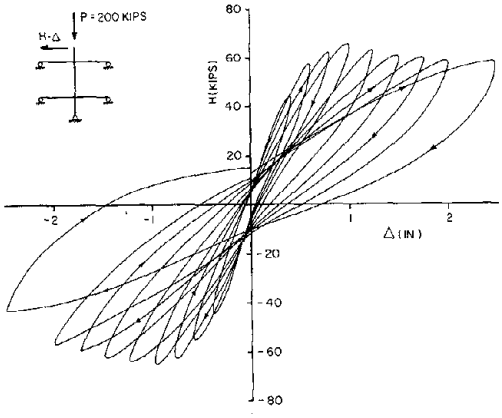

FIG. 3.49 FIRST CYCLE SHEAR FORCE-TIP DISPLACEMENT HYSTERETIC LOOPS FOR MODEL 2S (1 KIP = 4.448 kN, 1 IN. = 25.4 MM)

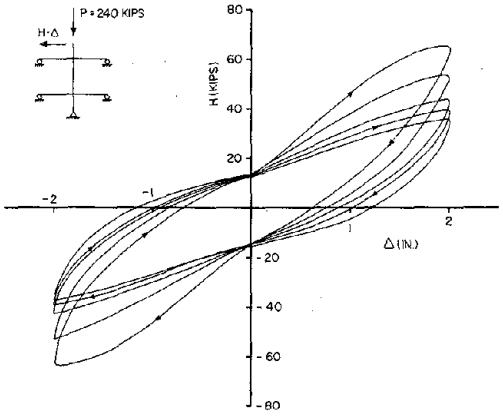

FIG. 3.50 SHEAR FORCE-TIP DISPLACEMENT HYSTERETIC LOOPS AT 2.0 INCHES FOR MODEL 3R (1 KIP = 4.448 kN, 1 IN. = 25.4 MM)

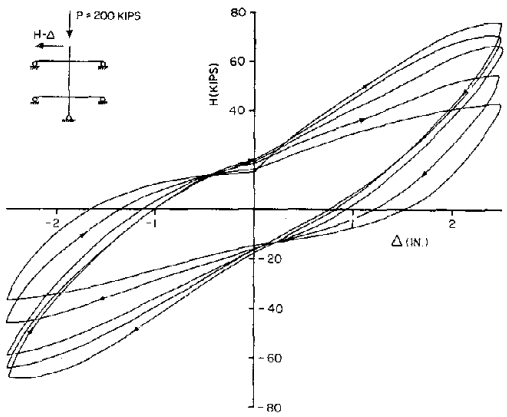

FIG. 3.51 SHEAR FORCE-TIP DISPLACEMENT HYSTERETIC LOOPS AT 2.5 INCHES FOR MODEL 5R (1 KIP = 4.448 kN, 1 IN. = 25.4 MM)

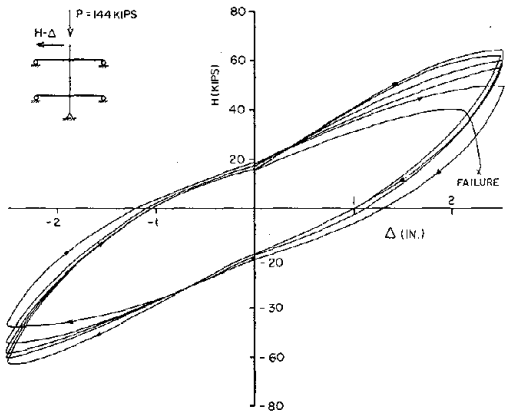

FIG. 3.52 SHEAR FORCE-TIP DISPLACEMENT HYSTERETIC LOOPS AT 2.5 INCHES FOR MODEL 6R (1 KIP = 4.448 kN, 1 IN. = 25.4 MM)

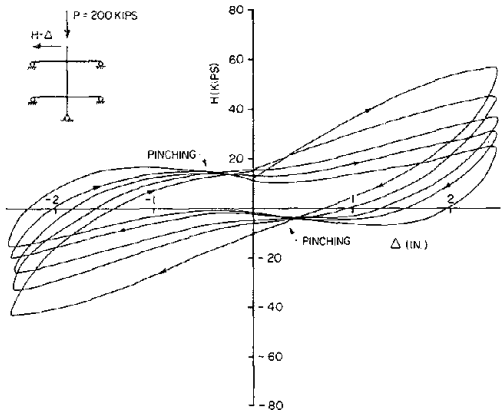

FIG. 3.53 SHEAR FORCE-TIP DISPLACEMENT HYSTERETIC LOOPS AT 2.5 INCHES FOR MODEL 2S (1 KIP = 4.448 kN, 1 IN. = 25.4 MM)

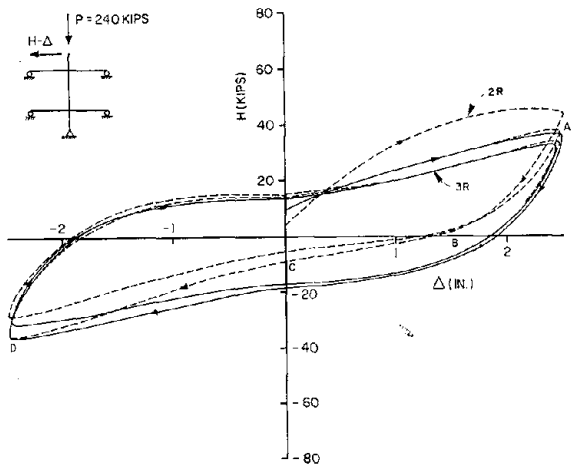

FIG. 3.54 COMPARISON OF SHEAR FORCE-TIP DISPLACEMENT HYSTERETIC LOOPS AT 2.5 INCHES FOR MODELS 2R AND 3R (1 KIP = 4.448 kN, 1 IN. = 25.4 MM)

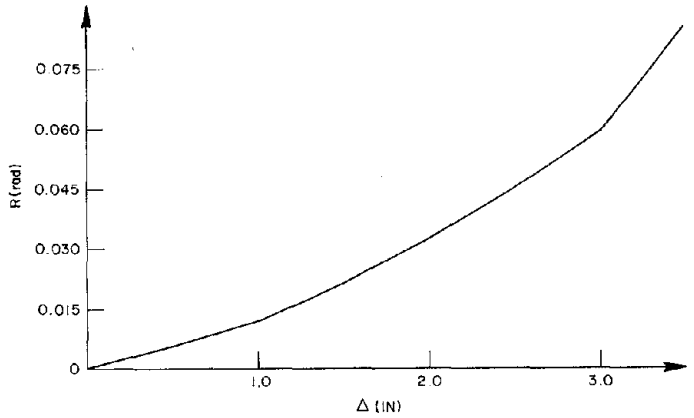

FIG. 3.55 STORY ROTATION-TIP DISPLACEMENT RELATIONSHIP FOR MODEL 4R (1 IN. = 25.4 MM)

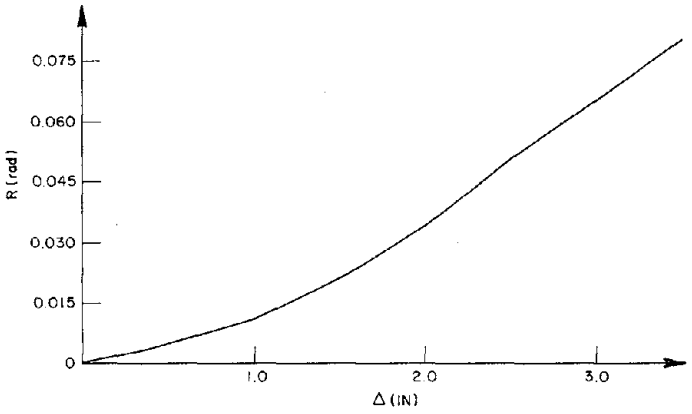

FIG. 3.56 STORY ROTATION-TIP DISPLACEMENT RELATIONSHIP FOR MODEL 1S (1 IN. = 25.4 MM)

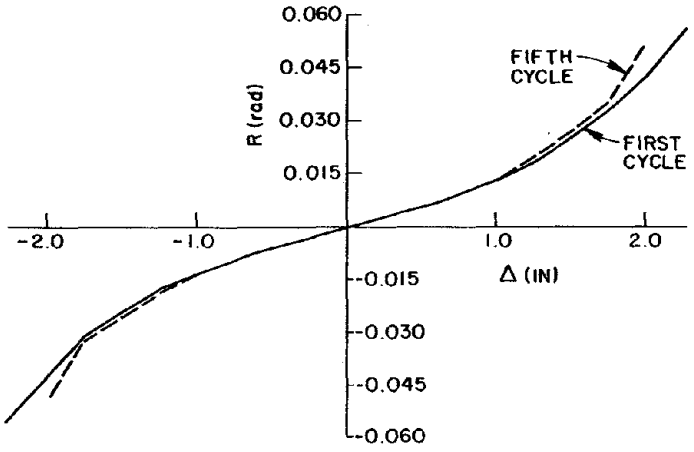

FIG. 3.57 STORY ROTATION-TIP DISPLACEMENT CYCLIC ENVELOPES FOR MODEL 3R (1 IN. = 25.4 MM)

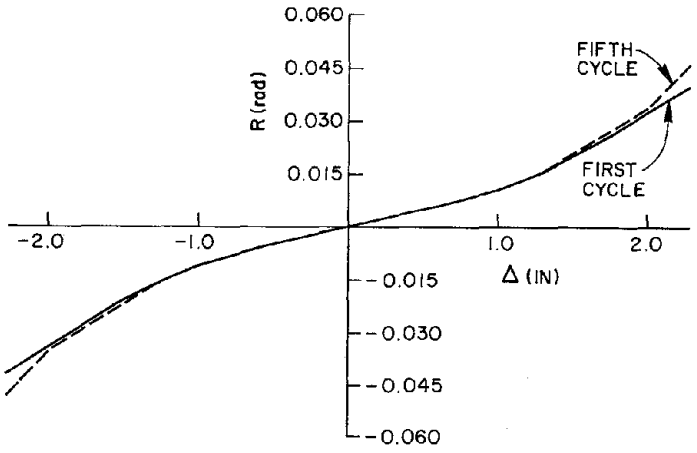

FIG. 3.58 STORY ROTATION-TIP DISPLACEMENT CYCLIC ENVELOPES FOR MODEL 5R (1 IN. = 25.4 MM)

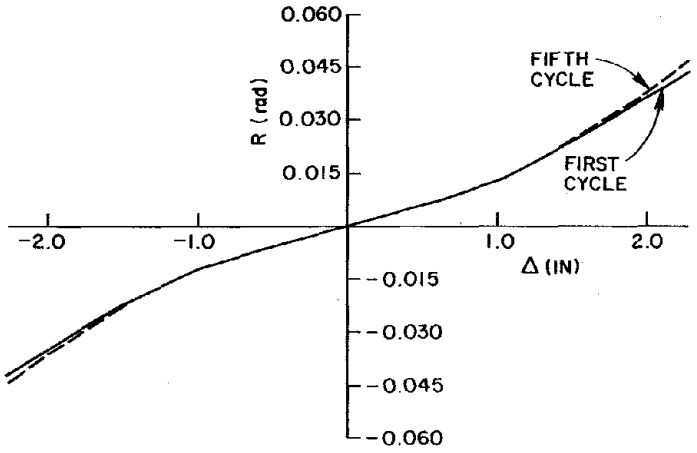

FIG. 3.59 STORY ROTATION-TIP DISPLACEMENT CYCLIC ENVELOPES FOR MODEL 6R (1 IN. = 25.4 MM)

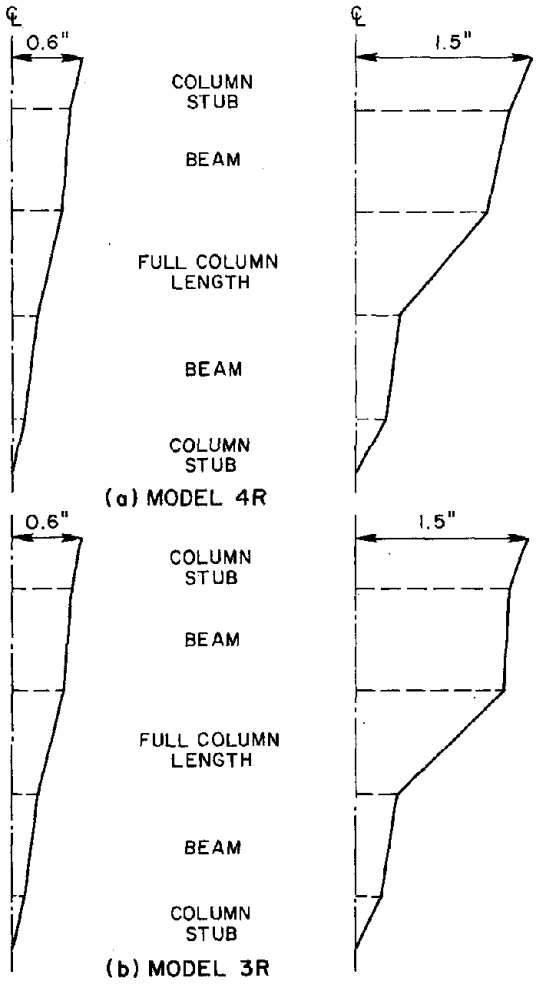

FIG. 3.60 MEASURED DEFLECTED SHAPES (1 IN. = 25.4 MM)

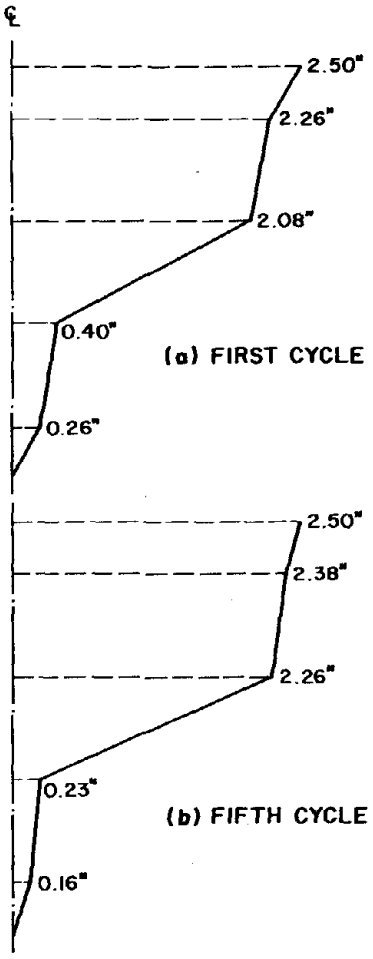

FIG. 3.61 MEASURED DEFLECTED SHAPES AT 2.5 INCHES MODEL 5R (1 IN. = 25.4 MM)

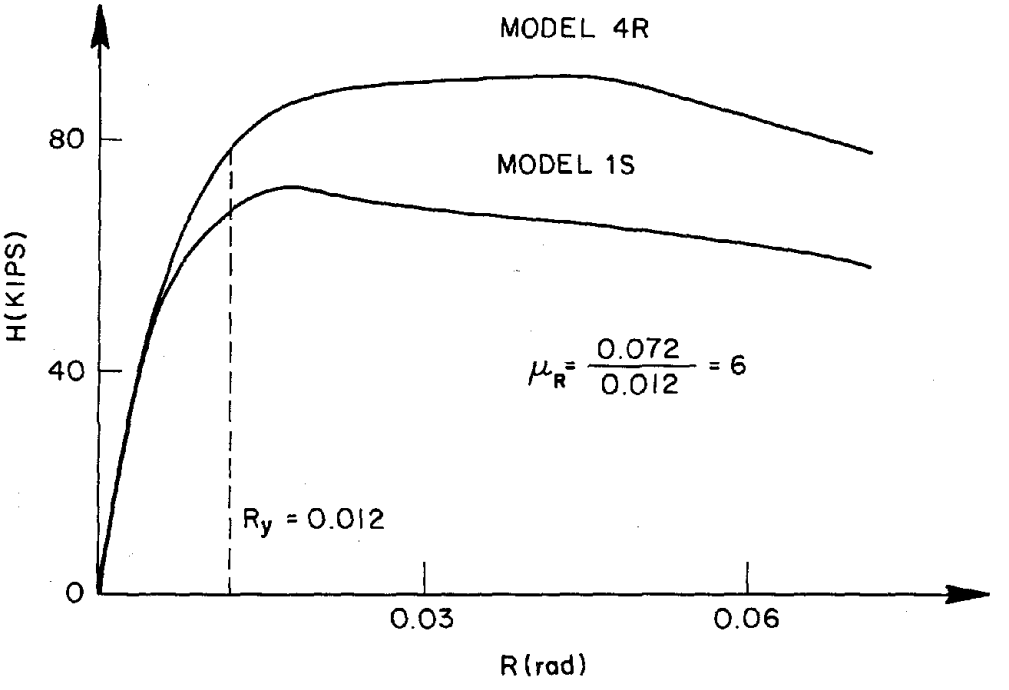

FIG. 3.62 MONOTONIC SHEAR STORY ROTATION RELATIONSHIPS
(1 KIP = 4.448 kN)

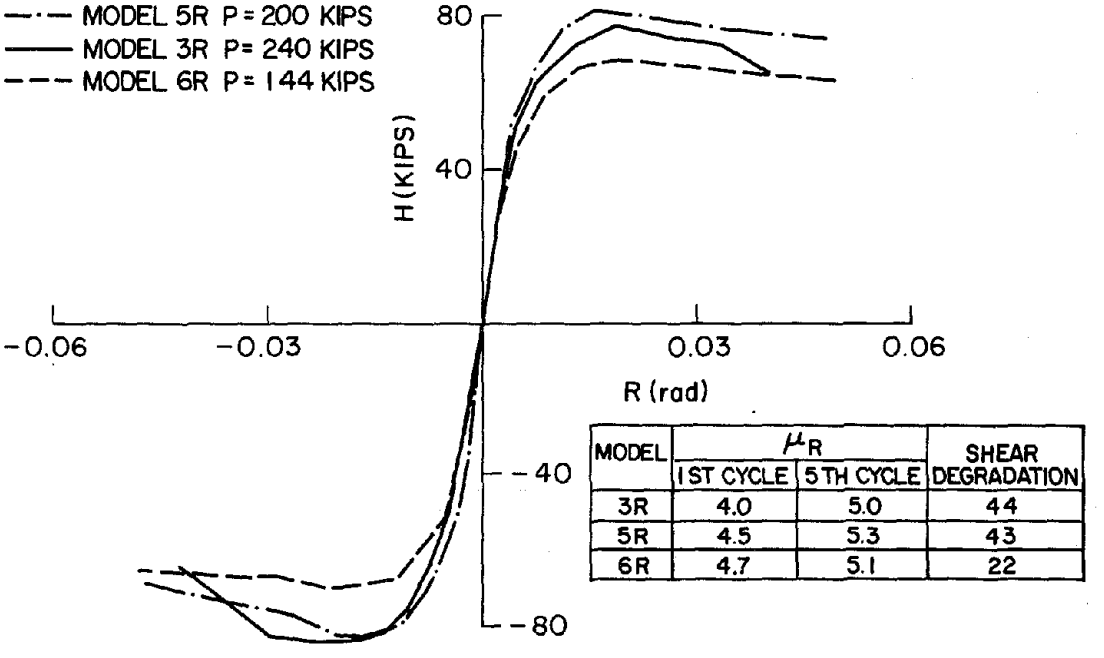

MODEL	μ_R		SHEAR DEGRADATION
	1ST CYCLE	5TH CYCLE	
3R	4.0	5.0	44
5R	4.5	5.3	43
6R	4.7	5.1	22

FIG. 3.63 SHEAR STORY ROTATION CYCLIC ENVELOPES
(1 KIP = 4.448 kN)

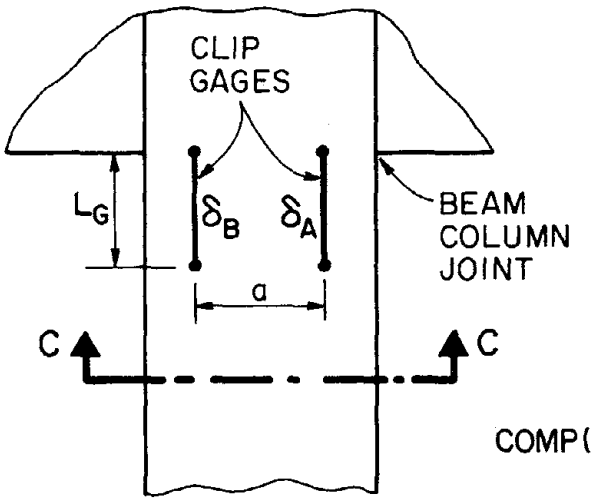

$$\theta_{AVG.} = \frac{\delta_A - \delta_B}{a}$$

$$\phi_{AVG.} = \frac{\theta_{AVG.}}{L_G}$$

$$\epsilon_{AVG.} = \frac{COMP(\delta_A, \delta_B)}{L_G}$$

$COMP(\delta_A, \delta_B)$ = COMPRESSION DATA READING

(a) CALCULATION FOR AVERAGE CURVATURE

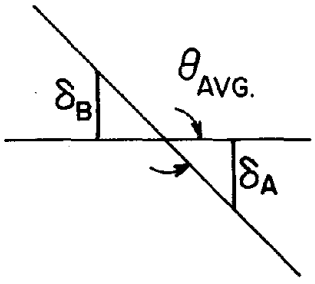

$$\epsilon_{CORE} = \frac{\theta_{AVG.} * a_c - TEN(\delta_A, \delta_B)}{L_G}$$

$TEN(\delta_A, \delta_B)$ = TENSION DATA READING

(b) LINEAR STRAIN DISTRIBUTION

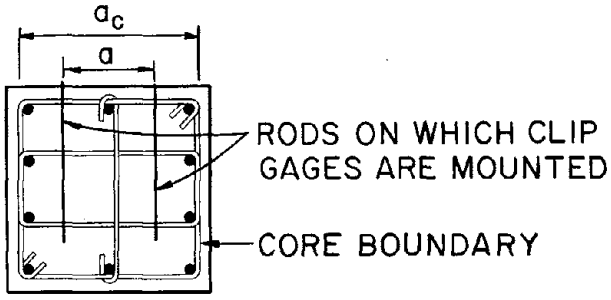

(c) CROSS SECTION C-C

FIG. 3.64 DEFINITION OF CURVATURE AND COMPRESSIVE STRAIN DATA

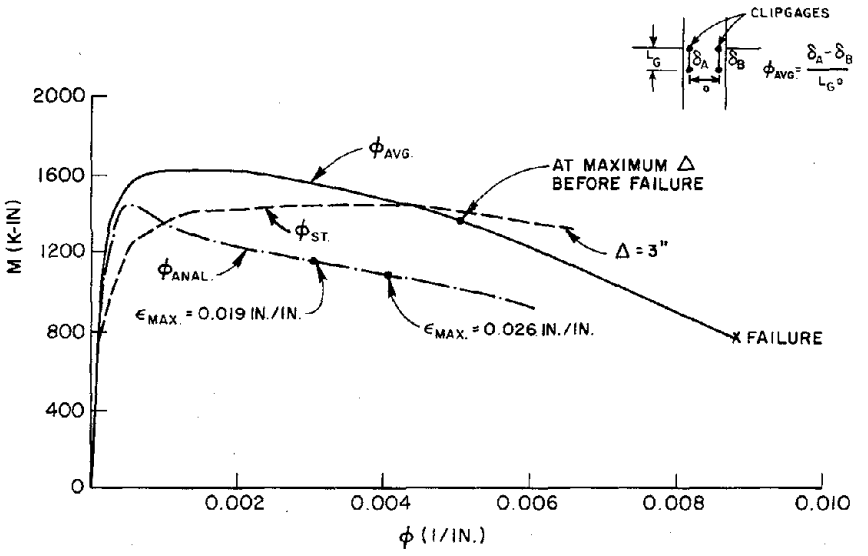

FIG. 3.65 MOMENT CURVATURE RELATIONSHIPS FOR MODEL 4R
(1 K-IN. = 0.113 kN•M, 1 IN. = 25.4 MM)

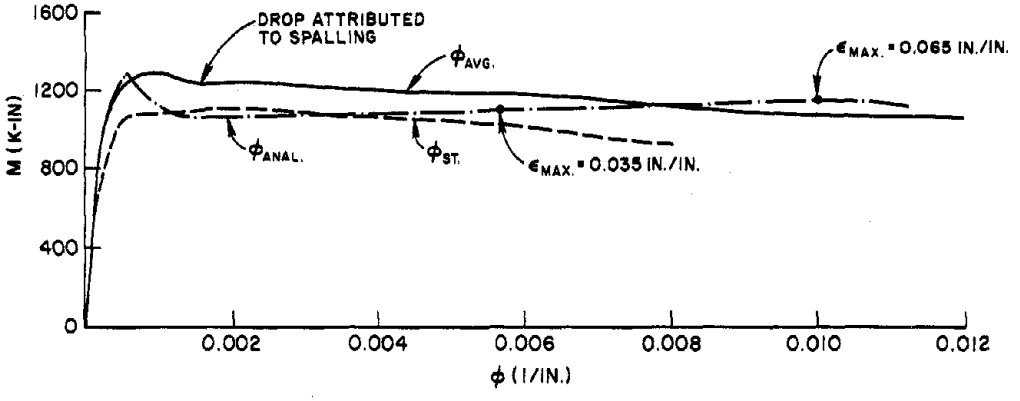

FIG. 3.66 MOMENT CURVATURE RELATIONSHIPS FOR MODEL 1S
(1 K-IN. = 0.113 kN•M, 1 IN. = 25.4 MM)

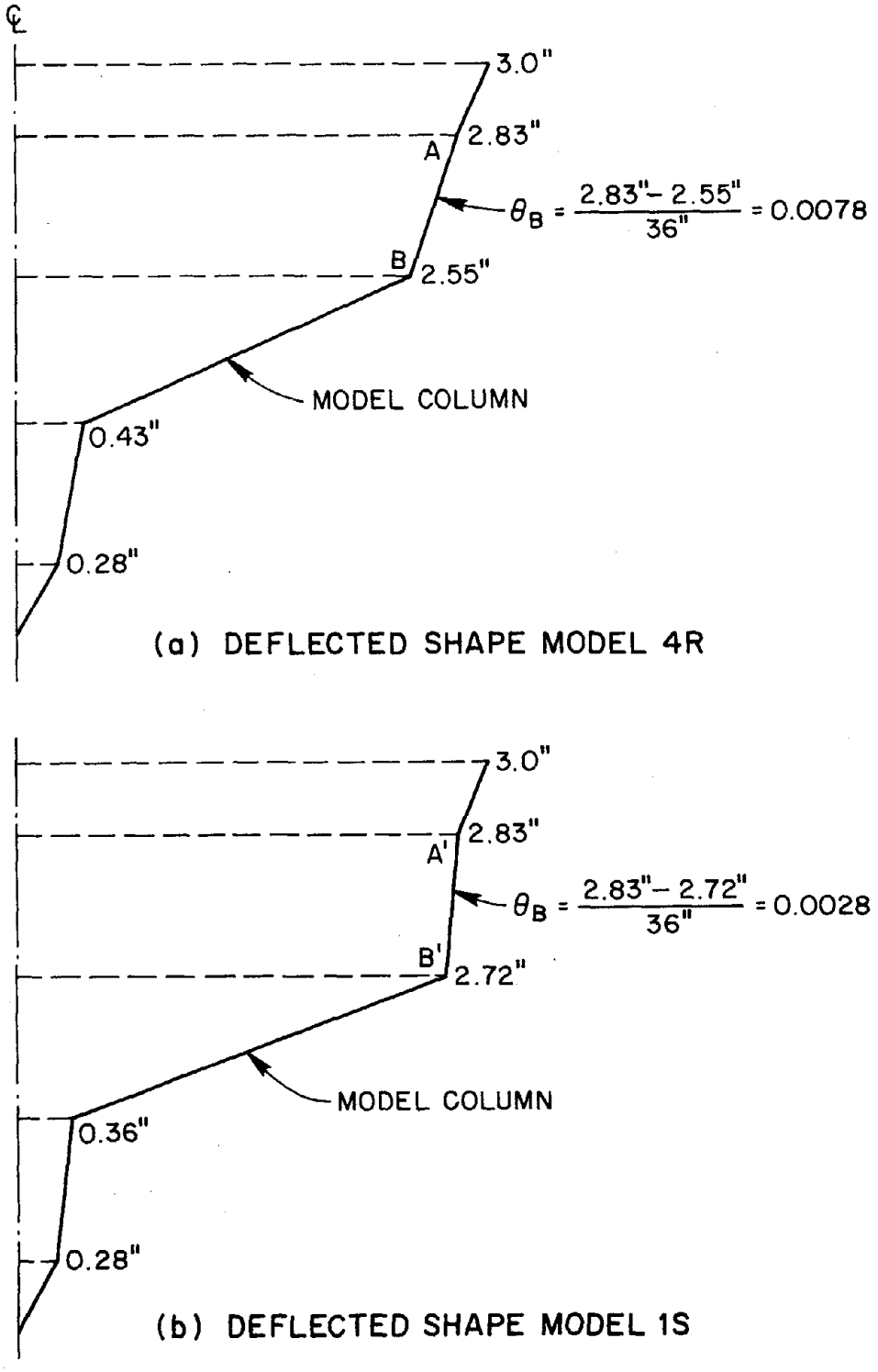

FIG. 3.67 MEASURED DEFLECTED SHAPES AT A TIP DISPLACEMENT OF 3 INCHES (1 IN. = 25.4 MM)

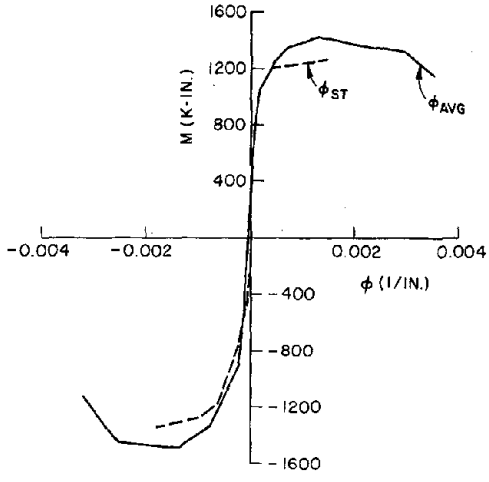

FIG. 3.68 MOMENT CURVATURE CYCLIC ENVELOPES FOR MODEL 3R (1 K-IN. = 0.113 kN•M, 1 IN. = 25.4 MM)

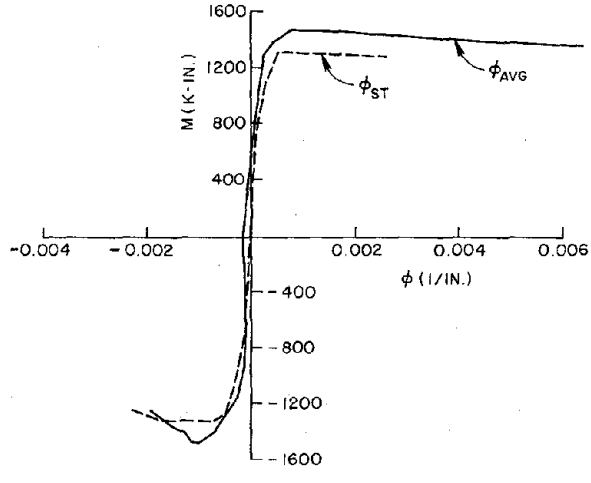

FIG. 3.69 MOMENT CURVATURE CYCLIC ENVELOPES FOR MODEL 5R (1 K-IN. = 0.113 kN•M, 1 IN. = 25.4 MM)

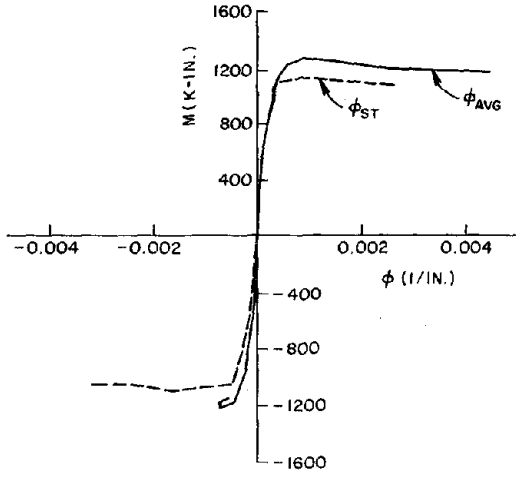

FIG. 3.70 MOMENT CURVATURE CYCLIC ENVELOPES FOR MODEL 6R (1 K-IN. = 0.113 kN•M, 1 IN. = 25.4 MM)

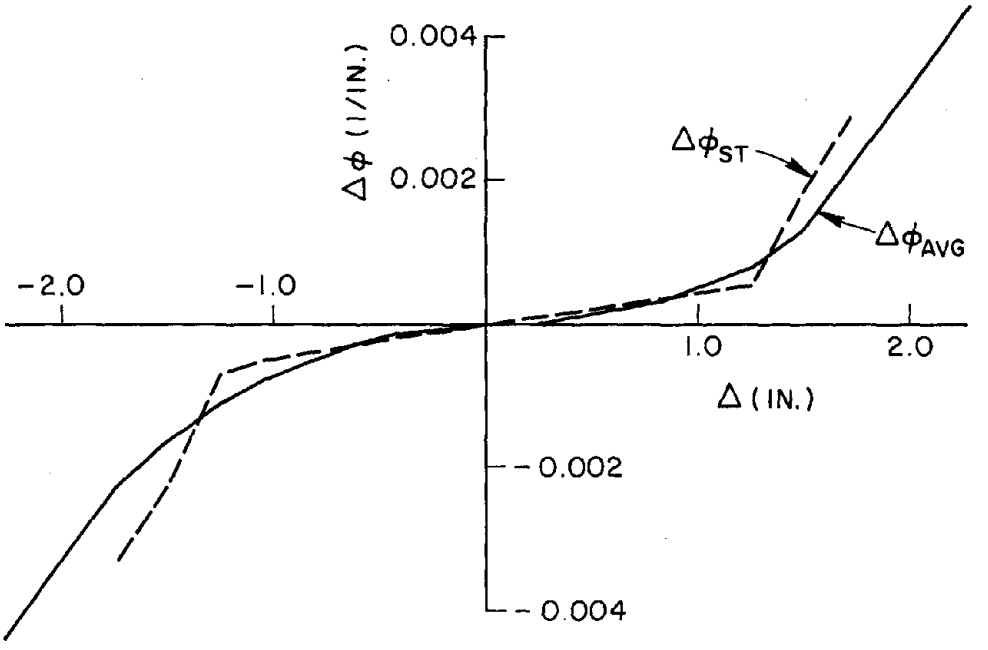

FIG. 3.71 CYCLIC VARIATION OF CHANGE IN CURVATURE WITH DISPLACEMENT FOR MODEL 5R (1 IN. = 25.4 MM)

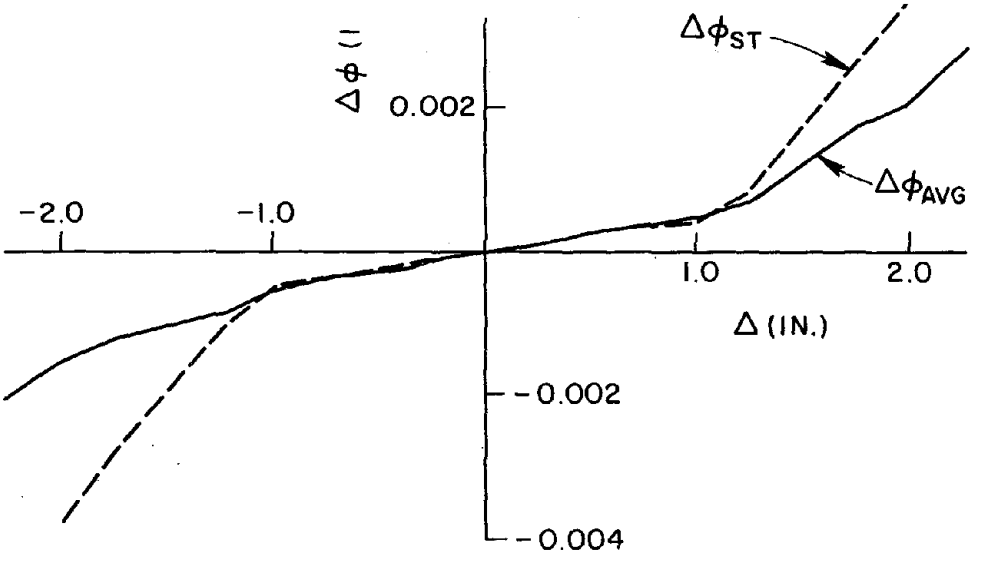

FIG. 3.72 CYCLIC VARIATION OF CHANGE IN CURVATURE WITH DISPLACEMENT FOR MODEL 6R (1 IN. = 25.4 MM)

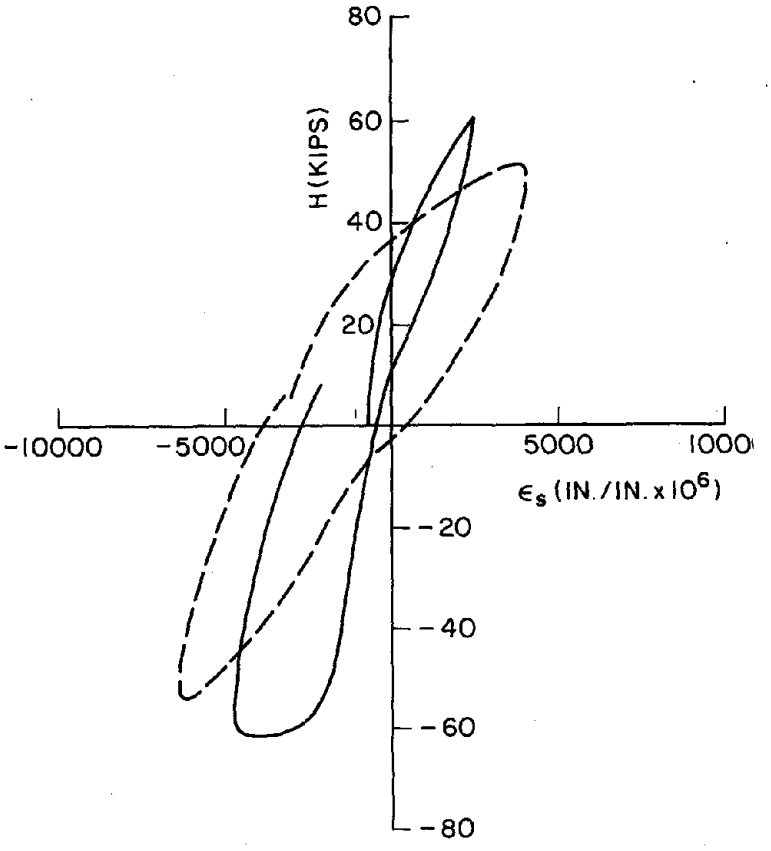

FIG. 3.73 SHEAR-STEEL STRAIN HYSTERETIC BEHAVIOR AT 1.25 INCHES IN MODEL 2S (1 KIP = 4.448 kN, 1 IN. = 25.4 MM)

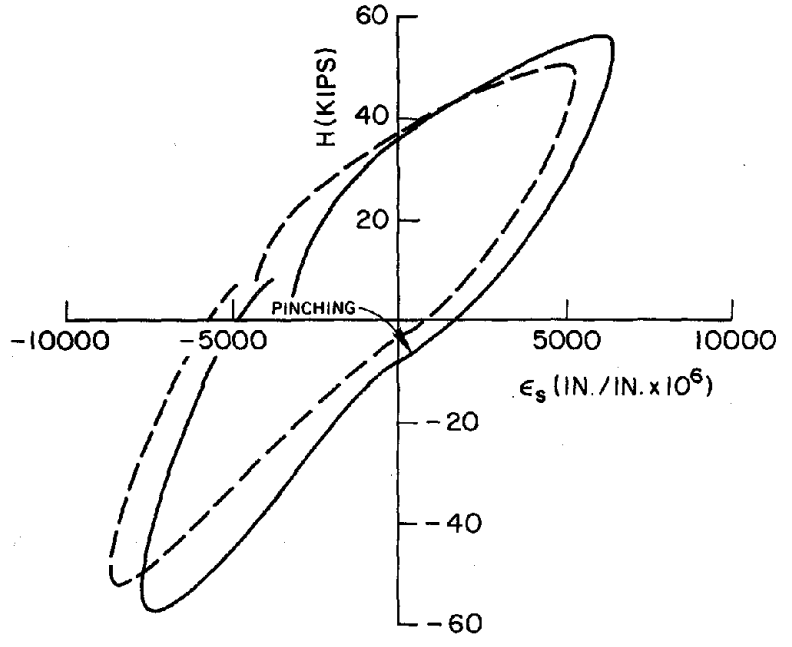

FIG. 3.74 SHEAR-STEEL STRAIN HYSTERETIC BEHAVIOR AT 1.5 INCHES IN MODEL 2S (1 KIP = 4.448 kN, 1 IN. = 25.4 MM)

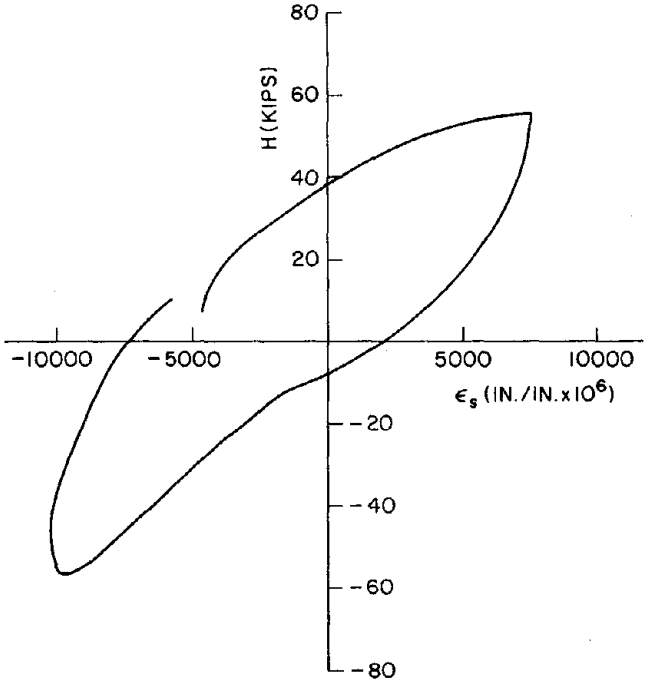

FIG. 3.75 SHEAR-STEEL STRAIN HYSTERETIC BEHAVIOR AT 1.75 INCHES IN MODEL 2S (1 KIP = 4.448 kN, 1 IN. = 25.4 MM)

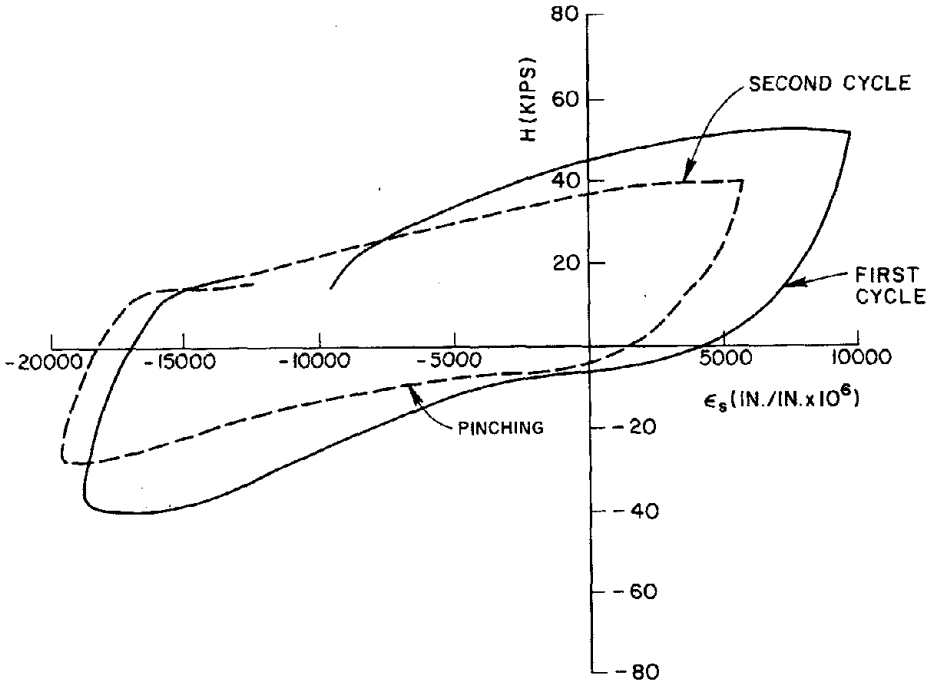

FIG. 3.76 SHEAR-STEEL STRAIN HYSTERETIC BEHAVIOR AT 2.5 INCHES IN MODEL 2S (1 KIP = 4.448 kN, 1 IN. = 25.4 MM)

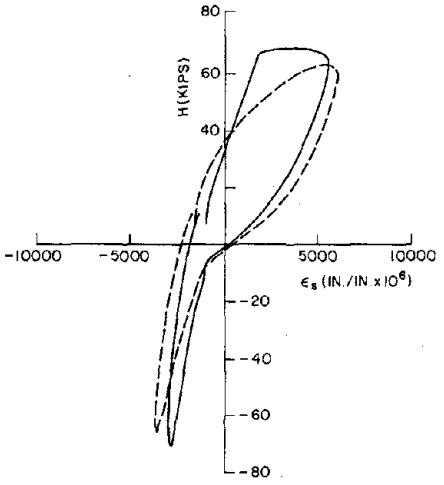

FIG. 3.77 SHEAR-STEEL STRAIN HYSTERETIC BEHAVIOR AT 1.25 INCHES IN MODEL 6R (1 KIP = 4.448 kN, 1 IN. = 25.4 MM)

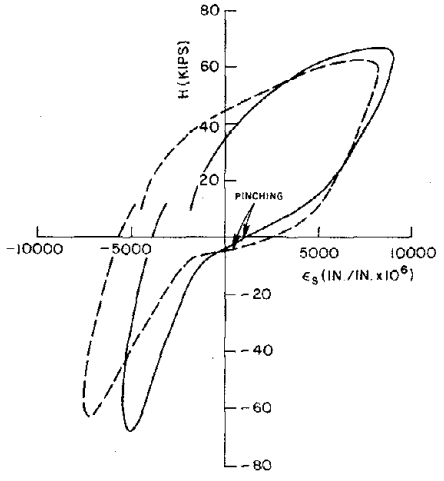

FIG. 3.78 SHEAR-STEEL STRAIN HYSTERETIC BEHAVIOR AT 1.5 INCHES IN MODEL 6R (1 KIP = 4.448 kN, 1 IN. = 25.4 MM)

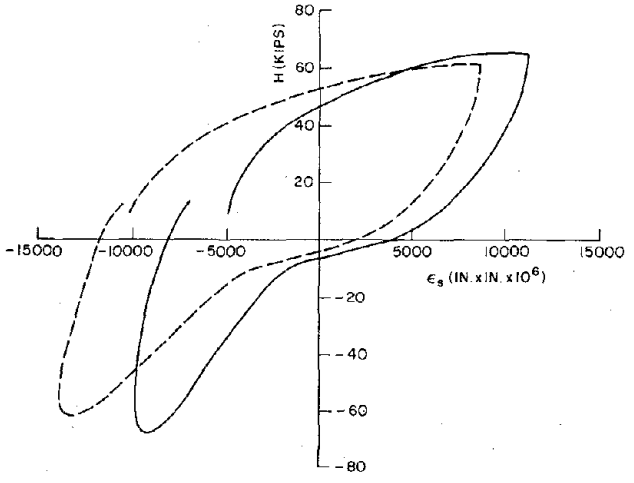

FIG. 3.79 SHEAR-STEEL STRAIN HYSTERETIC BEHAVIOR AT 1.75 INCHES IN MODEL 6R (1 KIP = 4.448 kN, 1 IN. = 25.4 MM)

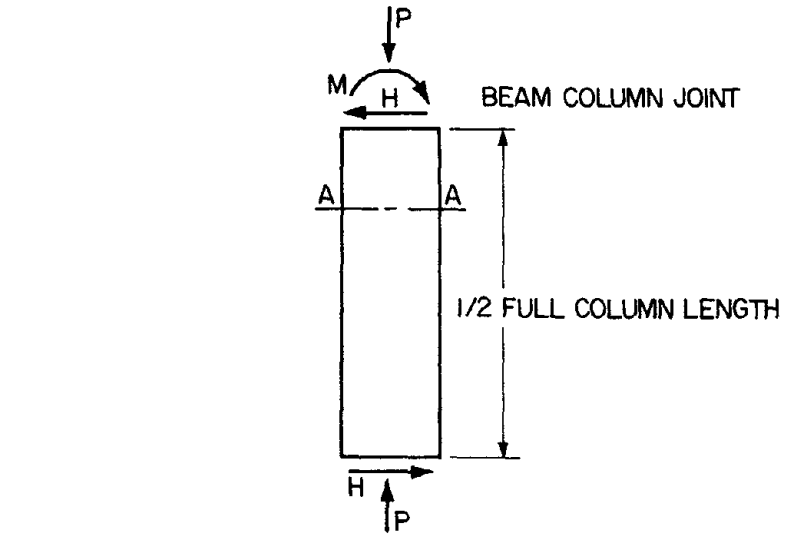

(a) FREE BODY DIAGRAM

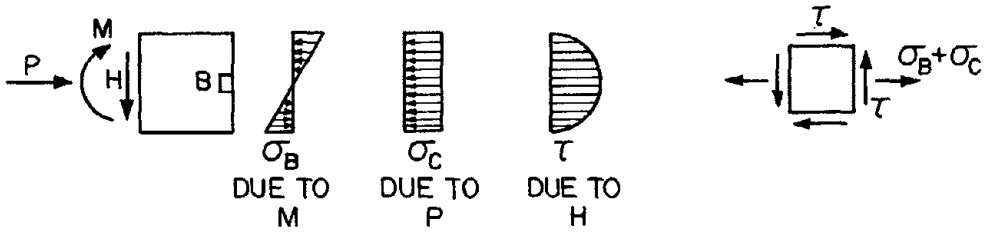

(b) IDEALIZED STRESSES ON SECTION A-A

(c) STRESSES ON ELEMENT B

FIG. 4.1 MAJOR STRESS COMPONENTS IN EXPERIMENTAL COLUMN

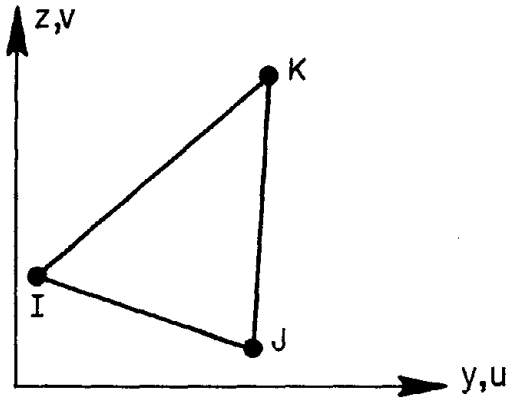

(a) CONSTANT STRAIN TRIANGLE (CST)

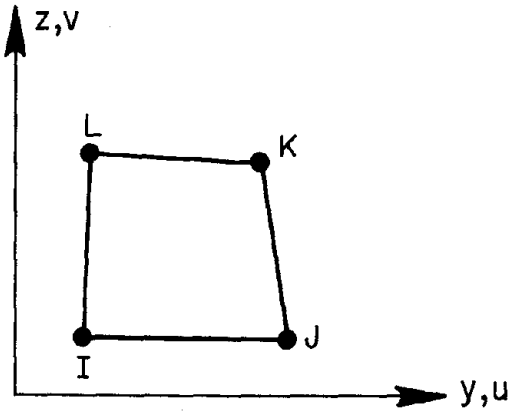

(b) FOUR-NODED QUADRILATERAL (Q4)

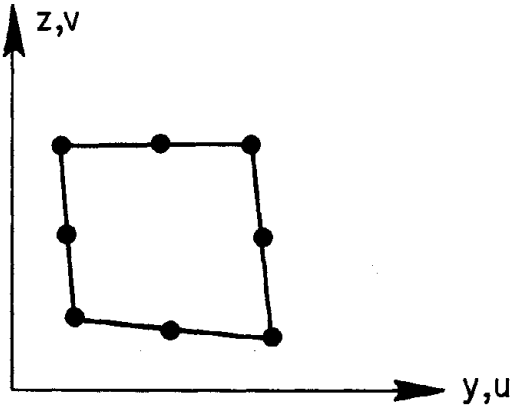

(c) EIGHT-NODED QUADRILATERAL (Q8)

FIG. 4.2 TWO-DIMENSIONAL FINITE ELEMENTS

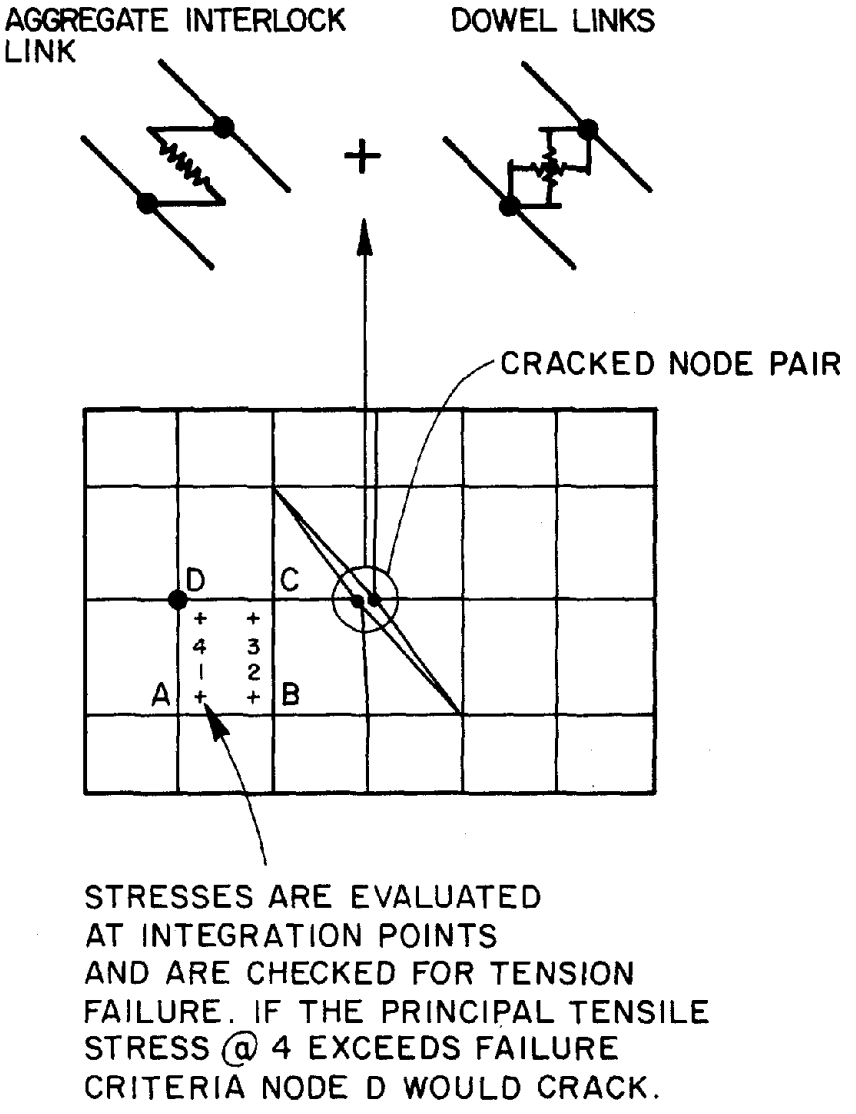

FIG. 4.3 CRACK DEFINITION

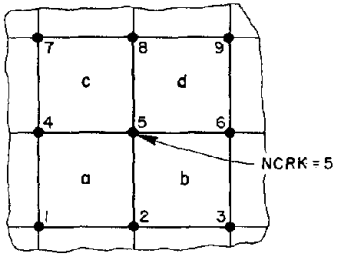

(a) TYPICAL SUBSTRUCTURE

NODE #	CONNECTED ELEMENTS			
1	a			
2	a	b		
3	b			
4	a	c		
5	a	b	c	d
6	b	d		
7	c			
8	c	d		
9	d			

(b) NODE-ELEMENT CONNECTIVITY ARRAY (NPP)

ELEMENT	ADJACENT ELEMENTS	
a	b	c
b	a	d
c	a	d
d	b	c

(c) ELEMENT-ELEMENT CONNECTIVITY ARRAY (KEL)

FIG. 4.4 EXAMPLE SUBSTRUCTURE AND CONNECTIVITY ARRAYS

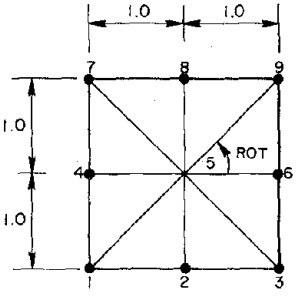

IF BETA = 315 OR 135
BETA = 45 & 225
NT = NODE ≠ NCRK
WITH ROT CLOSEST
TO BETA

NODE #	ROT VALUE	
1	225	← NT
2	270	
3	315	
4	180	
5	–	← #5 = NCRK
6	0	
7	135	
8	90	
9	45	← NT

FIG. 4.5 ROT ARRAY AND DETERMINATION OF CRACK TIP

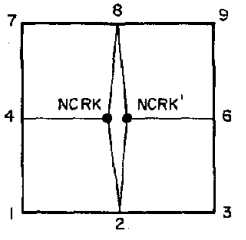

NCRK' = 1 + CURRENT NUMBER OF NODAL POINTS

(a) NT = 8

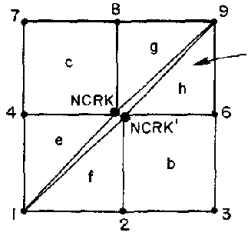

NEW TRIANGULAR ELEMENTS

(b) NT = 9 & 1

FIG. 4.6 CRACKED SUBSTRUCTURE

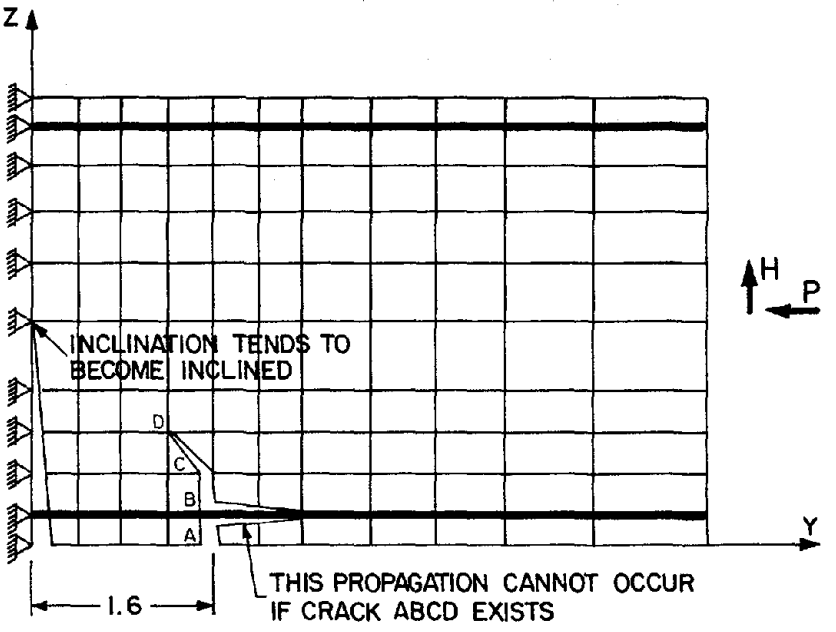

FIG. 4.7 LIMITATIONS OF CRACK FORMATION PROCEDURE

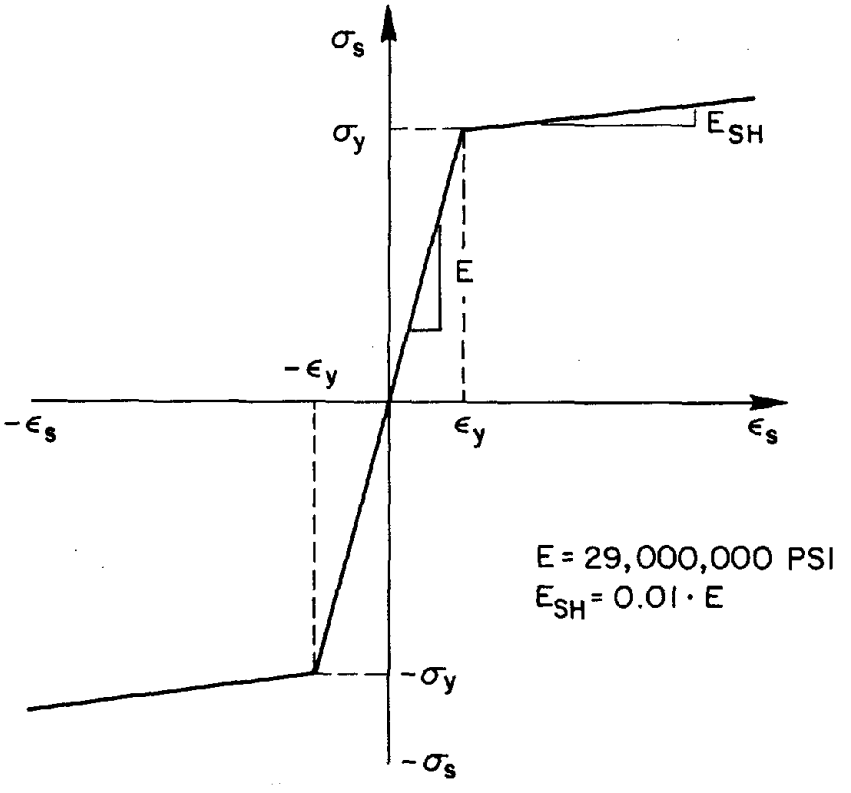

FIG. 4.8 STEEL MATERIAL LAW (1000 PSI = 6.895 MPa)

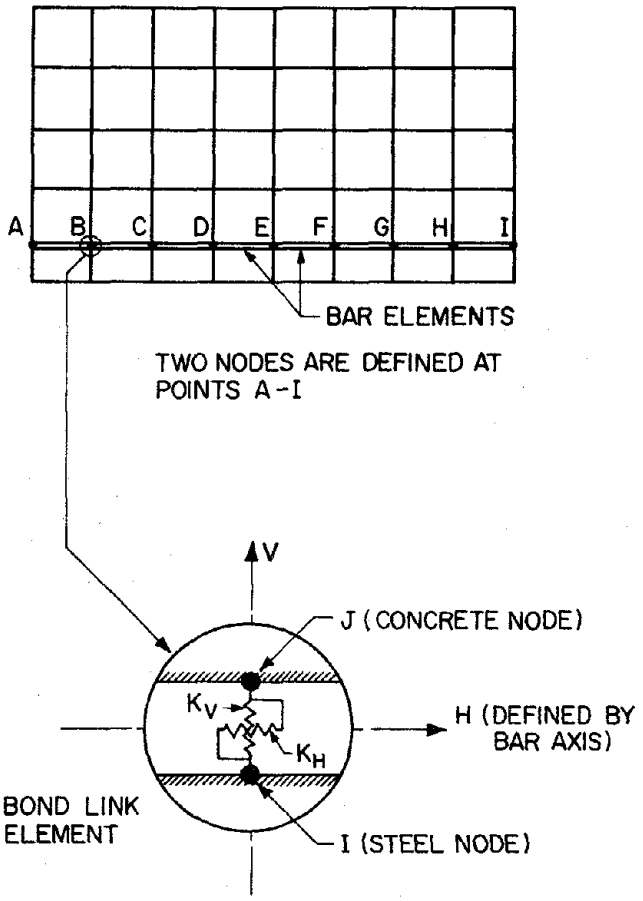

FIG. 4.9 BOND MODEL

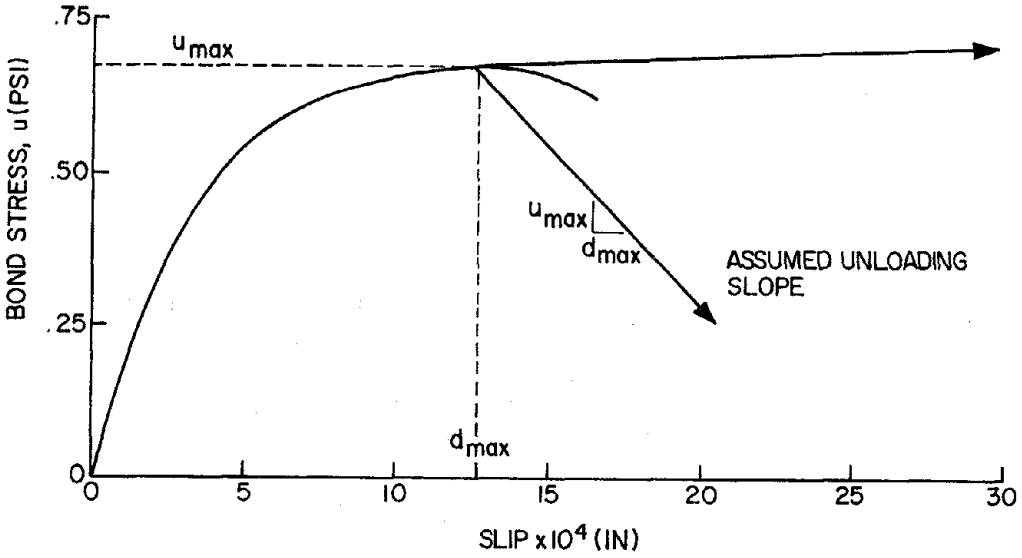

FIG. 4.10 BOND STRESS-SLIP RELATIONSHIP
(1 KSI = 6.895 MPa, 1 IN. = 25.4 MM)

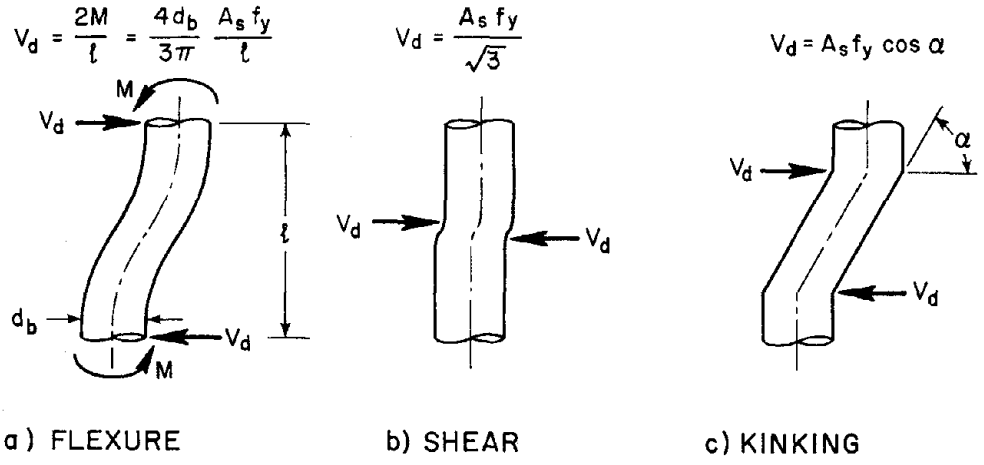

FIG. 4.11 DOWEL ACTION MECHANISMS [30]

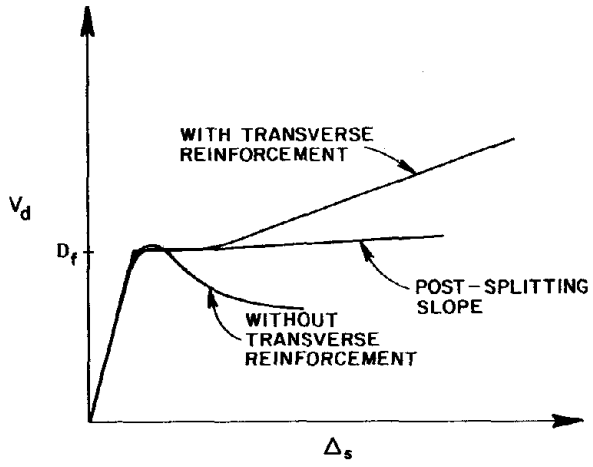

FIG. 4.12 TYPICAL DOWEL SHEAR-SHEAR DISPLACEMENT RELATIONSHIPS

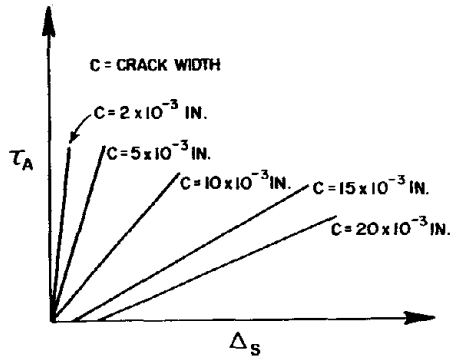

FIG. 4.13 TYPICAL AGGREGATE INTERLOCK SHEAR STRESS-SHEAR DISPLACEMENT RELATIONSHIPS [33] (1 IN. = 25.4 MM)

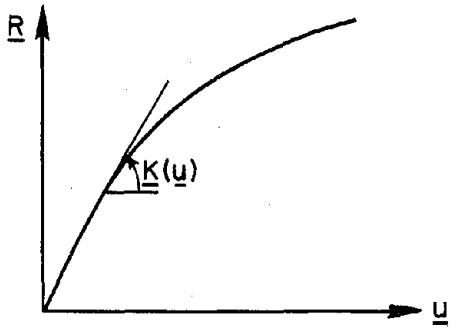

(a) RELATIONSHIP BETWEEN $\underline{R}$ AND $\underline{u}$

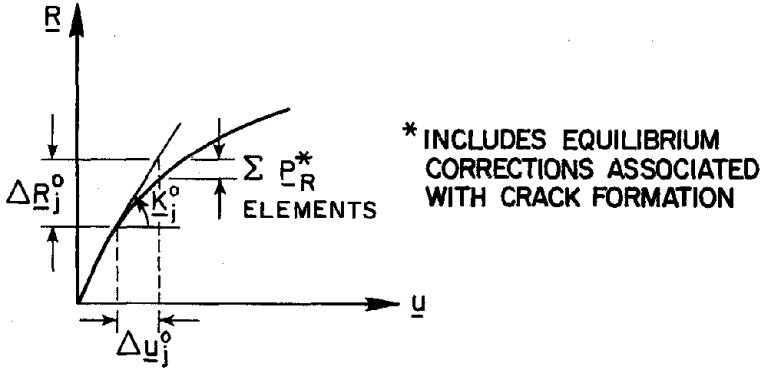

*INCLUDES EQUILIBRIUM CORRECTIONS ASSOCIATED WITH CRACK FORMATION

(b) SOLUTION STEPS a-c

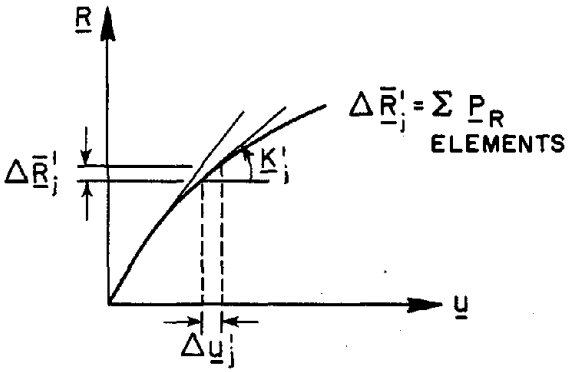

(c) SOLUTION STEPS IN FIRST ITERATION

FIG. 4.14 SOLUTION OF NONLINEAR EQUILIBRIUM EQUATIONS

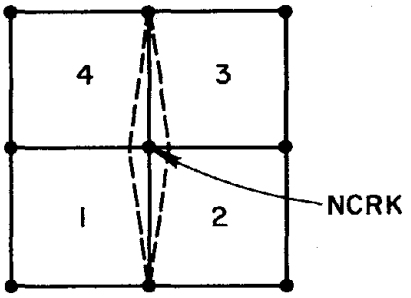

(a) SUBSTRUCTURE TO CONTAIN NEW CRACKLINE

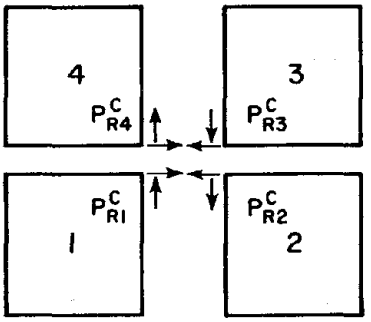

$\underset{\sim}{P}^C_{R_i} = \int \underset{\sim}{B}^T_{C_i}\ \underset{\sim}{\sigma}^T_i\ dVOL$

i = ELEMENT NO.

(b) FORCES EXISTING AT CRACKED NODE BEFORE CRACKING

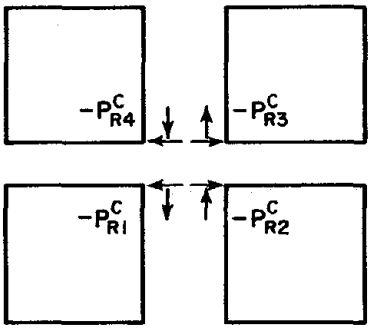

(c) RESIDUAL NODAL FORCES TO BE APPLIED IN NEXT SOLUTION STEP

FIG. 4.15 FORCE REDISTRIBUTION WITH CRACK FORMATION

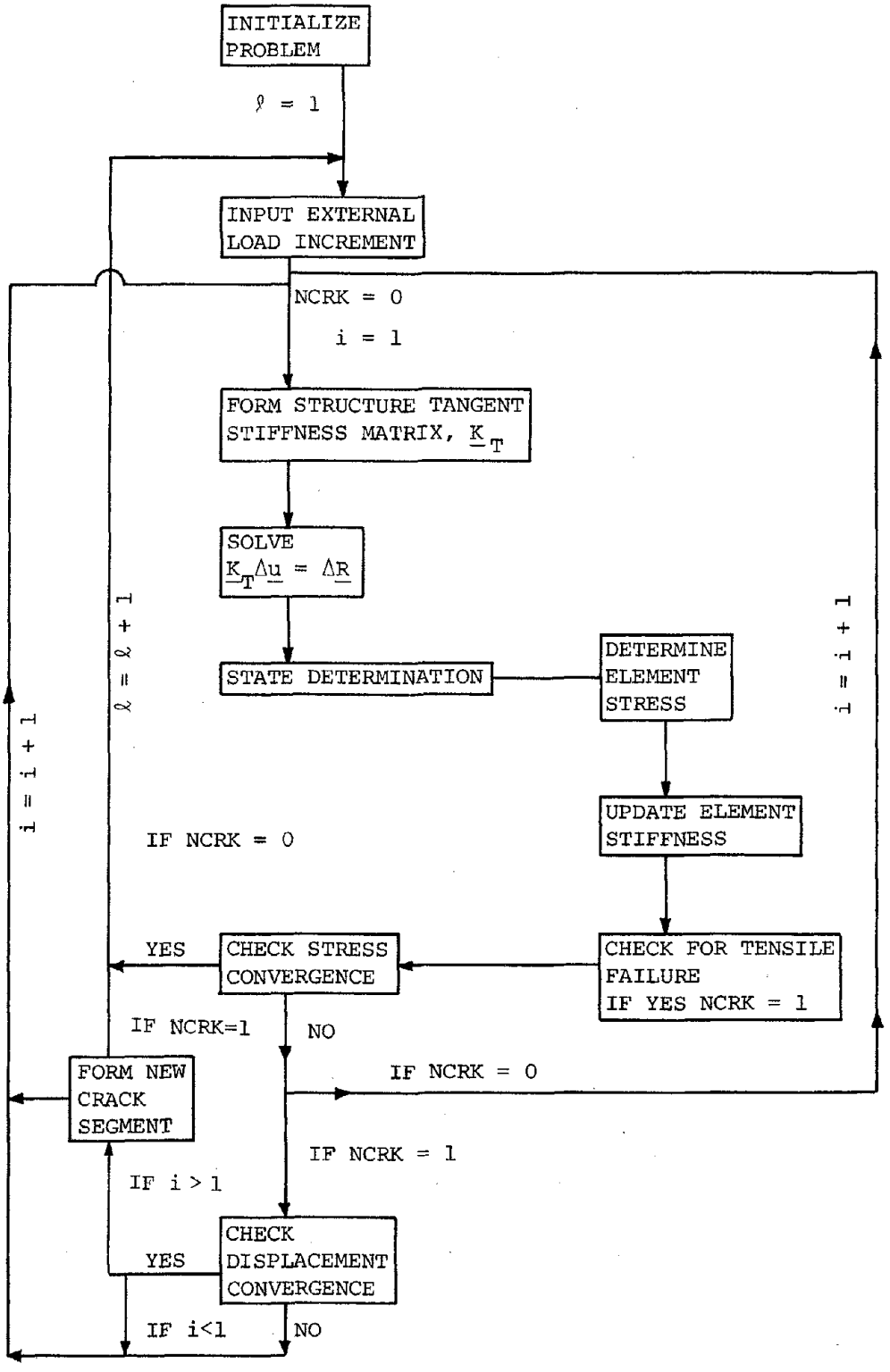

FIG. 4.16 FLOW CHART OF SOLUTION SCHEME

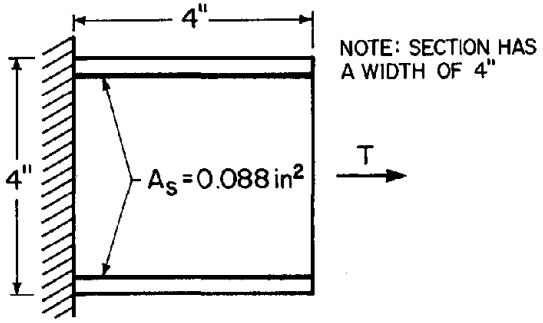

(a) CANTILEVER SUBJECTED TO AXIAL TENSION

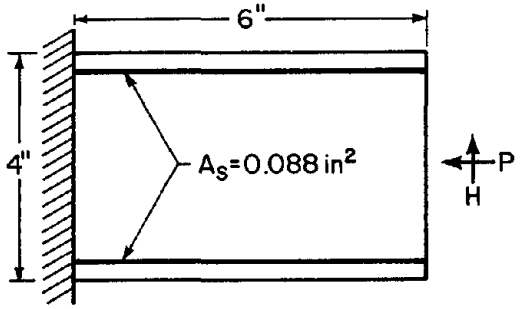

$E_s = 29000KSI$, $\sigma_y = 70KSI$

$E_c = 3600KSI$, $f'_c = 5KSI$, $f'_t = 0.5KSI$, $\nu_c = 0.2$

(b) CANTILEVER SUBJECTED TO AXIAL COMPRESSION AND SHEAR

FIG. 4.17 PROBLEMS ANALYZED (1 KSI = 6.895 MPa, 1 IN. = 25.4 MM, 1 IN^2 = 645.2 MM^2)

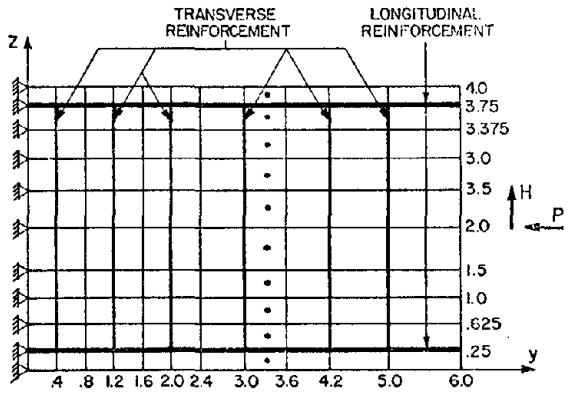

(a) MESH DEFINITION (in)

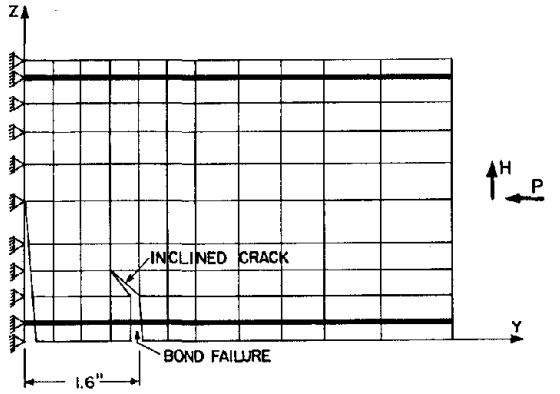

(b) CRACK PATTERN

FIG. 4.18 CANTILEVER SUBJECTED TO AXIAL COMPRESSION AND TIP SHEAR FORCE (1 IN. = 25.4 MM)

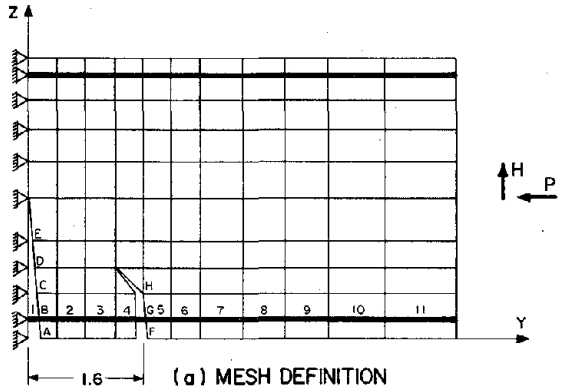

BAR	STRESS	
	INCREMENTAL SOLUTION	RESTART SOLUTION
1	19710	20120
2	12490	12630
3	9393	9430
4	7554	7553
5	7554	7553
6	4270	4278
7	980	1045
8	-2350	-2274
9	-5098	-5033
10	-8000	-7964
11	-11170	-11180

b) BAR STRESSES (psi)

NODE	CO-ORDINATE	DISPLACEMENT	
		INCREMENTAL SOLUTION	RESTART SOLUTION
A	Y	.997	.977
	Z	.008	.008
B	Y	.809	.789
	Z	.010	.011
C	Y	.553	.543
	Z	.019	.023
D	Y	.316	.307
	Z	.027	.034
E	Y	.041	.046
	Z	.046	.059
F	Y	1.51	1.51
	Z	1.33	1.32
G	Y	1.16	1.16
	Z	1.33	1.33
H	Y	.693	.696
	Z	1.38	1.37

c) CRACK DISPLACEMENTS (inches · 10^{-3})

FIG. 4.19 COMPARISONS OF INCREMENTAL AND RESTART SOLUTIONS; BAR STRESSES AND CRACK DISPLACEMENTS (1000 PSI = 6.895 MPa, 1 IN. = 25.4 MM)

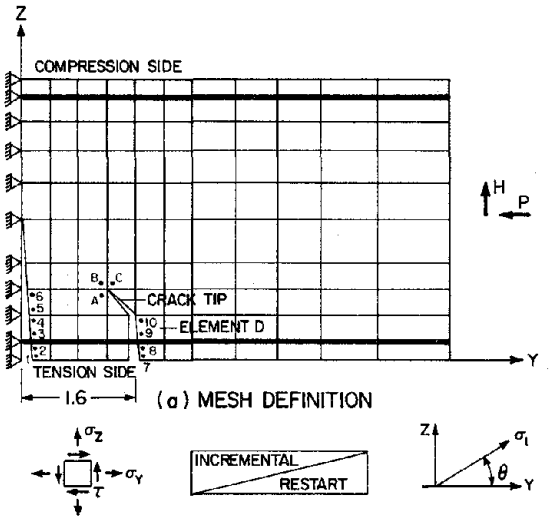

STRESS POINT	STRESSES		
	σ_y	σ_z	τ
1	13 / 21	38 / 33	22 / 12
2	-74 / -57	41 / 17	18 / 6
3	-79 / -49	91 / 70	117 / 73
4	27 / 20	71 / 84	28 / 44
5	38 / 33	54 / 61	62 / 72
6	7 / 10	52 / 57	35 / 32
7	-36 / -39	43 / 44	33 / 42
8	-90 / -91	30 / 34	34 / 37
9	-69 / -55	307 / 313	213 / 216
10	-82 / -73	302 / 311	122 / 118

ELEMENT D

b) Stress Comparison Adjacent to Crackline (psi)

ELEMENT	PRINCIPAL STRESSES		
	σ_1	σ_2	θ
A	210 / 252	-262 / -308	47° / 44°
B	105 / 124	-351 / -280	52° / 53°
C	330 / 374	-580 / -611	51° / 52°

c) Stress Comparison At Crack Tip E (psi)

FIG. 4.20 COMPARISON OF INCREMENTAL AND AND RESTART SOLUTIONS; CONCRETE STRESSES NEAR CRACKS (1 PSI = 6,895 Pa, 1 IN. = 25.4 MM)

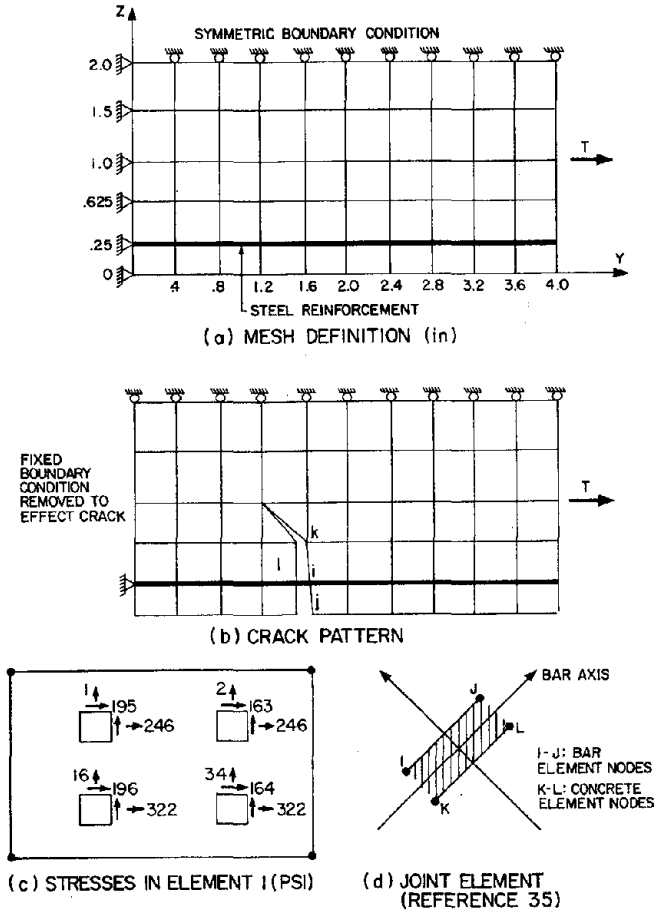

FIG. 4.21 CANTILEVER SUBJECTED TO AXIAL TENSION (1 PSI = 6,895 Pa, 1 IN. = 25.4 MM)

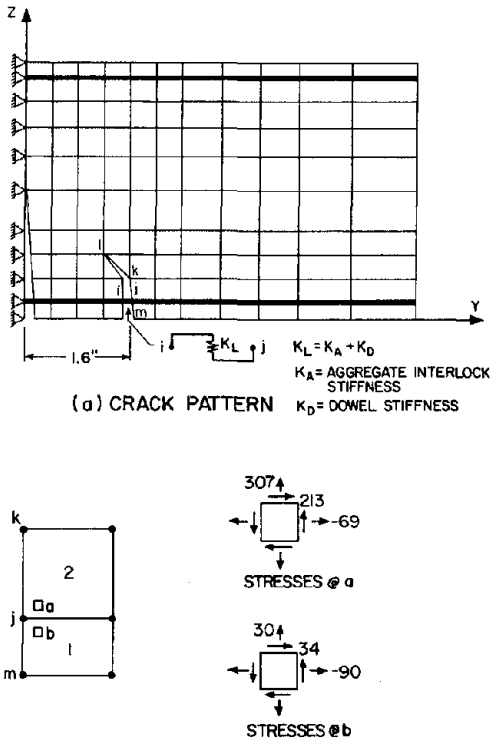

FIG. 4.22 STRESS CONCENTRATION CAUSED BY AGGREGATE INTERLOCK AND DOWEL ACTION LINKS (1 PSI = 6,895 Pa, 1 IN. = 25.4 MM)

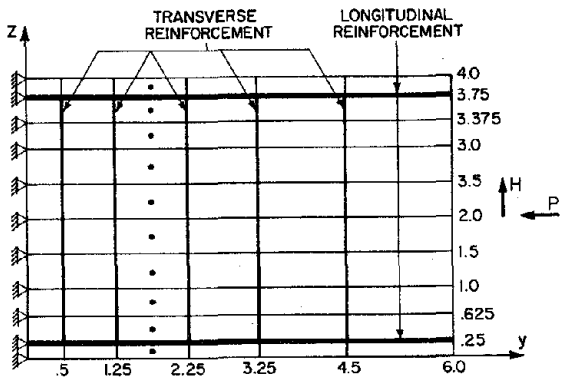

(a) MESH A (in)

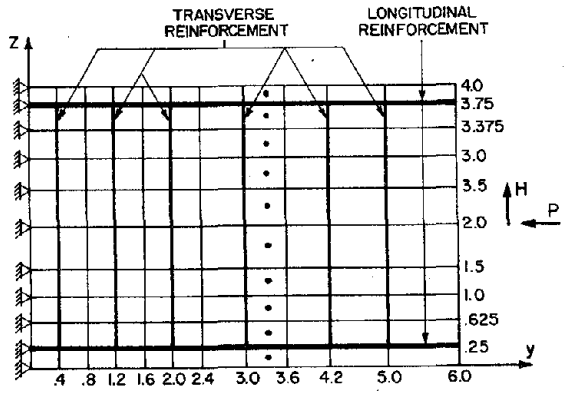

(b) MESH B (in)

FIG. 4.23 DIFFERENT FINITE ELEMENT MESHES CONSIDERED IN ANALYSIS OF CANTILEVER WITH AXIAL COMPRESSION AND TIP SHEAR (1 IN. = 25.4 MM)

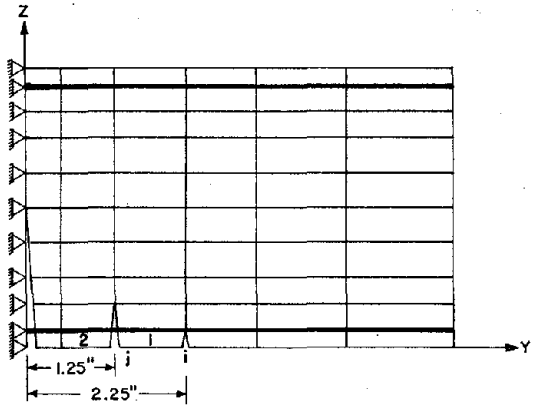

(a) MESH A

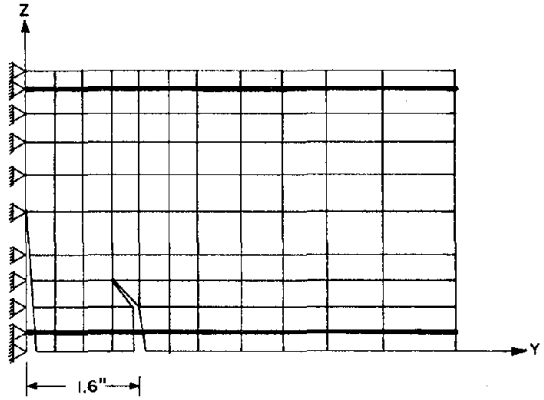

(b) MESH B

FIG. 4.24 COMPARISON OF CRACK PATTERNS OBTAINED WITH DIFFERENT MESH SIZES (1 IN. = 25.4 MM)

A P P E N D I X E S

APPENDIX A. MATERIAL PROPERTIES

A.1 Concrete

A.1.1 Concrete Mix

The concrete mix was designed and prepared in the University of California Concrete Laboratory. Typical concrete mix properties are shown in Table A1.

A.1.2 Concrete Control Tests

Four types of control tests were performed on concrete specimens:

a) Stress-strain measurements on 6 in. × 12 in.[a] cylinders. Typical stress-strain results are shown in Fig. A1.

b) Compressive strength tests on 6 in. × 12 in. cylinders.

c) Tensile splitting tests on 6 in. × 12 in. cylinders.

d) Beam rupture tests on 5 in. × 6 in. × 20 in. prisms.

Control test results are summarized in Table A2.

A.2 Steel

The following reinforcement was used in the test models.

a) Grade 60 No. 4[b] and No. 5 deformed bars were used as the column longitudinal reinforcement.

b) Grade 40 No. 4 and No. 5 deformed bars were used as the beam

---

a. One inch is equal to 25.4 mm

b. The bar size number, N, refers to a bar with a nominal diameter equal to N/8 of an inch[N·(3.1)mm].

longitudinal reinforcement.

c) Grade 40 No. 2 deformed bars were used as the transverse reinforcement in the rectangular tied columns.

d) Grade 40 No. 2 plain bar was used as the transverse reinforcement in the spiral columns.

e) Grade 40 No. 2 plain bars were used as the beam transverse reinforcement.

Typical stress-strain relationships for the materials used are summarized in Fig. A2-A4.

TABLE A1

CONCRETE MIX PROPERTIES

MATERIAL	SSD Aggregates	
	Parts by Weight	Weight for 1 yd^3 batch (lb)
Cement Type II Santa Cruz	1.00	679
Water	0.477	324
Coarse Sand; Olympia #0 2.55 FM	2.03	1378
Fine Gravel; Fair Oaks 1/2" × 1/4"	2.47	1675

Note: 1 in = 2.54 mm; 1 yd^3 = .765 m^3; 1 lb = 4.45N

TABLE A2

RESULTS OF CONCRETE CONTROL TESTS

MODEL	Compressive Strength f'_c (psi)	Tensile Splitting Strength f_{st} (psi)	Modulus of Rupture f_{rt} (psi)
2R	5270	550	520
3R	5260	480	550
4R	5280	530	520
5R	5100	476	615
6R	4700	-	-
1S	5050	500	400
2S	5200	470	620

Note: 1000 psi = 1 ksi = 6.895 MPa

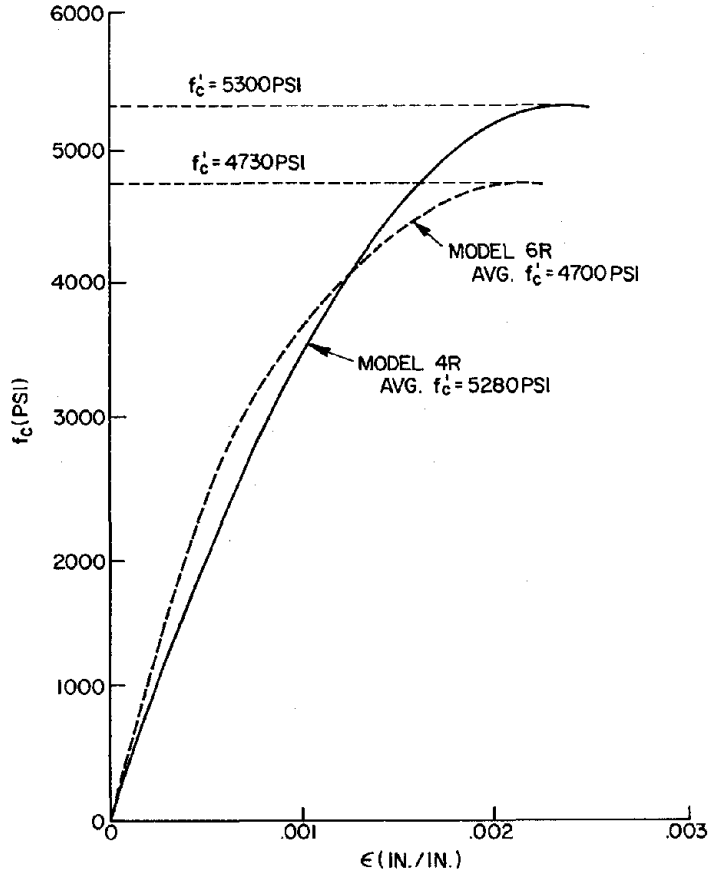

FIG. A1 TYPICAL CONCRETE STRESS-STRAIN RELATIONSHIPS (1 PSI = 6,895 Pa)

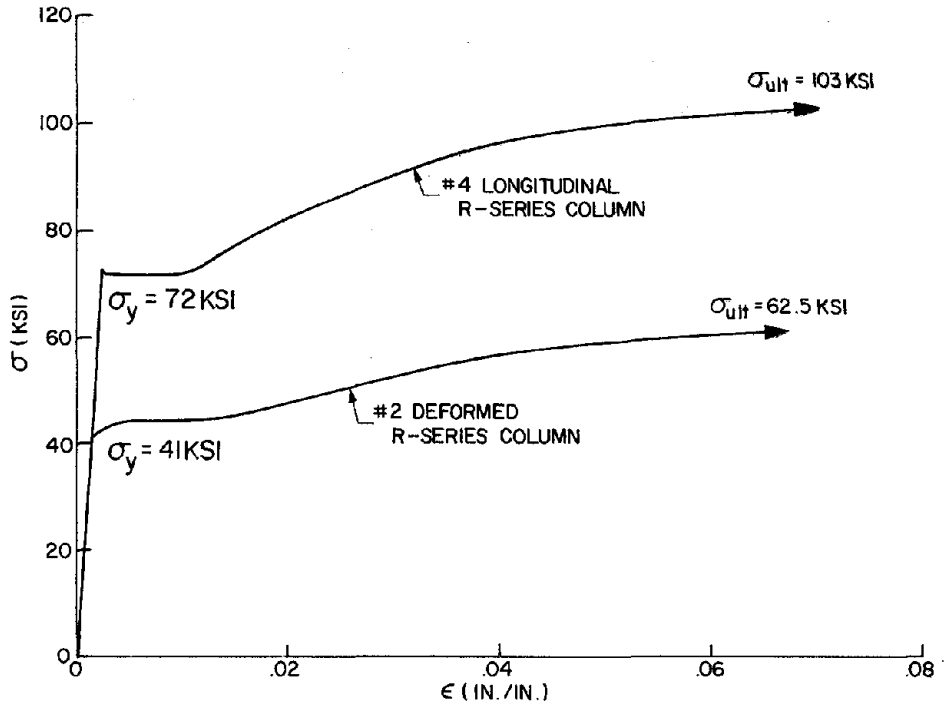

FIG. A2 STEEL STRESS-STRAIN RELATIONSHIPS FOR R-SERIES COLUMNS (1 KSI = 6.895 MPa)

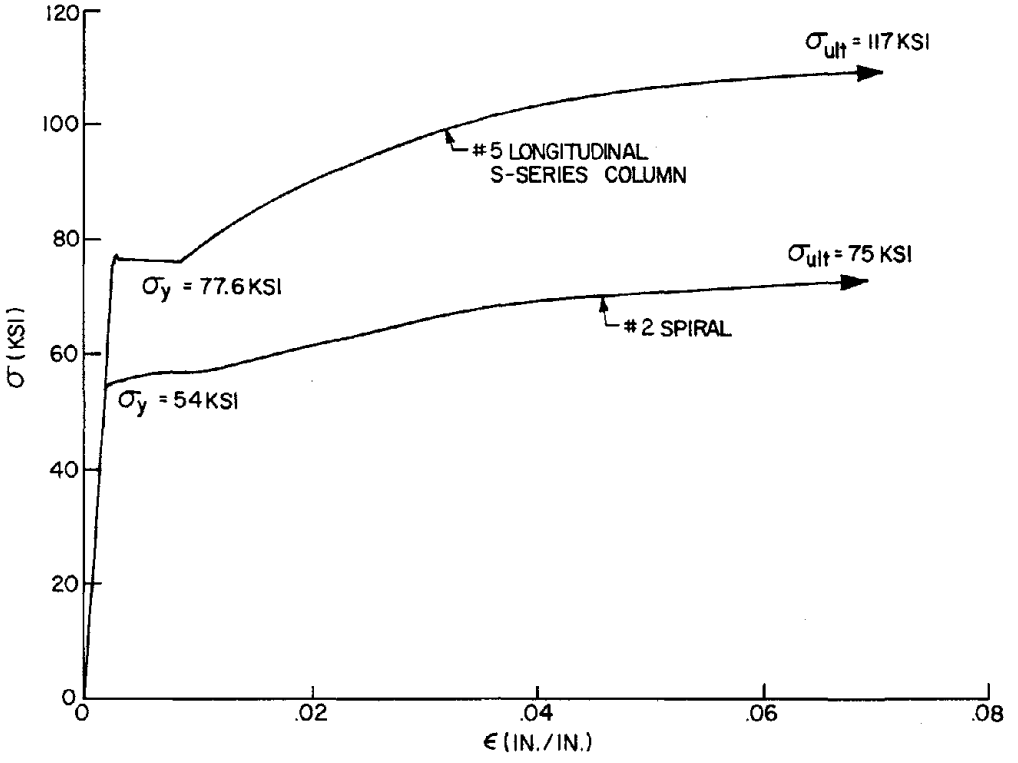

FIG. A3 STEEL STRESS-STRAIN RELATIONSHIPS FOR S-SERIES COLUMNS (1 KSI = 6.895 MPa)

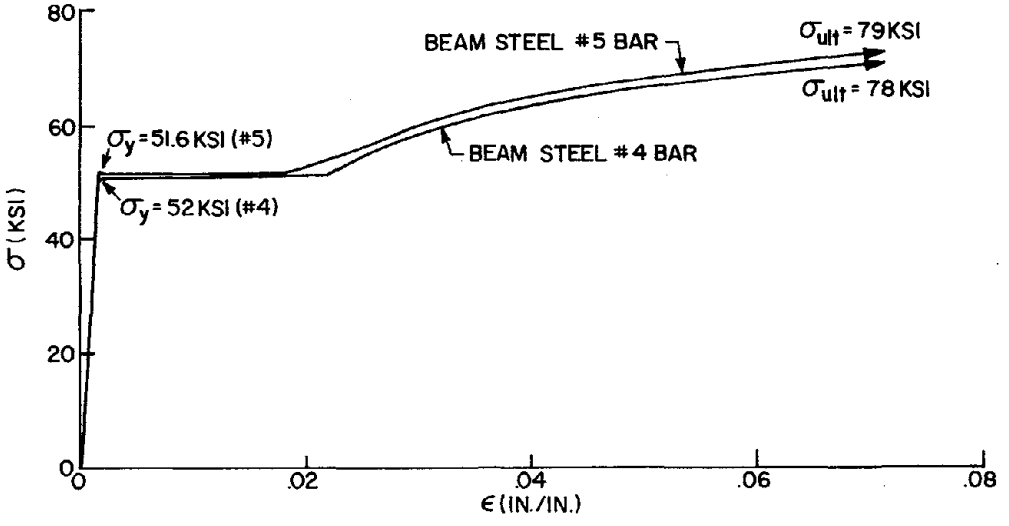

FIG. A4 STEEL STRESS-STRAIN RELATIONSHIPS FOR BEAM REINFORCEMENT (1 KSI = 6.895 MPa)

APPENDIX B. DESIGN OF PROTOTYPE STRUCTURE AND TEST MODEL

B.1

A floor plan and elevation of the prototype structure are given in Fig. 2.4. The structure is 120 feet high* (10 stories at 12 feet) and 120 feet by 120 feet in plan. The structural system consists of two spandrel-wall frames and four typical gravity load frames in each principal direction. The spandrel frames are assumed to resist all lateral loads. The assumed cross-sectional dimensions of the spandrel beams and columns and the interior frame beam and columns are indicated in Fig. B1 and B2. The floor slab is assumed to be 4 1/2 in. deep.

B.2 Determination of Loading

a. Gravity Loads

The gravity load is computed using the member sizes indicated above.

Slab (t = 4.5 in.)	56 psf
Ceiling (assumed)	10 psf
Partitions	20 psf
Beams $\frac{14\ \text{in} \times 20\ \text{in}}{144\ \text{in}^2/\text{ft}^2} \cdot 150\ \text{lb/ft}^3 \cdot \frac{1}{8\text{ft}}$	35 psf
Girders $\frac{18\ \text{in} \times 20\ \text{in}}{144\ \text{in}^2/\text{ft}^2} \cdot 150\ \text{lb/ft}^3 \cdot \frac{1}{24\text{ft}}$	20 psf
Columns $\frac{24\ \text{in} \times 24\ \text{in}}{144\ \text{in}^2/\text{ft}^2} \cdot 150\ \text{lb/ft}^3 \cdot \frac{12\text{ft}}{24\text{ft} \cdot 24\text{ft}}$	12 psf
	153 psf

Assume DL = 150 psf

*Necessary conversions to SI units are given in Section B.5

b. Live Load

LL = 50 psf (office building)

Maximum reduction in live load for lower story column (UBC 2306)

$$R = 23.1 \left(1 + \frac{DL}{LL}\right)$$

$$R = 23.1 \left(1 + \frac{150\ psf}{50\ psf}\right) = 92.4\% > 60\%$$

$$LL = 50 \left(1 - \frac{60.0}{100}\right) = 20\ psf$$

c. Design Loads

DL = 150 psf

LL = 20 psf

d. Dynamic (Earthquake) Loading

The earthquake loads are determined on the basis of UBC-2314. It is assumed that the earthquake shear forces are distributed equally to the columns of the spandrel frame*. As a result, the following calculations are made for only one column.

Z = 1

$$T = \frac{0.05\ h_n}{\sqrt{D}} = \frac{0.05 \times 120}{\sqrt{120}} = 0.55\ sec$$

$$C = \frac{0.05}{\sqrt[3]{T}} = \frac{0.05}{\sqrt[3]{0.55}} = 0.061$$

* This assumption is made for its simplicity and is not accurate. Interior columns of a frame will typically resist a larger force than an exterior column.

$K = 1$

$W = (.150 \text{ ksf} \cdot 24 \text{ ft} \cdot 60 \text{ ft}) \times 10 = 2170 \text{ kips/column}$

$V = ZKCW = 1 \times 1 \times 0.061 \times 2170 \text{ kip}$

$V = 132 \text{ kip}$ (total base shear for one column)

$$\frac{h_n}{D_o} = \frac{120ft}{120ft} = 1 < 3 \qquad \therefore F_t = 0$$

$$F_x = \frac{w_x h_x}{\Sigma w_i h_i} \cdot V \qquad \text{where } w_i = 217 \text{ k/floor}$$

Since the first story conditions are used in the design of the test model, only the total base shear is required.

B.3 Design of Members

Assumptions:

B.3.1 Loading

The loads to be considered in the design will be the loads that are going to be applied on the test model. Therefore:

a) Distributed loads on the beams will not be considered in the design of the spandrel beams.

b) The moments in the direction perpendicular to the plane of the frame will not be considered in the design of the column.

B.3.2 Method of Design

The ultimate strength theory was employed in the design of sections. The assumptions and constants will be the same as required by UBC (1973). The nominal concrete compression strength of 5,000 psi was assumed for

both beams and columns. The respective steel yield strengths employed in beam and column design were 52,000* psi and 60,000 psi.

B.3.3 Column Design

h = 6 ft. Assume Section: 24 in. × 24 in.

Axial Load:

D. L. = 10 × 0.15 ksf × 12 ft × 24 ft = 432 kip

Reduced L. L. = 10 × .020 ksf × 12 ft. × 24 ft. = 58 kip

Factored Load:

$P_u = 0.75(1.4\,D.L. + 1.7\,L.L.) = 0.75\ [1.4(432\ kip) + 1.7(58\ kip)]$

$= 528$ kip

$V = 132$ kip

$M = V \times \frac{h}{2} = 132\ kip \times \frac{6\ ft}{2} = 396$ K-ft

$M_u = 0.75 \times 1.7 \times 1.1 \times 396$ K-ft = 556 K-ft = 6670 K-in

Therefore design for:

$P_u = 528$ kip

$M_u = 6670$ K-in.

Use ACI Ultimate Strength Design Handbook**

Assume

$\gamma = 0.8$

$\delta = 1.0$

---

* The yield strength of the beam reinforcement is based on stress-strain tests of the steel used in the test beams. (Appendix A)

**ACI Publication SP-17(73) Volume 1

$$e = \frac{M_u}{P_u} = \frac{6670 \text{ K-in.}}{528 \text{ kip}} = 12.6 \text{ in.}$$

$$\frac{\delta e}{h} = \frac{12.6 \text{ in.}}{24 \text{ in.}} = 0.524$$

$$\frac{P_u}{A_g} = \frac{528 \text{ kip}}{24 \text{ in.} \times 24 \text{ in.}} = 0.92 \text{ ksi}$$

For a tied column:

$$\frac{A_s}{A_g} = 0.012 \qquad \text{for } \gamma = 0.9$$

$$= 0.014 \qquad \text{for } \gamma = 0.75$$

$$A_s = 0.0135 \times 24 \text{ in.} \times 24 \text{ in.} = 7.8 \text{ in.}^2 \qquad \text{for } \gamma = 0.80$$

Use 10 #8 - 7.9 in.^{2} (Fig. 1.4a shows half scale test section)

$\gamma = 0.79$ for #8 bars Okay.

For a spiral column:

$$\frac{A_s}{A_g} = 0.015 \qquad \text{for } \gamma = 0.9$$

$$= 0.018 \qquad \text{for } \gamma = 0.75$$

$$A_s = 0.017 \times 24 \text{ in.} \times 24 \text{ in.} = 9.7 \text{ in.}^2 \qquad \text{for } \gamma = .80$$

Use 8 #10 = 10.1 in.^{2} (Fig. 1.4b shows half scale test section)

$\gamma = 0.78$ for #10 bars okay

The arrangement of the steel in the spirally reinforced column was selected to alleviate congestion of reinforcement in the beam-column joint.

B.4 Design of the Column Transverse Reinforcement and Beam Reinforcement

The maximum axial load which was to be applied to the test columns was the balance point axial load which is defined as the point on the axial force-bending moment interaction relationship at which simultaneous yielding and concrete failure occur. The balance point, and the axial force-bending moment (P-M) interaction relationship are determined with the aid of a computer program. The basic assumptions employed in the program are listed below.

a. A linear strain distribution is assumed.

b. Concrete has zero tensile strength.

c. The concrete stress-strain relationship is defined by the expression (Fig. 2.15a):

$$f_c = f'_c\left[2\left(\frac{\varepsilon_c}{\varepsilon_o}\right)-\left(\frac{\varepsilon_c}{\varepsilon_o}\right)^2\right] \qquad \varepsilon_c \leq \varepsilon_o$$

$$f_c = f'_c\left[1 - 0.5\,\frac{(\varepsilon_c - \varepsilon_o)}{(\varepsilon_{50u} - \varepsilon_o)}\right] \qquad \varepsilon_c > \varepsilon_o$$

where

f'_c = maximum concrete strength

ε_o = concrete strain at f'_c

$$\varepsilon_{50u} = \frac{3 + .002\, f'_c}{f'_c - 1000}$$

For confined concrete the descending branch is defined by the expression:

$$f_c = f'_c\,[1 - z(\varepsilon_c - \varepsilon_o)]$$

where

$$z = \frac{0.5}{\varepsilon_{50_h} + \varepsilon_{50u} - \varepsilon_o}$$

$$\varepsilon_{50h} = \frac{3}{4} p'' \frac{b''}{h}$$

$$p'' = 2(b'' + d'') \frac{A''_s}{b''d''s}$$

s = stirrup spacing

b" = width of one stirrup, outside to outside

d" = depth of one stirrup, outside to outside

A''_s = area of transverse reinforcement

For a spiral column, p" was taken as:

$$p'' = \frac{4A''_s}{sd_c}$$

where

s = spiral pitch

d_c = core diameter

d. The steel stress strain relationship is indicated in Fig. 2.15b. E is assumed equal to 29,000,000 psi, and σ_y is the value found from stress-strain tests of the steel used in the model columns (Appendix A).

e. A point on the P-M interaction relationship is determined by a compressive failure of the outer concrete fibers. The failure strain is taken as 0.003 in/in (ε_{max}).

The program uses the following procedure (Fig. B3)

a. The axial load, P and ε_{max} are defined.

b. The neutral axis is determined by iteration. A basic cycle is:

   i. kd is assumed

   ii. determined C_s, C, and T from σ-ε relationships

   iii. check equilibrium $C_s + C$ and $T - P$ = ERROR

   iv. if ERROR is less than a preset convergence tolerance kd is taken as the current value. If not, kd is adjusted (a bisection algorithm is used), and the loop is started again at i

c. Once kd is determined, the moment is found by summing moments about the plastic centroid (Fig. B3). For a symmetric section, the plastic centroid is at mid-depth.

$$M = T\, d_s + C\, d_c + C_s\, d'_c$$

The above procedure defines one point of the P-M interaction relationship. The axial load is incremented and additional points are determined. The balance point is taken as the point on the interaction relationship with the largest moment capacity. It should be noted that if there was only one layer of tension steel the balance point could be determined directly by setting the outer concrete strain to the failure strain and the steel strain to the yield value. The neutral axis is established by these two strains, and P_B and M_B could be found from statics.

The design of the column transverse reinforcement is based on the UBC 1973 requirements for a ductile moment resisting frame.

Design shear is found by the expression:

$$V_D = \frac{M_B}{a}$$

where

M_B = balance point moment

a = shear span (assumed equal to 18 in. in the test column)

i. Rectangular tied column

Design shear V_d

$$V_d = \frac{1380 \text{ K-in.}}{18 \text{ in.}} = 77 \text{ kip}$$

Allowable concrete shear stress, v_c

$$v_c = 2(1 + 0.5 \frac{P}{A_g})\sqrt{f'_c} = 260 \text{ psi}$$

Since

$$\frac{P}{A_g} = 1{,}660 \text{ psi} > .12 f'_c = 600 \text{ psi}$$

the concrete may be considered effective in shear.

The shear force resisted by concrete, V_c, is then

$$V_c = v_c A_c$$

A_c = core area = 110 in.^2

$$V_c = 28.5 \text{ kip}$$

The transverse reinforcement must resist the remaining shear.

$$V_u - V_c = 77 \text{ kip} - 28.5 \text{ kip} = 48.5 \text{ kip}$$

$$\frac{A_v f_y d_c}{\phi\ s} = V_u - V_c$$

f_y = 40,000 psi (specified design value)

Assume 2 #2 ties $A_v = 0.2$ in.^{2}, $\phi = 0.85$

$$s = \frac{A_v f_y d_c}{\phi (V_u - V_c)}$$

By substituting the appropriate values, s is found to be 2.04 in. A spacing of 2 in. is selected.

Check minimum requirements.

$$A_{sh} \geq 0.3\ s_h h_c \frac{f'_c}{f_{yh}} \left(\frac{A_g}{A_{core}} - 1 \right)$$

$$= 0.3\ (2\text{ in.})(7.5\text{ in.}) \frac{5000\text{ psi}}{40000\text{ psi}} \left(\frac{144\text{ in.}^2}{110\text{ in.}^2} - 1 \right)$$

$$= 0.17\text{ in.}^2 < 0.2\text{ in.}^2 \quad \text{Okay} \qquad \text{(UBC 26-5)}$$

$$A_{sh} \geq 0.12\ s_h h_c \frac{f'_c}{f_{yh}} = 0.12\ (2\text{ in.})(7.5\text{ in.}) \frac{5000\text{ psi}}{40000\text{ psi}}$$

$$= 0.11\text{ in.}^2 < 0.2\text{ in.}^2 \quad \text{Okay} \qquad \text{(UBC 26-6)}$$

To use 2 #2 rectangular ties at 2 in.

ii. Spiral Reinforcement

Design Shear

$$V_D = \frac{M_B}{a} = \frac{1260\text{ K-in.}}{18\text{ in.}} = 70\text{ kip}$$

Allowable concrete shear stress

$$v_c = 2\left(1 + 0.5 \frac{P}{A_g}\right) \sqrt{f'_c} = 2[1 + 0.5\ (1.390)]\ 70.7$$

$$= 2\ (1 + .69)\ 70.7 = 239 \text{ psi}$$

$$V_c = v_c A_c = 239 \text{ psi } (86.3 \text{ in.}^2) = 20.6 \text{ kip}$$

$$V_u - V_c = 70 \text{ kip} - 20.6 \text{ kip} = 49.4 \text{ kip}$$

$$s = \frac{A_v f_y (d_c)}{\phi (V_u - V_c)} = 0.1 \frac{(40 \text{ ksi})(10.5 \text{ in.})}{0.85(49.5 \text{ kip})}$$

$$s = 1.0 \text{ in.}$$

UBC 2626 (f)5 defines A_v as the "total cross-sectional area of special transverse reinforcement in tension within a distance s, except that two-thirds of such area shall be used in the case of circular spirals." Consequently,

$$s = \frac{2}{3}\ 1.0 \text{ in.} = .66 \text{ in.}$$

However, UBC 2607(m)2 stipulates that "the clear spacing between spirals shall not exceed 3 in. or be less than 1 in." Since the model column was a half scale model of the prototype structure, the lower limit of 1 in. becomes 1/2 in. in the test model. For a 1/4 inch-diameter spiral, this requirement results in a pitch of 0.75 inch instead of the above value computed from shear requirements. Since the difference between the two values is small, the shear strength should be adequate.

iii. Beam Design

The design of the model beams is based on the desire to limit inelastic deformation to the columns, i.e., a weak column-strong beam design philosophy is followed. The design shear forces and moments are based on the column balance point moment. The beam design moment may be expressed in terms of the column moment by the expression (Fig. B4):

$$M = \frac{M_B \ell_b}{2a}$$

where

a = column shear span

ℓ_b = beam shear span

Since the beams in both the S and R series models were to be the same, the tied column moment capacity is used in the beam design. The beam cross section of 5 in. by 36 in. was established by architectural considerations. A symmetric reinforcement arrangement is assumed.

$$M = \frac{1380 \text{ K-in.} \times 66 \text{ in.}}{18 \text{ in.} \times 2} = 2520 \text{ K-in.}$$

For an under-reinforced section:

$$M \simeq A_s f_y jd$$

$$A_s = \frac{M}{f_y} jd$$

Assume jd = 7/8 d $\simeq$ 30 in.

$$f_y = 52 \text{ ksi}$$

$$A_s = \frac{2520 \text{ K-in.}}{52 \text{ ksi} \cdot 30 \text{ in.}} = 1.62 \text{ in.}^2$$

Use two layers with 3 #5 in top layer and 2 #4 and 1 #5 in bottom layer. A_s for this arrangement is 1.64 in.^{2}

Additional longitudinal reinforcement was provided in accordance with UBC 2610 g which states, "If the depth of the web exceeds 3 feet, longitudinal reinforcement having a total area at least equal to 10 percent of the main tension steel area shall be placed near the faces of the web and distributed in the zone of flexural tension with a spacing not more than 12 in. or a width of the web, whichever is less."

Since the depth of the prototype was 6 feet, this reinforcement was required and 2 #2 bars spaced at 5 in. were placed through the depth of the beam (Fig. 2.9a). In addition, diagonal reinforcement was included to provide added safety against a shear failure in the beams, in particular, a sliding shear failure at the beam-column joint (Fig. 2.9a).

The computed moment capacity of a cross section which included all the reinforcement indicated above at first yield of the reinforcement was 3325 k-in. Thus the subassemblage beams have been overdesigned with respect to the estimated column capacities by a factor of 1.3. This should ensure that inelastic behavior will be limited to the columns.

iv. Design of Shear Reinforcement

Design shear is based on the computed value of M_y = 3326 K-in.

$$V_D = \frac{3326 \text{ K-in.}}{60 \text{ in.}} = 50 \text{ kip}$$

The allowable concrete shear stress is:

$$v_c = 2\sqrt{f'_c} = 140 \text{ psi}$$

and the concrete contribution is

$$V_c = v_c bd = (140 \text{ psi})(5 \text{ in.})(34 \text{ in.}) = 23.8 \text{ kip}$$

To determine shear reinforcement, the expression:

$$\frac{A_v f_y d_c}{s} = V_u - V_c$$

is used. #2 stirrups are assumed with $A_s = 0.1 \text{ in.}^2$

$$s = \frac{0.1 \text{ in.}^2 (40 \text{ ksi})(33 \text{ in.})}{50 \text{ kip} - 23.8 \text{ kip}} = \frac{132}{26.2} = 5 \text{ in.}$$

Use #2 stirrups at 4 in.

B.5 SI Unit Conversions

1 ft. = .3048 m

1 in. = 25.4 mm

1 in.^2 = 645.2 mm^2

1 lb/ft^3 = 16.03 kg/m^3

1 k/ft^2 = 1000 lb/ft^2 = 47.9 kN/m^2

1 ksi = 1000 psi = 6.895 MPa

1 K-ft = 1.356 kN·m

1 K-in = 0.113 kN·m

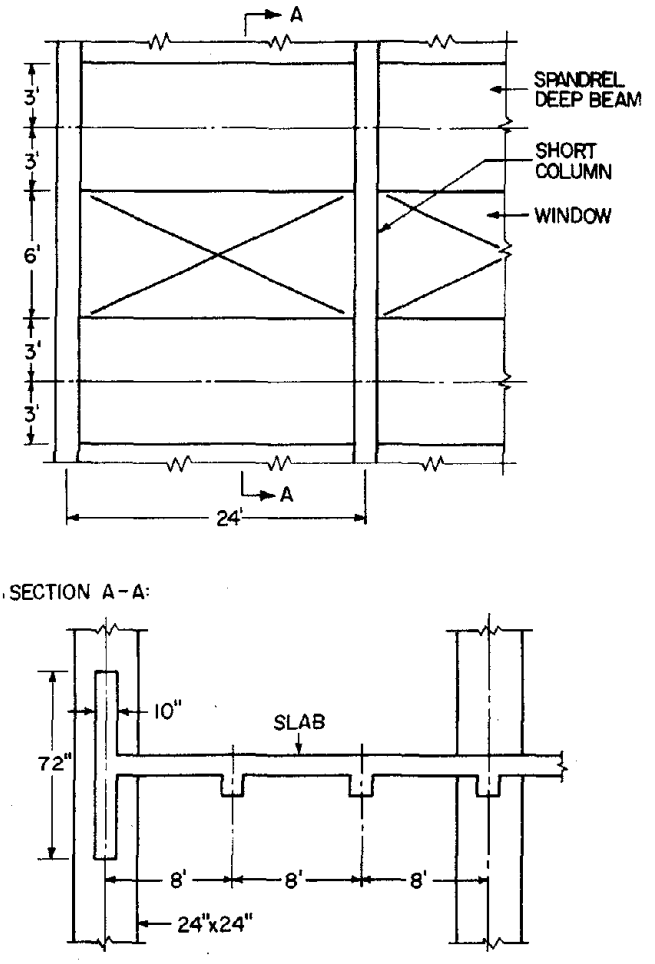

FIG. B1 ASSUMED STRUCTURAL SYSTEM
(1 FT = 0.305 M, 1 IN. = 25.4 MM)

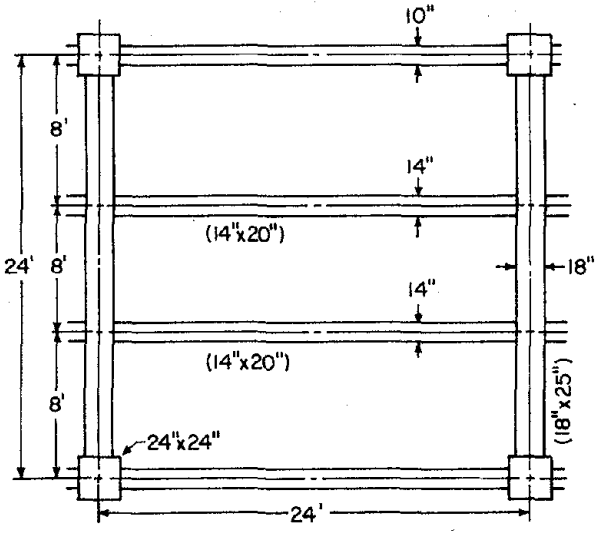

FIG. B2 ASSUMED MEMBER SIZES (1 FT = 0.305 M,
1 IN. = 25.4 MM)

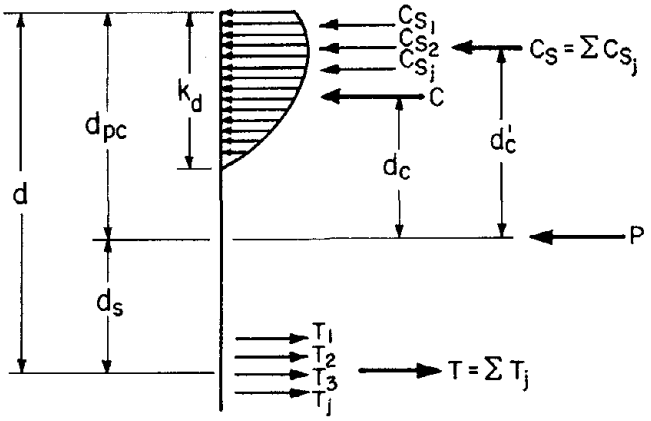

FIG. B3 SECTION EQUILIBRIUM

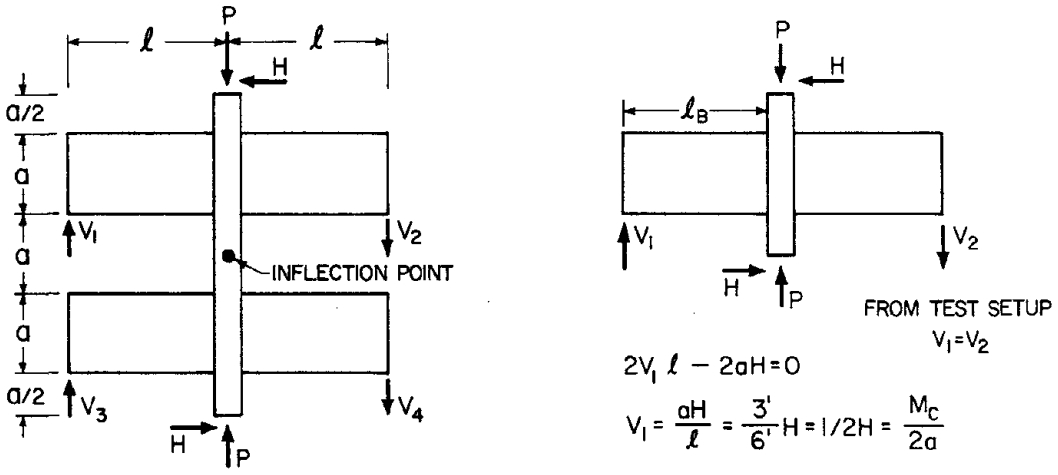

(a) ENTIRE SUBASSEMBLAGE

FIG. B4 SUBASSEMBLAGE EQUILIBRIUM (1 FT = 0.305 M)

APPENDIX C. ELEMENT PROPERTIES

The properties of the various finite elements used in this investigation are presented in the following sections. All element properties are based on the undeformed configuration.

C.1 Q-4 ELEMENT

The basic element used to represent concrete is a 4-node isoparametric quadrilateral (Fig. C.1). For a general quadrilateral element, the local and global coordinate systems are related by:

$$y = \sum_{i=1}^{4} h_i y_i \qquad \text{C.1a}$$

$$z = \sum_{i=1}^{4} h_i z_i \qquad \text{C.1b}$$

where the interpolation functions are given by:

$$h_1 = \frac{1}{4}(1 - s)(1 - t) \qquad \text{C.2a}$$

$$h_2 = \frac{1}{4}(1 + s)(1 - t) \qquad \text{C.2b}$$

$$h_3 = \frac{1}{4}(1 + s)(1 + t) \qquad \text{C.2c}$$

$$h_4 = \frac{1}{4}(1 - s)(1 + t) \qquad \text{C.2d}$$

In order to ensure rigid body displacement modes, the same interpolation functions are used in the displacement approximation.

$$d\bar{u}_y(s,t) = \sum h_i du_{yi} \qquad \text{C.3a}$$

$$d\bar{u}_z(s,t) = \sum h_i du_{zi} \qquad \text{C.3b}$$

where $d\bar{u}$ and du_i indicate increments in the element displacement field and element nodal displacements, respectively.

For two dimensional analyses the incremental strain-displacement relationships are given by:

$$d\varepsilon_{yy} = \frac{\partial du_y}{\partial y} = \sum h_{i,y} du_{yi} \qquad \text{C.4a}$$

$$d\varepsilon_{zz} = \frac{\partial du_z}{\partial z} = \sum h_{i,z} du_{zi} \qquad \text{C.4b}$$

$$d\varepsilon_{yz} = \frac{\partial du_y}{\partial z} + \frac{\partial du_z}{\partial y} = \sum h_{i,z} du_{yi} + \sum h_{i,y} du_{zi} \qquad \text{C.4c}$$

or, in matrix form,

$$d\underline{\varepsilon} = \underline{B}(s,t)\ d\underline{u} = \begin{bmatrix} \underline{H},y & 0 \\ 0 & \underline{H},z \\ \underline{H},z & \underline{H},y \end{bmatrix} \begin{bmatrix} d\underline{u}_y \\ d\underline{u}_z \end{bmatrix} \qquad \text{C.5}$$

where

$$\underline{H},y = \begin{bmatrix} h_{1,y} & h_{2,y} & h_{3,y} & h_{4,y} \end{bmatrix} \qquad \text{C.6a}$$

$$\underline{H},z = \begin{bmatrix} h_{1,z} & h_{2,z} & h_{3,z} & h_{4,z} \end{bmatrix} \qquad \text{C.6b}$$

$$\underline{du}_y = \begin{bmatrix} du_{y1} \\ du_{y2} \\ du_{y3} \\ du_{y4} \end{bmatrix} \quad \underline{du}_z = \begin{bmatrix} du_{z1} \\ du_{z2} \\ du_{z3} \\ du_{z4} \end{bmatrix} \qquad \text{C.6c}$$

Since the functions, h_i, are in terms of s and t, the chain rule is applied in order to compute the derivatives with respect to the global, y-z coordinate system.

$$h_{i,y} = h_{i,s}\, s,y + h_{i,t}\, t,y \qquad \text{C.7a}$$

$$h_{i,z} = h_{i,s}\, s,z + h_{i,t}\, t,z \qquad \text{C.7b}$$

In general, the chain rule can be written as:

$$\begin{bmatrix} \frac{\partial}{\partial s} \\ \frac{\partial}{\partial t} \end{bmatrix} = \begin{bmatrix} y,s & z,s \\ y,t & z,t \end{bmatrix} \begin{bmatrix} \frac{\partial}{\partial y} \\ \frac{\partial}{\partial z} \end{bmatrix} \qquad \text{C.8}$$

or inverted as:

$$\begin{bmatrix} \frac{\partial}{\partial y} \\ \frac{\partial}{\partial z} \end{bmatrix} = \begin{bmatrix} s,y & t,y \\ s,z & t,z \end{bmatrix} \begin{bmatrix} \frac{\partial}{\partial s} \\ \frac{\partial}{\partial t} \end{bmatrix} \qquad \text{C.9}$$

Therefore the derivatives required in Equation C.7 are given by:

$$\begin{bmatrix} s,y & t,y \\ s,z & t,z \end{bmatrix} = \frac{1}{J} \begin{bmatrix} z,t & -z,s \\ -y,t & y,s \end{bmatrix} \qquad \text{C.10}$$

where the Jacobian, J, is:

$$J = y,s \cdot z,t - y,t \cdot z,s \qquad \text{C.11}$$

and

$$y,s = \sum h_{i,s} y_i \qquad \text{C.12a}$$

$$y,t = \sum h_{i,t} y_i \qquad \text{C.12b}$$

$$z,s = \sum h_{i,s} z_i \qquad \text{C.12c}$$

$$z,t = \sum h_{i,t} z_i \qquad \text{C.12d}$$

For given numerical values of s and t the derivatives of the interpolating functions can be evaluated. Then all derivatives required for the evaluation of the strain displacement relationship can be determined from Equations C.10 and C.12.

For a constant element thickness, the element tangent stiffness matrix is given by:

$$\underline{K}_T = t \int_{\text{Area}} \underline{B}^T \underline{D}_T \underline{B} \, dA \qquad \text{C.13}$$

where $\underline{D}_T$ is the current constitutive matrix, and the integration is carried out over the area of the element.

For the purpose of numerical integration, Equation C.13 is written in the local s-t coordinate system as:

$$\underline{K}_T = t \int_{-1}^{1} \int_{-1}^{1} \underline{B}^T \underline{D}_T \underline{B} \, J \, ds \, dt \qquad C.14$$

The direct application of one-dimensional numerical integration formulas yield:

$$\underline{K}_T = \sum_j \sum_k W_j W_k J \underline{B}^T(s_j, t_k) \underline{D}_T(s_j, t_k) \underline{B}(s_j, t_k) \qquad C.15$$

in which s_j and t_k are integration points and W_j and W_k are the appropriate weight functions. Four point Gaussian quadrature is used in this investigation.

$$\begin{aligned} s_j &= \pm 0.57735 \qquad j = 1,2 \\ t_k &= \pm 0.57735 \qquad k = 1,2 \\ W_j &= W_k = 1.0 \end{aligned} \qquad C.16$$

The increment in element stresses is given by:

$$d\underline{\sigma}(s,t) = \underline{D}_T(s,t) d\underline{\varepsilon}(s,t) \qquad C.17$$

Substituting Equation C.5 into C.17 yields:

$$d\underline{\sigma}(s,t) = \underline{D}_T(s,t) \underline{B}(s,t) d\underline{u} \qquad C.18$$

The stress increment is evaluated at the numerical integration points used in evaluation of the element stiffness matrix.

C.2 CONSTANT STRAIN TRIANGLE

Constant strain triangles are employed to include inclined cracks in the analysis (Fig. C.2a). The incremental element displacements are given by Equation C.3. The interpolation functions are:

$$H_i = \frac{1}{2\Delta}(a_i + b_i y + c_i z) \quad i = 1 \tag{C.19}$$

where

$$2\Delta = \det\begin{bmatrix} 1 & y_1 & z_1 \\ 1 & y_2 & z_2 \\ 1 & y_3 & z_3 \end{bmatrix} = 2 * \text{area of triangle} \tag{C.20}$$

y_i and z_i are the nodal coordinates

$$a_i = y_j z_m - y_m z_j \tag{C.21a}$$

$$b_i = z_j - z_m \tag{C.21b}$$

$$c_i = y_m - y_j \tag{C.21c}$$

where i = 1,2,3 and j and m are the remaining terms in the cyclic permutation of the sequence 1,2,3. For example, if i =2, j =3, m = 1.

Using these interpolation functions, the incremental strain displacement transformation matrix, B, is given by:

$$\underline{B} = \frac{1}{2\Delta}\begin{bmatrix} b_1 & 0 & b_2 & 0 & b_3 & 0 \\ 0 & c_1 & 0 & c_2 & 0 & c_3 \\ c_1 & b_1 & c_2 & b_2 & c_3 & b_3 \end{bmatrix} \tag{C.22}$$

It is seen that $\underline{B}$ is dependent only on the nodal coordinates, which are assumed constant. Therefore $\underline{B}$ is a constant.

The element tangent stiffness matrix is given by Equation C.13. Since $\underline{B}$ is constant and $\underline{D}_T$ is assumed constant within the element*, the tangent stiffness is given by:

$$\underline{K}_T = \underline{B}^T \underline{D}_T \underline{B} t \Delta \qquad \text{C.23}$$

C.3 BAR ELEMENT

A two-dimensional bar element is used to model the steel reinforcement. A typical element connected between nodes i,j is shown in Fig. C.2b. The axial displacement increment in the s-direction is assumed to vary linearly along the length of element.

$$du_s = du_{si} + \frac{s}{L}(du_{sj} - du_{si}) \qquad \text{C.24}$$

where

$$s = 0 \text{ at } i \qquad \text{C.25a}$$

$$L = \sqrt{L_y^2 + L_z^2} \qquad \text{C.25b}$$

$$L_y = y_j - y_i \qquad \text{C.25c}$$

$$L_z = z_j - z_i \qquad \text{C.25d}$$

Therefore, the increment in axial strain is:

---

* The element is a constant strain (stress) element.

$$d\varepsilon_s = \frac{\partial du_s}{\partial s} = \frac{1}{L} (du_{sj} - du_{si}) \qquad C.26$$

The axial displacement increment, du_s, is given in terms of the global displacement increments by:

$$du_s = \frac{L_y}{L} du_y + \frac{L_z}{L} du_z \qquad C.27$$

Substituting Equation C.27 into Equation C.26 yields the following incremental strain-displacement transformation matrix, $\underline{B}$:

$$\underline{B} = \frac{1}{L^2} [-L_y \; -L_z \; L_y \; L_z] \qquad C.28$$

If the cross sectional area and the tangent stress-strain modulus, E_T, are assumed constant over the element length, the element tangent stiffness is given by:

$$\underline{K_T} = \frac{AE_T}{L^3} \underline{B}^T \underline{B} \qquad C.29$$

where A is the element area.

C.4 LINKAGE ELEMENTS

In order to include bond between steel and concrete elements and also to include the shear forces developed across a crack by aggregate interlock and dowel action of the reinforcement, various linkage elements with appropriate tangent link stiffness have been formulated. The basic component of these elements is a dimensionless link (spring) with a tan-

gent stiffness, K_T. The bond element consists of two links, one parallel to the axis of the reinforcement bar, the other perpendicular to it. Aggregate interlock is modeled by a link parallel to a crack and dowel action is modeled by two links, one perpendicular to any transverse reinforcement crossing the crack, the other perpendicular to any longitudinal reinforcement crossing the crack. To simplify the data transfer within the computer program, the aggregate interlock and dowel links are grouped as a single linkage element. Since the individual component links have the same global degrees of freedom, the addition of the component stiffness can be completed in the element formation.

The stiffness matrix of a typical link is derived below. In the computer code, the formation of the element stiffness matrix is explicit, i.e., the indicated matrix multiplications have been completed algebraically, and the resulting expressions are used in the stiffness formation.

The local incremental force developed by the link is:

$$\underline{K}_L \underline{du}_L = K_T \begin{bmatrix} 1 & -1 \\ -1 & 1 \end{bmatrix} \begin{Bmatrix} du_{L_1} \\ du_{L_2} \end{Bmatrix} \qquad \text{C.30}$$

where $\underline{du}_L$ is the local incremental displacement associated with a given link (Fig. C.3c).

In order to express the link tangent stiffness in global coordinates, the following transformations are used:

$$\underline{du}_L = \begin{bmatrix} \cos\theta & 0 & \sin\theta & 0 \\ 0 & \cos\theta & 0 & \sin\theta \end{bmatrix} \begin{Bmatrix} du_{1y} \\ du_{2y} \\ du_{1z} \\ du_{2z} \end{Bmatrix} \qquad \text{C.31a}$$

$$= \underline{B}\,\underline{du} \qquad \text{C.31b}$$

where θ is the angle which defines the orientation of the link with respect to the global coordinates (Fig. C.3c), and $\underline{du}$ is the global displacement increment at the element nodes; and

$$\underline{dF} = \underline{B}^T \underline{dF}_L \qquad \text{C.32}$$

where $\underline{dF}$ is the global link force increment.

Substituting Equations C.31 and C.32 into Equation C.30 results in the following expression:

$$\underline{dF} = \underline{B}^T \underline{K}_L \underline{B}\,du \qquad \text{C.33}$$

The global tangent stiffness matrix for a given link is then:

$$\underline{K}_T^{global} = \underline{B}^T \underline{K}_L \underline{B} \qquad \text{C.34}$$

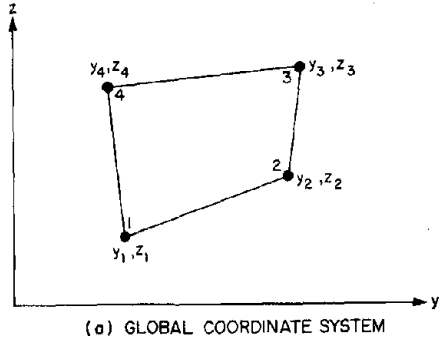

(a) GLOBAL COORDINATE SYSTEM

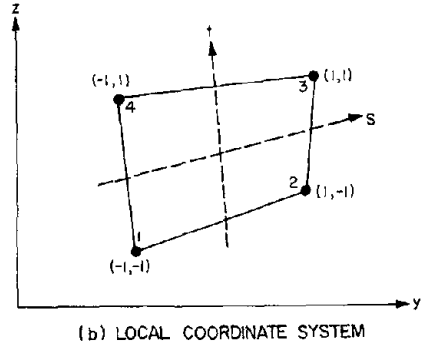

(b) LOCAL COORDINATE SYSTEM

FIG. C1 GENERAL FOUR-NODE QUADRILATERAL

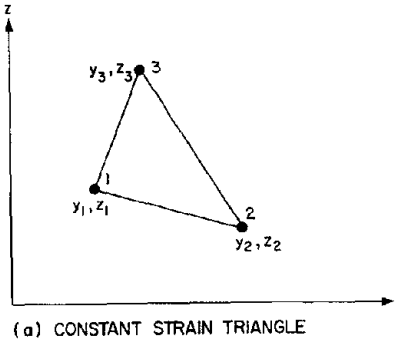

(a) CONSTANT STRAIN TRIANGLE

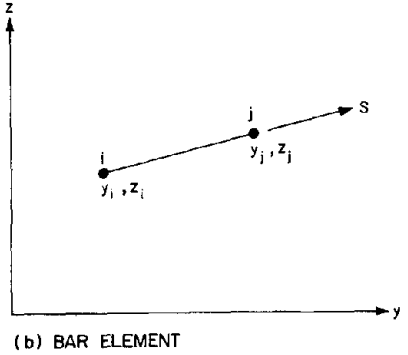

(b) BAR ELEMENT

FIG. C2 TRIANGULAR AND BAR FINITE ELEMENTS

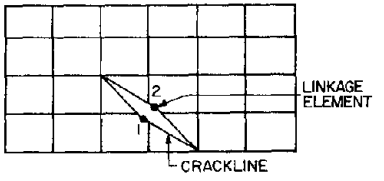

(a) COUPLING ACROSS A CRACK LINE

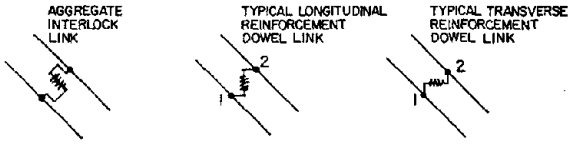

NOTE: ALL LINKS ARE DIMENSIONLESS

(b) LINK COMPONENTS

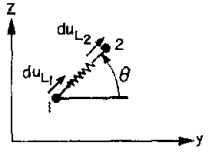

(c) TYPICAL LINK

FIG. C3 DOWEL ACTION AND AGGREGATE INTERLOCK LINKAGE ELEMENT

APPENDIX D. MATERIAL LAW

D.1 INTRODUCTION

It is important to include the essential characteristics of the actual material behavior if an accurate analytical model is to result. In the case of concrete, the highly nonlinear compressive behavior (Fig. D.1), the brittle behavior in tension, and the effects of biaxial stresses on the stress-strain behavior (Fig. D.2) and on the material strength (Fig. D.3) are considered important characteristics and attempts are made to include them in the proposed model. The constitutive relationship and the analytical representation of the biaxial stress-strain behavior used in this investigation are from previous work by Darwin and Pecknold (22).

D.2 ORTHOTROPIC CONSTITUTIVE LAW

The experimental biaxial stress-strain behavior of plain concrete led Darwin and Pecknold to consider an orthotropic material law. Concrete is assumed to be an incrementally linear orthotropic material. The general constitutive equation in material coordinates is:

$$\begin{Bmatrix} d\sigma_1 \\ d\sigma_2 \\ d\tau_{12} \end{Bmatrix} = \frac{1}{1-\nu_1\nu_2} \begin{bmatrix} E_1 & \nu_2 E_1 & 0 \\ \nu_1 E_2 & E_2 & 0 \\ 0 & 0 & G(1-\nu_1\nu_2) \end{bmatrix} \begin{Bmatrix} d\varepsilon_1 \\ d\varepsilon_2 \\ d\gamma_{12} \end{Bmatrix} \qquad \text{D.1}$$

where E_1, E_2, G, ν_1, and ν_2 are stress dependent material properties and the material axes coincide with the current principal stress axes.

Darwin and Pecknold made the following modifications to simplify the constitutive equation and to insure that no particular direction is favored with respect to the Poisson ratios, ν_1 and ν_2, and the shear modulus, G.

a. From energy considerations it may be shown that

$$\nu_1 E_2 = \nu_2 E_1 \qquad \text{D.2}$$

Defining an equivalent Poisson's ratio by the expression:

$$\nu^2 = \nu_1\nu_2 \qquad \text{D.3}$$

and substituting Equations D.2 and D.3 into Equation D.1, the following constitutive relationship results.

$$\begin{Bmatrix} d\sigma_1 \\ d\sigma_2 \\ d\tau_{12} \end{Bmatrix} = \frac{1}{1-\nu^2} \begin{bmatrix} E_1 & \nu\sqrt{E_1 E_2} & 0 \\ & E_2 & 0 \\ \text{SYM} & & (1-\nu^2)G \end{bmatrix} \begin{Bmatrix} d\varepsilon_1 \\ d\varepsilon_2 \\ d\gamma_{12} \end{Bmatrix} \qquad \text{D.4}$$

b. A second modification involves G, the shear modulus. By re-

quiring G', the shear modulus resulting from an arbitrary coordinate transformation defined by an angle, θ, to be independent of θ, it may be established that:

$$(1-\nu^2)G = (1-\nu^2)G' = \frac{1}{4}(E_1+E_2-2\nu\sqrt{E_1E_2}) \qquad \text{D.5}$$

and Equation D.4 becomes:

$$\begin{Bmatrix} d\sigma_1 \\ d\sigma_2 \\ d\tau_{12} \end{Bmatrix} = \frac{1}{1-\nu^2}\begin{bmatrix} E_1 & \nu\sqrt{E_1E_2} & 0 \\ & E_2 & 0 \\ \text{SYM} & & \frac{1}{4}(E_1+E_2-2\nu\sqrt{E_1E_2}) \end{bmatrix}\begin{Bmatrix} d\varepsilon_1 \\ d\varepsilon_2 \\ d\gamma_{12} \end{Bmatrix} \qquad \text{D.6}$$

With the above modifications, the constitutive relationship is defined completely by three quantities, E_1, E_2 and ν. The constitutive relationship for a coordinate system rotated by an angle, θ, with respect to the material coordinates is:

$$\begin{Bmatrix} d\sigma_1' \\ d\sigma_2' \\ d\tau_{12}' \end{Bmatrix}$$

$$= \frac{1}{1-\nu^2}\begin{bmatrix} E_1\cos^2\theta+E_2\sin^2\theta & \nu\sqrt{E_1E_2} & \frac{1}{2}(E_1-E_2)\sin\theta\cos\theta \\ & E_1\sin^2\theta+E_2\cos^2\theta & \frac{1}{2}(E_1-E_2)\sin\theta\cos\theta \\ \text{SYM} & & \frac{1}{4}(E_1+E_2-2\nu\sqrt{E_1E_2}) \end{bmatrix}\begin{Bmatrix} d\varepsilon_1' \\ d\varepsilon_2' \\ d\gamma_{12}' \end{Bmatrix} \qquad \text{D.7}$$

D.3 EQUIVALENT UNIAXIAL STRAIN

Darwin and Pecknold developed the concept of "equivalent uniaxial strain" in order to predict analytically the biaxial stress-strain behavior of plain concrete from uniaxial stress-strain curves. For a biaxial state of stress, the strain in one direction is a function not only of stress in that direction but also of the stress in the orthogonal direction. The concept of equivalent uniaxial strain provides a method to separate the Poisson strain effect from the cumulative strain.

The equivalent uniaxial strain in the i^{th} principal direction, ε_{iu}, is defined by the expression:

$$\varepsilon_{iu} = \int d\varepsilon_{iu} = \int \frac{d\sigma_i}{E_i} \qquad \text{D.8}$$

where

$d\varepsilon_{iu}$ = the differential change in the equivalent uniaxial strain in the i^{th} direction.

$d\sigma_i$ = the differential change in stress in the i^{th} direction

E_i = tangent modulus of elasticity in the i^{th} direction

For an incremental analysis, Equation D.8 becomes:

$$\varepsilon_{iu} = \sum_{j=1}^{N} \frac{\Delta\sigma_i^j}{E_i^j} \qquad \text{D.9}$$

where

N = number of load increments

$\Delta\sigma_i^j$ = the stress increment in the i^{th} direction in the j^{th} load increment

E_i^j = the tangent modulus in the i^{th} direction in the j^{th} increment

The equivalent uniaxial strains, ε_{1u} and ε_{2u}, are associated with the principal stress axes.

In the material model, the material axes coincide with the direction of the current principal stresses. In the incremental solution process the material axes rotate as the principal stresses rotate. By allowing the material axes to rotate with the principal stresses, the tangent stiffnesses, E_1 and E_2, always represent the moduli corresponding to the extreme values of stress.

To insure that the stress and equivalent uniaxial strain history developed at one orientation continues to control the material behavior in essentially the same orientation, the rotation of the material axes is limited. If the principal stress axes rotate by more than 45 degrees from their original orientation, the material axes are reoriented as illustrated in Fig. D.4.

D.4 EQUIVALENT UNIAXIAL STRESS-STRAIN CURVES

The concept of equivalent uniaxial strain is used in conjunction with a family of equivalent uniaxial compressive stress-strain relationships to model the biaxial compressive behavior of plain concrete. In

tension, concrete is assumed to be a linear-elastic brittle material.

The family of compressive loading curves, which are dependent on the existing biaxial stress state, is based on an equation suggested by Saenz (26) and is illustrated in Fig. D.5.

$$\sigma_i = \frac{\varepsilon_{iu} E_o}{1 + \left[\frac{E_o}{E_s} - 2\right]\frac{\varepsilon_{iu}}{\varepsilon_{ic}} + \left[\frac{\varepsilon_{iu}}{\varepsilon_{ic}}\right]^2} \qquad \text{D.10}$$

where

E_o = tangent modulus at zero stress

E_s = secant modulus at the point of maximum compressive stress, σ_{ic}
= $\sigma_{ic}/\varepsilon_{ic}$

ε_{ic} = the equivalent uniaxial strain at σ_{ic}

Equation D.10 is completely defined by the quantities E_o, σ_{ic} and ε_{ic}. The value of E_o can be derived from standard relationships such as the UBC relationship [2608(c)], or it can be based on experimental stress-strain data. The values of σ_{ic} and ε_{ic} are dependent on the existing biaxial stress condition. How σ_{ic} and ε_{ic} depend on the existing state of stress is presented below.

a. Determination of σ_{ic}. Recent experimental investigations into the biaxial behavior of plain concrete (27, 28, 29) have indicated that an increase in compressive strength occurs in the presence of even a small secondary compressive stress. This is considered

an essential feature of the biaxial behavior of concrete and is included in the material model by the quantity, σ_{ic}. The maximum strength envelope suggested by Kupfer and Gerstle (34) and modified slightly by Darwin and Pecknold is used to determine the value of σ_{ic} corresponding to a particular biaxial stress state (Fig. D.3).

The maximum compressive strength of concrete, σ_{2c}, for a given biaxial stress ratio, α

$$\alpha = \frac{\sigma_1}{\sigma_2} \qquad \text{D.11}$$

where $\sigma_1 \geq \sigma_2$*, is determined as a function of the uniaxial compressive strength, f'_c, by the expression:

$$\sigma_{2c} = \frac{1 + \beta\alpha}{1 + \alpha^2} f'_c \qquad \text{D.12}$$

where β is a constant dependent on α:

if $\alpha > 0$ then $\beta = 3.64$ (biaxial compression)

if $0 \geq \alpha > \gamma$ then $\beta = 3.28$ (tension-compression)

for $\alpha > \gamma$ σ_{2c} = a constant = $0.65\ f'_c$

The limiting value of α for a tension-compression stress state, γ, is needed because of the assumption that the strength envelope has a constant tensile strength until:

---

* algebraic sign convention is in effect and compressive stresses are negative

$$|\sigma_{2c}| > |0.65\ f'_c| \qquad \text{D.13}$$

This corresponds to a value of γ of -0.17.

b. Determination of ε_{ic}. To complete the definition of the equivalent uniaxial stress-strain relationship, the value of ε_{ic}, the equivalent uniaxial strain at the peak compressive stress must be defined. Experimental investigations of the biaxial behavior of plain concrete (27, 28) have indcated that for compressive strengths greater than f'_c, an increase in the strain at the maximum stress occurs. Darwin and Pecknold proposed the following equation to quantify this phenomenon:

$$\varepsilon_{ic} = \varepsilon_{cu}\left[\frac{\sigma_{ic}}{f'_c} \cdot R - (R-1)\right] \qquad \text{D.14}$$

where

ε_{cu} = strain at the peak stress for the uniaxial stress-strain relationship

$$R = \frac{\dfrac{\varepsilon_{ic}(\alpha=1)}{\varepsilon_{cu}} - 1}{\dfrac{\sigma_{ic}(\alpha=1)}{f'_c} - 1} \qquad \text{D.15}$$

where

$\varepsilon_{ic}(\alpha=1)$ = the equivalent uniaxial strain at the maximum compressive stress, σ_{ic}, for equal biaxial compression

In this study, R in Equation D.13 is set equal to 3. For cases when the magnitude of σ_{ic} is less than the magnitude of f'_c however, Darwin and Pecknold found that better results for ε_{ic} were obtained with the expression:

$$\varepsilon_{ic} = \varepsilon_{cu}\left[-1.6\left(\frac{\sigma_{ic}}{f'_c}\right)^3 + 2.25\left(\frac{\sigma_{ic}}{f'_c}\right)^2 + 0.35\left(\frac{\sigma_{ic}}{f'_c}\right)\right] \qquad \text{D.16}$$

A restriction is placed on ε_{ic} to insure that the ratio E_o/E_s in Equation D.10 is always greater than or equal to 2. This prevents the shape of the σ-ε curve from becoming concave upward.

c. Summary. With E_o, σ_{ic} and ε_{ic} defined, the equivalent uniaxial stress-strain relationship can be determined in each material direction from the existing stress condition. The tangent moduli in each direction can then be obtained and used in the incremental orthotropic constitutive law.

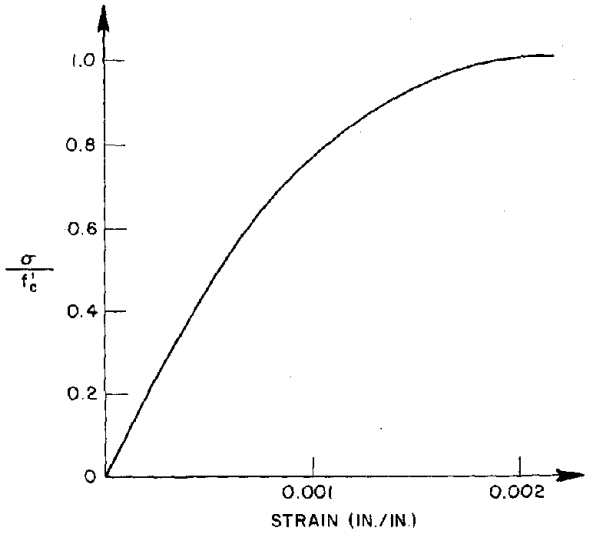

FIG. D1 NONLINEAR COMPRESSIVE STRESS-STRAIN BEHAVIOR

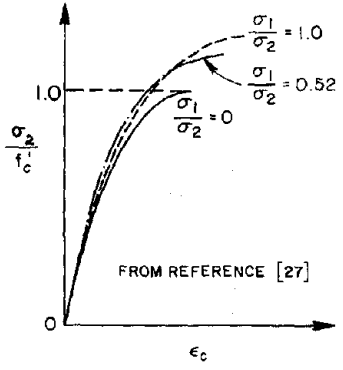

FIG. D2 EFFECT OF BIAXIAL STRESSES ON STRESS-STRAIN BEHAVIOR

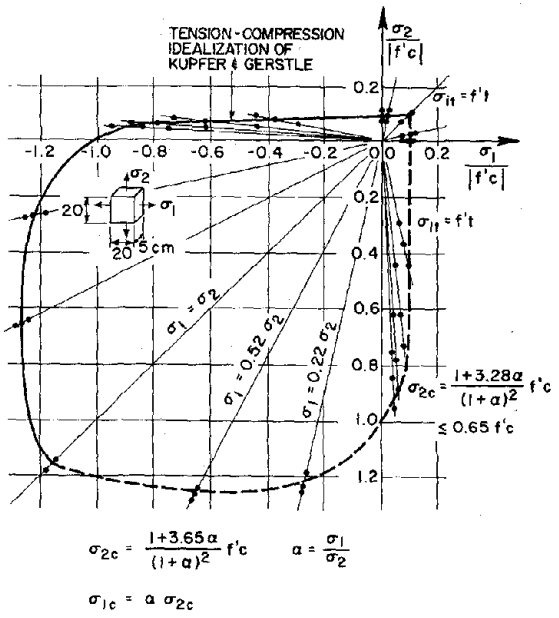

FIG. D3 BIAXIAL STRENGTH ENVELOPE FOR PROPOSED MODEL [22]

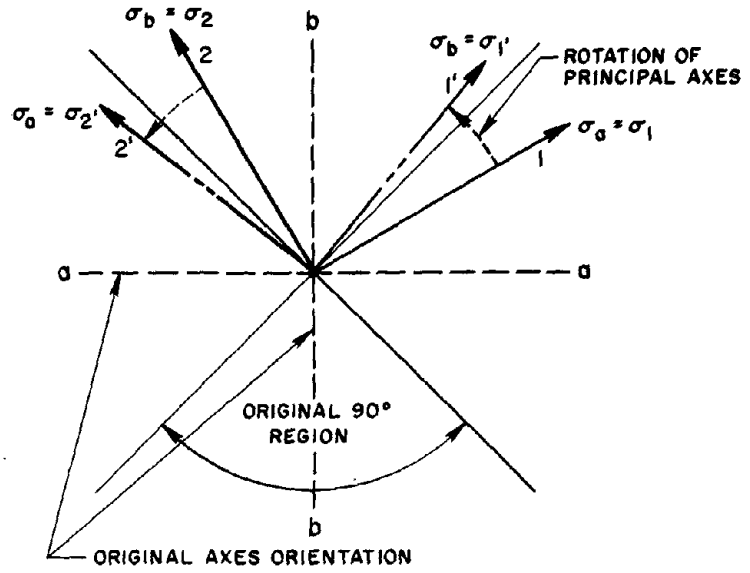

FIG. D4 ROTATION OF PRINCIPAL AXES OUT OF ORIGINALLY DEFINED REGIONS

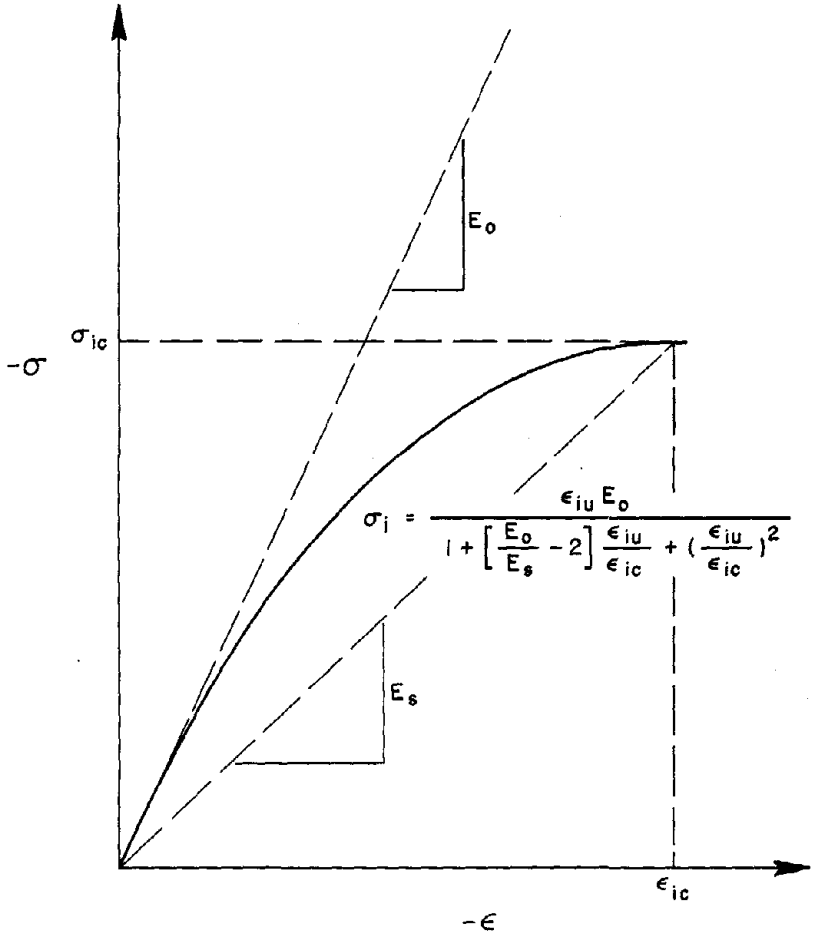

FIG. D5 EQUIVALENT UNIAXIAL STRESS-STRAIN CURVE

EARTHQUAKE ENGINEERING RESEARCH CENTER REPORTS

EARTHQUAKE ENGINEERING RESEARCH CENTER REPORTS

NOTE: Numbers in parentheses are Accession Numbers assigned by the National Technical Information Service; these are followed by a price code. Copies of the reports may be ordered from the National Technical Information Service, 5285 Port Royal Road, Springfield, Virginia, 22161. Accession Numbers should be quoted on orders for reports (PB--- ---) and remittance must accompany each order. Reports without this information were not available at time of printing. Upon request, EERC will mail inquirers this information when it becomes available.

EERC 67-1 "Feasibility Study of Large-Scale Earthquake Simulator Facility," by J. Penzien, J. G. Bouwkamp, R. W. Clough, and D. Rea - 1967 (PB 187 905)A07

EERC 68-1 Unassigned

EERC 68-2 "Inelastic Behavior of Beam-to-Column Subassemblages under Repeated Loading," by V. V. Bertero - 1968 (PB 184 888)A05

EERC 68-3 "A Graphical Method for Solving the Wave Reflection-Refraction Problem," by H. D. McNiven and Y. Mengi - 1968 (PB 187 943)A03

EERC 68-4 "Dynamic Properties of McKinley School Buildings," by D. Rea, J. G. Bouwkamp, and R. W. Clough - 1968 (PB 187 902)A07

EERC 68-5 "Characteristics of Rock Motions during Earthquakes," by H. B. Seed, I. M. Idriss, and F. W. Kiefer - 1968 (PB 188 338)A03

EERC 69-1 "Earthquake Engineering Research at Berkeley," - 1969 (PB 187 906)A11

EERC 69-2 "Nonlinear Seismic Response of Earth Structures," by M. Dibaj and J. Penzien - 1969 (PB 187 904)A08

EERC 69-3 "Probabilistic Study of the Behavior of Structures during Earthquakes," by R. Ruiz and J. Penzien - 1969 (PB 187 886)A06

EERC 69-4 "Numerical Solution of Boundary Value Problems in Structural Mechanics by Reduction to an Initial Value Formulation," by N. Distefano and J. Schujman - 1969 (PB 187 942)A02

EERC 69-5 "Dynamic Programming and the Solution of the Biharmonic Equation," by N. Distefano - 1969 (PB 187 941)A03

EERC 69-6 "Stochastic Analysis of Offshore Tower Structures," by A. K. Malhotra and J. Penzien - 1969 (PB 187 903)A09

EERC 69-7 "Rock Motion Accelerograms for High Magnitude Earthquakes," by H. B. Seed and I. M. Idriss - 1969 (PB 187 940)A02

EERC 69-8 "Structural Dynamics Testing Facilities at the University of California, Berkeley," by R. M. Stephen, J. G. Bouwkamp, R. W. Clough and J. Penzien - 1969 (PB 189 111)A04

EERC 69-9 "Seismic Response of Soil Deposits Underlain by Sloping Rock Boundaries," by H. Dezfulian and H. B. Seed - 1969 (PB 189 114)A03

EERC 69-10 "Dynamic Stress Analysis of Axisymmetric Structures under Arbitrary Loading," by S. Ghosh and E. L. Wilson - 1969 (PB 189 026)A10

EERC 69-11 "Seismic Behavior of Multistory Frames Designed by Different Philosophies," by J. C. Anderson and V. V. Bertero - 1969 (PB 190 662)A10

EERC 69-12 "Stiffness Degradation of Reinforcing Concrete Members Subjected to Cyclic Flexural Moments," by V. V. Bertero, B. Bresler, and H. Ming Liao - 1969 (PB 202 942)A07

EERC 69-13 "Response of Non-Uniform Soil Deposits to Travelling Seismic Waves," by H. Dezfulian and H. B. Seed - 1969 (PB 191 023)A03

EERC 69-14 "Damping Capacity of a Model Steel Structure," by D. Rea, R. W. Clough, and J. G. Bouwkamp - 1969 (PB 190 663)A06

EERC 69-15 "Influence of Local Soil Conditions on Building Damage Potential during Earthquakes," by H. B. Seed and I. M. Idriss - 1969 (PB 191 036)A03

EERC 69-16 "The Behavior of Sands under Seismic Loading Conditions," by M. L. Silver and H. B. Seed - 1969 (AD 714 982)A07

EERC 70-1 "Earthquake Response of Gravity Dams," by A. K. Chopra - 1970 (AD 709 640)A03

EERC 70-2 "Relationships between Soil Conditions and Building Damage in the Caracas Earthquake of July 29, 1967," by H. B. Seed, I. M. Idriss, and H. Dezfulian - 1970 (PB 195 762)A05

EERC 70-3 "Cyclic Loading of Full Size Steel Connections," by E. P. Popov and R. M. Stephen - 1970 (PB 213 545)A04

EERC 70-4 "Seismic Analysis of the Charaima Building, Caraballeda, Venezuela," by Subcommittee of the SEAONC Research Committee: V. V. Bertero, P. F. Fratessa, S. A. Mahin, J. H. Sexton, A. C. Scordelis, E. L. Wilson, L. A. Wyllie, H. B. Seed, and J. Penzien, Chairman - 1970 (PB 201 455)A06

EERC 70-5 "A Computer Program for Earthquake Analysis of Dams," by A. K. Chopra and P. Chakrabarti - 1970 (AD 723 994)A05

EERC 70-6 "The Propagation of Love Waves Across Non-Horizontally Layered Structures," by J. Lysmer and L. A. Drake - 1970 (PB 197 896)A03

EERC 70-7 "Influence of Base Rock Characteristics on Ground Response," by J. Lysmer, H. B. Seed, and P. B. Schnabel - 1970 (PB 197 897)A03

EERC 70-8 "Applicability of Laboratory Test Procedures for Measuring Soil Liquefaction Characteristics under Cyclic Loading," by H. B. Seed and W. H. Peacock - 1970 (PB 198 016)A03

EERC 70-9 "A Simplified Procedure for Evaluating Soil Liquefaction Potential," by H. B. Seed and I. M. Idriss - 1970 (PB 198 009)A03

EERC 70-10 "Soil Moduli and Damping Factors for Dynamic Response Analysis," by H. B. Seed and I. M. Idriss - 1970 (PB 197 869)A03

EERC 71-1 "Koyna Earthquake of December 11, 1967 and the Performance of Koyna Dam," by A. K. Chopra and P. Chakrabarti - 1971 (AD 731 496)A06

EERC 71-2 "Preliminary In-Situ Measurements of Anelastic Absorption in Soils using a Prototype Earthquake Simulator," by R. D. Borcherdt and P. W. Rodgers - 1971 (PB 201 454)A03

EERC 71-3 "Static and Dynamic Analysis of Inelastic Frame Structures," by F. L. Porter and G. H. Powell - 1971 (PB 210 135)A06

EERC 71-4 "Research Needs in Limit Design of Reinforced Concrete Structures," by V. V. Bertero - 1971 (PB 202 943)A04

EERC 71-5 "Dynamic Behavior of a High-Rise Diagonally Braced Steel Building," by D. Rea, A. A. Shah, and J. G. Bouwkamp - 1971 (PB 203 584)A06

EERC 71-6 "Dynamic Stress Analysis of Porous Elastic Solids Saturated with Compressible Fluids," by J. Ghaboussi and E. L. Wilson - 1971 (PB 211 396)A06

EERC 71-7 "Inelastic Behavior of Steel Beam-to-Column Subassemblages," by H. Krawinkler, V. V. Bertero, and E. P. Popov - 1971 (PB 211 355)A14

EERC 71-8 "Modification of Seismograph Records for Effects of Local Soil Conditions," by P. Schnabel, H. B. Seed, and J. Lysmer - 1971 (PB 214 450)A03

EERC 72-1 "Static and Earthquake Analysis of Three Dimensional Frame and Shear Wall Buildings," by E. L. Wilson and H. H. Dovey - 1972 (PB 212 904)A05

EERC 72-2 "Accelerations in Rock for Earthquakes in the Western United States," by P. B. Schnabel and H. B. Seed - 1972 (PB 213 100)A03

EERC 72-3 "Elastic-Plastic Earthquake Response of Soil-Building Systems," by T. Minami - 1972 (PB 214 868)A08

EERC 72-4 " Stochastic Inelastic Response of Offshore Towers to Strong Motion Earthquakes," by M. K. Kaul - 1972 (PB 215 713)A05

EERC 72-5 "Cyclic Behavior of Three Reinforced Concrete Flexural Members with High Shear," by E. P. Popov, V. V. Bertero, and H. Krawinkler - 1972 (PB 214 555)A05

EERC 72-6 "Earthquake Response of Gravity Dams Including Reservoir Interaction Effects," by P. Chakrabarti and A. K. Chopra - 1972 (AD 762 330)A08

EERC 72-7 "Dynamic Properties of Pine Flat Dam," by D. Rea, C. Y. Liaw, and A. K. Chopra - 1972 (AD 763 928)A05

EERC 72-8 "Three Dimensional Analysis of Building Systems," by E. L. Wilson and H. H. Dovey - 1972 (PB 222 438)A06

EERC 72-9 "Rate of Loading Effects on Uncracked and Repaired Reinforced Concrete Members," by S. Mahin, V. V. Bertero, D. Rea and M. Atalay - 1972 (PB 224 520)A08

EERC 72-10 "Computer Program for Static and Dynamic Analysis of Linear Structural Systems," by E. L. Wilson, K.-J. Bathe, J. E. Peterson and H. H. Dovey - 1972 (PB 220 437)A04

EERC 72-11 "Literature Survey - Seismic Effects on Highway Bridges," by T. Iwasaki, J. Penzien, and R. W. Clough - 1972 (PB 215 613)A19

EERC 72-12 "SHAKE - A Computer Program for Earthquake Response Analysis of Horizontally Layered Sites," by P. B. Schnabel and J. Lysmer - 1972 (PB 220 207)A06

EERC 73-1 "Optimal Seismic Design of Multistory Frames," by V. V. Bertero and H. Kamil - 1973

EERC 73-2 "Analysis of the Slides in the San Fernando Dams during the Earthquake of February 9, 1971," by H. B. Seed, K. L. Lee, I. M. Idriss, and F. Makdisi - 1973 (PB 223 402)A14

EERC 73-3 "Computer Aided Ultimate Load Design of Unbraced Multistory Steel Frames," by M. B. El-Hafez and G. H. Powell - 1973 (PB 248 315)A09

EERC 73-4 "Experimental Investigation into the Seismic Behavior of Critical Regions of Reinforced Concrete Components as Influenced by Moment and Shear," by M. Celebi and J. Penzien - 1973 (PB 215 884)A09

EERC 73-5 "Hysteretic Behavior of Epoxy-Repaired Reinforced Concrete Beams," by M. Celebi and J. Penzien - 1973 (PB 239 568)A03

EERC 73-6 "General Purpose Computer Program for Inelastic Dynamic Response of Plane Structures," by A. Kanaan and G. H. Powell - 1973 (PB 221 260)A08

EERC 73-7 "A Computer Program for Earthquake Analysis of Gravity Dams Including Reservoir Interaction," by P. Chakrabarti and A. K. Chopra - 1973 (AD 766 271)A04

EERC 73-8 "Behavior of Reinforced Concrete Deep Beam-Column Subassemblages under Cyclic Loads," by O. Küstü and J. G. Bouwkamp - 1973 (PB 246 117)A12

EERC 73-9 "Earthquake Analysis of Structure-Founation Systems," by A. K. Vaish and A. K. Chopra - 1973 (AD 766 272)A07

EERC 73-10 "Deconvolution of Seismic Response for Linear Systems," by R. B. Reimer - 1973 (PB 227 179)A08

EERC 73-11 "SAP IV: A Structural Analysis Program for Static and Dynamic Response of Linear Systems," by K.-J. Bathe, E. L. Wilson, and F. E. Peterson - 1973 (PB 221 967)A09

EERC 73-12 "Analytical Investigations of the Seismic Response of Long, Multiple Span Highway Bridges," by W. S. Tseng and J. Penzien - 1973 (PB 227 816)A10

EERC 73-13 "Earthquake Analysis of Multi-Story Buildings Including Foundation Interaction," by A. K. Chopra and J. A. Gutierrez - 1973 (PB 222 970)A03

EERC 73-14 "ADAP: A Computer Program for Static and Dynamic Analysis of Arch Dams," by R. W. Clough, J. M. Raphael, and S. Mojtahedi - 1973 (PB 223 763)A09

EERC 73-15 "Cyclic Plastic Analysis of Structural Steel Joints," by R. B. Pinkney and R. W. Clough - 1973 (PB 226 843)A08

EERC 73-16 "QUAD-4: A Computer Program for Evaluating the Seismic Response of Soil Structures by Variable Damping Finite Element Procedures," by I. M. Idriss, J. Lysmer, R. Hwang, and H. B. Seed - 1973 (PB 229 424)A05

EERC 73-17 "Dynamic Behavior of a Multi-Story Pyramid Shaped Building," by R. M. Stephen, J. P. Hollings, and J. G. Bouwkamp - 1973 (PB 240 718)A06

EERC 73-18 "Effect of Different Types of Reinforcing on Seismic Behavior of Short Concrete Columns," by V. V. Bertero, J. Hollings, O. Küstü, R. M. Stephen, and J. G. Bouwkamp - 1973

EERC 73-19 "Olive View Medical Center Materials Studies, Phase I," by B. Bresler and V. V. Bertero - 1973 (PB 235 986)A06

EERC 73-20 "Linear and Nonlinear Sesismic Analysis Computer Programs for Long Multiple-Span Highway Bridges," by W. S. Tseng and J. Penzien - 1973

EERC 73-21 "Constitutive Models for Cyclic Plastic Deformation of Engineering Materials," by J. M. Kelly and P. P. Gillis - 1973 (PB 226 024)A03

EERC 73-22 "DRAIN-2D User's Guide," by G. H. Powell - 1973 (PB 227 016)A05

EERC 73-23 "Earthquake Engineering at Berkeley - 1973 " 1973 (PB 226 033)A11

EERC 73-24 Unassigned

EERC 73-25 "Earthquake Response of Axisymmetric Tower Structures Surrounded by Water," by C. Y. Liaw and A. K. Chopra - 1973 (AD 773 052)A09

EERC 73-26 "Investigation of the Failures of the Olive View Stairtowers during the San Fernando Earthquake and Their Implications on Seismic Design," by V. V. Bertero and R. G. Collins - 1973 (PB 235 106)A13

EERC 73-27 "Further Studies on Seismis Behavior of Steel Beam-Column Subassemblages," by V. V. Bertero, H. Krawinkler, and E. P. Popov - 1973 (PB 234 172)A06

EERC 74-1 "Seismic Risk Analysis," by C. S. Oliveira - 1974 (PB 235 920)A06

EERC 74-2 "Settlement and Liquefaction of Sands under Multi-Directional Shaking," by R. Pyke, C. K. Chan, and H. B. Seed - 1974

EERC 74-3 "Optimum Design of Earthquake Resistant Shear Buildings," by D. Ray, K. S. Pister, and A. K. Chopra - 1974 (PB 231 172)A06

EERC 74-4 "LUSH - A Computer Program for Complex Response Analysis of Soil-Structure Systems," by J. Lysmer, T. Udaka, H. B. Seed, and R. Hwang - 1974 (PB 236 796)A05

EERC 74-5 "Sensitivity Analysis for Hysteretic Dynamic Systems: Applications to Earthquake Engineering," by D. Ray - 1974 (PB 233 213)A06

EERC 74-6 "Soil Structure Interaction Analyses for Evaluating Seismic Response," by H. B. Seed, J. Lysmer, and R. Hwang - 1974 (PB 236 519)A04

EERC 74-7 Unassigned

EERC 74-8 "Shaking Table Tests of a Steel Frame - A Progress Report," by R. W. Clough and D. Tang - 1974 (PB 240 869)A03

EERC 74-9 "Hysteretic Behavior of Reinforced Concrete Flexural Members with Special Web Reinforcement," by V. V. Bertero, E. P. Popov, and T. Y. Wang - 1974 (PB 236 797)A07

EERC 74-10 "Applications of Realiability-Based, Global Cost Optimization to Design of Earthquake Resistant Structures," by E. Vitiello and K. S. Pister - 1974 (PB 237 231)A06

EERC 74-11 "Liquefaction of Gravelly Soils under Cyclic Loading Conditions," by R. T. Wong, H. B. Seed, and C. K. Chan - 1974 (PB 242 042)A03

EERC 74-12 "Site-Dependent Spectra for Earthquake-Resistant Design," by H. B. Seed, C. Ugas, and J. Lysmer - 1974 (PB 240 953)A03

EERC 74-13 "Earthquake Simulator Study of a Reinforced Concrete Frame," by P. Hidalgo and R. W. Clough - 1974 (PB 241 944)A13

EERC 74-14 "Nonlinear Earthquake Response of Concrete Gravity Dams," by N. Pal - 1974 (AD/A 006 583)A06

EERC 74-15 "Modeling and Identification in Nonlinear Structural Dynamics - I. One Degree of Freedom Models," by N. Distefano and A. Rath - 1974 (PB 241 548)A06

EERC 75-1 "Determination of Seismic Design Criteria for the Dumbarton Bridge Replacement Structure, Vol. I: Description, Theory and Analytical Modeling of Bridge and Parameters," by F. Baron and S.-H. Pang - 1975 (PB 259 407)A15

EERC 75-2 "Determination of Seismic Design Criteria for the Dumbarton Bridge Replacement Structure, Vol. II: Numerical Studies and Establishment of Seismic Design Criteria," by F. Baron and S.-H. Pang - 1975 (PB 259 408)A11 [For set of EERC 75-1 and 75-2 (PB 241 454)A09]

EERC 75-3 "Seismic Risk Analysis for a Site and a Metropolitan Area," by C. S. Oliveira - 1975 (PB 248 134)A09

EERC 75-4 "Analytical Investigations of Seismic Response of Short, Single or Multiple-Span Highway Bridges," by M.-C. Chen and J. Penzien - 1975 (PB 241 454)A09

EERC 75-5 "An Evaluation of Some Methods for Predicting Seismic Behavior of Reinforced Concrete Buildings," by S. A. Mahin and V. V. Bertero - 1975 (PB 246 306)A16

EERC 75-6 "Earthquake Simulator Story of a Steel Frame Structure, Vol. I: Experimental Results," by R. W. Clough and D. T. Tang - 1975 (PB 243 981)A13

EERC 75-7 "Dynamic Properties of San Bernardino Intake Tower," by D. Rea, C.-Y Liaw and A. K. Chopra - 1975 (AD/A 008 406)A05

EERC 75-8 "Seismic Studies of the Articulation for the Dumbarton Bridge Replacement Structure, Vol. 1: Description, Theory and Analytical Modeling of Bridge Components," by F. Baron and R. E. Hamati - 1975 (PB 251 539)A07

EERC 75-9 "Seismic Studies of the Articulation for the Dumbarton Bridge Replacement Structure, Vol. 2: Numerical Studies of Steel and Concrete Girder Alternates," by F. Baron and R. E. Hamati - 1975 (PB 251 540)A10

EERC 75-10 "Static and Dynamic Analysis of Nonlinear Structures," by D. P. Mondkar and G. H. Powell - 1975 (PB 242 434)A08

EERC 75-11 "Hysteretic Behavior of Steel Columns," by E. P. Popov, V. V. Bertero, and S. Chandramouli - 1975 (PB 252 365)A11

EERC 75-12 "Earthquake Engineering Research Center Library Printed Catalog " - 1975 (PB 243 711)A26

EERC 75-13 "Three Dimensional Analysis of Building Systems (Extended Version)," by E. L. Wilson, J. P. Hollings, and H. H. Dovey - 1975 (PB 243 989)A07

EERC 75-14 "Determination of Soil Liquefaction Characteristics by Large-Scale Laboratory Tests," by P. De Alba, C. K. Chan, and H. B. Seed - 1975 (NUREG 0027)A08

EERC 75-15 "A Literature Survey - Compressive, Tensile, Bond and Shear Strength of Masonry," by R. L. Mayes and R. W. Clough - 1975 (PB 246 292)A10

EERC 75-16 "Hysteretic Behavior of Ductile Moment-Resisting Reinforced Concrete Frame Components," by V. V. Bertero and E. P. Popov - 1975 (PB 246 388)A05

EERC 75-17 "Relationships Between Maximum Acceleration, Maximum Velocity, Distance from Source, Local Site Conditions for Moderately Strong Earthquakes," by H. B. Seed, R. Murarka, J. Lysmer, and I. M. Idriss - 1975 (PB 248 172)A03

EERC 75-18 "The Effects of Method of Sample Preparation on the Cyclic Stress-Strain Behavior of Sands," by J. Mulilis, C. K. Chan, and H. B. Seed - 1975 (Summarized in EERC 75-28)

EERC 75-19 "The Seismic Behavior of Critical Regions of Reinforced Concrete Components as Influenced by Moment, Shear and Axial Force," by M. B. Atalay and J. Penzien - 1975 (PB 258 842)A11

EERC 75-20 "Dynamic Properties of an Eleven Story Masonry Building," by R. M. Stephen, J. P. Hollings, J. G. Bouwkamp, and D. Jurukovski - 1975 (PB 246 945)A04

EERC 75-21 "State-of-the-Art in Seismic Strength of Masonry - An Evaluation and Review," by R. L. Mayes and R. W. Clough - 1975 (PB 249 040)A07

EERC 75-22 "Frequency Dependent Stiffness Matrices for Viscoelastic Half-Plane Foundations," by A. K. Chopra, P. Chakrabarti, and G. Dasgupta - 1975 (PB 248 121)A07

EERC 75-23 "Hysteretic Behavior of Reinforced Concrete Framed Walls," by T. Y. Wang, V. V. Bertero, and E. P. Popov - 1975

EERC 75-24 "Testing Facility for Subassemblages of Frame-Wall Structural Systems," by V. V. Bertero, E. P. Popov, and T. Endo - 1975

EERC 75-25 "Influence of Seismic History on the Liquefaction Characteristics of Sands," by H. B. Seed, K. Mori, and C. K. Chan - 1975 (Summarized in EERC 75-28)

EERC 75-26 "The Generation and Dissipation of Pore Water Pressures during Soil Liquefaction," by H. B. Seed, P. P. Martin, and J. Lysmer - 1975 (PB 252 648)A03

EERC 75-27 "Identification of Research Needs for Improving Aseismic Design of Building Structures," by V. V. Bertero - 1975 (PB 248 136)A05

EERC 75-28 "Evaluation of Soil Liquefaction Potential during Earthquakes," by H. B. Seed, I. Arango, and C. K. Chan - 1975 (NUREG 0026)A13

EERC 75-29 "Representation of Irregular Stress Time Histories by Equivalent Uniform Stress Series in Liquefaction Analyses," by H. B. Seed, I. M. Idriss, F. Makdisi, and N. Banerjee - 1975 (PB 252 635)A03

EERC 75-30 "FLUSH - A Computer Program for Approximate 3-D Analysis of Soil-Structure Interaction Problems," by J. Lysmer, T. Udaka, C.-F. Tsai, and H. B. Seed - 1975 (PB 259 332)A07

EERC 75-31 "ALUSH - A Computer Program for Seismic Response Analysis of Axisymmetric Soil-Structure Systems," by E. Berger, J. Lysmer, and H. B. Seed - 1975

EERC 75-32 "TRIP and TRAVEL - Computer Programs for Soil-Structure Interaction Analysis with Horizontally Travelling Waves," by T. Udaka, J. Lysmer, and H. B. Seed - 1975

EERC 75-33 "Predicting the Performance of Structures in Regions of High Seismicity," by J. Penzien - 1975 (PB 248 130)A03

EERC 75-34 "Efficient Finite Element Analysis of Seismic Structure-Soil-Direction," by J. Lysmer, H. B. Seed, T. Udaka, R. N. Hwang, and C.-F. Tsai - 1975 (PB 253 570)A03

EERC 75-35 "The Dynamic Behavior of a First Story Girder of a Three-Story Steel Frame Subjected to Earthquake Loading," by R. W. Clough and L.-Y. Li - 1975 (PB 248 841)A05

EERC 75-36 "Earthquake Simulator Story of a Steel Frame Structure, Volume II - Analytical Results," by D. T. Tang - 1975 (PB 252 926)A10

EERC 75-37 "ANSR-I General Purpose Computer Program for Analysis of Non-Linear Structural Response," by D. P. Mondkar and G. H. Powell - 1975 (PB 252 386)A08

EERC 75-38 "Nonlinear Response Spectra for Probabilistic Seismic Design and Damage Assessment of Reinforced Concrete Structures," by M. Murakami and J. Penzien - 1975 (PB 259 530)A05

EERC 75-39 "Study of a Method of Feasible Directions for Optimal Elastic Design of Frame Structures Subjected to Earthquake Loading," by N. D. Walker and K. S. Pister - 1975 (PB 247 781)A06

EERC 75-40 "An Alternative Representation of the Elastic-Viscoelastic Analogy," by G. Dasgupta and J. L. Sackman - 1975 (PB 252 173)A03

EERC 75-41 "Effect of Multi-Directional Shaking on Liquefaction of Sands," by H. B. Seed, R. Pyke, and G. R. Martin - 1975 (PB 258 781)A03

EERC 76-1 "Strength and Ductility Evaluation of Existing Low-Rise Reinforced Concrete Buildings - Screening Method," by T. Okada and B. Bresler - 1976 (PB 257 906)A11

EERC 76-2 "Experimental and Analytical Studies on the Hysteretic Behavior of Reinforced Concrete Rectangular and T-Beams," by S.-Y. M. Ma, E. P. Popov, and V. V. Bertero - 1976 (PB 260 843)A12

EERC 76-3 "Dynamic Behavior of a Multistory Triangular-Shaped Building," by J. Petrovski, R. M. Stephen, E. Gartenbaum, and J. G. Bouwkamp - 1976

EERC 76-4 "Earthquake Induced Deformations of Earth Dams," by N. Serff and H. B. Seed - 1976

EERC 76-5 "Analysis and Design of Tube-Type Tall Building Structures," by H. de Clercq and G. H. Powell - 1976 (PB 252 220)A10

EERC 76-6 "Time and Frequency Domain Analysis of Three-Dimensional Ground Motions,San Fernando Earthquake," by T. Kubo and J. Penzien - 1976 (PB 260 556)A11

EERC 76-7 "Expected Performance of Uniform Building Code Design Masonry Structures," by R. L. Mayes, Y. Omote, S. W. Chen, and R. W. Clough - 1976

EERC 76-8 "Cyclic Shear Tests on Concrete Masonry Piers, Part I - Test Results," by R. L. Mayes, Y. Omote, and R. W. Clough - 1976 (PB 264 424)A06

EERC 76-9 "A Substructure Method for Earthquake Analysis of Structure-Soil Interaction," by J. A. Gutierrez and A. K. Chopra - 1976 (PB 247 783)A08

EERC 76-10 "Stabilization of Potentially Liquefiable San Deposits using Gravel Drain Systems," by H. B. Seed and J. R. Booker - 1976 (PB 248 820)A04

EERC 76-11 "Influence of Design and Analysis Assumptions on Computed Inelastic Response of Moderately Tall Frames," by G. H. Powell and D. G. Row - 1976

EERC 76-12 "Sensitivity Analysis for Hysteretic Dynamic Systems: Theory and Applications," by D. Ray, K. S. Pister, and E. Polak - 1976 (PB 262 859)A04

EERC 76-13 "Coupled Lateral Torsional Response of Buildings to Ground Shaking," by C. L. Kan and A. K. Chopra - 1976 (PB 257 907)A09

EERC 76-14 "Seismic Analyses of the Banco de America," by V. V. Bertero, S. A. Mahin, and J. A. Hollings - 1976

EERC 76-15 "Reinforced Concrete Frame 2: Seismic Testing and Analytical Correlation," by R. W. Clough and J. Gidwani - 1976 (PB 261 323)A08

EERC 76-16 "Cyclic Shear Tests on Masonry Piers, Part II - Analysis of Test Results," by R. L. Mayes, Y. Omote, and R. W. Clough - 1976

EERC 76-17 "Structural Steel Bracing Systems: Behavior under Cyclic Loading," by E. P. Popov, K. Takanashi, and C. W. Roeder - 1976 (PB 260 715)A05

EERC 76-18 "Experimental Model Studies on Seismic Response of High Curved Overcrossings," by D. Williams and W. G. Godden - 1976

EERC 76-19 "Effects of Non-Uniform Seismic Disturbances on the Dumbarton Bridge Replacement Structure," by F. Baron and R. E. Hamati - 1976

EERC 76-20 "Investigation of the Inelastic Characteristics of a Single Story Steel Structure using System Identification and Shaking Table Experiments," by V. C. Matzen and H. D. McNiven - 1976 (PB 258 453)A07

EERC 76-21 "Capacity of Columns with Splice Imperfections," by E. P. Popov, R. M. Stephen and R. Philbrick - 1976 (PB 260 378)A04

EERC 76-22 "Response of the Olive View Hospital Main Building during the San Fernando Earthquake," by S. A. Mahin, V. V. Bertero, A. K. Chopra, and R. Collins," - 1976

EERC 76-23 "A Study on the Major Factors Influencing the Strength of Masonry Prisms," by N. M. Mostaghel, R. L. Mayes, R. W. Clough, and S. W. Chen - 1976

EERC 76-24 "GADFLEA - A Computer Program for the Analysis of Pore Pressure Generation and Dissipation during Cyclic or Earthquake Loading," by J. R. Booker, M. S. Rahman, and H. B. Seed - 1976 (PB 263 947)A04

EERC 76-25 "Rehabilitation of an Existing Building: A Case Study," by B. Bresler and J. Axley - 1976

EERC 76-26 "Correlative Investigations on Theoretical and Experimental Dynamic Behavior of a Model Bridge Structure," by K. Kawashima and J. Penzien - 1976 (PB 263 388)A11

EERC 76-27 "Earthquake Response of Coupled Shear Wall Buildings," by T. Srichatrapimuk - 1976 (PB 265 157)A07

EERC 76-28 "Tensile Capacity of Partial Penetration Welds," by E. P. Popov and R. M. Stephen - 1976 (PB 262 899)A03

EERC 76-29 "Analysis and Design of Numerical Integration Methods in Structural Dynamics," by H. M. Hilber - 1976 (PB 264 410)A06

EERC 76-30 "Contribution of a Floor System to the Dynamic Characteristics of Reinforced Concrete Buildings," by L. E. Malik and V. V. Bertero - 1976

EERC 76-31 "The Effects of Seismic Disturbances on the Golden Gate Bridge," by F. Baron, M. Arikan, R. E. Hamati - 1976

EERC 76-32 "Infilled Frames in Earthquake-Resistant Construction," by R. E. Klingner and V. V. Bertero - 1976 (PB 265 892)A13

UCB/EERC-77/01 "PLUSH - A Computer Program for Probabilistic Finite Element Analysis of Seismic Soil-Structure Interaction," by M. P. Romo Organista, J. Lysmer, and H. B. Seed - 1977

UCB/EERC-77/02 "Soil-Structure Interaction Effects at the Humboldt Bay Power Plant in the Ferndale Earthquake of June 7, 1975," by J. E. Valera, H. B. Seed, C.-F. Tsai, and J. Lysmer - 1977 (B 265 795)A04

UCB/EERC-77/03 "Influence of Sample Disturbance on Sand Response to Cyclic Loading," by K. Mori, H. B. Seed, and C. K. Chan - 1977 (PB 267 352)A04

UCB/EERC-77/04 "Seismological Studies of Strong Motion Records," by J. Shoja-Taheri - 1977 (PB 269 655)A10

UCB/EERC-77/05 "Testing Facility for Coupled Shear Walls," by L.-H. Lee, V. V. Bertero, and E. P. Popov - 1977

UCB/EERC-77/06 "Developing Methodologies for Evaluating the Earthquake Safety of Existing Buildings," No. 1 - B. Bresler; No. 2 - B. Bresler, T. Okada, and D. Zisling; No. 3 - T. Okada and B. Bresler; No. 4 - V. V. Bertero and B. Bresler - 1977 (PB 267 354)A08

UCB/EERC-77/07 "A Literature Survey - Transverse Strength of Masonry Walls," by Y. Omote, R. L. Mayes, S. W. Chen, and R. W. Clough - 1977

UCB/EERC-77/08 "DRAIN-TABS: A Computer Program for Inelastic Earthquake Response of Three Dimensional Buildings," by R. Guendelman-Israel and G. H. Powell - 1977

UCB/EERC-77/09 "SUBWALL: A Special Purpose Finite Element Computer Program for Practical Elastic Analysis and Design of Structural Walls with Substructure Option," by D. Q. Le, H. Petersson, and E. P. Popov - 1977

UCB/EERC-77/10 "Experimental Evaluation of Seismic Design Methods for Broad Cylindrical Tanks," by D. P. Clough - 1977

UCB/EERC-77/11 "Earthquake Engineering Research at Berkeley - 1976," - 1977

UCB/EERC-77/12 "Automated Design of Earthquake Resistant Multistory Steel Building Frames," by N. D. Walker, Jr. - 1977

UCB/EERC-77/13 "Concrete Confined by Rectangular Hoops and Subjected to Axial Loads," by J. Vallenas, V. V. Bertero, and E. P. Popov - 1977

UCB/EERC-77/14 "Seismic Strain Induced in the Ground during Earthquakes," by Y. Sugimura - 1977

UCB/EERC-77/15 "Bond Deterioration under Generalized Loading," by V. V. Bertero, E. P. Popov, and S. Viwathanatepa - 1977

UCB/EERC-77/16 "Computer-Aided Optimum Design of Ductile Reinforced Concrete Moment-Resisting Frames," by S. W. Zagajeski and V. V. Bertero - 1977

UCB/EERC-77/17 "Earthquake Simulation Testing of a Stepping Frame with Energy-Absorbing Devices," by J. M. Kelly and D. F. Tsztoo - 1977

UCB/EERC-77/18 "Inelastic Behavior of Eccentrically Braced Steel Frames under Cyclic Loadings," by C. W. Roeder and E. P. Popov - 1977

UCB/EERC-77/19 "A Simplified Procedure for Estimating Earthquake-Induced Deformation in Dams and Embankments," by F. I. Makdisi and H. B. Seed - 1977

UCB/EERC-77/20 "The Performance of Earth Dams during Earthquakes," by H. B. Seed, F. I. Makdisi, and P. de Alba - 1977

UCB/EERC-77/21 "Dynamic Plastic Analysis using Stress Resultant Finite Element Formulation," by P. Lukkunapvasit and J. M. Kelly - 1977

UCB/EERC-77/22 "Preliminary Experimental Study of Seismic Uplift of a Steel Frame," by R. W. Clough and A. A. Huckelbridge - 1977

UCB/EERC-77/23 "Earthquake Simulator Tests of a Nine-Story Steel Frame Allowed to Uplift," by A. A. Huckelbridge - 1977

UCB/EERC-77/24 "Nonlinear Soil-Structure Interaction of Skew Highway Bridges," by M.-C. Chen and J. Penzien - 1977

UCB/EERC-77/25 "Seismic Analysis of an Offshore Structure Supported on Pile Foundations," by D. D.-N. Liou - 1977

UCB/EERC-77/26 "Dynamic Stiffness Matrices for Homogeneous Viscoelastic Half-Planes," by G. Dasgupta and A. K. Chopra - 1977

UCB/EERC-77/27 "A Practical Soft Story Earthquake Isolation System," by J. M. Kelly and J. M. Eidinger - 1977

UCB/EERC-77/28 "Seismic Safety of Existing Buildings and Incentives for Hazard Mitigation in San Francisco: An Exploratory Study," by A. J. Meltsner - 1977

UCB/EERC-77/29 "Dynamic Analysis of Electrohydraulic Shaking Tables," by D. Rea, S. Abedi-Hayati, and Y. Takahashi - 1977

UCB/EERC-77/30 "An Approach for Improving Seismic-Resistant Behavior of Reinforced Concrete Interior Joints," by B. Galunic, V. V. Bertero, and E. P. Popov - 1977

UCB/EERC-78/01 "The Development of Energy-Absorbing Devices for Aseismic Base Isolation Systems," by J. M. Kelly and D. F. Tsztoo - 1978

UCB/EERC-78/02 "Effect of Tensile Prestrain on the Cyclic Response of Structural Steel Connections," by J. G. Bouwkamp and A. Mukhopadhyay - 1978

UCB/EERC-78/03 "Experimental Results of an Earthquake Isolation System using Natural Rubber Bearings," by J. M. Eidinger and J. M. Kelly - 1978

UCB/EERC-78/04 "Seismic Behavior of Tall Liquid Storage Tanks," by A. Niwa - 1978

UCB/EERC-78/05 "Hysteretic Behavior of Reinforced Concrete Columns Subjected to High Axial and Cyclic Shear Forces," by S. W. Zagajeski, V. V. Bertero, and E. P. Popov - 1978

UCB/EERC-78/06 "Inelastic Beam-Column Elements for the ANSR-I Program," by A. Riahi, D. G. Row, and G. H. Powell - 1978

UCB/EERC-78/07 "Studies of Structural Response to Earthquake Ground Motion," by O. A. Lopez and A. K. Chopra - 1978